Author:
Del Broccolo, Simone

Title:
Sandwich core periodic cell topology effects

SANDWICH CORE PERIODIC CELL TOPOLOGY EFFECTS

Kirigami-inspired cellular cores with improved dynamic properties

By

Simone Del Broccolo

Department of Applied Mechanics
Université Bourgogne Franche-Comté

Faculty of Aerospace Engineering
University of Bristol

February 2020

A dissertation submitted to the University of Bristol in accordance with the requirements of the degree of DOCTOR OF PHILOSOPHY in the Faculty of Engineering

Word count: 38415

ABSRACT

This research work is part of the VIPER project, a European Joint Doctorate network focused on research in vibroacoustics of periodic media. It has received funding from the European Union's Horizon 2020 research and innovation programme under Marie Curie grant agreement No 675441. The Universities involved are the E.U. academic partners Université de Franche-Comté (FR.) and University of Bristol (U.K.). Since VIPER is part of an Innovative Training Network (MSCA-ITN) this research work was also carried out in collaboration with the non-EU academic partner Georgia Institute of Technology (U.S.A.) and the EU industrial partner iChrome, based in Bristol (U.K.). The aim of the project is to improve the vibroacoustic properties of periodic structures which are widely used in the engineering domain due to their main characteristic, periodicity, which makes them a convenient solution for manufacturing guidelines aspects. Real life macroscopic examples are railway tracks, bridges, and airplane fuselages, amongst many others. Honeycomb sandwich panels are another example and are well known to provide interesting static out of plane properties because of their high equivalent stiffness whilst containing mass and for this reason, they are widely used as a 'building brick' in the Aerospace, Automotive and Naval industries. The environment in which these materials operate involve external forces which excites them in the mid-low frequency range. However, while a high stiffness/mass ratio is a desirable static property, the vibration frequency domain is usually in the high range and therefore they become poor mechanical and acoustic insulators within the frequency range they are usually subject to. The question addressed then is simple: how periodic concepts can improve the broadband vibroacoustic signatures and performances of those structures? Most of vibroacoustic solutions are frequency band limited, specific, and usually include the addition of mass, which for certain engineering segments is disadvantageous. Including vibroacoustic design rules at early stage of product development is one of the main research targets to improve their performance and would allow to design tuned structures without any later intervention or mass increment. This work focuses on investigating existing sandwich panel core topologies and attempt to create novel improved structures. The research was carried out trying to maintain the desired structural properties which justifies the usage of such solution in the first place but also considering its potential use as a platform for Multiphysics resonating periodic material inserts. Such cellular cores had to

manufactured using Kirigami, which is a variation of Origami, an ancient Japanese technique that consists in creating 3D structures by folding a 2D sheet of material. This manufacturing technique can be used as a systematic way to produce general honeycomb configurations with off-the-shelf long fibre composites by thermoforming and/or autoclaving, which by itself, is a novelty in the honeycomb domain as they are often produced using metals or plastics. The main indicator on which I will focus to evaluate the vibroacoustic performance of the proposed innovative topologies will be the number and range of stopbands, also known as a bandgaps, which describe the frequency ranges in which elastic waves are not transmitted within the structure, in combination with the constituent material and its damping properties. This manuscript is organised in four chapters. The first consists of an overview of periodic structures in the various engineering domains followed by an introduction on elastic wave propagation in periodic media. Sandwich panels and their most popular manufacturing techniques will also be described. Also, phenomena like Bragg or resonant bandgaps will be explained as well as the Floquet-Bloch theory applied to macro-scale structures such as aeronautical cellular cores. The latter mathematical derivation will be merged with the Finite Element Analysis approach and implemented as the basis for the numerical prediction tools specially developed to allow parametric investigations on the complete sandwich panels or bare cores. The Floquet-Bloch theory allows us to harvest crucial information on the dynamic behaviour of the whole structure by performing our analysis only on a small portion of it which will be called now on the 'unit cell'. In the second chapter, a preliminary bandgap investigation on a simple beam truss structure, and later, on kirigami derived tessellations is carried out. The reduced number of cell geometries obtainable with kirigami motivated me to invent Interlocking, which still respects all kirigami rules and unleashes the geometrical constraints of the parent technique. It also adds the possibility of obtaining long fibre composites multi material cores, which introduces a second level of periodicity, and may represent a novel platform able to accommodate and quickly interchange foams, viscoelastic patches, or resonators. The concept, manufacturing technique and the parametric bandgap investigation of some interlocking examples will be widely discussed in this chapter. The fourth chapter will focus on another vibration index, which is the out of plane transmissibility of interlocked cellular structures. Various Flax fibre composite honeycombs with thermoset as well as thermoplastic matrix were manufactured and tested. Finally, the manuscript will end with a conclusive paragraph where conclusions are drawn and possible future work as well as applications proposed. The coded software tools used for the investigations and the material characterisation used for the kirigami manufacturing will constitute the appendix.

ACKNOWLEDGEMENTS

This Doctoral thesis is part of the VIPER project (vibroacoustics of periodic media) which is an ITN (Innovative training Network) part of the European funded Marie Skłodowska-Curie Actions. It is indeed the result of a three-year long programme which produced innovative work reachable only through intense and complex training shared amongst the scientific community both academic and industrial. During this journey, an ITN Researcher inevitably interacts with a certain number of people who help, directly or not, in transforming an intuition into something tangible. If you are lucky enough, this number is relatively high, which means that other than accomplishing your research work duties, you also have achieved another important goal, which is to create a network of friends and colleagues around you. There are different aspects which make an ITN MSCA PhD programme unique but the most fascinating one is the international profile which confers you. Not only you have the chance of meeting people from around the globe, but you can also live in different countries, which by itself it is a source of knowledge that no book can really teach. For these reasons, I feel the necessity to thank a certain number of them, starting from those who contributed to my scientific development.

I would like to equally thank my thesis co-supervisors, Professors Morvan Ouisse and Fabrizio Scarpa, from the University of Bourgogne Franche Comte (France) and the University of Bristol (United Kingdom) respectively as well as my second supervisor during my stay at UBFC, Professor Emmanuel Foltete. The scientific contribution they brought to this work will never be forgotten, not only because together we produced various conference and journal papers, but mainly because it is during our meetings and under their guidance that I developed my knowledge about wave propagation in periodic media and composite manufacturing processes. Thanks to the ITN MSCA programme, they have always encouraged me to take part at trainings and conferences which has contributed to produce novel work, as this represented a positive motivational feature. Both Fabrizio and Morvan were also very helpful and understanding under a human point of view and helped in preparation and during the compulsory secondment periods, never denying me anything which could have helped in those delicate moments.

I would also like to thank Professor Massimo Ruzzene for hosting me at the Georgia Institute of Technology (U.S.A.) where I spent three months working in the Aerospace department laboratories. We had multiple meetings despite his busy schedule.

The development of a numerical tool, linked with the manufacturing technique used, was suggested by the industrial partner iChrome (Bristol – UK) and therefore I would like to thank Dr. Luca Lanzi for this opportunity.

Thank you to Professors Dimitrios Chronopoulos (University of Nottingham - UK) and Professor Bing Tie (CentraleSupélec Paris - FR) for reviewing the manuscript.

A big thank you goes also to all the Professors involved with the supervision of my colleagues, part of VIPER ITN MSCA Project, as well as all the ESR fellows. You all improved the quality of my work with your constructive critical comments and suggestions.

This thesis work included a complex and time demanding manufacturing process as well as experimental set ups. For this reason, amongst the many technicians who helped me, I cannot avoid mentioning Ian Chorley who is the most helpful and competent composite material and autoclave "lighthouse" technician at the Advanced Composites Centre laboratories (ACCIS – University of Bristol).

I would like to thank my friends and project colleagues Rita Palumbo and Dario Magliacano with whom I shared conferences, trainings, and enjoyable life moments. A heartily thank you goes to Marc-Antoine Campana, with whom I shared all the above as well as my time at GeorgiaTech. Thank you for the precious comments, shared knowledge and for being a good friend.

During these years I have committed all my energy into this project and the absence from home as well as the continuous travelling has affected my beloved ones. A MSCA PhD is not a usual job. The more you research the more questions arise and often the latter do not stay on the office desk when you head towards home affecting inevitably your lifestyle. I know these years have not been easy for any of us and I will always be thankful to all of you, who supported me and loved me regardless. For this I am forever grateful to my whole family, my parents, my sister Federica, my nephews Mattia and Beatrice and my cousin Farah, with whom I shared the homesickness from UK. Finally, this PhD gave me the chance of meeting a unique person, my partner. I want to deeply thank you Shamin for all the love and support offered throughout this life stage and for the commitment and sacrifices made. This shall not be forgotten.

AUTHOR'S DECLARATION

I declare that the work in this dissertation was carried out in accordance with the requirements of the University's Regulations and Code of Practice for Research Degree Programmes and that it has not been submitted for any other academic award. Except where indicated by specific reference in the text, the work is the candidate's own work. Work done in collaboration with, or with the assistance of, others, is indicated as such. Any views expressed in the dissertation are those of the author.

SIGNED: ..... DATE: .....

THESIS OBJECTIVES

Honeycomb sandwich panels are well known to provide interesting static out of plane properties (compression) because of their high equivalent stiffness whilst containing mass. However, this makes such structures possess a very high stiffness/mass ratio and therefore, their vibration frequency domain is usually in the high range. Sandwich panels are widely used in the Aerospace, Automotive and Naval industries because they all have the preference of obtaining lightweight structures but at the same time, the frequencies to be dealt with in their operating environments are in the mid-low range.

The aim of this PhD work is to obtain sandwich panel cores with improved vibroacoustic performances thanks to a honeycomb core topology investigation. This needs to be carried out trying to maintain the desired structural properties, which justifies the usage of such solution in the first place and considering its potential use as a platform for Multiphysics resonating periodic material inserts. Such cellular cores must be manufactured using Kirigami, which is a variation of Origami, an ancient Japanese technique that consists in creating 3D structures by folding a 2D sheet of material. This manufacturing technique can be used as a systematic way to produce general honeycomb configurations with off-the-shelf composites by thermoforming and/or autoclaving.

The main indicator chosen to evaluate the vibroacoustic performance was the number and range of stopbands that the structure might possess. A stopband, also known as a bandgap, describes frequency ranges in which elastic waves are not transmitted within the structure. It has been shown, starting from Brillouin[1], how geometrical periodicity or periodic changes in constituent material, attenuate the wave propagation (in the direction of the periodicity) because of the interaction between incident, reflected and transmitted waves at the discontinuity points. Since honeycombs are periodic structures themselves, they will act as passive mechanical filters due to their geometry. The investigation will be carried out changing, parametrically, the in-plane periodic topology of the sandwich cores and evaluate the evolution of the bandgaps, to control unwanted vibrations that could compromise and shorten the structures lifespan.

My research will therefore be organized as follows:

- Develop Kirigami tessellation patterns based on centre symmetric topology configurations and a tool that can create systematic honeycomb topologies easily implemented in CAD/CAM tools. The Kirigami patterns will also accommodate topologies

for inserts of different materials and devices, to be also used as potential platform for multiphysics resonating periodic materials for vibroacoustics.

- Perform numerical wave propagation analysis using Bloch wave theory to investigate the bandgap behaviour of the Kirigami 3D honeycombs. The numerical simulations will be carried out in a parametric form to identify optimized cell configurations able to perform bandgaps at specific frequency bandwidths, and compatible with mechanical and manufacturing constraints. Numerical models of the honeycombs with face skins for sandwich applications will be also developed.
- Manufacturing samples of the down selected Kirigami topologies using state-of-the-art production processes for thermoplastics and thermoset composites using a combination of CNC cutting/autoclaving/thermoforming with modular molds. The samples will be used to produce sandwich panels with skin laminates having aerospace or automotive grade.
- Perform experimental campaigns including bandgap validation, vibration transmissibility tests of the sandwich panels to measure the vibroacoustics behaviour of the Kirigami sandwich panels with the new honeycomb topologies and compare the results with predicted data from the numerical simulations. Selected mechanical tests will be also performed (flatwise compression) to assess the structural integrity of the sandwich concept.

TABLE OF CONTENTS

NOMENCLATURE

A_i	-	Vibrational input
A_o	-	Vibrational output
T_g	-	Glass transition temperature
v_g	-	Wave group velocity
$v_{longitudinal}$	-	Longitudinal propagation velocity
v_p	-	Wave phase velocity
$v_{transverse}$	-	Transverse propagation velocity
ρ_c	-	Unit cell's effective density
ω_n	-	Natural frequency
$\mathbb{C}$	-	Complex number
e	-	Child cell side dimension
f	-	Force vector
f	-	Frequency
n	-	Number of unit cells in the chain
q	-	Displacement vector
Q	-	Amplification factor
T	-	Period
$A1, A2$	-	Beam structure sections 1 and 2
t_1, t_2	-	Beam structure cross-section's height and width
B	-	Bulk modulus
$H(\omega)$	-	Frequency response function (linear domain)
Im	-	Imaginary component of $\mathbb{C}$
k	-	Wavenumber

L, L_x, L_y, L_z	-	Unit cell's encumbrance in x, y and z directions
Re	-	Real component of $\mathbb{C}$
S	-	Shear modulus
$X(\omega)$	-	Input signal
$Y(\omega)$	-	Output signal
j	-	$\sqrt{-1}$
K	-	Angular wavenumber
$\mathbb{T}$	-	Transmissibility
γ	-	Shift ratio between interlocked honeycombs
η	-	Loss factor
λ	-	Propagation constant and solution of the wave propagation eigenvalue problem
μ	-	Reduced wavenumber
ξ	-	Damping
ρ	-	Density
φ	-	Phase lag
ψ	-	Wavelength
ω	-	Angular frequency
ϑ	-	Internal angle referred to the unit cell
$\widetilde{\boldsymbol{D}}$	-	Condensed dynamic stiffness matrix
$\boldsymbol{K_r}$	-	Reduced stiffness matrix
$\boldsymbol{K_{uc}}$	-	Unit cell's stiffness matrix
$\boldsymbol{M_r}$	-	Reduced mass matrix
$\boldsymbol{M_{uc}}$	-	Unit cell's mass matrix
$\boldsymbol{\Lambda_R}, \boldsymbol{\Lambda_L}$	-	Transformation matrix for a substructure's displacement and force vectors
$\boldsymbol{\phi_{bd}}$	-	Static modes matrix
$\boldsymbol{\phi_c}$	-	Reduced basis of the fixed interface modes matrix

CB	-	Craig Bampton transformation matrix
T	-	Transfer Matrix
$\boldsymbol{D}$	-	Dynamic stiffness matrix
$\boldsymbol{I}$	-	Identity matrix
$\boldsymbol{K}$	-	Stiffness matrix
$\boldsymbol{K1}, \boldsymbol{K2}, \boldsymbol{K3}$	-	Stiffness matrix components of the quadratic formulation
$\boldsymbol{M}$	-	Mass matrix
$\boldsymbol{M1}, \boldsymbol{M2}, \boldsymbol{M3}$	-	Mass matrix components of the quadratic formulation
$\boldsymbol{P}, \boldsymbol{N}$	-	Transfer matrix decomposition matrices

SUBSCRIPTS

b	-	Bottom boundary degrees of freedom
bd	-	Boundary degrees of freedom
c	-	Condensed internal degrees of freedom
H	-	Horizontal direction
i	-	Internal degrees of freedom
l	-	Left boundary degrees of freedom
lb	-	*left-bottom corner boundary degrees of freedom*
lt	-	*left-top corner boundary degrees of freedom*
r	-	*right degrees of freedom*
rb	-	*right- bottom corner boundary degrees of freedom*
rt	-	*right-top corner boundary degrees of freedom*
t	-	*to-p boundary degrees of freedom*
V	-	Vertical direction
x	-	x-component
y	-	y-component

z	-	z-component
f	-	Front boundary degrees of freedom
p	-	Back boundary degrees of freedom
flb	-	Front-left-bottom boundary degrees of freedom
flt	-	Front-left-top boundary degrees of freedom
frb	-	Front-right-bottom boundary degrees of freedom
frt	-	Front-right-top boundary degrees of freedom
plt	-	Back-left- top boundary degrees of freedom
plb	-	Back-left-bottom boundary degrees of freedom
prb	-	Back-right-bottom boundary degrees of freedom
prt	-	Back-right-top boundary degrees of freedom

ACRONYMS

1D	-	Mono-dimensional
2D	-	Bi-dimensional
3D	-	Tri-dimensional
ACCIS	-	Bristol Composites Institute
ASCII	-	American Standard Code for Information Interchange
ASTM	-	American Society for Testing and Materials
BEAM4	-	ANSYS APDL beam element type (Timoshenko)
BEM	-	Boundary element method
CAD	-	Computer-aided design
CAM	-	Computer-aided manufacturing
CFRP	-	Carbon fibre reinforced plastics
CNC	-	Computer numerically controlled
DOF's	-	Degrees of freedom

EU	-	European Union
FE	-	Finite elements
FEM	-	Finite element method
FR	-	France
GIF	-	Graphics Interchange Format
GUI	-	Graphic user interface
IBZ	-	Irreducible Brillouin zone
ITN	-	Innovative training network
MAC	-	Modal assurance criterion
MSCA	-	Marie Skłodowska-Curie Actions
NI	-	National Instruments
PEEK	-	Poly-ether-ether-ketone
PFA	-	Polyfurfuryl Alcohol
PP	-	Polypropylene
RGB	-	Red, Green, Blue colour space
RHS	-	Right-hand side
SEA	-	Statistical energy analysis
SHELL 181	-	ANSYS APDL shell element type
TMM	-	Transfer matrix method
U.K.	-	United Kingdom
U.S.A.	-	United States of America
UBFC	-	Université Bourgogne Franche-Comté
VIPER	-	Vibroacoustics of periodic media (project acronym)
WFEM	-	Wave finite element method

CHAPTER 1

PERIODIC STRUCTURES AND WAVE PROPAGATION

The word Periodic finds its root in both the Latin "Periodus" and Greek "Periodos" language and it is composed by "Peri", which means 'around' and "odos", which means 'path'. This word was used to describe anything that would recur in time or space. When we associate the word periodic to a structure therefore, we intend to describe matter which exhibits some form of spatial periodicity. Such characteristic can be in its constituent material, internal geometry, or boundary conditions. We are constantly surrounded by periodic structures in every day's life. Nature has developed and produced during the centuries countless types of periodic structures using various materials. One of the first images that probably struck the mind of the reader as soon as the association of periodicity and nature was made is the insect engineering cellular honeycomb found in bee hives (*Figure 1*), which is a geometrically perfect repetition of hexagonal cells tightly packed and optimized in space occupancy used as storage for pollen, honey or larvae growth chambers. The hexagonal shape is not causal as it is the polygon with the smallest perimeter that fills a plane without leaving any gaps. Scientists and Engineers have always been inspired by nature and although mimicking perfection has not been reached, we are slowly and increasingly designing structures that resemble it.

In the civil engineering domain examples of applied structural periodicity are skyscrapers and bridges which have now surpassed the kilometre in height and length respectively, all assembled with identical components for most of their structure. In the transportation industry we have trains and train rails as well as space launchers or airplane fuselages. Those examples show macroscopic periodicity but if we look at them more carefully, engineered structural components such as classic bricks found in walls or stratified plates like composite sandwich structures are also periodic and have an effect in their static and dynamic behaviour. One of the main reasons periodic structures became so popular is because the chain-line manufacturing brought huge advantages to the industry in terms of cost-efficiency, as it is easier to produce a single item that can be used to create different final shapes rather than having to customize the manufacturing process to each application

or product. Also, smaller components are easier to handle and transport and can usually be stored more efficiently.

1.1 SANDWICH PANELS

The Aerospace segment is in favour of using low mass materials since the flying cost of the payload, whereas that may be airplane passengers or an interplanetary mission satellite, increases with the propellant consumption, as it is closely dependent with the overall mass. At the same time, the solicitations they undergo are considerable, and for this reason, honeycomb sandwich panels are a widely used solution as they are well known to provide good static out of plane properties because of their high equivalent stiffness. A sandwich panel is an assembled structure composed by two laminates kept apart by a low-density core as shown in *Figure 1*. The core can be made of a homogeneous porous material such as foams or be an assembled cellular structure produced from strips of aluminium, paper, or plastic glued or soldered into three-dimensional structures.

The use of sandwich panels has nowadays become a habit but the first application of those materials in this field has been patented by Hugo Junkers in 1915[2]. He described the possibility of replacing the fabric that used to cover aircrafts at that time, with metallic sheets, adding also that an eventual compression load could have been sustained by arranging side by side a series of cellular structures that could have had square, rectangular, triangular or hexagonal shape.

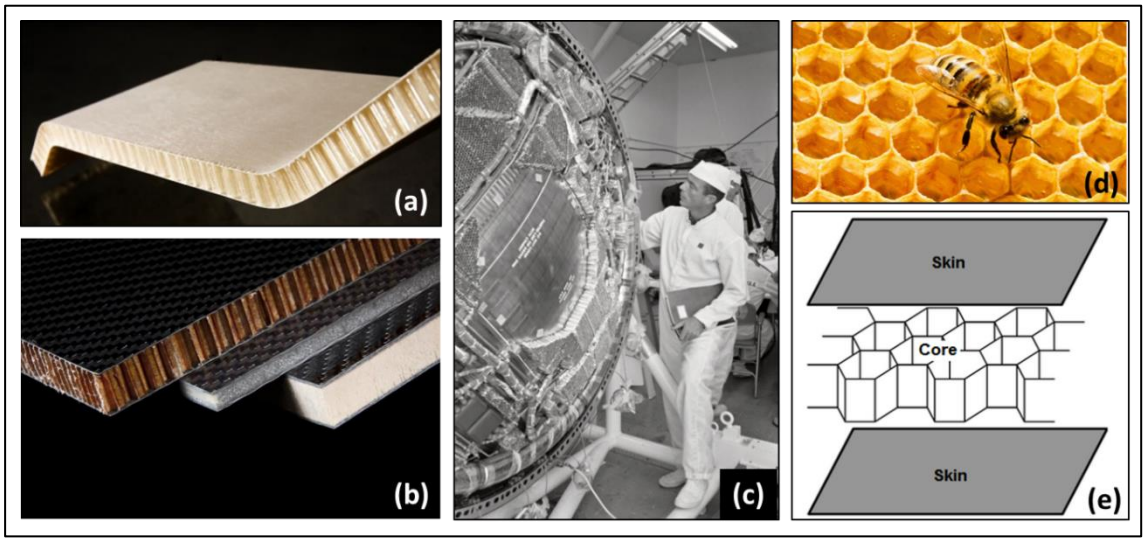

Figure 1 -(a) Curved sandwich panel[3] *(b); Sandwich panels with various types of cores*[4] *(c); Sandwich panels adopted on the Mercury capsule*[5]*; (d) Bee honeycomb*[6]*; (e) Sandwich panel structure*[7]

The production processes of sandwich panels depend upon the core type, geometry, and material, with the latter also involving the laminates as the bonding technologies might vary

accordingly. Generally, we can divide them in two: continuous and discontinuous processes. In discontinuous processes the laminate skins are produced separately from the core and then bonded together while in continuous processes, the chain-line produces a continuous panel that is cut to the desired length without interruptions. One of the main drawbacks of a discontinuous production is the low level of productivity but it is still the most used technology when exotic materials are being used or complex geometries desired. Both cellular core and laminate skins can be made of metal, plastic, or paper. In case the core is a foam, the material palette has fewer choices but includes metals and plastics.

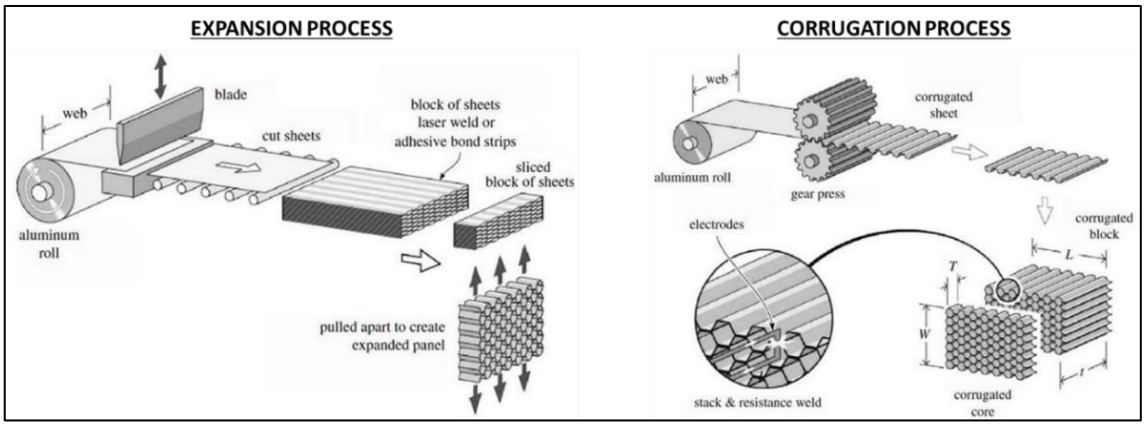

Figure 2 - Expansion and corrugation manufacturing processes for hexagonal cell honeycomb cores[8]

Cellular cores can be produced with various techniques. For metal cores, the sheet is pressed into half-hexagonal profiles which are then soldered or glued together or more commonly, glue is applied to metal strips with periodical spacing equal to the length of the hexagon side, and once the number of stacked strips, is sufficient to obtain a final core of desired dimensions, the stacked sheets are pulled apart (expanded) obtaining the honeycomb panel, as shown in *Figure 2*. Paper-resin honeycombs are also made with this technique but contrary to metal which keeps the final shape due to plastic deformation, the expanded paper honeycomb needs to be dipped into phenolic resin to stiffen it as well as providing protection from humidity which would decrease mechanical performance and cause swelling. Honeycombs can also be casted into a mold; silicone, rubber and many other materials which can be melted can be shaped into honeycombs thanks to this technique. Another way of creating honeycombs, especially made of ceramic material, is by extrusion; the ceramic honeycombs used to support exhaust catalysts in automobiles are made this way. Most of the honeycombs in available off shelf are created with the above-mentioned techniques but none of these allow to produce continuous long fibre honeycombs nor give the opportunity to create variable thickness cores without creating scrap material.

1.1.1 Art in engineering (Kirigami)

Kirigami is an ancient Japanese technique which derives from the more popular form of art known as Origami, which consists in folding a thin sheet of material which can be described as a bidimensional object, into a three-dimensional structure. The term Kirigami derives from the Japanese words "Kiru" which means "to cut" and "Kami" which is the word for paper. It is natural to think therefore that contrary to Origami, which only allows folding, Kirigami includes the possibility to cut the sheet of material, allowing to produce much more complex structures, as shown in *Figure 3*. This technique has received broad attention in various fields and if initially it was considered only a form of Art, in the past decade, Mathematicians and Engineers focused on it their studies, because of its potential applications.

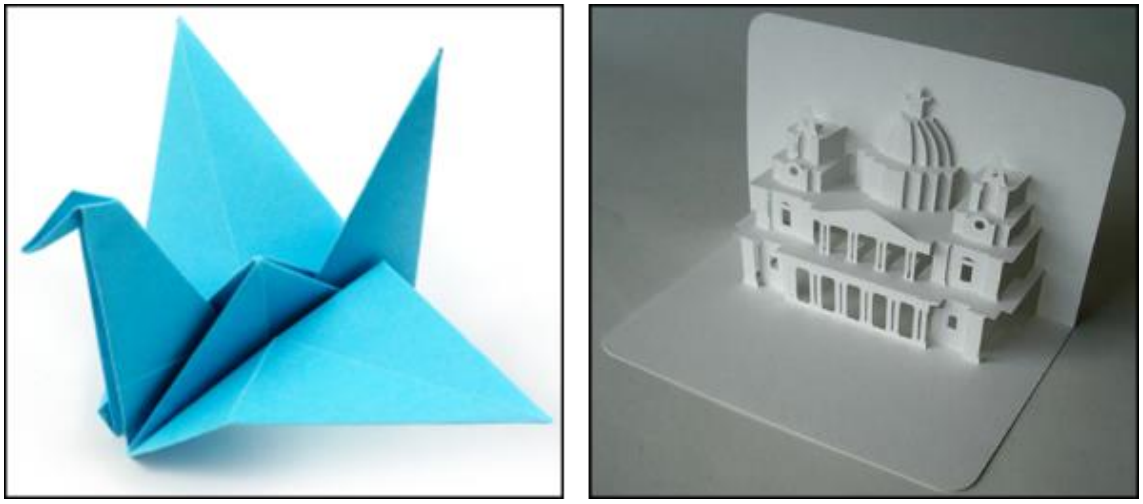

Figure 3 - Origami crane[9] *(left) and St. Paul's Cathedral Kirigami artwork*[10] *(right)*

Especially in the aerospace sector, the use of cellular cores is maximized because it allows to reduce the overall mass. Airplane fuselages or the body of a launcher, as well as antenna reflectors are often obtained with curved sandwich panels, which are very complex to produce and involve many steps of production as well as increased costs and limited to few but crucial applications. While the sandwich panel curved skins can be obtained with high accuracy nowadays, the internal core often has a cross section geometry which does not optimally match the required curvature. Phenomena like synclastic or anticlastic curvatures appear when folding along one axis and therefore the cores in-plane Poisson's ratio needs to be considered at the design stage. If classic hexagonal cores were to be used to produce a sandwich walled cylinder for example, it would require a certain degree of plastic deformation to force the core to follow the skin curvature. Clearly this would lead to prestress conditions as well as mechanical property non-homogeneity. The idea of

engineering Kirigami was first explored by Nojima and Saito[11],[12]; since then, the technique has been widely applied to both composite and thermoplastic materials to convert a 2D sheet material into a 3D structure[13],[14],[15]. In the Aerospace field, Scarpa, Saito and Agnese[16] designed and manufactured an autoclave cured woven Kevlar cellular wing box using Kirigami and, in 2015, Scarpa and Neville exploited this technique to create morphing open cell honeycombs, including embedded actuating cables[17]. Both work outcomes are shown in *Figure 5*.

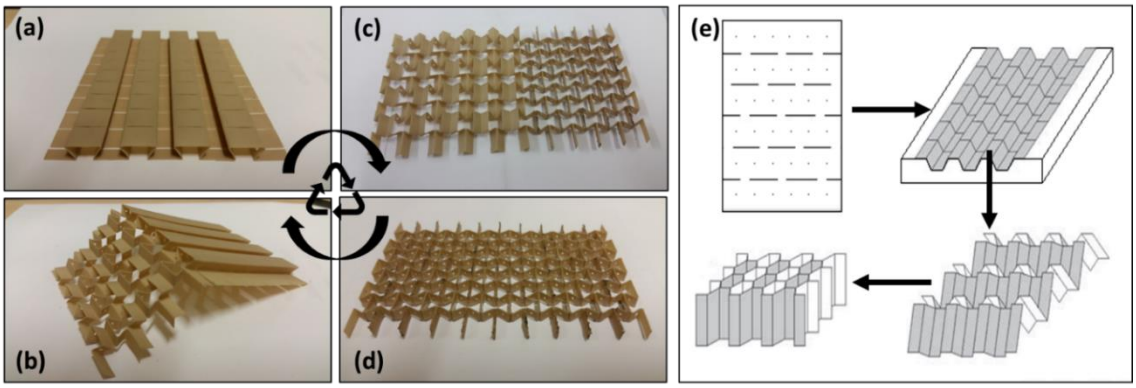

Figure 4 – Kirigami assembly sequence of an original recyclable thermoplastic PEEK cellular structure - (a) Thermoformed sheet; (b) folding; (c) gluing; (d) complete structure; (e) Kirigami full cycle scheme inspired by the one represented in Saito's work[16]

This technique is of great interest when producing cellular structures like honeycombs because of the many different pre-process treatments easily applicable whilst this usually is not possible with the classic manufacturing techniques. Kirigami has not been embraced by the industrial community as a standard manufacturing technique for cellular structures yet, but it is potentially suitable for mass continuous production. The possibility to pre-treat the material sheet before creating the 3D structure as well as reducing material scraps is very appealing. Traditional aluminium or paper honeycombs, in fact, require a contour cutter, 3D tracer and a numerically controlled machine, to obtain such geometries. The amount of material wasted during the machining is considerable and the post-process structural damage, although this can be reduced by using expensive machines, cannot be avoided. Furthermore, the possibility of using recyclable materials like thermoplastics, allows to reuse both, eventual scraps, and failed components to create new laminates and subsequently, new 3D structures. An example of Poly-ether-ether-ketone (PEEK) thermoplastic honeycomb is shown in *Figure 4.*

In 2014, Nojima, Saito and Pellegrino[18] developed a mathematical tool that creates Kirigami cutting/folding line diagrams, shown in *Figure 5* and *Figure 6*, for honeycombs that require complex curvatures, without any machining. Ventilation holes in cellular sandwich

cores destined to space purposes could be drilled in advance (*Figure 6*), when it's much easier to perform, than on ready-made honeycombs. They are required as they allow the escape of expanding air "trapped" into the cells during the manufacturing processes. Another possible pre-treatment could be spraying hydrophilic nano-coatings onto the sheets in order to protect the final artefact from dust and chemical attacks or improve it damping properties[19].

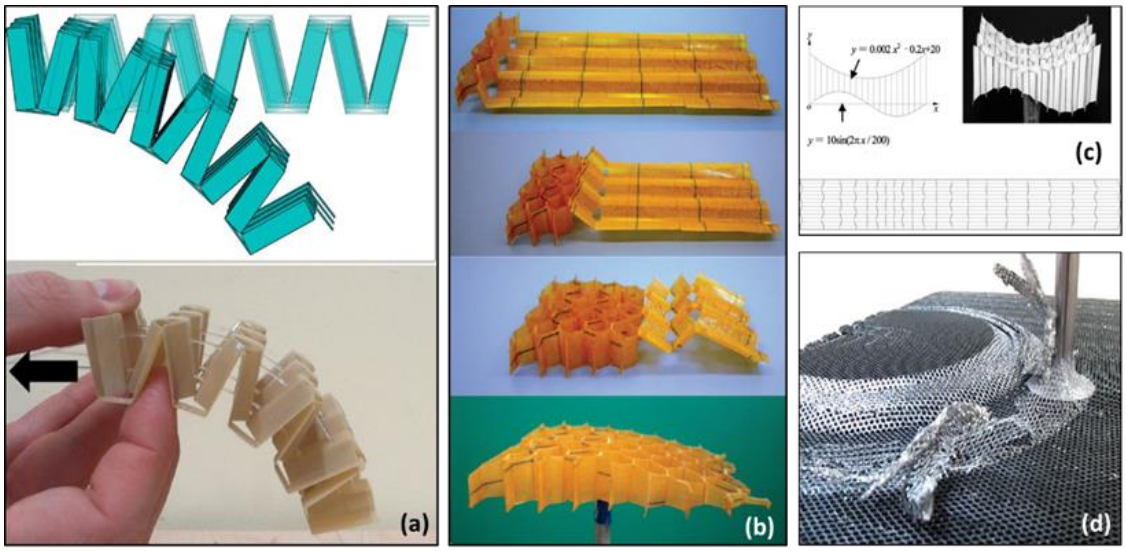

Figure 5 - Kirigami morphing PEEK structure[20]*; (b) Aramid paper kirigami Wing-box*[16]*; (c) Kirigami variable thickness honeycomb cutting pattern and paper demonstrator*[18]*; (d) Aluminium honeycomb machining*[21]

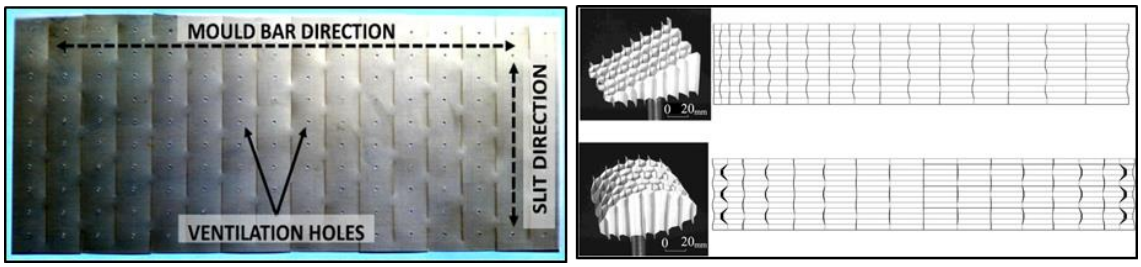

Figure 6 - Detail of honeycomb ventilation holes performed as a pre-process thanks to kirigami (left) Variable thickness honeycombs and their cutting patterns proposed by Nojima, Saito and Pellegrino[18] *(right)*

The tools and materials used so far for engineering applications of Kirigami are very diverse. Materials go from paper, thin metallic sheets, graphene, thermoplastics, elastomers, and composite materials like carbon fibre reinforced plastics (CFRP) or aramid paper (Kevlar fibers) [22]. Those materials can all be cut using the desired cut/fold Kirigami pattern and then used to create/thermoform a corrugated sheet with a multi-piece mold, constituted by a flat metallic surface where long metallic bars can be fixed on it, and a second plate, which closes the mold. The cutting pattern will end up orthogonal to the longitudinal axis of the bars used in the mold. The corrugated sheet then is folded back and forwards as shown in *Figure 7* obtaining our honeycomb.

Figure 7 - Natural fibre kirigami corrugated sheet and its folding process[23]

The Kirigami manufacturing process can be described as four main steps:

- CUTTING: A pattern of slits is generally produced according to the final cell geometry the user wants to obtain. Different tools can be used to produce such slits such as numerically controlled blades as well as laser cutters. The technique needs to be chosen accordingly to the material the user intends to use.
- MOLD PREFOLDING: The 2D silted and pierced sheet is then pre-folded according to the type of mold the user intends to use. The mold is then carefully closed and is ready to undergo the thermal treatment.
- THERMOFORMING / AUTOCLAVING: According to the material used, different thermal treatments can be used. Thermoplastics and composite materials with thermoplastic matrix are easier to use compared to thermosets prepregs since no curing time is required in the first case. Thermoplastics can also be reshaped as the thermal treatment for them is reversible. After this thermal process, a corrugated sheet is obtained, and it is ready for the next and final step.
- FOLDING/ADHESIVE: The corrugated sheet is folded onto itself forward and backwards along the slits. Once folded, the slits open into the final cell geometry and the zig-zag corrugated sheet is then glued into a 3D cellular structure with the desired thickness and cell shape.

Different types of composites which make use of various types of fibers and braiding can be used. Depending on the shape and dimension of the bars, experience showed that weaves which possess less threads perpendicular to the bar length direction are easier to be placed in the mold. In *Figure 8*, a diagram with different classes of materials, heat treatments and assembly technologies is proposed to underline the versatility of kirigami in the production of non-conventional cellular structures. A combination of bars with different cross-sections is also possible, but they must be compatible (they are so if they are all sliced out from the same plate without waste of material).

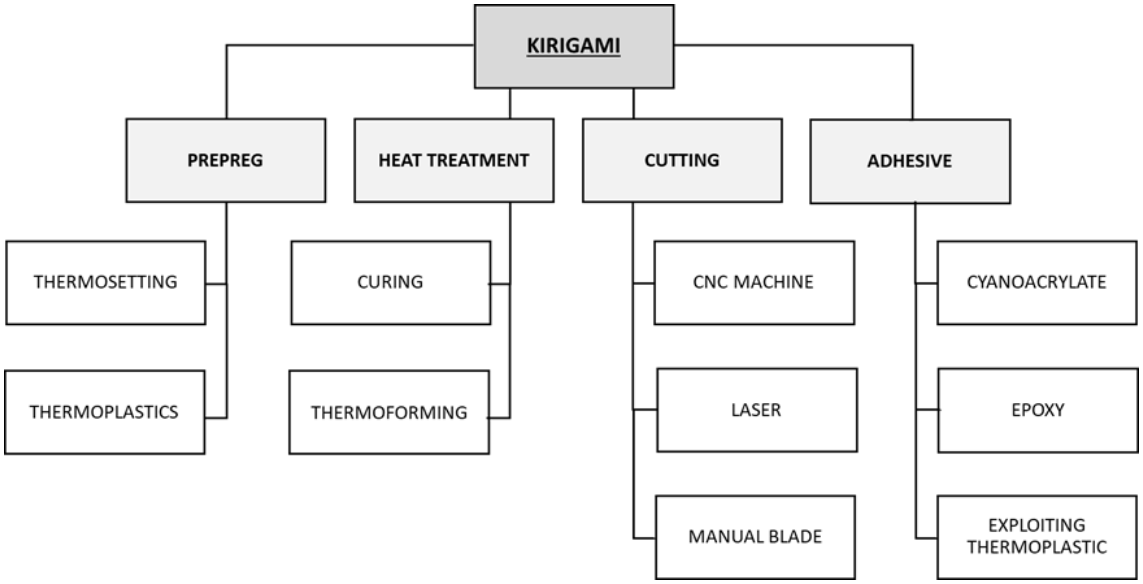

Figure 8 - Kirigami combination outline

By changing the inclination or height of the bar cross-section we can change the geometry of our honeycomb as well as its out of plane thickness to confer different elastic modulus and shear strength as suggested by Fadel, Ju and Summers [24].

1.1.2 Self-tessellating cores

A tessellation of a 2D surface consists in occupying the plane with one or more geometric shapes. Now this is possible with any type of shape if they can be tightly packed. Tessellations therefore can be made using abstract geometries as well as regular polygons. The mathematical classification of a two-dimensional periodic pattern is called wallpaper group or plane symmetry group[25]. E. Fedorov in 1891 proved that there were only seventeen distinct groups of possible patterns which consisted in self tessellating regular patterns as well as semi-regular ones[26]. The latter ones are patterns produced through a combination of regular polygons while a self-tessellating geometric shape can effectively fill the surface through a repetition of itself without leaving any gap nor overlapping in any point and therefore, without producing any other polygon as bypass product. A special kind of pattern is the regular tiling with regular polygons. These are also known as Euclidean tiling's and the polygons which satisfy the requirements are the triangle, the square and the hexagon. Those tessellations, in fact any tessellation, can be used to produce a cellular core structure, because the cells are simply extruded from the surface pattern. Not all are kirigami friendly because the folding/cutting lines can't happen in correspondence of the cell vertex, but, since they are some of the most common cores and grid structures found in engineering, they represented the starting point of this work.

1.1.3 Kirigami manufacturing limitations

Kirigami allows the creation of honeycombs with cells of different shapes. To obtain a regular tessellation kirigami honeycomb, one must guarantee that the cell cross-section has two parallel sides, of same dimensions, which face each other once the sheet is folded back. This can be obtained if the bars used to form the corrugated sheet have a cross section with a side parallel to the base. Bars with Trapezoid cross section (Trapeziums, Rectangles, Squares, Parallelograms and Rhombus) are all compatible with Kirigami and shown in *Figure 9*. Some of them though might make the process slightly more difficult, especially if the sheet must be folded over acute angles.

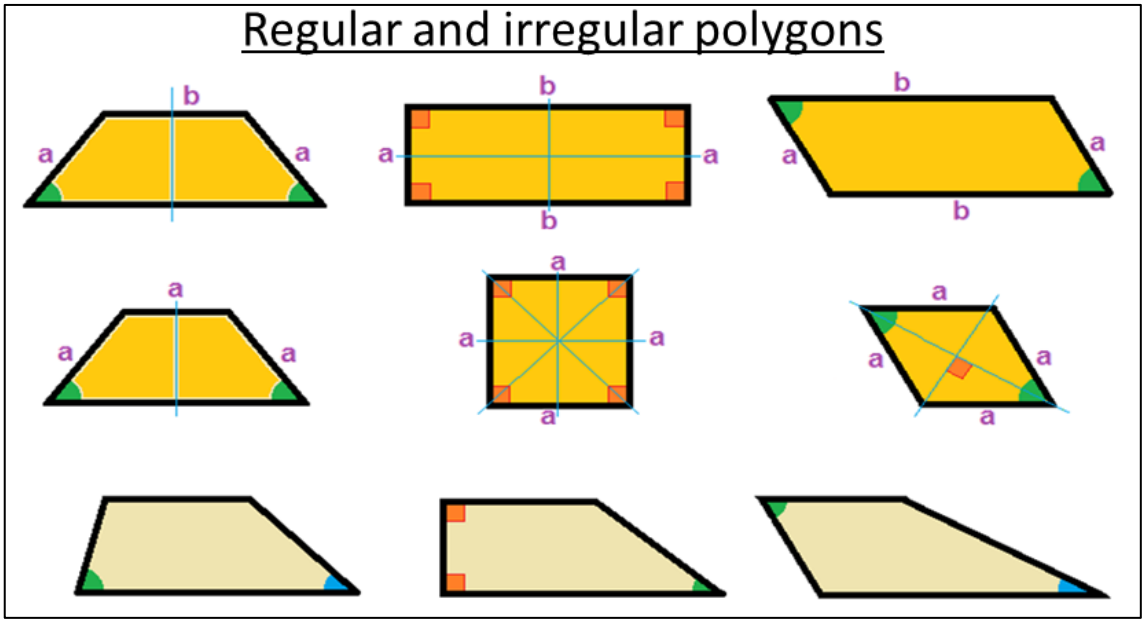

Figure 9 – Examples of Kirigami allowed bar cross sections derived from regular and irregular polygons

Clearly, if the cross section of the bars is compatible, it is possible to mix them to create hybrid cores, like the AuxHex configuration[15] which was analysed in section *2.3.4*. In *Figure 10* a diagram of the homogeneous cross section tool bars to produce regular hexagonal cores as well as the mixed bars used to produce the AuxHex core is shown, and it is clear how the same tool bars used for the hexagonal core can be used to produce the re-entrant configuration. In blue, the selected prepreg or thermoplastic is represented in blue. The tessellation freedom thought felt quite restrictive and a summary of advantages and disadvantages for the kirigami technique applied to the manufacturing and design of cellular core structures for sandwich panels is outlined in *Table 1*. Cross reference with some basic kirigami concepts presented in section *1.1.1* should be considered.

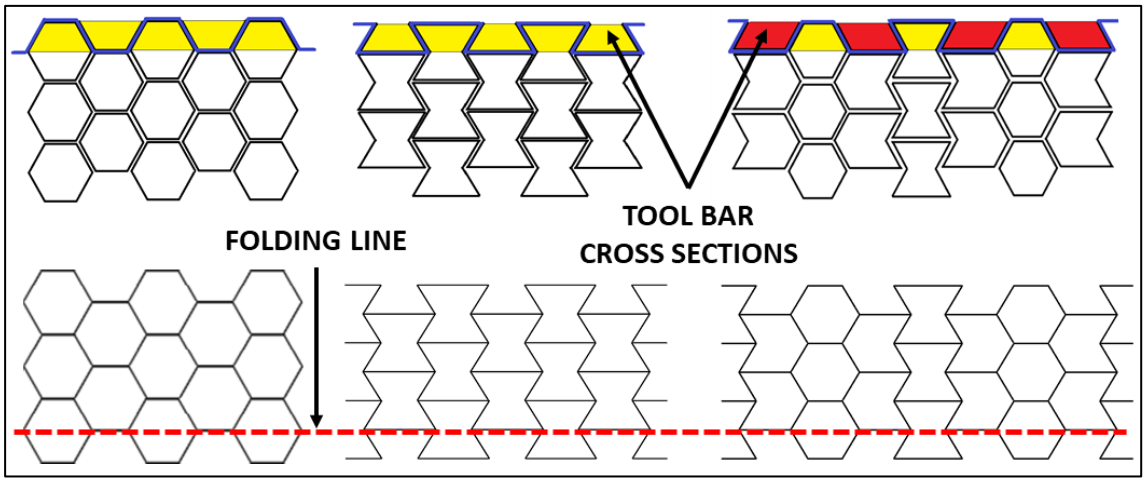

Figure 10- Examples of kirigami allowed patterns and mold bar cross-sections: Trapezoidal bars in yellow and parallelogram bars in red.

ADVANTAGES	DISADVANTAGES
• Composite materials with thermoplastic and thermoset matrix can be used to produce cellular structures. • No post process machining. • Hybrid panels (panels contain cells with different shapes). • Ventilation holes included in the early stage of manufacturing. • Surface treatment included in the early stage of manufacturing. • Resonating surfaces cut-out.	• Cells are geometrically limited by mold bar cross section to allow the folding. • Sample manufacturing uncertainty. • Technique using composite materials not industrially ready.

Table 1 - Kirigami advantages and disadvantages summary

1.1.4 Meta-sandwich panels

Sandwich panels are widely used for the purposes just mentioned in the above paragraph but despite their qualities, they have some drawbacks which raised as they were adopted for performing engineering applications. This was the main reason the concept of meta-sandwich panels started to pick up momentum. In Greek, "Meta" means beyond and there is no better way of describing a class of engineered structures manufactured with common materials but with such architecture that gives them an overall behaviour which goes beyond their original capabilities. It is a concept that is even broader than the ones which governs composite materials. In a certain way, Engineers have started to create a new

category of materials by assigning them physical properties that are not usually found in nature and might not be intuitively related, through the application of architectural design rules.

An example of metamaterial that exploits the Japanese art of Kirigami is electrically conductive carbon-nanotube composite metamaterials (*Figure 11*) with increased strain[27]. Electrically conductive materials are often brittle and therefore cannot be significantly stretched as microcracks soon appear and the concentrated stress around the apexes quickly leads to structural failure. By strategically placing cuts and slits using photolithography into the composite sheet the material when stretched behaved like the uncut sheets, however, as the stress increased further, the structure began to absorb the extra strain energy by opening the slit pattern, deforming the material out of plane. A secondary elastic plateau appeared as the cuts gradually rotated with increasing load, to align themselves with the applied stress. Eventually, the material finally failed, but not before the sheet stretched up to 370%. This phenomenon happens with any elastic kirigami cut material, but the crucial factor in this research, was that the electrical conductivity of the sheet remained virtually unchanged as they stretched. The idea of having stretchable conductive materials is very fascinating and has great potential for biomedical applications where a certain amount of elastic deformation might be required.

A similar application of Kirigami has been studied by McEuen with graphene sheets, which are known to have very low strain[28]. His study firstly concentrated on the stiffness measurement of a graphene cantilever which he measured to be about 4000 times stiffer than theoretical calculation predictions. From these results, graphene did not seem like a suitable material for deformable electronics, but by adding Kirigami cuts into the sheet, the behaviour of the latter under load changed significantly.

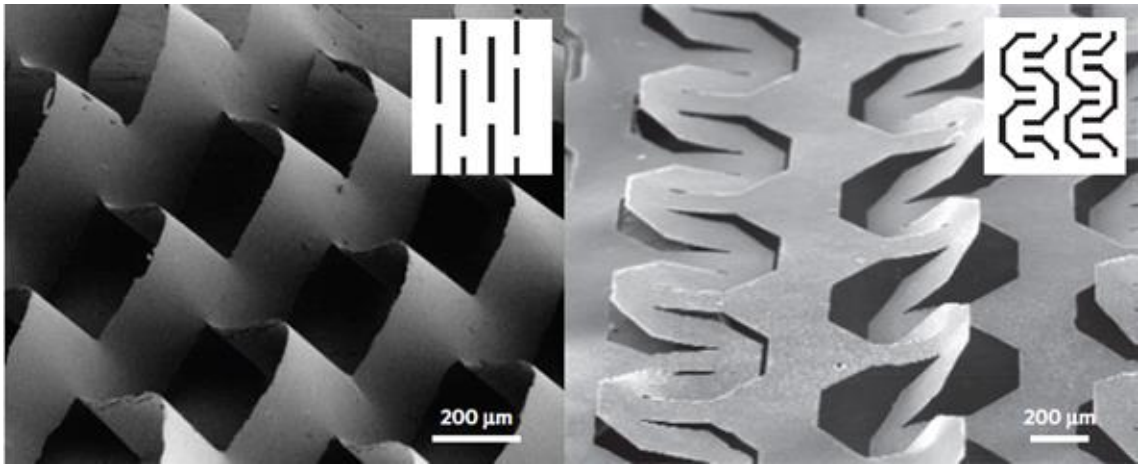

Figure 11 - Kirigami cuts applied to carbon-nanotube composite sheets with polymeric matrix[27].

A pattern of kirigami cuts was applied to a graphene sheet where gold pads were previously deposited. The sheet was then used to create electrolyte-gated transistors and found that the electrical properties of these transistors were virtually unchanged even after the transistors were stretched to 240% of their initial length. Cyclic tension/compression (fatigue) tests were also carried out revealing that these components could withstand 1000 cycles without degrading their electrical properties. The same team produced graphene hinges designed to operate either mechanically or magnetically, which survived 10000 cycles before the gold pads started to wrap.

They also created a kirigami cut pattern that becomes a pyramid-like structure when its golden tip is struck by a laser beam. The pyramid tip, shown in *Figure 12*, was measured to deploy up to 10μm above the graphene base.

In 2014, Scarpa presented a work at the International Conference and Exposition on Electrical and Power Engineering (EPE 2014), based on the Kirigami technique[29].

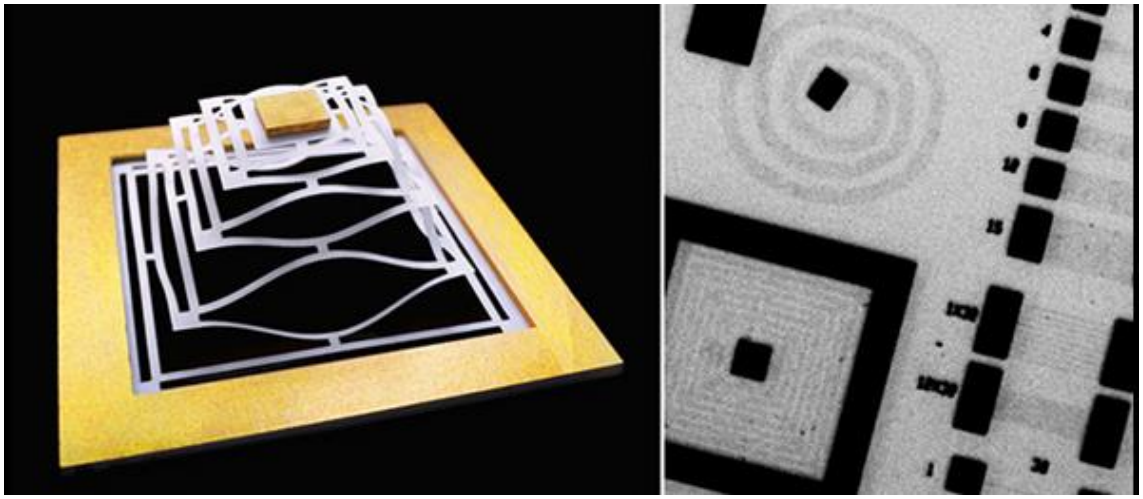

Figure 12 - Kirigami micro-springs in paper (left) and graphene (right)[28]

Among others, he manufactured PEEK corrugated sheets covered with copper/epoxy redux film to increase the conductivity of the substrate. Electro-magnetic and reflectance tests were carried out and showed the potential of using these composite materials in structures like antennas/reflectors.

Other examples of metamaterials are those who's architecture enables them to veer electromagnetic waves around them with no reflection and/or scatter occurring, making them "invisible"[30],[31],[32],[33]. Those are known as cloaking metamaterials. If we consider the visible spectrum, as light travels through empty space, in an isolated system, its path remains unchanged as the photon can travel without any energy exchange. If the photon hits an object or travels a medium, depending on whether it's translucent or not, the photon will either go through it changing its direction, just like it happens with glass or

water, or will be reflected and scattered after collision, creating a shadow. Our visible light sensor, the eye, does nothing but capture the resultant photon, detecting a change from those who do not come off the object. By manipulating the refractive index, permittivity and permeability of the medium, cloaking metamaterials can veer the wave around it and therefore sensors will not receive any information deriving from it, as if the object is not there at all. Other metamaterials maintain their structural properties while gaining new features so the concept of wave veering also becomes very interesting in the acoustic domain, where the cloaking concept could be exploited for sound-proofing rooms or to develop surface treatments to improve sound-stealth tech (based on wave scattering) as well creating sonar-invisibility technology.

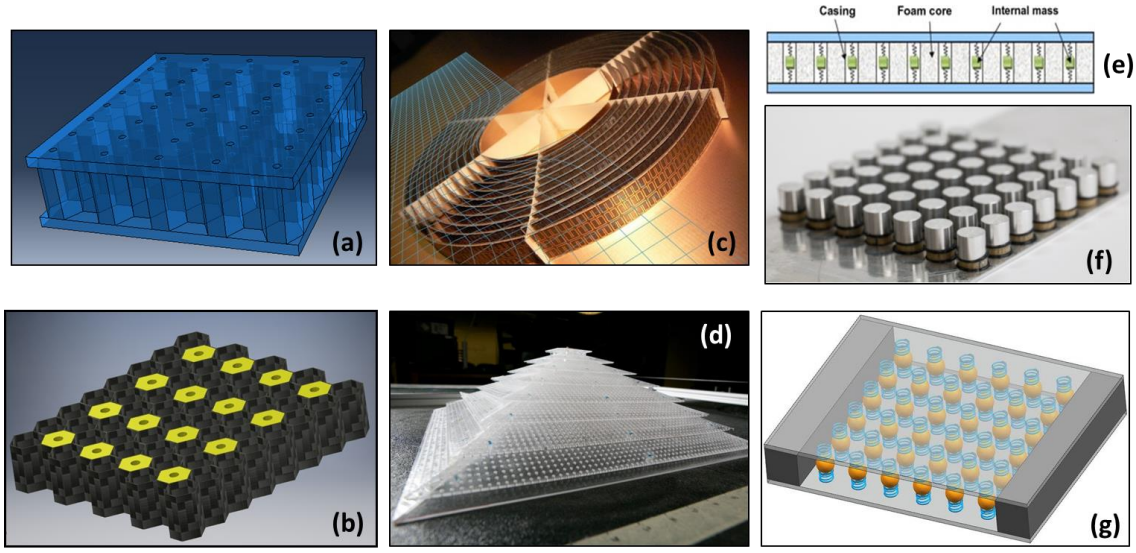

Figure 13 - (a) Sandwich panel with perforated skin; (b) Honeycomb core with Helmholtz resonator inserts; (c) Electromagnetic cloaking device[34]*; (d) Acoustic 3D cloak structure* [30] *(e) and (g) Sandwich panels with embedded mechanical resonators*[35]*; (f) Plate with array of mechanical resonators and polymeric substrate attached*[36].

The parameters that allow to create such meta-acoustic devices are the material's mass density and its elastic constant. Researchers from Duke university [30] have created an electromagnetic cloaking device based on split ring resonators as well as the first 3D acoustic cloak structure (*Figure 13*) which is able to hide the structure itself but also everything which lies beneath it.

The same principles used for electromagnetic and sound waves apply to mechanical waves where researchers have and are studying ways to amplify or decrease vibrations using different techniques and concepts. If the metamaterial concept is merged with sandwich panels, the outcome is a meta-sandwich panel which can adopt solutions which confers new properties, beyond their being lightweight and stiff. The possibilities and combinations are many and some are resumed in *Figure 14*. Engineers can alter the sandwich laminates

and/or the lightweight core surfaces with chemical or laser treatments, apply nano-coatings [19], exploit the cellular core cavities including mass-spring type mechanical resonators [37]for vibration attenuation/transmission as well as porous material with or without inclusions[35] and apply viscoelastic patches. They can also perform perforations (*Figure 13*) to create Helmholtz resonators [38] which is a solution adopted in jet-engine's nacelle to increase the acoustic comfort of the airplane's interior.

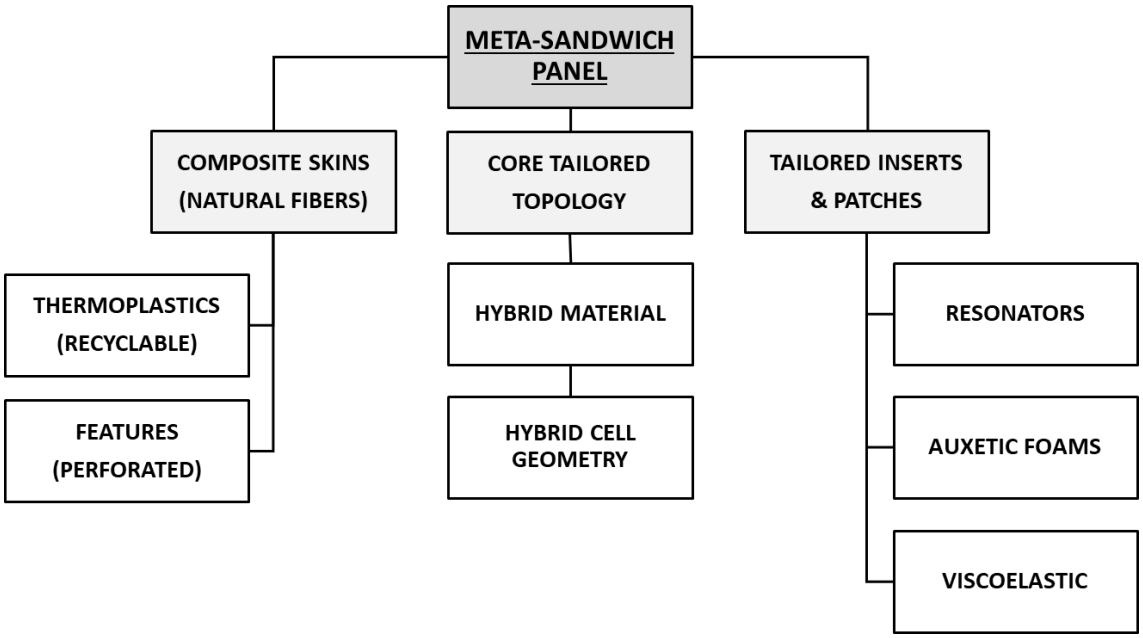

Figure 14 - Meta-Sandwich panel outline

Most of those solutions cause an increase in mass of the overall sandwich panel (resonators, coatings, foam inserts) and although they are effective passive solutions, meaning that there is no active or real-time manipulation of the material characteristics or structure, the investigation of ways to obtain comparable results maintaining mass and structural properties unaltered becomes relevant. For this reason, the attenuation of mechanical vibrations, adopting new sandwich core topologies manufacturable with the Kirigami technique became the core of this thesis and was made possible thanks to wave propagation fast prediction tools which were coded by the author.

1.2 ELASTIC WAVE PROPAGATION IN MEDIUMS

A mechanical wave is the propagation of a perturbation in matter, whether that may be gaseous, liquid, or solid. It is only possible if there is a perturbation source, a medium which experiences the effect of it and a connection between the medium directly affected and the adjacent one, which makes propagation possible. As the wave travels through the medium,

the matter undergoes an elastic deformation, which means that the atoms who constitute the medium, will be displaced of a certain quantity and will return to their original position once the wave amplitude goes back to zero. Displacement, speed, and mechanical energy of a unit mass are transmitted to the adjacent and therefore mechanical waves are the method with which we can transport mechanical energy though a medium. An elastic mechanical wave is therefore energy exchange which may happen longitudinally or transversally with respect to the direction of propagation.

Different types of waves can travel a medium. There are pressure (longitudinal) and shear (transverse) waves as well as a combination of the two (bending or flexural waves) as shown in *Figure 15*. Each one of them can be described by the motion which each particle undergoes. A particle subjected to a pressure wave, also known as a primary wave (P-wave), will displace along the wave's axis of motion while a shear wave (secondary S-wave) will displace the particle perpendicularly (vertical or horizontal) to the direction of propagation. In both cases, the displacement of the particle will be small and with the undisturbed position as the centre of oscillation. Bending waves are more complex and depend on both, the material and geometrical properties of the medium they are travelling through. The classic example of a pressure wave is the unidimensional compression of a gas done by a piston/cylinder system. The gas molecules are compressed by the piston (impulse) along the cylinders axis and once the piston returns to its starting position, the energy which was transferred to the first molecules adjacent to the piston is propagated to the following ones and so on until the energy is exchanged with the molecules at the end of the cylinder.

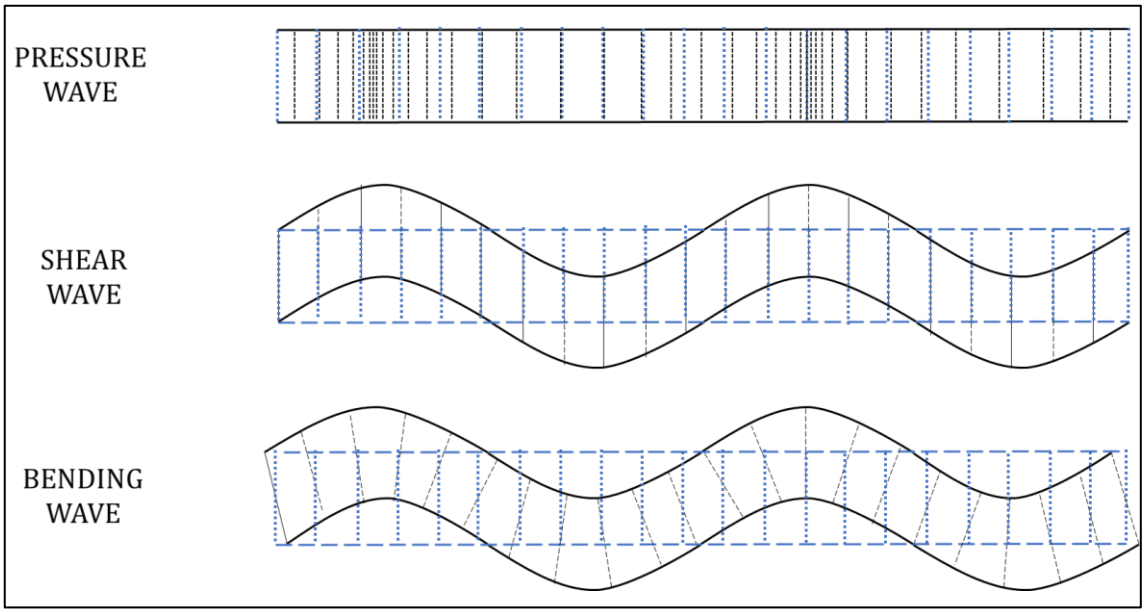

Figure 15 – Graphical representation of pressure, shear, and bending waves

Before proceeding with further description about wave mechanics, it is important to mention that all distinctions made so far were describing the type of displacements the particles would possess, without mentioning the speed at which they displace. Matter is solicited by multiple sources and therefore impinging waves of different types with different amplitude and or frequency, interact with each other, creating a resultant wave which displaces the particles. When the whole pack (waves with different frequency), and therefore its resultant, travel with the same speed (their propagative speed does not depend upon the wave frequency) is described as a non-dispersive medium. In a dispersive medium instead, each frequency travels at a different speed. Now the speed at which each wave travels in both mediums (dispersive and non) is called Phase Velocity which depends upon the material intrinsic properties and type of wave.

$$v_p = \sqrt{\frac{Material\ Elastic\ Modulus}{Density}} \tag{1.2.1}$$

More precisely, for Primary and Secondary waves, introducing the Lamé constants, we obtain:

$$v_{longitudinal} = \sqrt{\frac{\lambda_L + 2S}{\rho}} = \sqrt{\frac{B + (4/3)S}{\rho}} \tag{1.2.2}$$

$$v_{transverse} = \sqrt{\frac{S}{\rho}} \tag{1.2.3}$$

where λ_L is Lamé's first parameter, B and S are the compression bulk modulus and the shear modulus respectively and ρ the density. From the above equations, it is also clear how longitudinal waves are faster than transverse waves.

In a non-dispersive medium, waves of different frequency propagate with the same speed and therefore the resultant wave produced as a result of their interaction, travels at that same speed. In a dispersive medium instead, waves with different frequencies travel at different speed and so, also the resultant wave will propagate at a different speed. The velocity of the resultant wave produced by the pack is called Group velocity.

Summarizing, in a non-dispersive medium, phase and group velocity are equal while in a dispersive medium, being propagation in the latter frequency dependant, they differ. The idea that the two might be different came from W.R. Hamilton in 1839 but it was Rayleigh

in "Theory of Sound" who described the phenomena.

As an example, let's consider a metallic rod; depending upon the type of excitation, longitudinal (compression), if the rod hits the floor vertically, or bending, if the rod hits a table horizontally, the movement conferred to the rod particles by the initial impulse will be transferred to the surrounding medium (air) and in each case, this will reach our ear with a different pitch. The difference in pitch derives from the rod particles vibrating at a different frequency; Being both, the rod and air, dispersive mediums, the particles will oscillate and transmit the wave with different speeds (longitudinal waves are faster than bending waves).

A sub-class of waves which will be briefly mentioned is represented by the surface waves which are a composition of P and S waves and happen on the surface of the medium. Amongst them, Rayleigh and Love waves happen in both dispersive and non-dispersive medium, while Lamb waves only happen in frequency dependent medium. Rayleigh waves particle motion can be described with an ellipse in the plane parallel to the direction of energy propagation and the displacement is larger as we get closer to the surface of the medium. Love wave transverse particle motion increases as we are closer to the surface. A visual summary of those waves is shown in *Figure 16* where the base of the medium is fixed and only the particles on the upper layers are displaced.

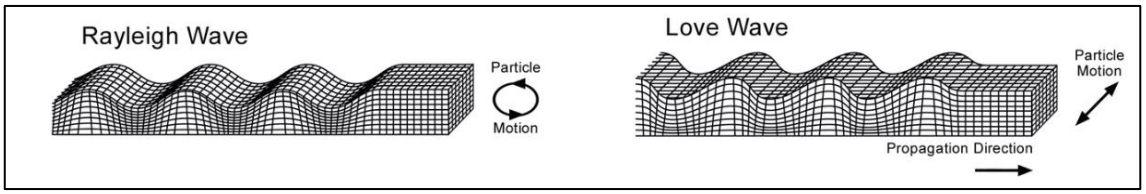

Figure 16 - Graphical representation of Rayleigh and Love waves [39]

Another way of describing the relation between frequency and speed of propagation, being phase or group velocity, is by reasoning in terms of wavenumber and angular frequency. An extended formulation of this form of dispersion relation is covered in section *1.4*.

1.2.1 Numerical methods overview

The metallic rod is a simple example of wave propagation in a homogeneous medium and the transmission of a mechanical wave in complex structures is not as straight forward. Structures can be subjected to various external solicitations and the methods to analyse their dynamic response strongly depends upon the wave's wavelength. Those methods can be divided into three categories as they are conceived to deal with three bandwidths which are defined as low, mid, and high frequency. The need to derive different methods according

to the considered frequency range was linked with accuracy and available computational power. This means that accurate results may still be achieved using different methods but at different speeds, which inevitably create a preference rank amongst them, depending on the objective. In the low frequency range, the most popular method is the Finite Element Method (FEM) which allows to analyse complex structures. This method can deal with all frequency ranges if the structure is discretized in elements whose size is sufficiently small to accurately compute the response, since the elements are frequency independent. This works well with low frequencies but as we increase the latter, the number of elements required rapidly augments, which inevitably leads into tremendous timely consuming simulations. For this reason, this method is avoided when considering high frequencies. In order to obtain reliable results using this technique and capture all possible destructive interference, the element size needs to be calculated considering the maximum frequency to be analysed; Perfectly destructive interference occurs when the impinging wave is double the length of the unit cell. If we aim for accuracy at sub-wavelengths, the element size must be calculated with the highest frequency value (smallest wavelength) considered. Furthermore, the minimum number of nodes required to describe a full harmonic period is five (zero crossings, positive and negative peaks). Now, if we and decide to concentrate on bending waves, the calculation depending upon the element type used for the model, is carried out as follows, where ε is the model's element size:

BEAM ELEMENT SIZE $\rightarrow$

$$f_{max}^{B} = \frac{\pi}{2\varepsilon^2}\sqrt{\frac{EI}{\rho A}} \tag{1.2.4}$$

SHELL ELEMENT SIZE $\rightarrow$

$$f_{max}^{S} = \frac{\pi}{2\varepsilon^2}\sqrt{\frac{t^2 E}{12(1-\upsilon^2)\rho}} \tag{1.2.5}$$

Another method used in low frequency analysis is the Boundary Element Method (BEM)[40], where, as the name anticipates, the discretization happens only for the external surface (boundary) of the body. Instead of directly solving the set of differential equations like in FEM, with BEM an integral equation is defined on the body's surface and solved for nodal displacements. Furthermore, in LF analyses can also be conducted using the Infinite method[41],[42] (IEM) and the spectral element method [43](SEM). Just like in FEM, these methods are deterministic, computationally demanding as we increase the frequency analysed, and appropriate for frequency ranges of low modal density. When the latter instead is high (which normally happens when dealing with high frequencies), the most diffused method is the statistical energy analysis (SEA)[44],[45],[46]. Here a structure is

divided into subsystems and a set of linear equations links each subsystem in terms of energy and or power input, dissipation, transmission, and storage. Statistical assumptions are made to simplify models which otherwise would be too complex and consequently large and computationally demanding to analyse with the previously mentioned methods. SEA reasoning is based on mean quantities possessed by subsystems which have a homogeneous response and it is those which become the equivalent "brick" to the elements used in a FE/BE approach. Neither of those techniques are optimal to analyse a structures response to solicitations within the mid-frequency range and although they can still be used, a time demanding calibration period for each case must be considered. Furthermore, the lower and upper limits of such range are not always so neat and are mostly defined by computational efficiency and appearing/disappearing of local resonances, topic which is linked to the modal density. The mid-frequency method "gap" has been, and still is, an area of intense research where deterministic methods have been adapted through model order reduction techniques and probabilistic ones have been tailored trough relaxation of certain stringent assumptions required to fulfil the method demands. It is in this gap that the Wave finite element method (WFEM)[47],[48],[49],[50], which is a wave-based method applied to periodic structures, finds its placement since it combines a traditional FE approach applied on a reduced model (the unit cell) with the periodic boundary conditions (Floquet-Bloch)[51],[52]. This method will be intensively used throughout this work, as a wave propagation prediction tool.

1.2.2 Numerical methods for periodic structures

Many efforts have been produced so far to better understand the dynamic behaviour of complex periodic structures. The solicitations that an airplane fuselage or a space launcher undergoes, derives from various sources, and understanding the consequent perturbation propagation, is crucial to avoid catastrophic failures and lengthen its average service lifespan.

The response of periodic structures to external excitation has already been investigated starting from the analytical origins, with Floquet[51], to further expansion, carried out by Bloch[52] and passing by the excellent work done by Brillouin [1] back in 1946. Mead et al. [50] produced a document, summarizing almost thirty years of work carried out at the University of Southampton, demonstrating how spatial periodicity in terms of structure, material, inserts or boundary conditions, interacts with travelling waves. Those periodic variations cause some of the incident waves to be reflected and some to be transmitted. The

destructive interaction (partial or full) between incident and reflected waves, causes attenuation (bandgaps) within certain frequency ranges, and therefore, periodic structures can act as passive filters. This also suggests that there is a relation between the geometrical dimensions of the periodic structure and the travelling wave characteristics.

Periodic structures though, can exhibit two types of stop bands which are created by different phenomena: Bragg Scattering and Local Resonance[53]. Bragg scattering stop bands are consequence of the spatial periodicity just mentioned and it appears when wavelengths are on the same order as the period (unit cell) length. Local resonance stop-bands instead, do not necessarily require periodicity and only depend on the properties of the local resonator and therefore they can lie in the sub-wavelength regime as the resonating component can be dimensioned as required and therefore may be more susceptible to a type of excitation than to another.

Many different methods have been developed in the years to examine periodic structures which can be found in literature. A good summary of those techniques which mostly are FEM based and neglect the structure's damping, can be found in the paper written by Hussein and Ruzzene[54]. Lately, the most commonly used is the Wave Finite Element Method (WFEM)[50],[54],[55],[56],[57], where the Mass and Stiffness matrices of the single repetitive component of the periodic structure, are calculated with the aid of FEM commercial software, extracted, and used to calculate the dynamics of the structure by applying the periodicity conditions described by the Floquet-Bloch Theory (explained in section *1.4.1*). Recently, the WFEM and periodic concept has been extended to composite materials[58] where the fibers and matrix constitute periodic material assemblies.

The following paragraphs will be divided in two fields, which describe the dynamic analysis of a finite periodic structure using FEM and the one using the "infinite periodic structure" approach. The first part will describe the classic structure's frequency response to harmonic excitations formulation while the second, will concentrate on the WFEM mathematical formulation, which will be described and outlined to analyse the dynamic behaviour of periodic structures for cases of 1D, 2D and 3D periodicity.

1.3 PREDICTION METHODS FOR FINITE PERIODIC STRUCTURES

1.3.1 Frequency Response to harmonic excitation

The Frequency response function is one of the most used quantities in the engineering domain and especially in vibration analysis because it provides information about the

natural frequencies, damping and mode shapes of the structure. For linear systems, the FRF, expressed in the frequency domain and usually indicated with $H(\omega)$, relates the input excitation $X(\omega)$, with the output signal reading $Y(\omega)$ and provided that $X(\omega) \neq 0$, the relationship is the following:

$$H(\omega) = \frac{Y(\omega)}{X(\omega)} \tag{1.3.1}$$

supposing the system is injected with a harmonic excitation $X(\omega) = X_0 e^{j\omega t}$.
Since $H(\omega) \in \mathbb{C}$, we can also express it as the product between the modulus and the phase:

$$H(\omega) = |H(\omega)| e^{-j\varphi} \tag{1.3.2}$$

$$\varphi = \angle(H) \tag{1.3.3}$$

equation(1.3.1) therefore becomes:

$$Y(\omega) = |H(\omega)| X_0(\omega) e^{j(\omega t - \varphi)} \tag{1.3.4}$$

where the output amplitude is equal to $|H(\omega)|X_0(\omega)$ and ϕ is the phase lag. To provide full information, two graphs are normally plotted, one concerning the amplitude of the response, $Re[H(\omega)]$, and one concerning the phase angle of lag between output and input, $Im[H(\omega)]$. The type of input and measured output might be different and the FRF's name changes accordingly. In this work the compliance of the structures, which is the displacement response to an input harmonic unit-force, will be produced and only the amplitude response plotted. This will be performed using commercial FE packages and will be used as a bandgap validation tool for the computed dispersion curves.

1.3.2 Transmissibility

The dynamic characteristics of structures can also be evaluated by computing the transmissibility, which is another well-known transfer function measurement, widely used for the evaluation of the vibration isolation performance. A SDOF mechanical system can be represented with a single spring-mass system, where a mass is connected to the base through a spring and a damper. When a force is applied to the mass and then removed, the system will start to oscillate at its natural frequency and the amplitude will decrease with time due to energy dissipation. If an external harmonic force is instead applied to the base

along its vertical axis, the system will start to oscillate at the frequency of the exciting force, and not at its natural frequency. However, the amplitude of the oscillation will vary according to the relation between the harmonic excitation and the natural frequency of the system. The transmissibility, $\mathbb{T}$, is the ratio between the harmonic base excitation, and the output reading which is usually done at the top of the mass. The transmissibility for a SDOF can be expressed as follows:

$$\mathbb{T} = \frac{A_o}{A_i} = \sqrt{\frac{1 + \left(2\xi \frac{\omega}{\omega_n}\right)^2}{\left[1 - \left(\frac{\omega}{\omega_n}\right)^2\right]^2 + \left[2\xi \left(\frac{\omega}{\omega_n}\right)\right]^2}} \tag{1.3.5}$$

where A_i and A_o are the amplitude of vibrational input and output response respectively, ξ the damping ratio and ω_n the natural frequency.

Let Q be the amplification or quality factor:

$$Q = \frac{1}{2\xi} \tag{1.3.6}$$

For a single degree of freedom system subjected to base excitation at its natural frequency, Q is equal to the peak magnitude of the transfer function. The damping was calculated as follows:

$$2\xi = \left(\frac{\omega_2 - \omega_1}{\omega_n}\right) \tag{1.3.7}$$

In the last chapter of this work, a transmissibility investigation is carried out for a sandwich panel modelled as a SDOF system.

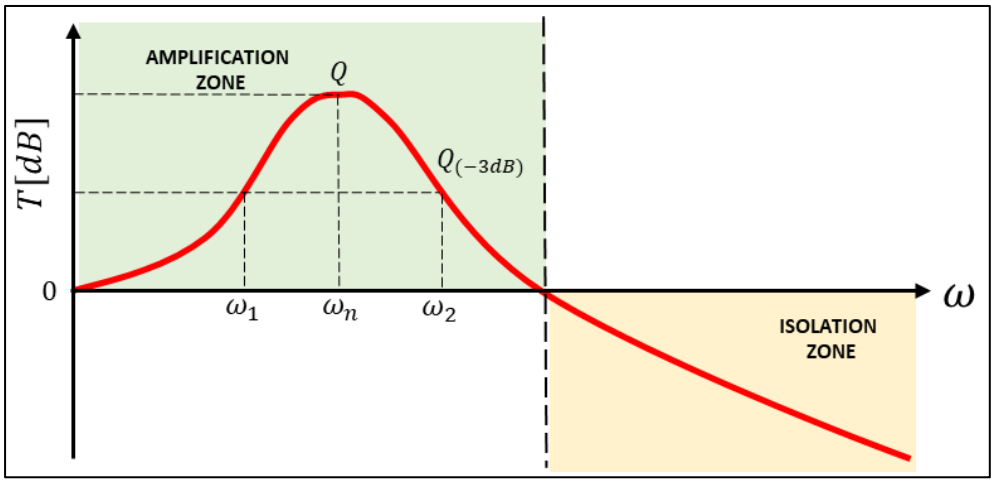

Figure 17 – Representative transmissibility graph and half power bandwidth method

1.3.3 Transfer Matrix Method

To investigate the dynamic behaviour of a periodic structure, a full-scale model can be produced, and through heavy calculation and therefore long computational time, the response of the structure (FRF) is obtained, just as it is normally done with non-periodic structures. This translates in a model with a very large number of nodes and therefore degrees of freedom that one needs to consider in the computation. For periodic structures instead, periodicity can be exploited, and the size of our model reduced to its fundamental repeatable component, the unit cell. By imposing the continuity and equilibrium relations at the unit cells interfaces, the numerical dynamic behaviour prediction can be carried out on a much less computational demanding model. Those concepts can be applied in the direction of the structure's periodicity through a single matrix $\boldsymbol{T}$, the transfer matrix, which contains the mathematical link between the forces and displacements at the interface of each cell. To link displacements (q) and forces (f) at the extremities of the unit cell, the starting point is the fundamental equation of motion. Neglecting damping, we obtain:

$$(\boldsymbol{K}_{\boldsymbol{uc}} - \omega^2 \boldsymbol{M}_{\boldsymbol{uc}}) \begin{pmatrix} q_l \\ q_i \\ q_r \end{pmatrix} = \begin{pmatrix} f_l \\ f_i \\ f_r \end{pmatrix} \tag{1.3.8}$$

where q_l, q_r and q_i are the left, right and internal nodal displacements and f_l, f_r and f_i are the respective nodal forces. $\boldsymbol{K}_{\boldsymbol{uc}}$ and $\boldsymbol{M}_{\boldsymbol{uc}}$ are instead the stiffness and mass matrices of the unit cell and ω the angular frequency. According to the continuity of displacements and equilibrium of forces (*Figure 18*), equations (1.3.9)and (1.3.10)are derived for $(n+1)$ unit cells, which constitute the dynamic ligaments between the unit cells.

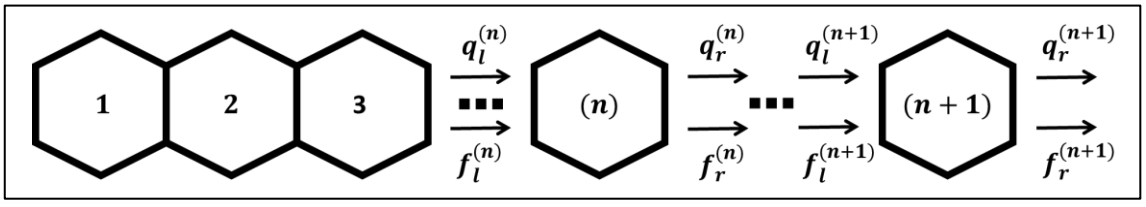

Figure 18 - Chain of unit cells

$$q_r^{(n)} = q_l^{(n+1)} = \lambda q_l^{(n)} \tag{1.3.9}$$

$$f_r^{(n)} = -f_l^{(n+1)} = -\lambda f_l^{(n)}. \tag{1.3.10}$$

For free wave propagation, no external forces act on the structure and the only ones considered are the ones at the interface between unit cells. The dynamic relation becomes:

$$(\boldsymbol{K}_{\boldsymbol{uc}} - \omega^2 \boldsymbol{M}_{\boldsymbol{uc}}) \begin{pmatrix} q_l \\ q_i \\ q_r \end{pmatrix} = \begin{pmatrix} f_l \\ 0 \\ f_r \end{pmatrix} \tag{1.3.11}$$

$$\boldsymbol{D}(\omega) \begin{pmatrix} q_l \\ q_i \\ q_r \end{pmatrix} = \begin{pmatrix} f_l \\ 0 \\ f_r \end{pmatrix} \tag{1.3.12}$$

$$\boldsymbol{D}(\omega) = \boldsymbol{K}_{\boldsymbol{uc}} - \omega^2 \boldsymbol{M}_{\boldsymbol{uc}} = \begin{bmatrix} \boldsymbol{D}_{ll} & \boldsymbol{D}_{li} & \boldsymbol{D}_{lr} \\ \boldsymbol{D}_{il} & \boldsymbol{D}_{ii} & \boldsymbol{D}_{ir} \\ \boldsymbol{D}_{rl} & \boldsymbol{D}_{ri} & \boldsymbol{D}_{rr} \end{bmatrix} \tag{1.3.13}$$

where $\boldsymbol{D}(\omega)$ is the Dynamic matrix which contains both, mass, and stiffness matrices of the unit cell, and $f_i = 0$. After a condensation procedure, the dynamic equation finally becomes:

$$\begin{bmatrix} \widetilde{\boldsymbol{D}}_{11} & \widetilde{\boldsymbol{D}}_{12} \\ \widetilde{\boldsymbol{D}}_{21} & \widetilde{\boldsymbol{D}}_{22} \end{bmatrix} \begin{pmatrix} q_l \\ q_r \end{pmatrix} = \widetilde{\boldsymbol{D}}(\omega) \begin{pmatrix} q_l \\ q_r \end{pmatrix} = \begin{pmatrix} f_l \\ f_r \end{pmatrix}. \tag{1.3.14}$$

$\widetilde{\boldsymbol{D}}(\omega)$ is the condensed dynamic matrix which possesses the following terms:

$$\widetilde{\boldsymbol{D}}_{11} = \boldsymbol{D}_{ll} - \boldsymbol{D}_{li} \times \boldsymbol{D}_{ii}^{-1} \times \boldsymbol{D}_{il} \tag{1.3.15}$$

$$\widetilde{\boldsymbol{D}}_{12} = \boldsymbol{D}_{lr} - \boldsymbol{D}_{li} \times \boldsymbol{D}_{ii}^{-1} \times \boldsymbol{D}_{ir} \tag{1.3.16}$$

$$\widetilde{\boldsymbol{D}}_{21} = \boldsymbol{D}_{rl} - \boldsymbol{D}_{ri} \times \boldsymbol{D}_{ii}^{-1} \times \boldsymbol{D}_{il} \tag{1.3.17}$$

$$\widetilde{\boldsymbol{D}}_{22} = \boldsymbol{D}_{rr} - \boldsymbol{D}_{ri} \times \boldsymbol{D}_{ii}^{-1} \times \boldsymbol{D}_{ir} \tag{1.3.18}$$

now, by rearranging the items and considering cells (n) and $(n+1)$, the Transfer Matrix can be expressed as:

$$\begin{pmatrix} q_l^{(n+1)} \\ f_l^{(n+1)} \end{pmatrix} = \begin{bmatrix} \boldsymbol{T}_{11} & \boldsymbol{T}_{12} \\ \boldsymbol{T}_{21} & \boldsymbol{T}_{22} \end{bmatrix} \begin{pmatrix} q_l^{(n)} \\ f_l^{(n)} \end{pmatrix} = \boldsymbol{T} \begin{pmatrix} q_l^{(n)} \\ f_l^{(n)} \end{pmatrix} \tag{1.3.19}$$

where,

$$\boldsymbol{T}_{11} = -\widetilde{\boldsymbol{D}}_{12}^{-1} \times \widetilde{\boldsymbol{D}}_{11} \tag{1.3.20}$$

$$\boldsymbol{T}_{12} = \widetilde{\boldsymbol{D}}_{12}^{-1} \tag{1.3.21}$$

$$\boldsymbol{T}_{21} = -\widetilde{\boldsymbol{D}}_{21} + \widetilde{\boldsymbol{D}}_{22} \times \widetilde{\boldsymbol{D}}_{12}^{-1} \times \widetilde{\boldsymbol{D}}_{11} \tag{1.3.22}$$

$$\boldsymbol{T}_{22} = -\widetilde{\boldsymbol{D}}_{22} \times \widetilde{\boldsymbol{D}}_{12}^{-1}. \tag{1.3.23}$$

The eigenvalues of $[\boldsymbol{T}]$, considering only one direction of propagation, correspond to the values of the unknown propagation constant $\lambda = e^{-jkL}$ as mentioned in the work by Ruzzene[59] and so, they relate the left and right nodal displacements and forces according to the Floquet-Bloch's theorem. By substituting equations (1.3.9) and (1.3.10)into (1.3.19) the

following eigenvalue problem is obtained:

$$\lambda \begin{pmatrix} q_l \\ f_l \end{pmatrix}^{(n)} = \boldsymbol{T} \begin{pmatrix} q_l \\ f_l \end{pmatrix}^{(n)}. \tag{1.3.24}$$

Under the numerical point of view, there are some issues due to the ill-conditioning of the matrix $[\boldsymbol{T}]$. This is because the latter depends on the inversion of T_{12} which is likely to contain numbers which are very disparate, affecting the eigenvalue sensitivity. This can be overcome by applying a decomposition in two matrices $[\boldsymbol{L}]$ and $[\boldsymbol{N}]$ as shown in the work by W.X. Zhong [60] and later recalled by E.D. Nobrega[61] where $[\boldsymbol{T}] = [\boldsymbol{L}][\boldsymbol{N}]^{-1}$.

1.4 PREDICTION METHODS FOR INFINITE PERIODIC STRUCTURES

1.4.1 WFEM and the Floquet-Bloch Theory

Wave propagation in media as mentioned in the introduction to this chapter, is governed by partial differential equations. In 1883 Floquet was the first to propose a mathematical solution to differential equations with periodic coefficients[51] and for this reason, he is the mind who opened a new frontier in this domain [50]. Initially, the attempt to support the analytical solutions consisted in discrete systems, mainly sets of masses connected through springs, and only later in 1887 Rayleigh proposed the study on a continuous structure by periodically varying its density. It was the Swiss physicist Felix Bloch who later in 1928 extended the work started by Floquet to 3D special periodicity[52]. Therefore, when periodic boundary conditions are applied to a structure to exploit its characteristic, the community refers to them as Floquet-Bloch conditions. This theory is the core of the WFEM method and was firstly introduced for engineering investigations by Brillouin [1].

1.4.1.1 WFEM 1D-Periodicity

When the Floquet-Bloch theory is applied to a structure which exhibits unidimensional periodicity, a relation between the displacements and forces of the nodes at the extremities of its unit cell is established. Thanks to this relation, it is enough to analyse a small portion of the structure, the unit cell, to understand and predict the overall dynamic behaviour of an infinitely large periodic structure. The Floquet-Bloch relations for forces (f) and displacements (q) for 1D periodicity are shown in equation (1.4.1) and (1.4.2)respectively, where, the subscripts l and r indicate the left or right boundaries of the unit cell, $\mu = kL$ is the reduced wavenumber, k is the wavenumber and L the representative length of the unit

cell along the periodic direction.

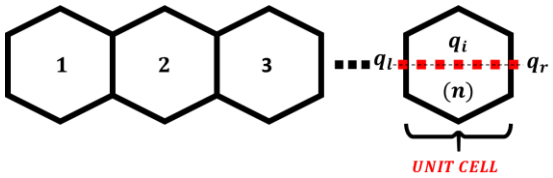

$$q_r^{(n)} = \lambda q_l^{(n)} = e^{j\mu} q_l^{(n)} \tag{1.4.1}$$

$$-f_r^{(n)} = \lambda f_l^{(n)} = e^{j\mu} f_l^{(n)} \tag{1.4.2}$$

Figure 19 - Periodic structure unit cell and 1D Floquet Bloch periodic relations

To understand the dynamic behaviour of a periodic structure, a dispersion curve, which represents the relation between the reduced wavenumber (μ) versus the angular frequency (ω) or the frequency (f) can be plotted. To produce a dispersion curve therefore, a relation between ω and $\lambda = e^{j\mu}$ is required, where λ are the eigenvalues. The starting point is represented by the Fundamental Dynamics Equation of the unit cell. Neglecting damping, such equation becomes:

$$(\boldsymbol{K}_{\boldsymbol{uc}} - \omega^2 \boldsymbol{M}_{\boldsymbol{uc}}) \begin{pmatrix} q_l \\ q_i \\ q_r \end{pmatrix} = \begin{pmatrix} f_l \\ f_i \\ f_r \end{pmatrix} \tag{1.4.3}$$

$$\boldsymbol{K}_{\boldsymbol{uc}} = \begin{bmatrix} \boldsymbol{K}_{ll} & \boldsymbol{K}_{li} & \boldsymbol{K}_{lr} \\ \boldsymbol{K}_{il} & \boldsymbol{K}_{ii} & \boldsymbol{K}_{ir} \\ \boldsymbol{K}_{rl} & \boldsymbol{K}_{ri} & \boldsymbol{K}_{rr} \end{bmatrix} \qquad \boldsymbol{M}_{\boldsymbol{uc}} = \begin{bmatrix} \boldsymbol{M}_{ll} & \boldsymbol{M}_{li} & \boldsymbol{M}_{lr} \\ \boldsymbol{M}_{il} & \boldsymbol{M}_{ii} & \boldsymbol{M}_{ir} \\ \boldsymbol{M}_{rl} & \boldsymbol{M}_{ri} & \boldsymbol{M}_{rr} \end{bmatrix}. \tag{1.4.4}$$

Let's consider the internal forces to be zero [50] $(f_i = 0)$. Now to satisfy the Floquet-Bloch conditions, matrix $[\boldsymbol{\Lambda_R}]$ is created:

$$\boldsymbol{q} = \begin{pmatrix} q_l \\ q_i \\ q_r \end{pmatrix} = \boldsymbol{\Lambda_R} \begin{pmatrix} q_l \\ q_i \end{pmatrix} = \begin{bmatrix} \boldsymbol{I} & \boldsymbol{0} \\ \boldsymbol{0} & \boldsymbol{I} \\ \lambda \boldsymbol{I} & \boldsymbol{0} \end{bmatrix} \begin{pmatrix} q_l \\ q_i \end{pmatrix}. \tag{1.4.5}$$

To proceed, some manipulation of $\boldsymbol{K}_{\boldsymbol{uc}}$ and $\boldsymbol{M}_{\boldsymbol{uc}}$ is required. This consists in a pre-multiplication of by $[\boldsymbol{\Lambda_R}]$ and a post multiplication of the result by its inverted transposed $[\boldsymbol{\Lambda_L}]$. For matrix $\boldsymbol{K}_{\boldsymbol{uc}}$ we obtain:

$$\begin{bmatrix} \boldsymbol{I} & \boldsymbol{0} & \frac{1}{\lambda}\boldsymbol{I} \\ \boldsymbol{0} & \boldsymbol{I} & \boldsymbol{0} \end{bmatrix} \begin{bmatrix} \boldsymbol{K}_{ll} & \boldsymbol{K}_{li} & \boldsymbol{K}_{lr} \\ \boldsymbol{K}_{il} & \boldsymbol{K}_{ii} & \boldsymbol{K}_{ir} \\ \boldsymbol{K}_{rl} & \boldsymbol{K}_{ri} & \boldsymbol{K}_{rr} \end{bmatrix} \begin{bmatrix} \boldsymbol{I} & \boldsymbol{0} \\ \boldsymbol{0} & \boldsymbol{I} \\ \lambda \boldsymbol{I} & \boldsymbol{0} \end{bmatrix} =$$

$$= \begin{bmatrix} \boldsymbol{K}_{ll} + \lambda \boldsymbol{K}_{lr} + \frac{1}{\lambda}\boldsymbol{K}_{rl} + \boldsymbol{K}_{rr} & \boldsymbol{K}_{li} + \frac{1}{\lambda}\boldsymbol{K}_{ri} \\ \boldsymbol{K}_{il} + \lambda \boldsymbol{K}_{ir} & \boldsymbol{K}_{ii} \end{bmatrix} =$$

$$= \frac{1}{\lambda}\left(\lambda^2 \begin{bmatrix} \boldsymbol{K}_{lr} & \boldsymbol{0} \\ \boldsymbol{K}_{ir} & \boldsymbol{0} \end{bmatrix} + \lambda \begin{bmatrix} \boldsymbol{K}_{ll} + \boldsymbol{K}_{rr} & \boldsymbol{K}_{li} \\ \boldsymbol{K}_{il} & \boldsymbol{K}_{ii} \end{bmatrix} + \begin{bmatrix} \boldsymbol{K}_{rl} & \boldsymbol{K}_{ri} \\ \boldsymbol{0} & \boldsymbol{0} \end{bmatrix}\right) =$$

$$= \frac{1}{\lambda}(\lambda^2[\boldsymbol{K1}] + \lambda[\boldsymbol{K2}] + [\boldsymbol{K3}]). \tag{1.4.6}$$

Now, by doing the exact same procedure for the mass matrix:

$$\begin{bmatrix} \boldsymbol{I} & \boldsymbol{0} & \frac{1}{\lambda}\boldsymbol{I} \\ \boldsymbol{0} & \boldsymbol{I} & \boldsymbol{0} \end{bmatrix} \omega^2 \begin{bmatrix} \boldsymbol{M}_{ll} & \boldsymbol{M}_{li} & \boldsymbol{M}_{lr} \\ \boldsymbol{M}_{il} & \boldsymbol{M}_{ii} & \boldsymbol{M}_{ir} \\ \boldsymbol{M}_{rl} & \boldsymbol{M}_{ri} & \boldsymbol{M}_{rr} \end{bmatrix} \begin{bmatrix} \boldsymbol{I} & \boldsymbol{0} \\ \boldsymbol{0} & \boldsymbol{I} \\ \lambda\boldsymbol{I} & \boldsymbol{0} \end{bmatrix} =$$

$$= \frac{1}{\lambda}\omega^2(\lambda^2[\boldsymbol{M1}] + \lambda[\boldsymbol{M2}] + [\boldsymbol{M3}]). \tag{1.4.7}$$

Finally, the quadratic eigenvalue problem is obtained where the frequency vector can be provided as input to obtain the values of μ.

$$\frac{1}{\lambda}(\lambda^2[\boldsymbol{K1} - \omega^2\boldsymbol{M1}] + \lambda[\boldsymbol{K2} - \omega^2\boldsymbol{M2}] + \cdots + [\boldsymbol{K3} - \omega^2\boldsymbol{M3}])q = \boldsymbol{0} \tag{1.4.8}$$

Remembering that the angular frequency which is the angular change per unit of time is:

$$\omega = 2\pi \mathrm{f} \tag{1.4.9}$$

and that the angular wavenumber is the proportionality between angular frequency and phase velocity,

$$K = \frac{\omega}{v_p} = \frac{2\pi}{\psi} \tag{1.4.10}$$

where ψ is the wavelength, we can express v_p in terms of ψ and the period (T) as follows:

$$v_p = \frac{\psi}{\mathrm{T}}. \tag{1.4.11}$$

We can finally derive the wavenumber as the number of wave cycles per unit length:

$$k = \frac{K}{2\pi} = \frac{1}{\psi}. \tag{1.4.12}$$

With some manipulation, we can rewrite the relation for the phase velocity as being:

$$\underline{\text{PHASE VELOCITY}}: \quad v_p = \frac{\omega}{K} = \frac{2\pi \mathrm{f}}{K}. \tag{1.4.13}$$

This allows to link the frequencies in input with the wavenumber and allows to plot the solutions. This type of plot is known with the terminology of "Dispersion Curves". The steepness of the dispersion curves (derivative of the phase velocity v_p) represents the group

velocity associated to that travelling wave.

$$\underline{\text{GROUP VELOCITY}}: \quad v_g = \frac{d\omega}{dk} \tag{1.4.14}$$

It follows that if the curve shows a vertical tangent $\left(\frac{d\omega}{dk} = 0\right)$ then there is no propagation, and this denotes the presence of a bandgap.

1.4.1.2 WFEM 1D-Periodicity (Inverse approach)

The same problem can be formulated imposing in input, real values for the reduced wavenumber and calculating the angular frequency vector as the eigenvalue problem output. The starting point is also represented by the Fundamental Dynamics Equation of the unit cell, shown in equation (1.4.3)and damping is still neglected. The objective is to convert this relation into an eigenvalue problem, by cancelling the force vector on the right-hand side of equation (1.4.3). This is obtained firstly rewriting the displacement vector as follows:

$$\boldsymbol{q} = \begin{pmatrix} q_l \\ q_i \\ q_r \end{pmatrix} = \begin{pmatrix} q_l \\ q_i \\ \lambda q_l \end{pmatrix} = \boldsymbol{\Lambda_R} \begin{pmatrix} q_l \\ q_i \end{pmatrix} \tag{1.4.15}$$

where $\boldsymbol{\Lambda_R}$ is the same matrix shown in equation (1.4.5). Now, assuming $f_i = 0$, the RHS of equation (1.4.3) becomes:

$$f = \begin{pmatrix} f_l \\ f_i \\ f_r \end{pmatrix} = \begin{pmatrix} f_l \\ 0 \\ f_r \end{pmatrix} \tag{1.4.16}$$

and by pre-multiplying f by $\boldsymbol{\Lambda_L} = \left[\frac{\mathbf{1}}{\boldsymbol{\Lambda_R}}\right]^T$, the force vector on the RHS of equation (1.4.3) are equal to zero and the desired result is obtained in equation (1.4.17), due to the Floquet-Bloch theory.

$$\boldsymbol{\Lambda_L} \begin{pmatrix} f_l \\ 0 \\ f_r \end{pmatrix} = \begin{bmatrix} \boldsymbol{I} & \mathbf{0} & \frac{1}{\lambda}\boldsymbol{I} \\ \mathbf{0} & \boldsymbol{I} & \mathbf{0} \end{bmatrix} \begin{pmatrix} f_l \\ 0 \\ f_r \end{pmatrix} = \mathbf{0} \tag{1.4.17}$$

By applying the latter, the relation which describes the dynamics of the unit cell along the considered direction of periodicity is obtained:

$$\boldsymbol{\Lambda_L}(\boldsymbol{K_{uc}} - \omega^2 \boldsymbol{M_{uc}})\boldsymbol{\Lambda_R} \begin{pmatrix} q_l \\ q_i \end{pmatrix} = \mathbf{0} \tag{1.4.18}$$

$$(\boldsymbol{\Lambda_L K_{uc} \Lambda_R} - \omega^2 \boldsymbol{\Lambda_L M_{uc} \Lambda_R}) \begin{pmatrix} q_l \\ q_i \end{pmatrix} = \mathbf{0} \tag{1.4.19}$$

$$\left(\boldsymbol{K_r}(\mu) - \omega^2 \boldsymbol{M_r}(\mu)\right) \boldsymbol{q}^{(r)} = \mathbf{0}. \tag{1.4.20}$$

We finally reached our standard eigenvalue problem. This is only possible though if $\boldsymbol{\Lambda_R}$ and $\boldsymbol{\Lambda_L}$ are Hermitian. This leads to a condition to be imposed on our reduced wavenumber μ which is that it must be a real number. Only if this is respected then $\boldsymbol{\Lambda_L} = \left[\frac{\mathbf{1}}{\boldsymbol{\Lambda_R}}\right]^T$.

Finally, the standard eigenvalue problem expressed in equation (1.4.20) is derived and by solving for $\mu \in [0; \pi]$, which represents the First Brillouin Zone (defined in section *1.4.1.3*), the frequency is obtained.

1.4.1.3 WFEM 2D-Periodicity

The method just outlined for 1D-periodic structures, can be extended to structures possessing periodicity along two dimensions. This simply means that the unit cell is repeated in two directions and therefore, the equations change slightly, as they need to consider this new factor. The directions are usually orthogonal to each other but not necessarily[62],[63]. Wave vectors can be expressed in terms of the reciprocal lattice basis which represents the Fourier transform of a periodic spatial function in real space also known as the direct lattice. Since the reciprocal lattice is also periodic, one can restrict the wave vectors to a certain region called first Brillouin zone. If there is symmetry in the reciprocal lattice, the wave vectors may be further restricted to the Irreducible Brillouin Zone (IBZ) (OABC), shown in *Figure 20* where the wavenumbers are positive. In some descriptions of the wave propagation characteristics, only the contour of the IBZ (O-A-B-C-O) is considered, where the band extrema always occur [11].

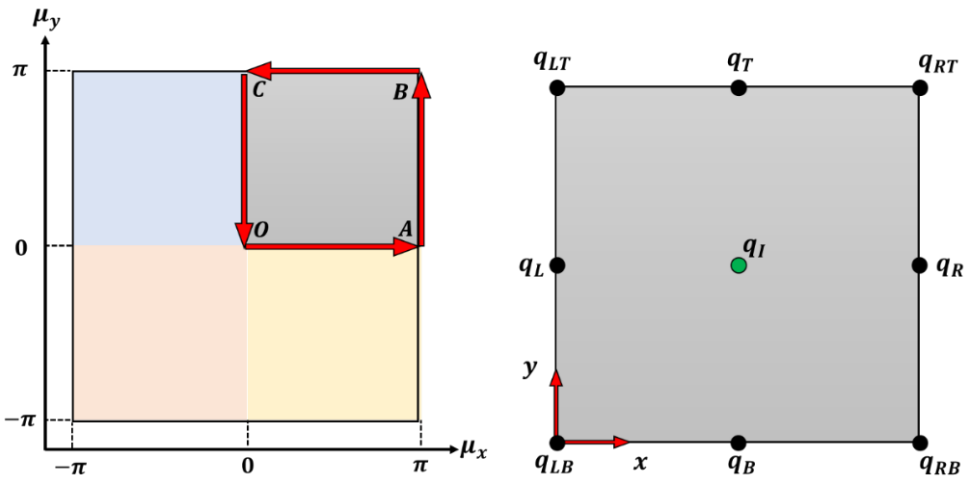

Figure 20 - Irreducible Brillouin Zone OABC (left) and representation of a 2D unit cell's boundary nodes (right)

A square 2D unit cell is shown in *Figure 20 (right)*. The reduced wavenumber this time has components both in the *x*- and *y*-direction, which are also the directions in which we would repeat our unit cell to obtain our 2D periodic finite structure.

Since the 1D analysis (wave propagation considered only in one direction) produced dispersion curves (μ, f), an analysis accounting for this second direction of wave propagation will produce instead a dispersion surface $\left(Re(\mu_x), Re\left(\mu_y\right), \mathrm{f}\right)$. The Floquet-Bloch relations are the following:

$$\begin{aligned} \lambda_x &= e^{j\mu_x} & \mu_x &= k_x L_x \\ \lambda_y &= e^{j\mu_y} & \mu_y &= k_y L_y \end{aligned} \tag{1.4.21}$$

where L_x and L_y are the unit cell occupancy dimensions in the *x*- and *y*-directions respectively and *k* the wave number. Just like for the 1DWFEM but considering this time the notation used in *Figure 20*, the Floquet-Bloch theory together with the continuity of displacements gives the following relations:

$$\begin{aligned} q_t &= \lambda_y q_b \\ q_r &= \lambda_x q_l \\ q_{lt} &= \lambda_y q_{lb} \\ q_{rb} &= \lambda_x q_{lb} \\ q_{rt} &= \lambda_x \lambda_y q_{lb}\,. \end{aligned} \tag{1.4.22}$$

In the same way, considering the equilibrium forces, we obtain:

$$\begin{aligned} f_{lb} + \lambda_x^{-1} f_{rb} + \lambda_y^{-1} f_{lt} + \lambda_x^{-1}\lambda_y^{-1} f_{rt} &= 0 \\ f_l + \lambda_x^{-1} f_r &= 0 \\ f_b + \lambda_y^{-1} f_t &= 0 \end{aligned} \tag{1.4.23}$$

Now the unit cell stiffness matrix this time is as follows:

$$\boldsymbol{K_{uc}} = \begin{bmatrix} \boldsymbol{K}_{lb-lb} & \boldsymbol{K}_{lb-lt} & \boldsymbol{K}_{lb-rb} & \boldsymbol{K}_{lb-rt} & \boldsymbol{K}_{lb-l} & \boldsymbol{K}_{lb-r} & \boldsymbol{K}_{lb-b} & \boldsymbol{K}_{lb-t} & \boldsymbol{K}_{lb-i} \\ \boldsymbol{K}_{lt-lb} & \boldsymbol{K}_{lt-lt} & \boldsymbol{K}_{lt-rb} & \boldsymbol{K}_{lt-rt} & \boldsymbol{K}_{lt-l} & \boldsymbol{K}_{lt-r} & \boldsymbol{K}_{lt-b} & \boldsymbol{K}_{lt-t} & \boldsymbol{K}_{lt-i} \\ \boldsymbol{K}_{rb-lb} & \boldsymbol{K}_{rb-lt} & \boldsymbol{K}_{rb-rb} & \boldsymbol{K}_{rb-rt} & \boldsymbol{K}_{rb-l} & \boldsymbol{K}_{rb-r} & \boldsymbol{K}_{rb-b} & \boldsymbol{K}_{rb-t} & \boldsymbol{K}_{rb-i} \\ \boldsymbol{K}_{rt-lb} & \boldsymbol{K}_{rt-lt} & \boldsymbol{K}_{rt-rb} & \boldsymbol{K}_{rt-rt} & \boldsymbol{K}_{rt-l} & \boldsymbol{K}_{rt-r} & \boldsymbol{K}_{rt-b} & \boldsymbol{K}_{rt-t} & \boldsymbol{K}_{rt-i} \\ \boldsymbol{K}_{l-lb} & \boldsymbol{K}_{l-lt} & \boldsymbol{K}_{l-rb} & \boldsymbol{K}_{l-rt} & \boldsymbol{K}_{l-l} & \boldsymbol{K}_{l-r} & \boldsymbol{K}_{l-b} & \boldsymbol{K}_{l-t} & \boldsymbol{K}_{l-i} \\ \boldsymbol{K}_{r-lb} & \boldsymbol{K}_{r-lt} & \boldsymbol{K}_{r-rb} & \boldsymbol{K}_{r-rt} & \boldsymbol{K}_{r-l} & \boldsymbol{K}_{r-r} & \boldsymbol{K}_{r-b} & \boldsymbol{K}_{r-t} & \boldsymbol{K}_{r-i} \\ \boldsymbol{K}_{b-lb} & \boldsymbol{K}_{b-lt} & \boldsymbol{K}_{b-rb} & \boldsymbol{K}_{b-rt} & \boldsymbol{K}_{b-l} & \boldsymbol{K}_{b-r} & \boldsymbol{K}_{b-b} & \boldsymbol{K}_{b-t} & \boldsymbol{K}_{b-i} \\ \boldsymbol{K}_{t-lb} & \boldsymbol{K}_{t-lt} & \boldsymbol{K}_{t-rb} & \boldsymbol{K}_{t-rt} & \boldsymbol{K}_{t-l} & \boldsymbol{K}_{t-r} & \boldsymbol{K}_{t-b} & \boldsymbol{K}_{t-t} & \boldsymbol{K}_{t-i} \\ \boldsymbol{K}_{i-lb} & \boldsymbol{K}_{i-lt} & \boldsymbol{K}_{i-rb} & \boldsymbol{K}_{i-rt} & \boldsymbol{K}_{i-l} & \boldsymbol{K}_{i-r} & \boldsymbol{K}_{i-b} & \boldsymbol{K}_{i-t} & \boldsymbol{K}_{i-i} \end{bmatrix}.$$

Just like for the 1D periodicity case, matrix $[\boldsymbol{\Lambda_R}]$ and $\boldsymbol{\Lambda_L} = [\boldsymbol{1}/\boldsymbol{\Lambda_R}]^T$ which contain the

Floquet-Bloch relations are created, and through pre- and post-multiplication and subsequent decomposition, finally the quadratic eigenvalue problem is obtained:

$$\boldsymbol{\Lambda_R} = \begin{bmatrix} I & 0 & 0 & 0 \\ I\lambda_x & 0 & 0 & 0 \\ I\lambda_y & 0 & 0 & 0 \\ I\lambda_x\lambda_y & 0 & 0 & 0 \\ 0 & I & 0 & 0 \\ 0 & I\lambda_x & 0 & 0 \\ 0 & 0 & I & 0 \\ 0 & 0 & I\lambda_y & 0 \\ 0 & 0 & 0 & I \end{bmatrix} \tag{1.4.24}$$

$$\frac{1}{\lambda}\left(\lambda_x^2\left[\boldsymbol{K1}(\lambda_y) - \omega^2\boldsymbol{M1}(\lambda_y)\right] + \lambda_x\left[\boldsymbol{K2}(\lambda_y) - \omega^2\boldsymbol{M2}(\lambda_y)\right]\right)\boldsymbol{q} + \cdots \\ \cdots + \frac{1}{\lambda}\left(\boldsymbol{K3}(\lambda_y) - \omega^2\boldsymbol{M3}(\lambda_y)\right)\boldsymbol{q} = \boldsymbol{0}\,. \tag{1.4.25}$$

To obtain the values of λ_x , the angular frequency ω and $\lambda_y \epsilon [0\,;\,\pi]$ must be provided.

The interval for λ_y depends on the type of unit cell and the values of the propagation constants μ_x and μ_y can be calculated from eigenvalues λ_x and λ_y respectively according to equation (1.4.21).

1.4.1.4 WFEM 2D-Periodicity (Inverse approach)

Once more, matrices $[\boldsymbol{\Lambda_L}]$ and $[\boldsymbol{\Lambda_R}]$ can be built and according to the 2D Floquet Bloch relations while keeping in mind that $f_i = 0$. The following equations are then derived:

$$\boldsymbol{q} = [\boldsymbol{\Lambda_L}]\boldsymbol{q}^{(r)} \tag{1.4.26}$$

$$[\boldsymbol{\Lambda_L}]f = \boldsymbol{0} \tag{1.4.27}$$

$$\boldsymbol{q} = \begin{pmatrix} q_{lb} \\ q_{rb} \\ q_{lt} \\ q_{rt} \\ q_l \\ q_r \\ q_b \\ q_t \\ q_i \end{pmatrix} \quad ; \quad \boldsymbol{f} = \begin{pmatrix} f_{lb} \\ f_{rb} \\ f_{lt} \\ f_{rt} \\ f_l \\ f_r \\ f_b \\ f_t \\ f_i \end{pmatrix} \quad ; \quad \boldsymbol{q}^{(r)} = \begin{pmatrix} q_{lb} \\ q_l \\ q_b \\ q_i \end{pmatrix} \tag{1.4.28}$$

$$\boldsymbol{\Lambda_L} = \left[\frac{\boldsymbol{1}}{\boldsymbol{\Lambda_R}}\right]^T. \tag{1.4.29}$$

Finally, the equation of motion scaled to our unit cell can be formulated, obtaining the following eigenvalue problem:

$$\left(\left[\boldsymbol{K_r}(\mu_x,\mu_y)\right]-\omega^2\left[\boldsymbol{M_r}(\mu_x,\mu_y)\right]\right)\boldsymbol{q}^{(r)}=\boldsymbol{0} \tag{1.4.30}$$

$$\boldsymbol{K_r}=\boldsymbol{\Lambda_L K}_{\boldsymbol{uc}}\boldsymbol{\Lambda_R} \tag{1.4.31}$$

$$\boldsymbol{M_r}=\boldsymbol{\Lambda_L M}_{\boldsymbol{uc}}\boldsymbol{\Lambda_R}. \tag{1.4.32}$$

1.4.1.5 WFEM 3D Periodicity

For completeness, a very brief explanation of the same method applied to structures which show periodicity along three directions is derived. For simplicity, in *Figure 21* the representative 3D unit cell is shown as a cube, which corresponds to the case where the periodicity occurs along three perpendicular directions:

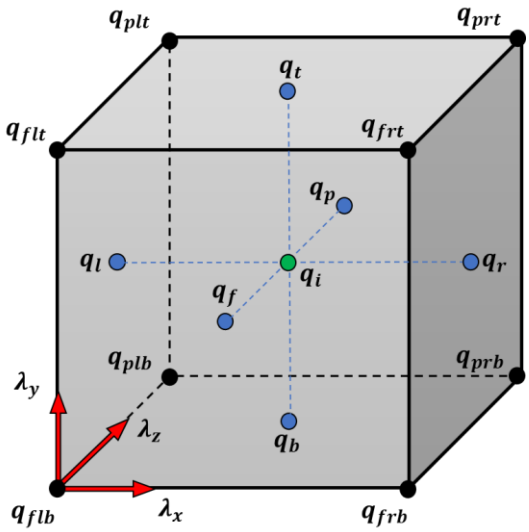

Figure 21 - representation of a 3D unit cell's boundary nodes

The Floquet-Bloch conditions are the following, where this time we have λ_x , λ_y andλ_z:

$$\begin{aligned} q_r &= \lambda_x q_l & q_{frt} &= \lambda_x\lambda_y q_{flb} \\ q_t &= \lambda_y q_b & q_{plb} &= \lambda_z q_{flb} \\ q_p &= \lambda_z q_f & q_{plt} &= \lambda_y\lambda_z q_{flb} \\ q_{frb} &= \lambda_x q_{flb} & q_{prb} &= \lambda_x\lambda_y q_{flb} \\ q_{flt} &= \lambda_y q_{flb} & q_{prt} &= \lambda_x\lambda_y\lambda_z q_{flb} \end{aligned} \tag{1.4.33}$$

The procedure for both, direct and indirect 3D methods is analogous to the previous ones. For the direct approach, the eigenvalue problem to be solved is the following:

$$\frac{1}{\lambda}\left(\lambda_x^2\left[\boldsymbol{K1}(\lambda_y,\lambda_z)-\ \omega^2\boldsymbol{M1}(\lambda_y,\lambda_z)\right]+\lambda_x\left[\boldsymbol{K2}(\lambda_y,\lambda_z)-\ \omega^2\boldsymbol{M2}(\lambda_y,\lambda_z)\right]\right)\boldsymbol{q}+\cdots \tag{1.4.34}$$

$$\ldots+\frac{1}{\lambda}\left(\boldsymbol{K3}(\lambda_y,\lambda_z)-\ \omega^2\boldsymbol{M3}(\lambda_y,\lambda_z)\right)\boldsymbol{q}=0$$

Where the values of λ_y,λ_z as well as the frequency must be provided in input. For the indirect method instead, the values of λ_x,λ_y and λ_z are varied one at the time to produce the three-dimensional arrays which will produce for each fixed couple of imposed wavenumbers a dispersion surface. To do so, the following eigenvalue problem must be solved:

$$\left(\left[\boldsymbol{K_r}(\mu_x,\mu_y,\mu_z)\right]-\omega^2\left[\boldsymbol{M_r}(\mu_x,\mu_y,\mu_z)\right]\right)\boldsymbol{q}^{(r)}=\boldsymbol{0} \tag{1.4.35}$$

1.4.1.6 Method considerations

The two approaches saw for both 1D and 2D periodicity differ in terms of the starting point. In one case we inject the angular frequency while in the "indirect" approach we inject real values of the reduced wavenumber. Both allow us to retrieve information about the propagative waves, but the computational load is reduced when using the inverse method (linear eigenvalue problem), since in the first case (equation (1.4.8)), a quadratic eigenvalue problem is obtained and the imaginary component (evanescent waves) is also computed. In case of analysis of structures possessing periodicity along three directions, the computational demand increases but not the complexity of the problem.

1.4.2 Model order reduction

To model a sandwich panel with skins, unit cell models using shell elements are used. This requires high computational time because of the large number of nodes and associated degrees of freedom which must be taken into consideration. In this work, a fixed interface component synthesis method is selected and used as it well combined with the Floquet-Bloch theory principles. This method was developed in 1968 by Craig and Bampton [64],[65] and in synthesis it condenses the nodal information coming from the internal unit cell nodes reducing significantly the number of total degrees of freedom, since the amount of boundary nodes of our models are much lower compared to the internal nodes and this difference increases as the element size decreases.

The relation between the condensed DOFs, q_c, and the full model is the following:

$$\begin{pmatrix} q_{bd} \\ q_i \end{pmatrix} = \boldsymbol{CB} \begin{pmatrix} q_{bd} \\ q_c \end{pmatrix} \tag{1.4.36}$$

where $\boldsymbol{q}_{bd}$ are the unit cell boundary DOF and $\boldsymbol{q}_c$ are the condensed internal DOF's. Now matrix $\boldsymbol{CB}$ has the following components:

$$\boldsymbol{CB} = \begin{bmatrix} \boldsymbol{I}_{bd} & \boldsymbol{0} \\ \boldsymbol{\phi}_{bd} & \boldsymbol{\phi}_c \end{bmatrix} \tag{1.4.37}$$

where $\boldsymbol{I}_{bd}$ is an identity matrix of the dimension of the boundary nodes, $\boldsymbol{\phi}_{bd}$ refers to the static modes and $\boldsymbol{\phi}_c$ is the reduced basis (first modes) of the fixed interface modes $\boldsymbol{\phi}_i$. Now $\boldsymbol{\phi}_c$ will have dimensions which depend on the arbitrary number of fixed interface modes kept while $\boldsymbol{\phi}_i$ is calculated solving the eigenvalue problem below:

$$[\boldsymbol{K}_{ii} - \omega_0^2 \boldsymbol{M}_{ii}]\boldsymbol{\phi}_i = \boldsymbol{0} \tag{1.4.38}$$

while the boundary nodes are:

$$\boldsymbol{\phi}_{bd} = -\boldsymbol{K}_{ii}^{-1}\boldsymbol{K}_{ibd}. \tag{1.4.39}$$

Finally, both the mass and stiffness matrices can be condensed as well by a pre and post multiplication of the matrix *CB:*

$$\boldsymbol{K}_{CB} = \boldsymbol{CB}^T \begin{bmatrix} \boldsymbol{K}_{ll} & \boldsymbol{K}_{li} & \boldsymbol{K}_{lr} \\ \boldsymbol{K}_{il} & \boldsymbol{K}_{ii} & \boldsymbol{K}_{ir} \\ \boldsymbol{K}_{rl} & \boldsymbol{K}_{ri} & \boldsymbol{K}_{rr} \end{bmatrix} \boldsymbol{CB} \tag{*1.4.40*}$$

The reduced matrices can be now used to proceed with the WFEM formulations keeping in mind that the size of $\boldsymbol{\phi}_c$ affects the accuracy of the final solution and therefore a convergence study should be performed before further analyses.

1.5 NUMERICAL PREDICTION TOOLS USING MATLAB AND ANSYS

The numerical tools developed during this work aim to predict and verify the presence of partial or full bandgaps as well as to quantify their width. To achieve this, the constituent material damping was neglected as shown from the considered equation of dynamics (8), where only mass and stiffness matrices appear. Formulations were initially created to predict the dynamic behaviour of simple structures and so beam elements were enough to completely describe them, but as structures became more complex (honeycombs require thin plate theory) the models were made using shell elements. In addition to this, scripts

were written to perform parametric analyses with the objective of understanding the impact of certain variables on the bandgap evolution. Due to the complexity of those structures, mass and stiffness matrices were not calculated analytically but instead, commercial finite element software was used to recover them when performing WFEM. The same software was used to obtain FRF's. All numerical tools involved at some stage MATLAB (pre or post process) and for harmonic, transient or modal simulations, the selected software was ANSYS APDL. The following diagram summarizes the different strategies used for both, classic methods and WFEM and the outline of the numerical tools as well as a brief motivation and description can be found in the APPENDIX.

1.5.1 Infinite structure

As described earlier in this chapter, whenever a WFEM analysis is performed, the model consists in a unit cell. It is enough to perform a modal analysis of the unit cell to retrieve its mass and stiffness matrices and command ANSYS to export them as a txt file. When the model contains less than 9999 degrees of freedom, ANSYS can write the txt correctly. With complex models and finer meshes, the txt file output request produces an error, due to a maximum number of digits per column when writing the file. This was solved adopting sparse matrix form output. This produces multiple advantages. The txt file is smaller in size which represents an advantage in memory occupancy and the digit problem which rises when the number of degrees of freedom increases is solved. Another advantageous fix is the gain in computational time as the txt file is composed of less lines to read. The sparse Mass and Stiffness matrices are brought back to its original dimensions before injecting them in the MATLAB scripts WFEM.

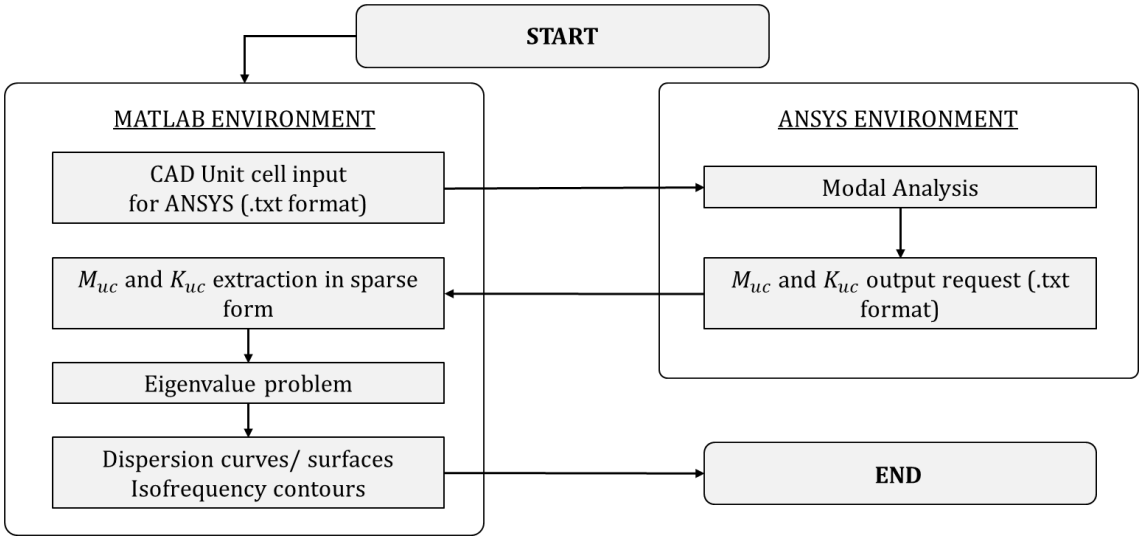

Figure 22 – Algorithm diagram of the main script used perform WFEM of the examined structure.

Supplementary increase in computational efficiency can be reached by writing the WFEM scripts in sparse form and furthermore, the performance could have been improved by writing all the scripts using ASCII notation. But the choice of reconverting the matrices to their original dimensions after reading the txt was taken because it eased the debugging procedure and assured the import was correct. Depending upon the type of analysis to be performed (1DWFEM or 2DWFEM) the number and type of boundaries to be considered are multiple. Starting from 1DWFEM, the model nodes to be considered are only the ones at the extremities of the direction of wave propagation of interest. These can be the left and right boundaries or the top and bottom. If the unit cell is symmetric, the number of boundary nodes will be the same on each extremity which is auspicial. The knowledge about which nodes are at the boundaries is essential because only in this way it is possible to separate them from the internal nodes and consequentially know which portions of the mass and stiffness matrices corresponds to what and are required to build the reduced dynamic stiffness matrix. Without this information it would not be possible to apply the Floquet-Bloch conditions. Depending on the geometry of the unit cell as well as the element size, the number of nodes may change and therefore the numbers assigned to the boundary nodes varies each time. Coding a universal program which could adapt to any unit cell and element size became urgent.

1.5.2 Finite structure

Here two main scripts were written, one for harmonic analyses and one for transient analyses. As mentioned before in this chapter, a harmonic analysis is performed to evaluate the behaviour of the real structure and the WFEM method opportunely "calibrated", acts as fast prototyping tool. To validate instead the iso-frequency findings (which are a propagation direction design tool covered in section *3.3*), a transient simulation with opportune boundary conditions and injected harmonic force is performed, and the results are stored to produce figures used to create GIF animations, where, thanks to a colour scaling, proportional to the out of plane displacements, the direction of the bending wave propagation becomes visible.

In this case, a transient analysis is performed because it allows to input the nodal displacement which would be produced if the structure would be solicited with a pure tone, while in a harmonic simulation all frequencies within the range are excited, one at the time, and the results show a steady state deformed shape, which due to the border effects, doesn't allow us to visually the propagating fringes at each time-step. Both of those analysis make

use of the same Matlab scripts used to create the unit cells for the WFEM analyses, but furthermore, it creates an array of unit cells (finite core panels), commands Ansys to run the simulation and it collects the nodal results which are then post-processed.

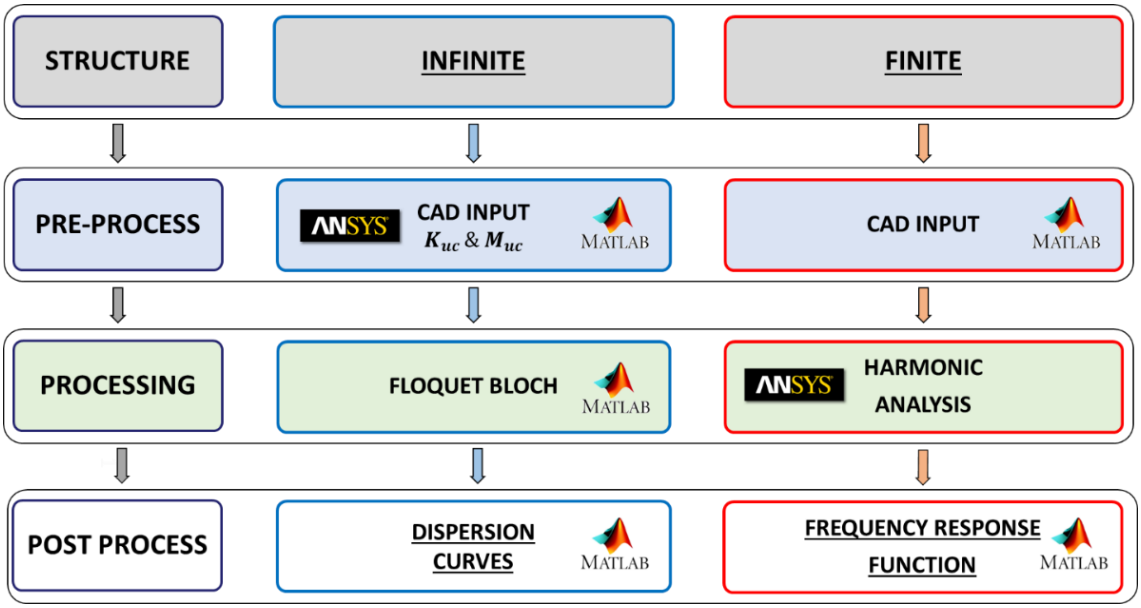

Figure 23 - Self developed numerical prediction tools outline

CHAPTER 2

WFEM APPLICATIONS

2.1 SIMPLE PERIODIC STRUCTURES

In this section, the methods explained in *chapter 1* are applied to simple structures using the coded tools which are outlined in the *Appendix*. A theoretical analysis on a similar structure was conducted by Tian and Tie[66]. The chosen structures are a periodic beam (1D) first and a periodic grating (2D) later, both modelled in ANSYS using BEAM4 elements.

2.1.1 Truss with periodically variable section

Starting from the periodic truss beam, the analysis will produce an FRF, which will be performed on a finite structure, while the WFEM and TMM, which will be performed on the unit cell, giving information about the behaviour of an "infinite" structure. As reference, both, dispersion curves and FRF for a simple beam with constant cross section in case of a longitudinal compression solicitation, neglecting damping, are shown in *Figure 25* while the periodic beam parameters are shown in *Table 2*. The structure is modelled in ANSYS using the BEAM4 element type and the element size is calculated according to the relation provided in equation (1.2.4).

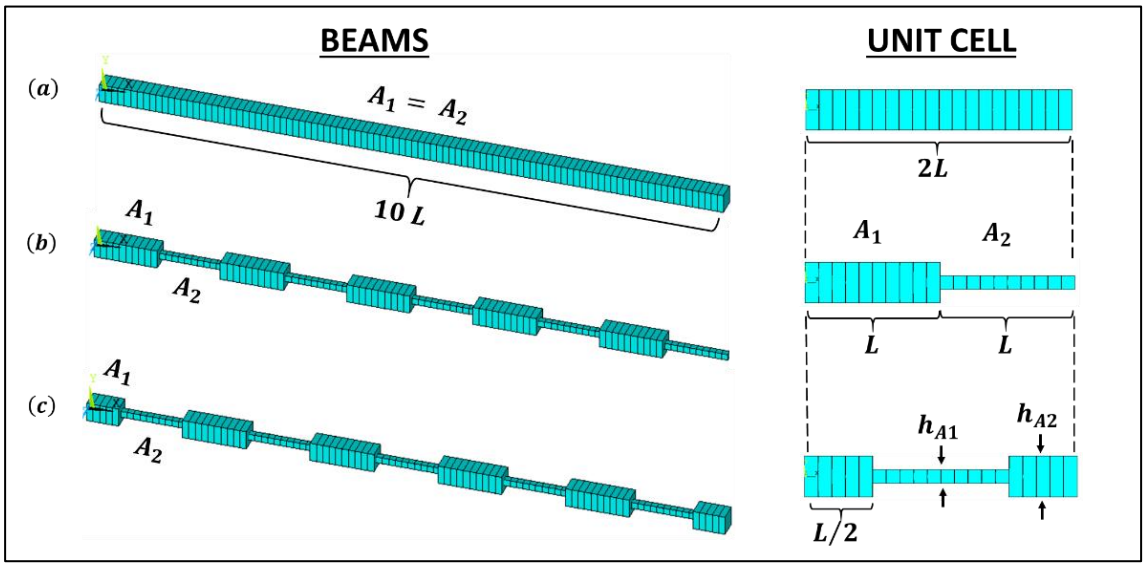

Figure 24 - (a) Homogeneous beam; (b) Periodic beam with asymmetric unit cell; (c) Periodic beam with symmetric unit cell

The FRF for undamped structures would have an infinite value when the considered frequency is equal to the natural frequency, ω_n.

In *Figure 25* the peak has a finite value because the frequency step (discretization) used during the analysis produces results which don't perfectly match the ω_n values. As a result, the FRF produces a plot which resembles an amplitude modulation since there is a relation between the frequency at which ω_n occurs and the chosen frequency step. Whenever we study a periodic structure, the first thing to do is to select the unit cell. This should be done to guarantee an equal and minimum number of boundary nodes to reduce the size of $\boldsymbol{K_{uc}}$ and $\boldsymbol{M_{uc}}$ which directly translate in reduced computational time. The structure shown in *Figure 24* can be cut in different ways to produce its unit cell and since the Floquet-Bloch periodic conditions can be applied to all possible unit cells, the result should be the same.

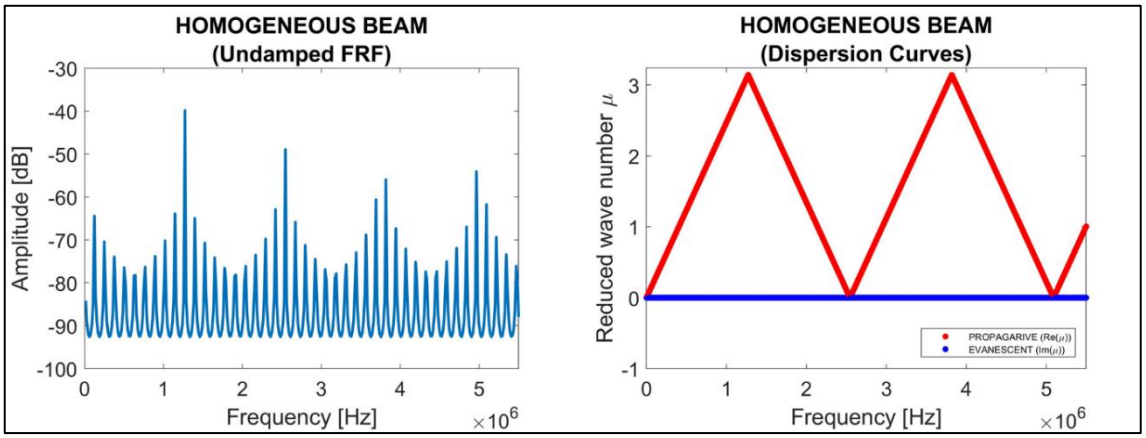

Figure 25 - Frequency response plot of a homogeneous undamped beam (left) and its dispersion curves (right) allowing only longitudinal axial pressure waves.

As a starting point, an asymmetric unit cell is chosen (visible in *Figure 24* and *Table 2),* where beams of section A1 and A2 are alternated and connected, are used.

PARAMETER (mm)	Section A1	Section A2	ASYMMETRIC UNIT CELL
$Length, L$	1	1	
$Width, w = Height, h$	0.1 – 0.5	0.5 – 0.1	
PARAMETER (mm)	**Section A1**	**Section A2**	**SYMMETRIC UNIT CELL**
$Length, L$	0.5	1	
$Width, w = Height, h$	0.1 – 0.5	0.5 – 0.1	

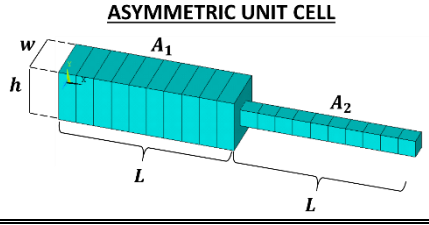

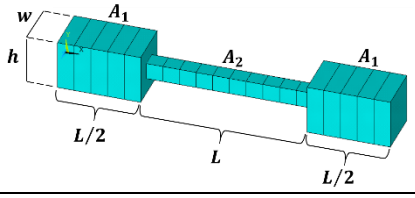

Table 2 - Periodic beam unit cell parameters

By shifting the cutting selection of a quantity equal to $L/2$, the symmetric unit cell is

obtained, which becomes an asset when analysing complex structures and multi-directional periodicity, as symmetry allows to reduce the Brillouin zone.

2.1.2 Frequency response

Suppose to have a finite structure made of ten unit cells (an example with 5 unit cells is shown in *Figure 24*) with the intent to measure the response displacement at one extremity when a compressive unit harmonic force is applied at the other end. The plot on the right in *Figure 26* shows frequency ranges (in grey) where the function reaches very low values. Those dips are typical of bandgap frequency ranges where the measured displacement amplitude is basically null.

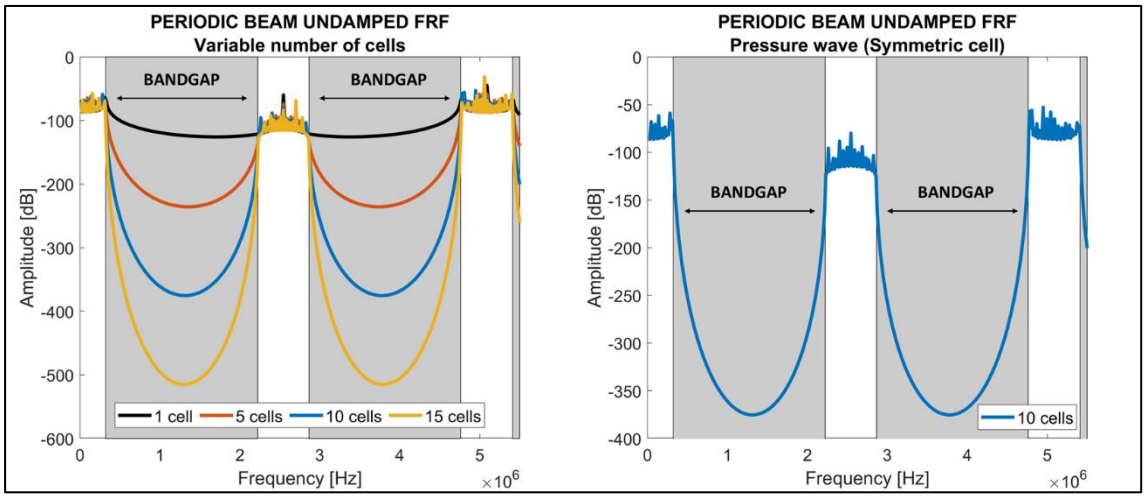

Figure 26 - Periodic beam undamped FRF's for increasing numbers of cells (left), and for 10 unit cell (right) allowing only longitudinal axial pressure waves.

An interesting fact is that by analysing a finite structure, the number of unit cells has an impact on the behaviour of the structure. As we increase the number of unit cells between the solicitation point and the output point, the amplitude of the displacement becomes progressively lower, as shown by the plot on the left in *Figure 26*. This does not depend on the structural damping but rather from the number of impedance mismatches that are represented by each unit cell. This can be used as a bandgap identification tool as sometimes, for complex structures, the bandgap is not so clear and increasing the number of cells, increases the periodic characteristics and makes the dips more evident. Depending on the degrees of freedom and type of element chosen for the CAD model, it is possible to perform aimed analyses to understand how the structure behaves and responds to selective types of solicitations. It is opportune to point out that when performing an FRF, the choice of the unit cell does not impact the overall computational time as it happens when using WFEM because the analysis is carried out on the full finite structure regardless of the chosen

unit cell used to create it.

Figure 27 and *Figure* 28 are parametric FRF plots of the finite periodic beam constituted of 5 unit cells for the asymmetric and symmetric unit cell case respectively. The aspect ratio is calculated as t_1 / t_2 where t_1 and t_2 are the value of the side of the cross section for the A1 and A2 sections when $(w = h)$. As we vary the aspect ratio while keeping a constant mass, the FRF parametric plot underlines the unit cell's reciprocal configurations.

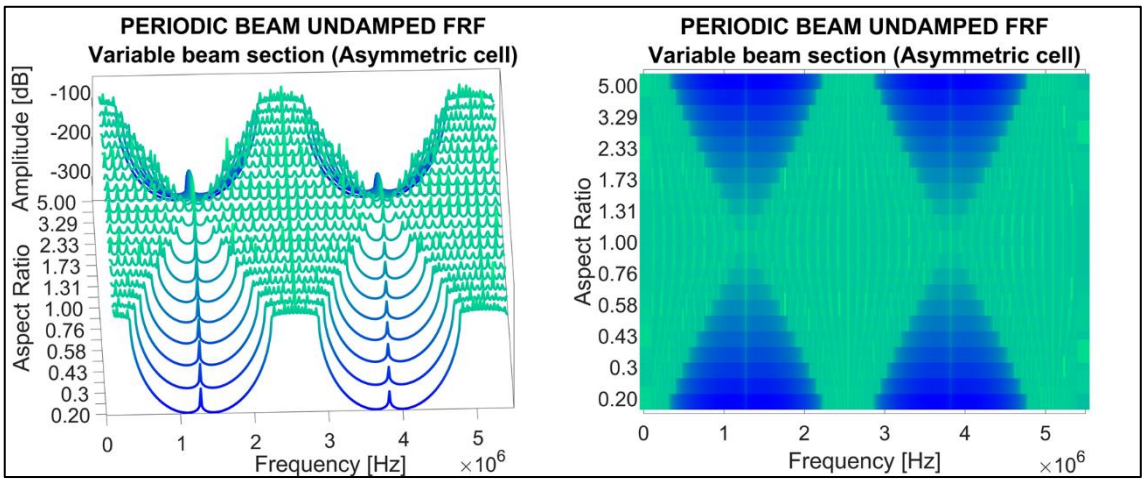

Figure 27 - Parametric FRF's for a periodic beam with variable aspect ratio (asymmetric cell), allowing only longitudinal axial pressure waves.

The only noticeable and surprising difference between the parametric plots caused by the unit cell selection is that when the asymmetric unit cell along the propagation path is chosen, something which resembles an internal resonance appears (clearly visible in *Figure 27* and not in *Figure 28).* This should not be the case because the FRF should be the same, no matter the choice of unit cell. This numerical error can probably be brought back to how the software deals with connecting beam elements with different cross-sections.

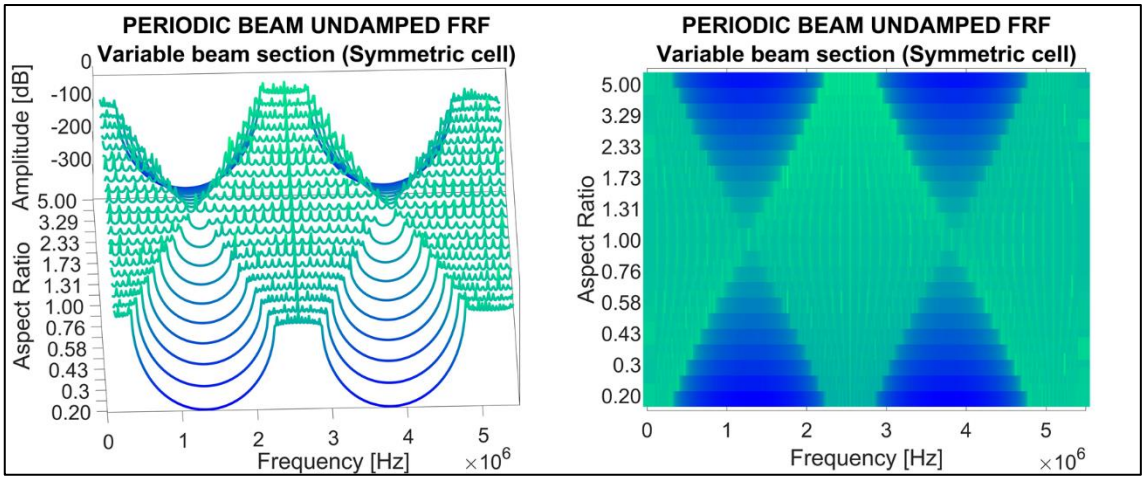

Figure 28 - Parametric FRF's for a periodic beam with variable aspect ratio (symmetric cell), allowing only longitudinal axial pressure waves.

2.1.3 Dispersion Curves

The dispersion curves, which are solutions to the eigenvalue problem proposed in section *1.4*, relate the frequency [Hz] to the reduced wavenumber. Remembering that $\mu = kL$ and that $\mu \in \mathbb{C}$, the real and imaginary components are represented with two different colours: the propagating wave which is the real part of the propagation constant ($Re(\mu)$) it's displayed in red, while the evanescent waves, which are the imaginary contribution of the propagation constant, ($Im(\mu)$), are displayed in blue. First studies used to plot both contributions in the positive y-axis quadrant but soon, the community preferred to plot them specular, which really helped to distinguish them better visually. In *Figure 29* it is noticeable that when the $Re(\mu) = 0$ or $Re(\mu) = \pi$, then $Im(\mu) \neq 0$. The vertical tangent of the red curve is followed by frequency ranges where the blue curve is different from zero and for what was explained in section *1.4.1.1*, that represents the beginning or the end of a bandgap zone (highlighted in grey).

The information that this type of plot can deliver though is not exclusive about the presence or absence of wave propagation. In this simple case, we only considered one degree of freedom including only the beams compression modes and therefore the interpretation is trivial. Comparing this dispersion curve with the FRF plot (*Figure 26* right) it is immediately visible that the bandgaps correspond accurately. Another crucial information provided, is that what seemed to be an internal resonance from the FRF plots, is evidently a numerical error, since performing WFEM or TMM on the two unit cells (asymmetric and symmetric), produces the same dispersion curves. Now for each dispersion curve point solution, we would be able to calculate the eigenvectors in addition to the eigenvalues. By summing the eigenvectors to the beam nodes initial positions, the deformed shape of the unit cell is obtained. In this simple example, we have four curves being four propagating compression waves where $Re(\mu) \neq 0$ or $Re(\mu) \neq \pi$. As the frequency range increases, the travelling waves wavelength decreases. The initial dimension of the unit cell though remains unchanged and therefore, it is intuitive that it can "accommodate" more wave cycles. The branches in fact represent compression modes of increasing number.

If we consider all degrees of freedom for this same structure, the dispersion curves become more intricate as shown in *Figure 31*. Each curve will be in fact related to a type of wave and depending on the number of degrees of freedom considered, they could be longitudinal, transverse, or a combination (torsional). The detection about which wave is associated to which branch though is not trivial at all and no available software is able to do this distinction.

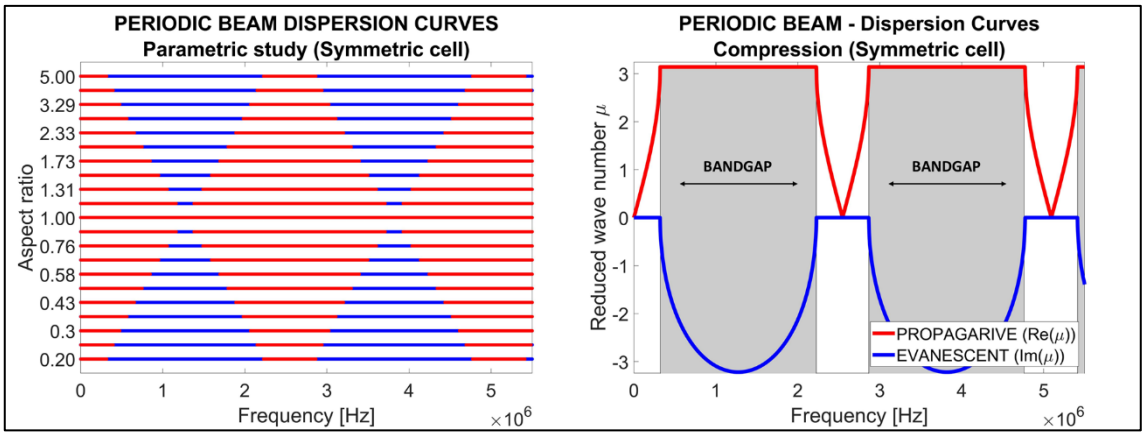

Figure 29 - Parametric plot of dispersion curves for variable aspect ratio (left), Dispersion curves for a single configuration with bandgaps. Both are performed allowing only longitudinal axial pressure waves.

The evolution in understanding dispersion curves and the tools developed by the author to aid with the wave modes distinction/detection will be discussed later in this chapter. In *Figure 29 (left)* a representation of the parametric analysis carried out using the coded Matlab tools and ANSYS is shown. The point solutions for which $Im(\mu) = 0$ or $Re(\mu) = 0$ or $Re(\mu) = \pi$ are neglected and the view is set into the page plane. In this way, it becomes intuitive that if for a certain frequency range, the plot shows a blue line, then we have a bandgap. This visual method which aids in understanding the evolution of the bandgaps was first produced, to the authors knowledge, by D. Chronopoulos [67] and afterwards was slightly modified, as initially, only the real part used to be plotted and therefore no blue line was included. Each horizontal line, made of red and blue segments, represents the dispersion relation for a certain configuration (aspect ratio).

2.1.4 FRF and dispersion curve interpretation

This paragraph will outline few advantages/disadvantages as well as differences between the information which can extract from an FRF and/or a Dispersion plot. This can be explained with the same beam structure discussed earlier. Let us consider the simply supported periodic beam allowing only displacements in one direction and let us consider a compression type of solicitation along that same longitudinal axis. Both, dispersion curves (*Figure 29*) and FRF (*Figure 26 (left)*) show the same bandgaps. If we allow instead displacements and rotations in-plane where the truss lies, and apply a solicitation within that plane, but at an angle to its longitudinal axes(exciting in-plane bending and compression modes at the same time), the FRF would display the overall response of the structure (*Figure 30 (right)*). Since the structure possesses full in-plane bandgaps, the plot shows deep amplitude drops. If this were not the case, the structure could have still

possessed selective bandgaps, but the detection would not be possible using this method.

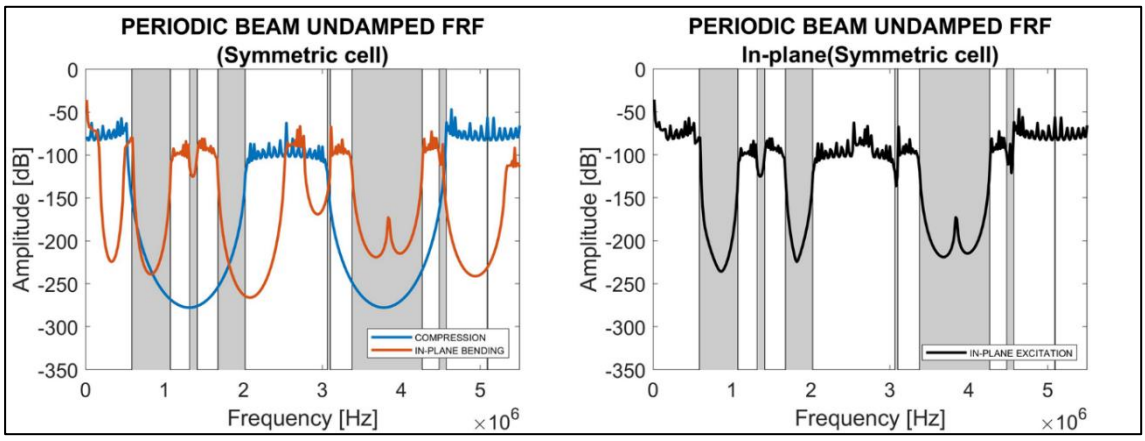

Figure 30 – FRFs for compression and in-plane bending for a periodic beam considering 3DOF and neglecting damping (left) and the FRF for the same structure considering multiple simultaneous excitations and 3 DOF (right)

By analysing the FRF on the left in *Figure 30*, it is visible that the bandgaps on the right are resultant bandgaps from the sum of the two separate FRF analyses conducted allowing only in-plane compression or bending. So, it is possible to encounter cases where FRF's obtained for structures which are excited by multiple wave types seem not to have bandgaps, only to discover that they possess selective filtering properties. The dispersion curve (*Figure 31*) is also taking all in-plane solicitations into account, but contrary to the FRF, it allows to distinguish full bandgaps as well as selective (partial) bandgaps since each dispersion curve relates to a type of wave. Under the computational time point of view, the FRF is clearly more dispendious since the number of nodes in the model (full scale), and therefore degrees of freedom, is considerably higher compared to the WFEM (unit cell).

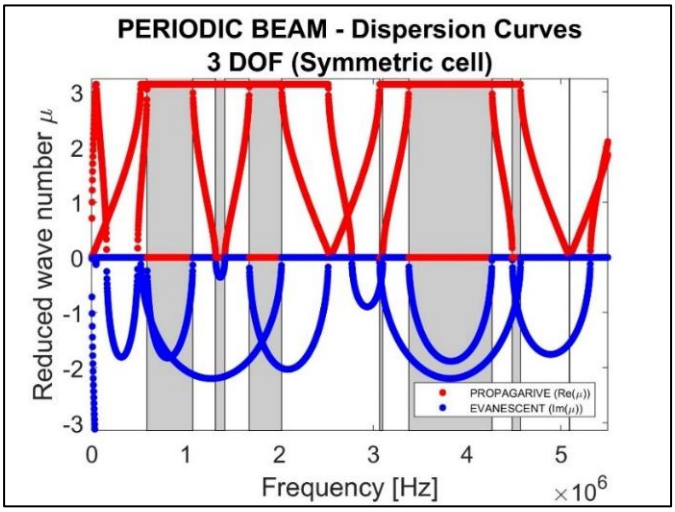

Figure 31 - Dispersion curves for a periodic beam with 3DOF and blocked out of plane displacements and rotations

The best approach, especially in case of complex structure analysis, is to use WFEM to produce dispersion diagrams, for design purposes, and then use the FRF to verify the

propagation or filtering capabilities of the finite structure.

2.1.5 Beam vs Solid elements

This section will focus on the peaks within the bandgap frequency range, appearing in the FRF produced by modelling the periodic truss using beam elements and selecting the asymmetric unit cell. We already underlined how the dispersion curve does not depict such behaviour and therefore, it is unlikely that the peak corresponds to a local resonance of the structure. A comparison using different type of elements, mesh, and constrains is carried out with the intention to understand if this phenomenon depends on the software (ANSYS) and the way it deals with connections between beams of different cross-section.

An analysis varying the element type for the model was performed. The elements used for the comparison were the ANSYS SOLID185 (hexahedral 8-node), and SOLID 187 (tetrahedral 10-node). Both meshes had an element size of 0.05mm, in agreement with what is mentioned in section 1.2.1. The structure was created repeating the unit cell 5 times in its axial direction, as done in section 2.1.1. The FRF plot shown in *Figure 32* denotes how allowing only the axial displacement, leads to a structural stiffening effect, which shifts and widens the bandgap to higher frequencies. The local resonance in the middle of the bandgap is still there if we allow only axial displacements, no matter the type of element used. This still resembled a numerical error because the deformed shape at the frequency was not showing global nor local resonances.

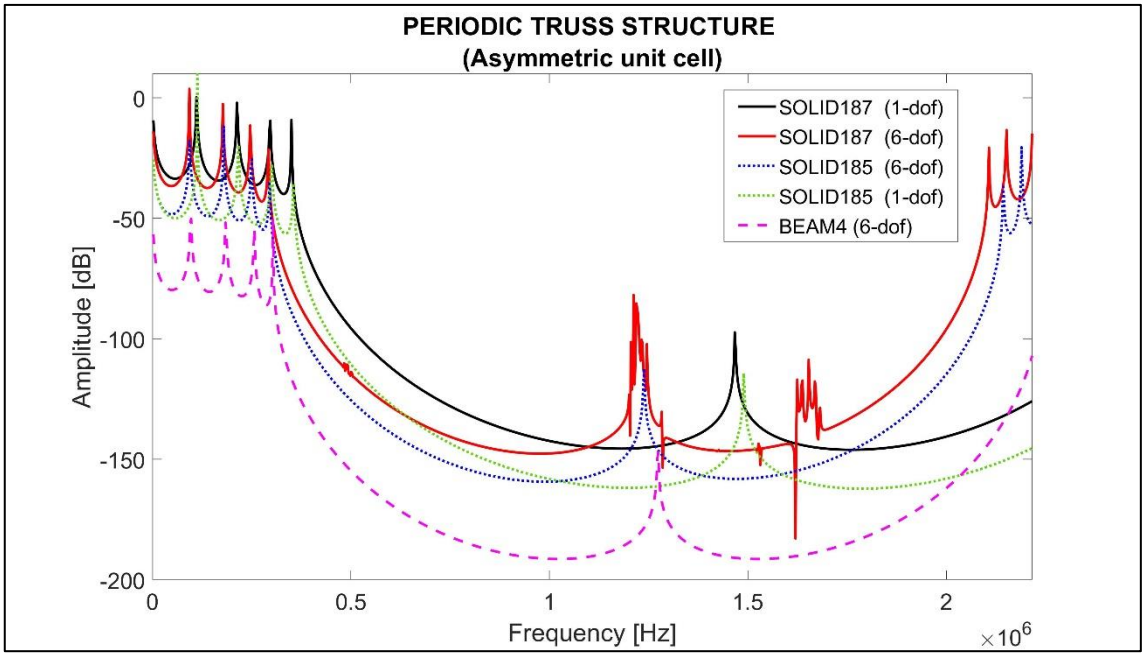

Figure 32 – FRF of the periodic truss structure assembled with 5 asymmetric unit cell subjected to axial pressure wave and modelled using various element types.

As the constrains were removed, the structure modelled with tetrahedral elements (SOLID187), showed multiple local resonant frequencies within the bandgap, all confirmed by the deformed structures, as visible in *Figure 33*. The presence of resonant frequencies within bandgaps, has been investigated before by Sorokin[68], who concluded that the eigenfrequencies of an asymmetrical periodic cell with constrained and free boundary conditions can appear within a bandgap of an infinite periodic structure. Furthermore, the eigenfrequencies of a finite structure made of repetition of unit cells may contain eigenfrequencies in the bandgaps, besides those located in the pass-bands, which become more densely populated. These observations probably explain the results obtained in the truss structure analysed.

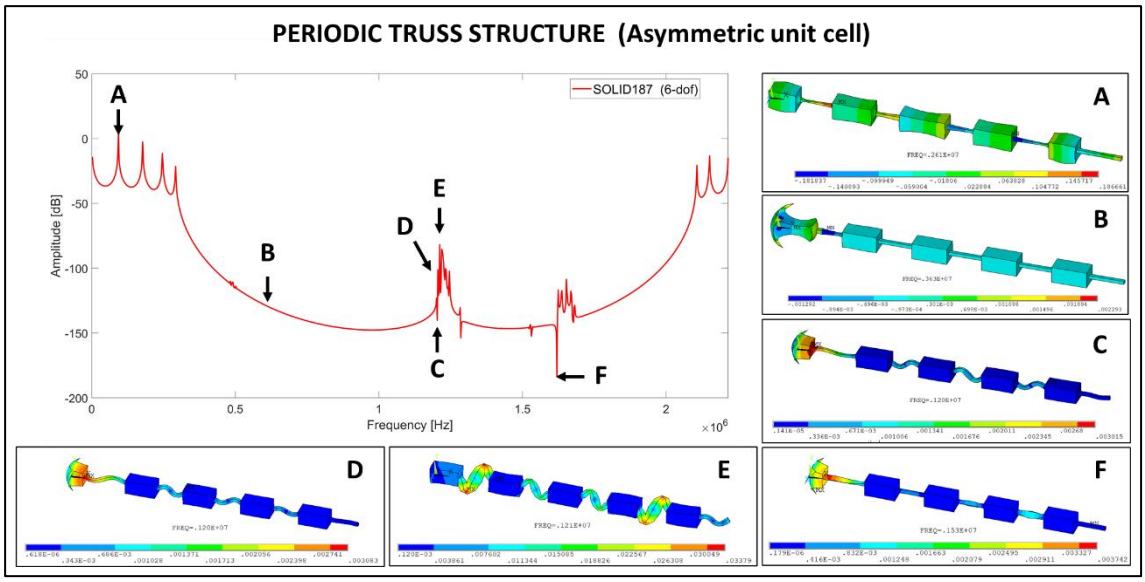

Figure 33 - FRF of the periodic truss structure assembled with 5 asymmetric unit cell using SOLID187 tetrahedral 10-node elements, subjected to axial pressure wave. The deformed shapes refer to the peaks indicated in the graph. More precisely: (A) structural second mode, (B) deformed shape within the bandgap, (C) out of plane bending local resonance mode, (D) in plane local resonance mode, (E) Combined bending and torsional local resonance mode , (F) torsional local resonance mode.

2.1.6 Grating with 2D periodically variable section

Using the 2DWFEM, the results of the analysis performed on a uniform and variable-section cross grating are proposed, with the intention to visually introduce dispersion surfaces $\left(Re(\mu_x), Re(\mu_y), \mathrm{f}\right)$ and dispersion surface contours $(k-\mathrm{space}, \mathrm{f})$. The grating's unit cell periodicity is enhanced using the same concept applied to the truss in section *2.1.1* so, one of the vertical and one of the horizontal cross-branches are thickened, maintaining fixed the out of plane thickness (geometrical parameters are listed in *Table 3)*. The structure is modelled in ANSYS using the SHELL181 elements and once more, the element size is calculated according to the relations provided in equation (1.2.5). The analysis is carried out

considering 6-DOF's per node. In *Figure 34* an array of 3x3 unit cells is shown to give a preview of what kind of structure would be created by repeating the unit cell in the x and y-direction, while the.

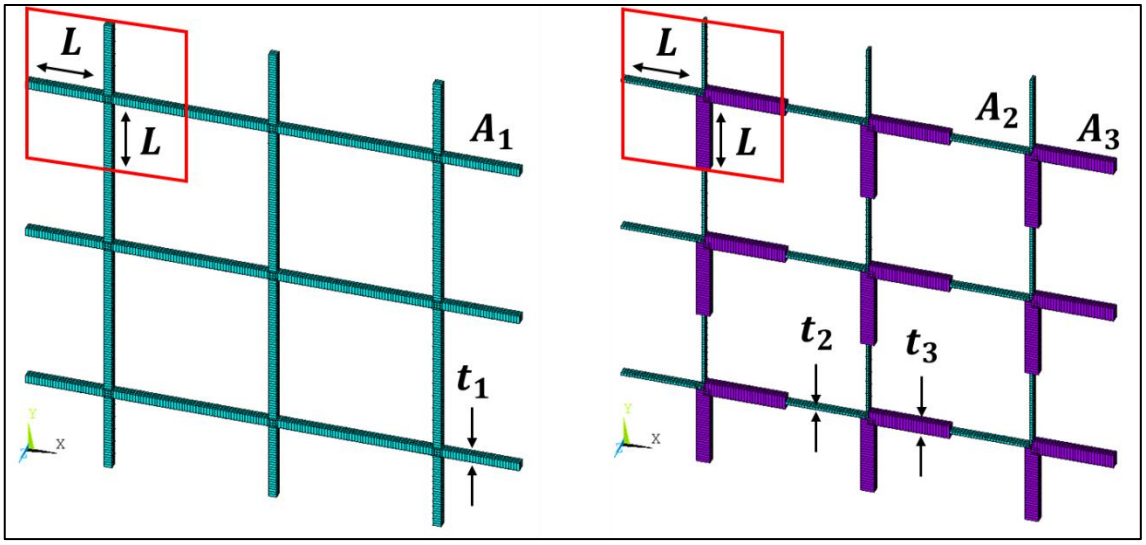

Figure 34 - 2D (3x3 array) and its unit cell highlighted in the red box for the uniform grating (left) and the grating with periodically variable sections A_1 and A_2

PARAMETER (mm)	Section A1	Section A2	Section A3
$Length, L$	6	6	6
$Width, t$	$t_1 = 0.3$	$t_2 = 0.1$	$t_3 = 0.5$
$Height, H$	0.3	0.3	0.3
$Skin\ thickness, h$	0.05		
$Element\ size$	0.1		

Table 3 –Cross grating model parameters for the shell elements used in both configurations: bare core and sandwich structure.

The dispersion surfaces (first 18 modes) for both periodic structures are shown in *Figure 35*. Although we notice change, from this angle it is not visible if the structures possess a bandgap within this frequency range. A projection on the $(Re(\mu_x), \mathrm{f})$ or $(Re(\mu_y), \mathrm{f})$ plane helps to locate frequency ranges where there is no surface plot. As it was possible for the 1D analysis, the study can be reduced to the IBZ exploiting the lattice symmetry and therefore, vary the reduced wavenumbers values in the range $[0, \pi]$. The dispersion contour, which has on the x-axis the k-space position (IBZ) also shows that there are no full bandgaps since there is no frequency range where we can draw a horizontal line without intersecting the eigenvalue branches. The k-space position is created by intercepting the dispersion surfaces with an imaginary parallelepiped shell which has a square base equal to the IBZ (O-A-B-C), shown in *Figure 20*, and the height of the frequency range analysed.

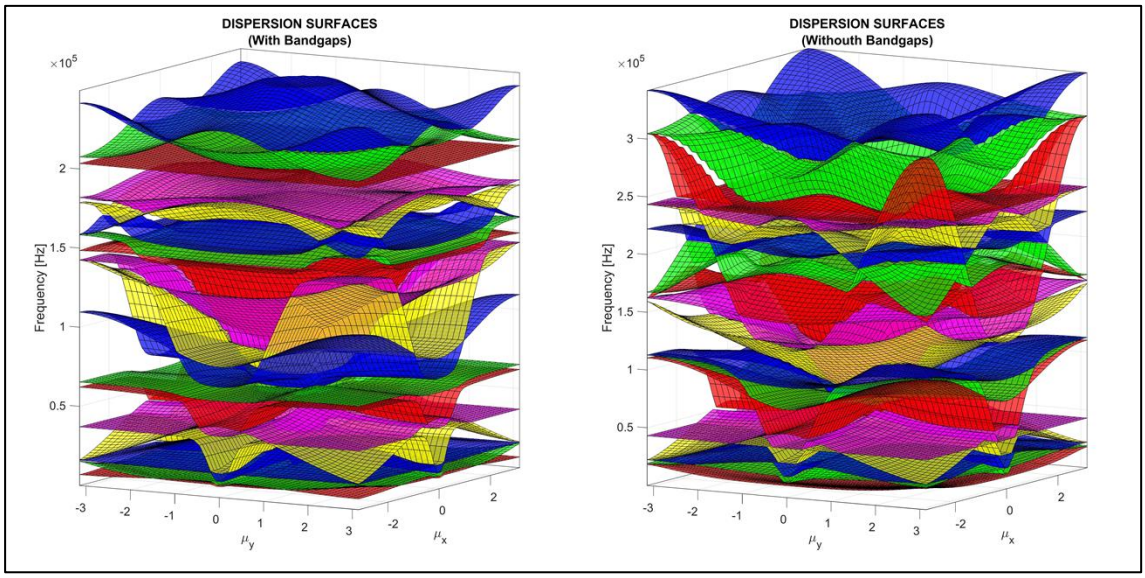

Figure 35 - Dispersion surfaces for the uniform grating (left) and the grating with periodically variable sections A_1 and A_2

Furthermore, it has been demonstrated that the set of maximal solutions can be obtained by taking as input values, the ones that lie along the surface contour[1]. In *Figure 37*, dispersion surfaces projections and contour for the grating with periodically variable sections are shown. Quadrant O-A has a direction along the unit cell's x-direction while quadrant C-O represents propagating waves along the y-direction. Quadrants A-B and B-C are waves travelling in every other direction but x and y. These results are obtained using the indirect method and solving the eigenvalue problem varying in magnitude μ_x and μ_y between $[0 - \pi]$. For contour quadrants O-A and C-O the values of μ_y and μ_x are set to zero respectively, while the other is varied between $[0 - \pi]$.

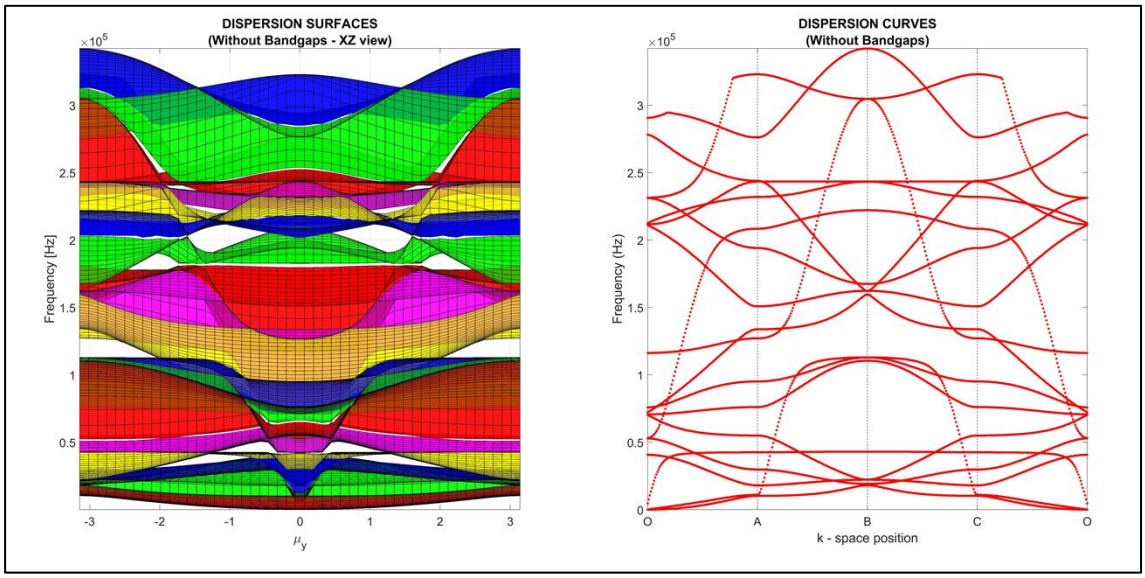

Figure 36 - Dispersion surfaces (XZ view) for the uniform grating (left) and its dispersion curves based on its IBZ surface contour (right). No full bandgaps are present as for each frequency range, there is either a curve or surface plotted.

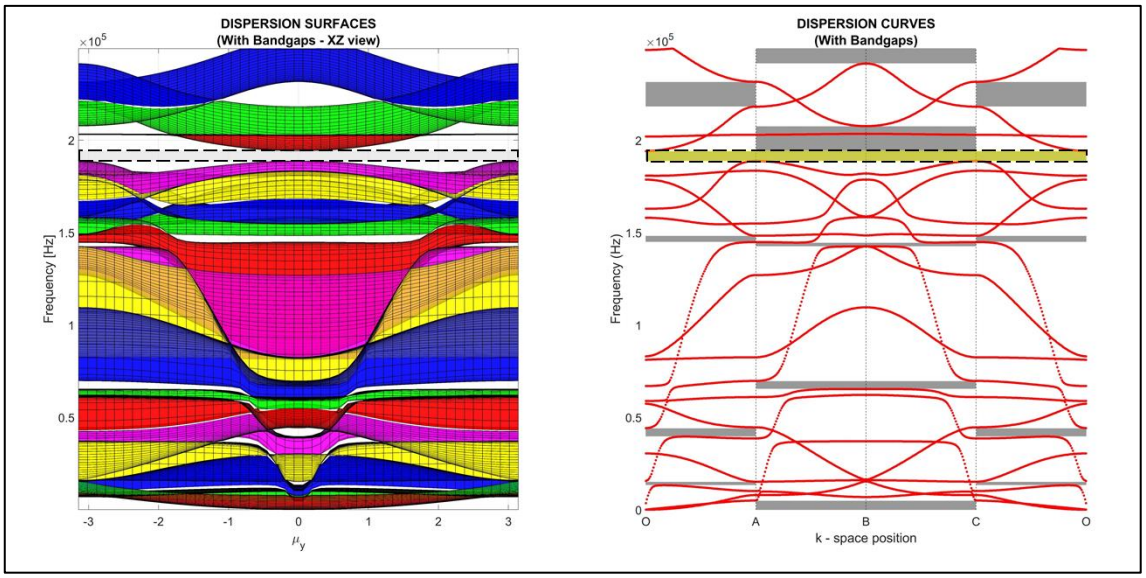

Figure 37 - Dispersion surfaces (XZ view) for the grating with periodically variable sections A_1 and A_2 (left) and its dispersion curves based on its IBZ surface contour. A full bandgap appears before the 2.0e5 Hz highlighted in grey in the surface plot, and yellow for the dispersion plot.

Quadrants A-B and B-C have one of the components of the reduced wave number set equal to π as the other is varied. Keeping in mind that the dispersion surfaces are created with real values of μ and therefore they represent the propagative waves, *Figure 37* shows full bandgaps. If a structure has preferential direction filtering properties for a certain frequency range, the bandgaps are said to be "partial". In the same figure, various partial bandgaps in the x and y direction as well as diagonal can be appreciated. The distinction between the two is that a full bandgap is a frequency range which is in common with all four quadrants, while a partial bandgap denotes absence of propagation across a specific direction. In *Figure 36* we also notice that there is a symmetry along the B vertex. This is because the analysed structure has a centre-symmetric unit cell and so waves impinging along the x-direction will find the same exact periodic structure as if they were travelling along the y-direction. This symmetry is also reflected in the dispersion curves (with respect to the boundary "B").

2.2 IMPACT OF FACE SKINS

A pair of face skins is now added to the structure analysed in section *2.1.6*, which possessed bandgaps in its variable section configuration (within its first 18 eigenvalues) to understand what consequence this has on the bandgaps. The structure's model parameters are shown in *Table 3* and the unit cell before and after attaching the face skins can be appreciated in *Figure 38*. The skins add mass to the unit cell and increases its out of plane thickness ($h + H$).

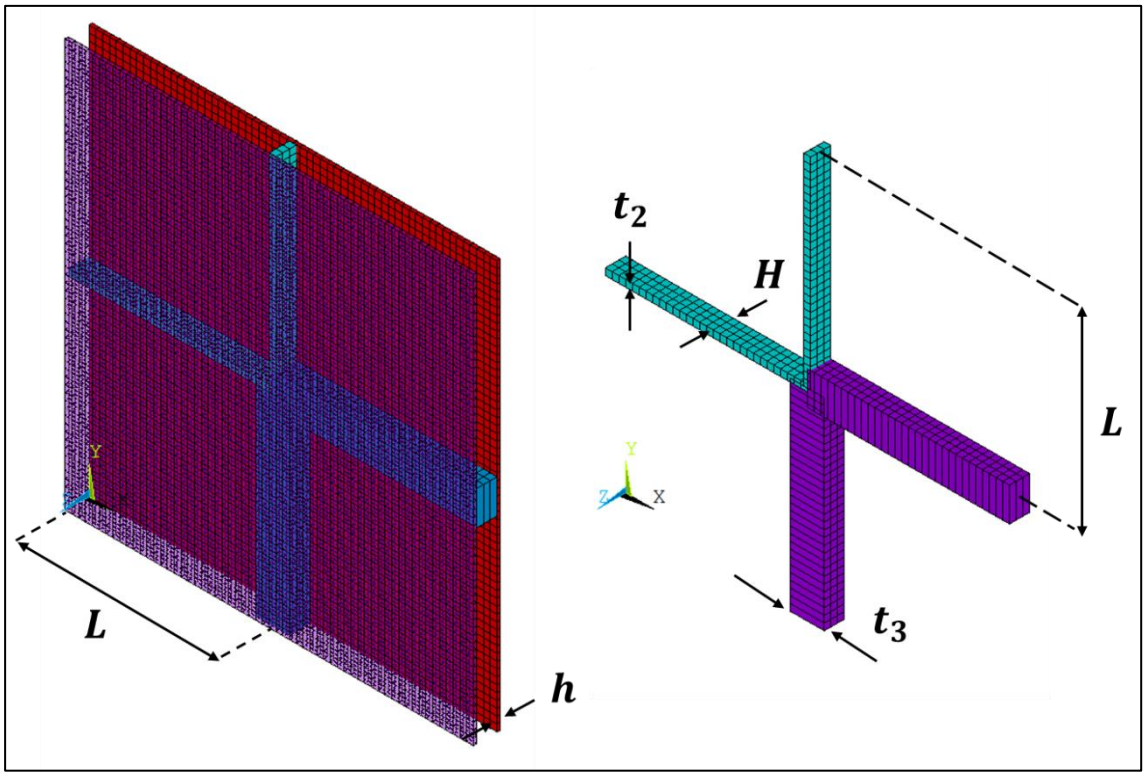

Figure 38 - Cross unit cell with face skins (left) and unit cell without face skins

At the same time, they have a stiffening effect. Both contributions affect the modes of the structure and therefore affect out dispersion surface contours, as visible in *Figure 39*.
On the left, the steepest branch, at low frequencies, is an in-plane pressure wave while on the right, two steep branches are one, an in plane pressure wave, and the other, an out of plane bending mode.

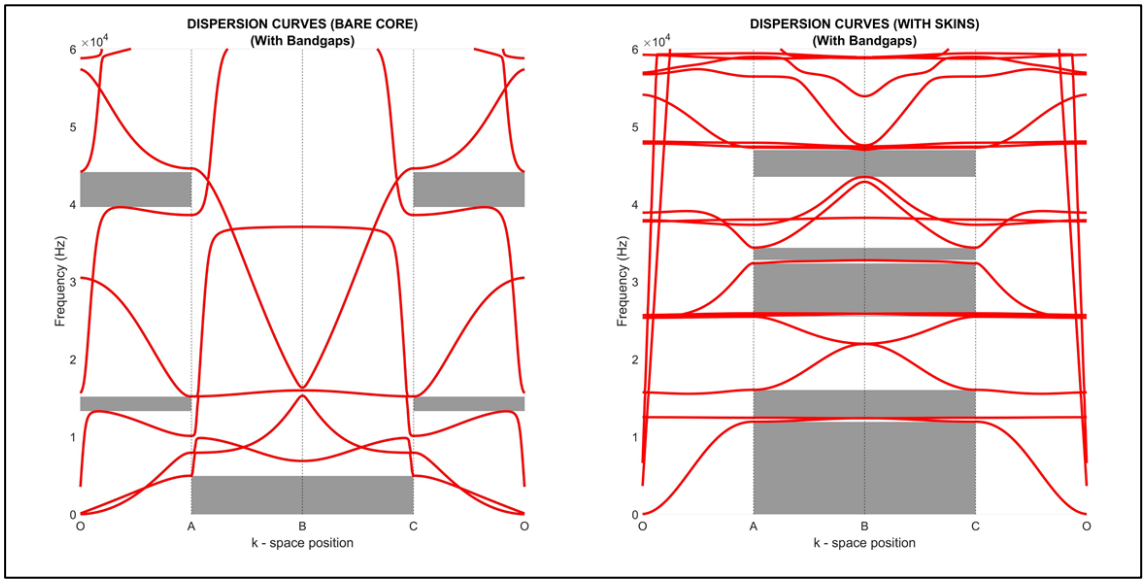

Figure 39 – Dispersion surface contours for the bare core (left) and the sandwich cell (right), this time with the frequency range fixed at 60 kHz.

The mentioned branches should start from zero, but they do not due to numerical issues. As a result of the stiffening, the same mode happens at much higher frequencies, as well as the in-plane pressure mode. Furthermore, the skins seem to destroy the partial bandgaps which are observable in the bare core for both x and y direction. Although every periodic structure will produce Bragg bandgaps at a certain frequency, we can conclude here that the skins modify the modal behaviour of the structure and destroy the full bandgap which the bare core produces within the first 18 surfaces computed.

This will be observable in most of the geometrical core patterns analysed in this work, which is why, most of the analysis will not include the addition of skins, as they are predominant on the dynamic behaviour of the core. A full model of a sandwich panel will be analysed in section **Error! Reference source not found.**, where a numerical campaign is carried out w ith the intent of predicting the out-of-plane plane transmissibility characteristics.

2.3 KIRIGAMI CELLULAR CORES

2.3.1 Constant relative density cores

A first comparison between topologies is carried out keeping constant the core relative density. In this way, the overall out of plane mechanical static compression properties as well as the overall weight of the core per unit area, are kept constant as described by Gibson in his book about cellular solids [69]. This seemed a reasonable way of comparing different topologies isolating the vibration performance of the latter. The relative density of the cellular structure is calculated as being the ratio between the volumes of the actual unit cell constituent material over the volume effectively occupied by it. The methods used so far to identify Bragg bandgaps worked well in case of simple structures like a beam with periodic cross section (1D). In this section, Bragg bandgap evaluation for more complex structures, like the kirigami compatible hexagonal, the re-entrant (also known as butterfly configuration) and the hybrid AuxHex tessellations were carried out applying the WFEM 1D The term hybrid here is used to describe the nature of the cellular core, which instead of possessing the same cell throughout the panel, it possesses different types of cells. To be precise, the Auxhex core is created with a combination of re-entrant and hexagonal unit cells. Before performing parametric analyses though, agreement between the bandgaps found using commercial software to produce FRF's and the ones found using WFEM (dispersion curves) was performed. For this purpose, the cores were modelled using Timoshenko beam elements. In this way, in-plane and out-of-plane equations are uncoupled and the dynamic behaviour in response to the respective solicitations can be analysed

separately. The elements selected in ANSYS APDL are called BEAM4, which although they do not appear in the software element menu, they still are available for users. The element size for all the numerical simulations was set to 0.5mm, in agreement with equation (1.2.5) where the highest frequency analysed is considered, and the material properties, which come from the datasheet of a flax/PP consolidated prepreg, are listed in *Table 4.*

$Young's\ Modulus, E\ [GPa]$	8.1
$Density, \rho\ [kg\ m^{-3}]$	1040
$Poisson's\ Ratio, \upsilon$	0.2

Table 4 - Numerical simulation parametric analysis material properties

The investigation is carried out only in-plane, by blocking out-of-plane displacements and rotations, therefore, only 3 degrees of freedom are considered. In-plane compression and in-plane bending were the only responses considered throughout this chapter. The harmonic response simulations were carried out without implementing any structural nor material damping. The intention here is to use those plots to confirm the frequency range of the bandgaps.

Topology	$\boldsymbol{l}$ **[mm]**	$\boldsymbol{\vartheta}$ **[deg]**	**Relative density**	**1st eigenfreq. [Hz]** $(\boldsymbol{\omega_n})$	**Max Freq. [Hz]** $(\boldsymbol{2\omega_n})$
Hexagonal	5.499	30.00	0.042	8373	16746
Re-entrant	7.331	30.00	0.042	4710	9420
Auxhex	6.415	30.00	0.042	6152	12304

Table 5 - Unit cell parameters for the hexagonal, re-entrant and AuxHex configurations

In *Table 5* instead, the geometrical values of the side length l and internal angle ϑ (visible in *Figure 40(b)*), which were computed to guarantee a constant relative density for each configuration are shown, as well as the 1st eigenfrequency of the smallest unit cell's constituent beam, which was used to normalize the plots.

2.3.2 Hexagonal topology

The unit cell as well as a representation of the hexagonal topology are shown in *Figure 40*. The FRF plots and the dispersion curves for the hexagonal topology, produced with the hexagonal unit cell, are shown instead in *Figure 41* and *Figure 42* respectively. The graphs are normalized according to the 1st eigenfrequency of the beam. The unit cell was modelled using ANSYS BEAM4 elements and as mentioned in section *2.3.1* the out of plane displacements and rotations were blocked. The FRF analysis was performed on a chain of 10 unit cells, for reasons explained in section *2.1.2.* A unit force was applied at one extremity

of the chain, while the output (displacement) was read at the other end of the structure. There is very good correspondence between dispersion curves (infinite structure) and the computed FRF plots (finite structure). The graphs both show the presence of bandgaps around ω/ω_n = 0.3, 0.45, 0.85, 1.2 and 1.7. Furthermore, in *Figure 42*, two peaks within the bandgaps, one for the in-plane bending waves ($\omega/\omega_n = 0.7$), and one for compression waves ($\omega/\omega_n = 0.95$), can be noticed. This probably is associated to the same numerical error discussed in section *2.1.2* .

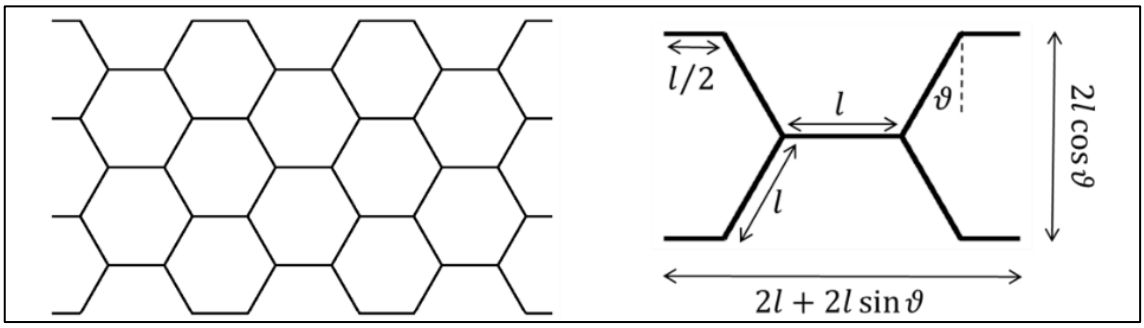

Figure 40 – (a) Hexagonal pattern, (b) Hexagonal unit cell for WFEM 1D analysis.

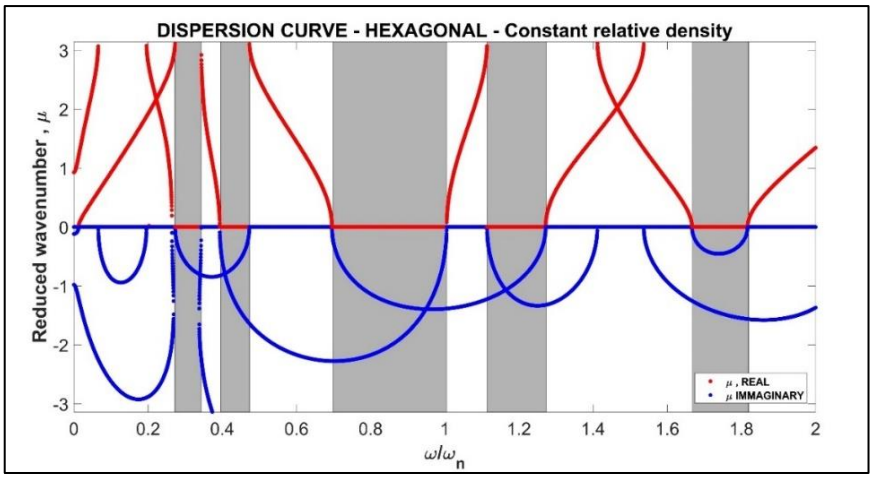

Figure 41 - Dispersion curves for the hexagonal pattern allowing only in-plane displacements and rotations.

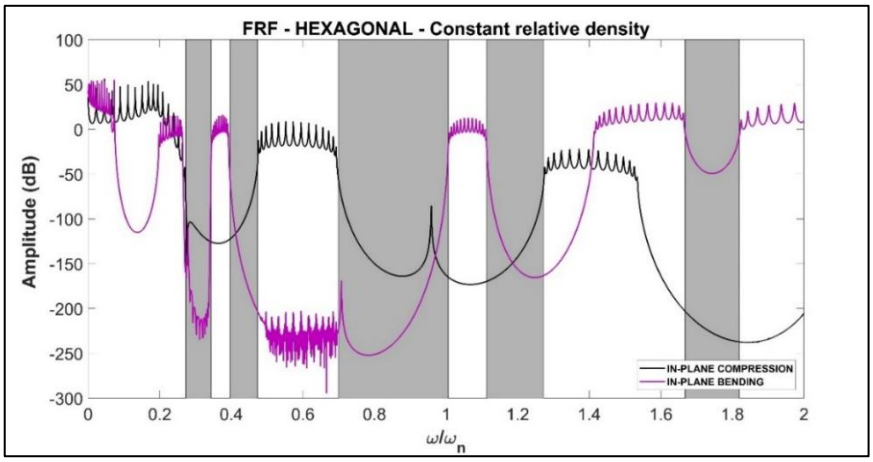

Figure 42 - In plane FRF for pressure wave (black) and in-plane bending(magenta) for the hexagonal pattern.

Before continuing with other topologies, a parametric analysis was carried out to understand the effect of selected geometrical variables on the bandgaps. Taking the hexagonal configuration as benchmark, parameters like the core wall thickness t, side length l, and internal angle ϑ were varied keeping everything else constant.

It is interesting to underline that by changing the internal angle of the hexagonal unit cell while keeping constant the overall dimensions L_x and L_y, the geometry firstly transforms into a square grid (for $\vartheta = 0°$) and finally into the re-entrant (for $\vartheta = -30°$). The results of such parametric analysis are summarized in *Figure 43, Figure 44* and *Figure* 45.

2.3.2.1 Variable wall thickness, side length and angle

Clear trends are visible when changing such variable. As we increase the thickness of the unit cell wall from 0.2 to 1.0 mm the bandgaps shift to higher frequencies. This is coherent with what was expected, since $\omega_n = \sqrt{K/M}$ and therefore a stiffer structure tends to possess natural modes at higher frequencies.

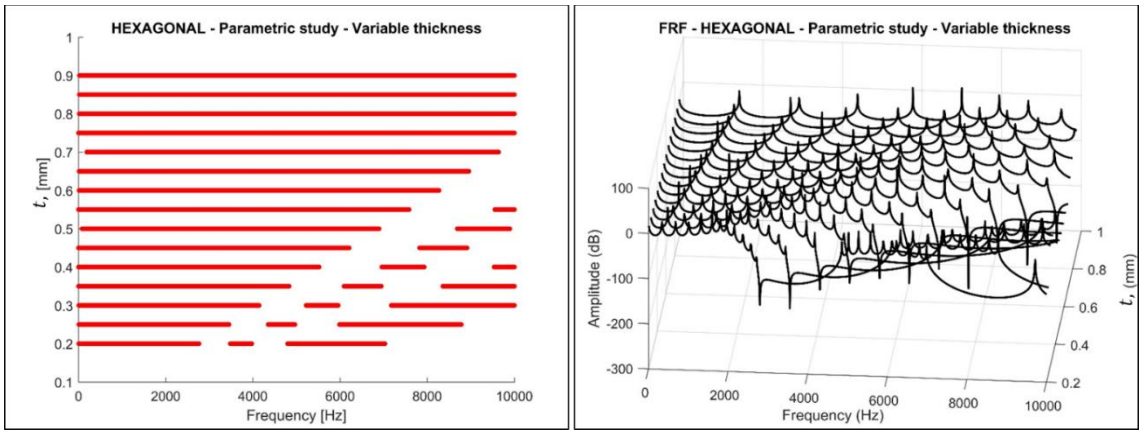

Figure 43- Hexagonal parametric analysis for variable cell wall thickness, t. Dispersion curves (left) and FRF's (right).

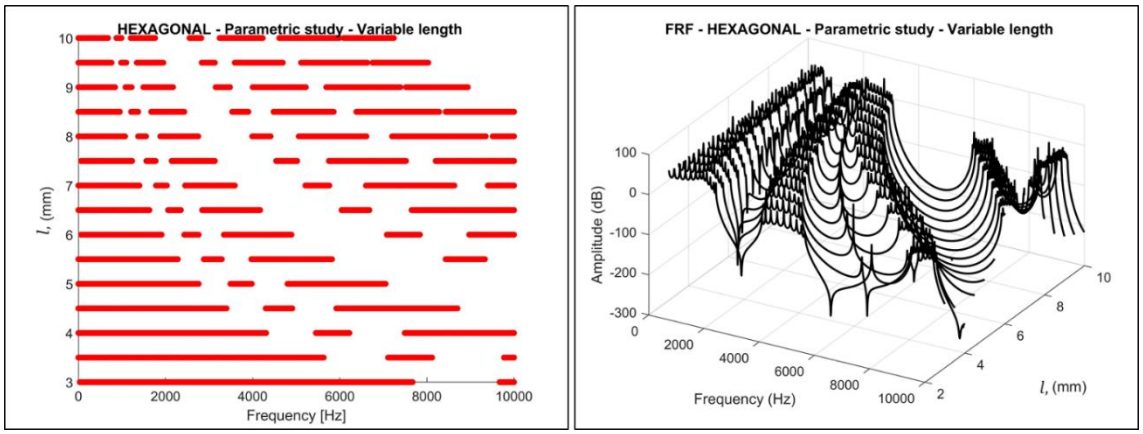

Figure 44- Hexagonal parametric analysis for variable side length, l: Dispersion curves (left) and FRF's (right).

As we increase l instead, since the cross section of the beam remains constant, the outcome

is a larger unit cell (for the way the parametric scripts were produced, l acts as a scaling factor) which translates in reduced stiffness. As consequence, the bandgaps shift to lower frequencies. Finally, the internal angle ϑ was varied and as a result the main bandgap within the frequency range widened. For negative ϑ values, the hexagonal configuration becomes a re-entrant cell. This causes a change in the overall unit cell occupancy due the way the parametric program was written. To compare cores with same relative densities, the code used for this investigation could not be used, and therefore a script dedicated to the re-entrant topology, which guaranteed the relative density as well as occupancy was created.

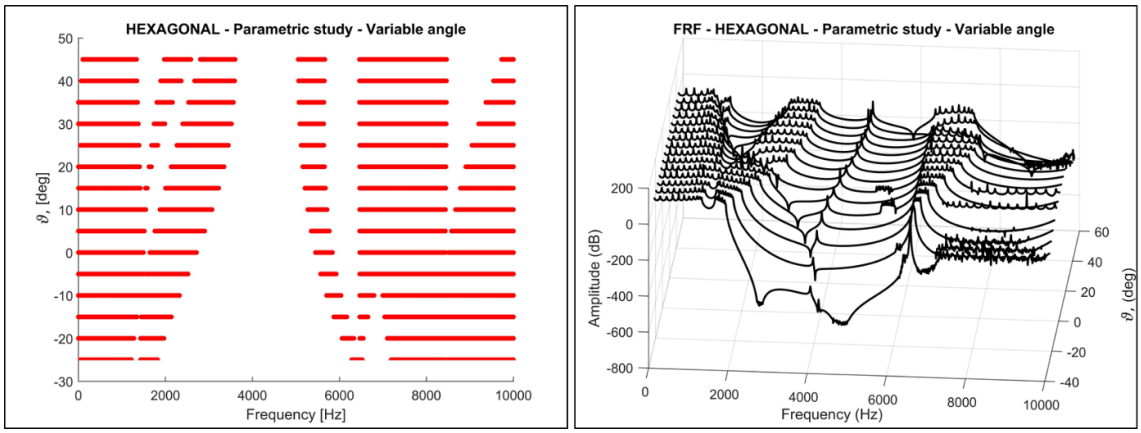

Figure 45- Hexagonal parametric analysis for variable internal angle,ϑ. Dispersion curves (left) and FRF's (right).

2.3.3 Re-entrant topology

The re-entrant configuration could be defined as the Hexagonal geometrical antagonist. As discussed in the previous section, this topology is obtainable by decreasing ϑ to negative values up to -30° but a specific script was used to guarantee constant relative density. The unit cell dimensions as well as the FRF and dispersion curves are shown from *Figure 46* to *Figure* 48*)*. The graphs both show the presence of bandgaps around ω/ω_n = 0.22, 0.35, 0.45, 0.9, 1.4 and above 1.85. Compared to the hexagonal cell core, the re-entrant possesses a wider bandgap ($\Delta\,\omega/\omega_n$ ~0.65) around ω/ω_n = 0.9.

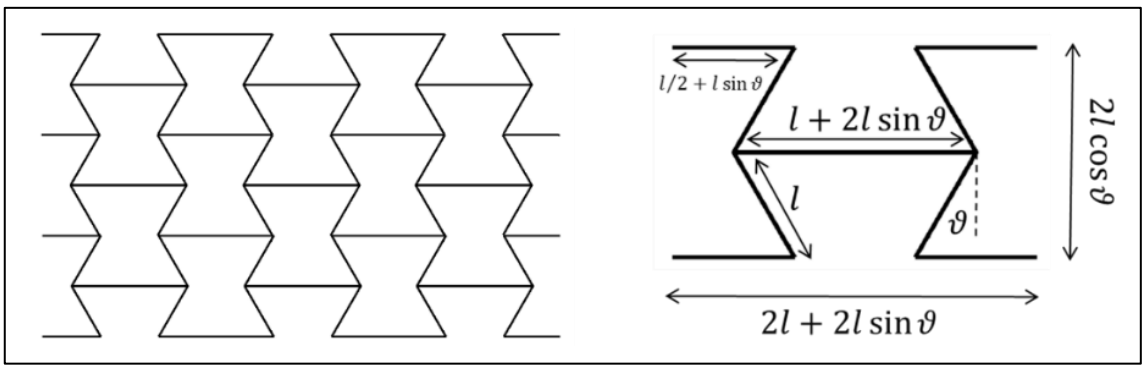

Figure 46 – Re-entrant pattern (left), Re-entrant unit cell for WFEM 1D analysis.

Within the main bandgap, the FRF computed for the axial pressure wave denotes two peaks, at $\omega/\omega_n = 0.4$ and 1.2 , which also appear in the dispersion curves. Contrary to what has been discussed in 2.1.2, where the resonance was not appearing in the dispersion curves, it is here confirmed, and its origin is probably intrinsic to the topology.

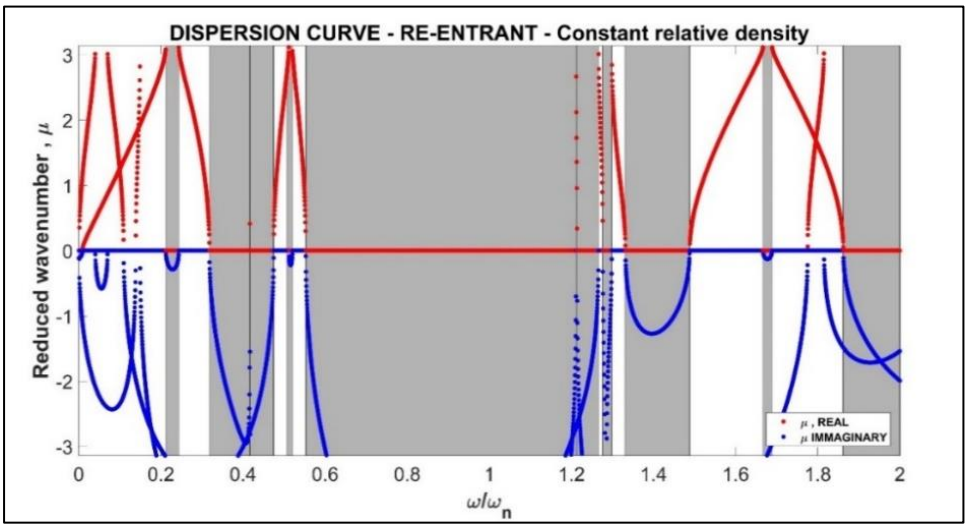

Figure 47 - Dispersion curves for the re-entrant pattern allowing only in-plane displacements and rotations.

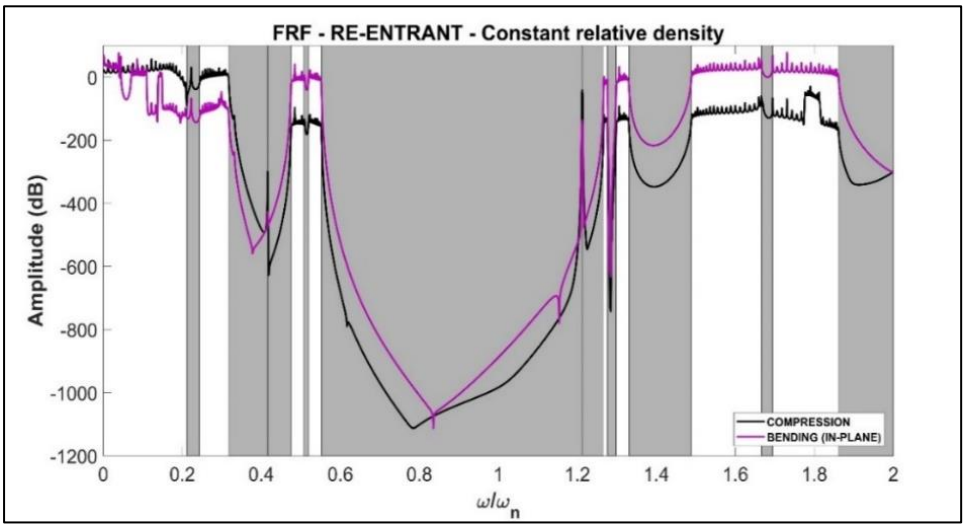

Figure 48 - In plane FRF for pressure wave (black) and in-plane bending(magenta) for the re-entrant pattern.

2.3.4 AuxHex topology

In this section, the previous two unit cells are combined to obtain a new configuration. This topology is called AuxHex [15] and its pattern is shown in *Figure 49(left)* as well as its unit cell *(right)*. This configuration has the peculiarity of possessing an in-plane zero Poisson's ratio. For this reason, it is a valuable candidate to be considered when designing cylindrical sandwich panels. Just like the previous topologies, the analysis is carried out on the unit cell which was modelled with BEAM4 elements in ANSYS APDL environment.

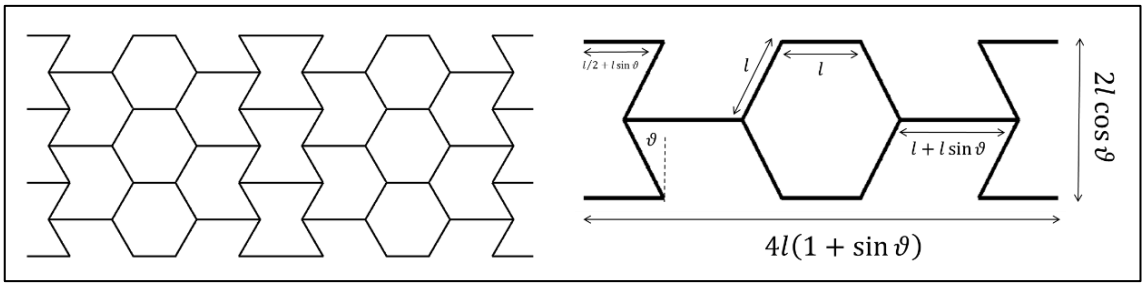

Figure 49 - AuxHex pattern (left), AuxHex unit cell for WFEM 1D analysis.

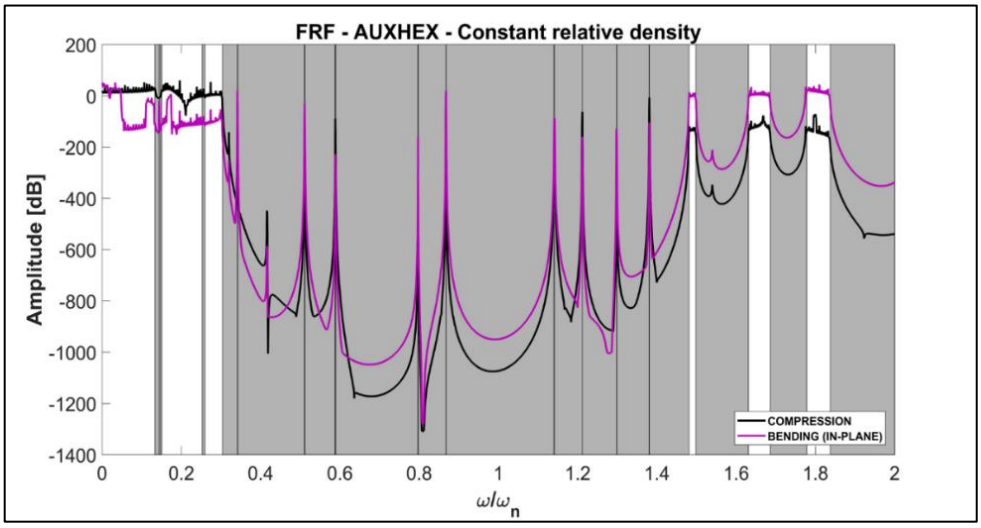

Figure 50 - In plane FRF for pressure wave (black) and in-plane bending(magenta) for the AuxHex pattern

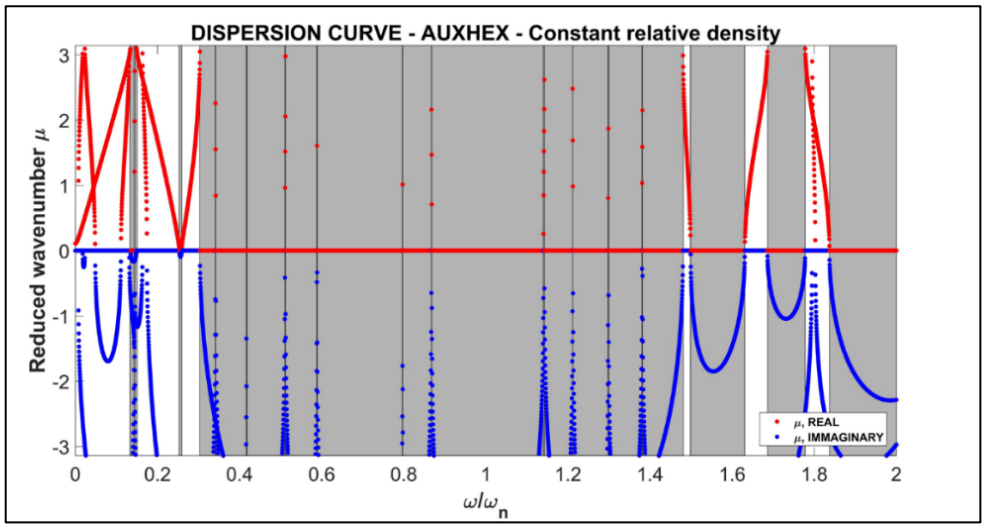

Figure 51 - Dispersion curves for the AuxHex pattern allowing only in-plane displacements and rotations.

Again, only the in-plane displacements and rotations were allowed. Various adjacent bandgaps appear in the range from ω/ω_n = 0.3 up to 1.5 as shown in *Figure 50* and *Figure 51*. Sharp resonant peaks interrupt the continuity of its widest bandgap (within this frequency range) which is unfortunate, although high bandgap density within a frequency range is still a positive characteristic. The bandgap density owned by this configuration is higher compared to both, classic hexagonal and re-entrant grids.

2.3.5 Performance comparison

Figure 52 is a summary plot of the configurations analysed in section 2.3. The relative density is kept constant and since the unit cell encumbrance of the AuxHex is larger than the hexagonal and the re-entrant, the beam thickness parameter was varied to guarantee the feature. In blue, green, and red, the $Re(\mu)$, which represents the propagative waves, over the audible frequency range that goes from 0 Hz to 20 kHz, which is of great interest for the aerospace and automotive industry, is shown. The horizontal coloured lines are the frequencies at which $Re(\mu) \neq 0$ and therefore waves can propagate in that direction. The absence of plot denotes therefore the presence of a bandgap. It is again visible how the re-entrant configuration produces the bandgap with the largest width.

The FRF peaks at $\omega/\omega_n = 0.4$ and 1.2 for the re-entrant configuration discussed earlier appear also in the AuxHex FRF. The results obtained with this investigation were of inspiration for further work as a sort of inherited spectral signature feature became visible. The initial parametric investigation instead, gave information about the bandgap's evolution and possible insight about how the variables discussed in section *2.3.2,* could be used to shift isolation capabilities to desired frequency ranges.

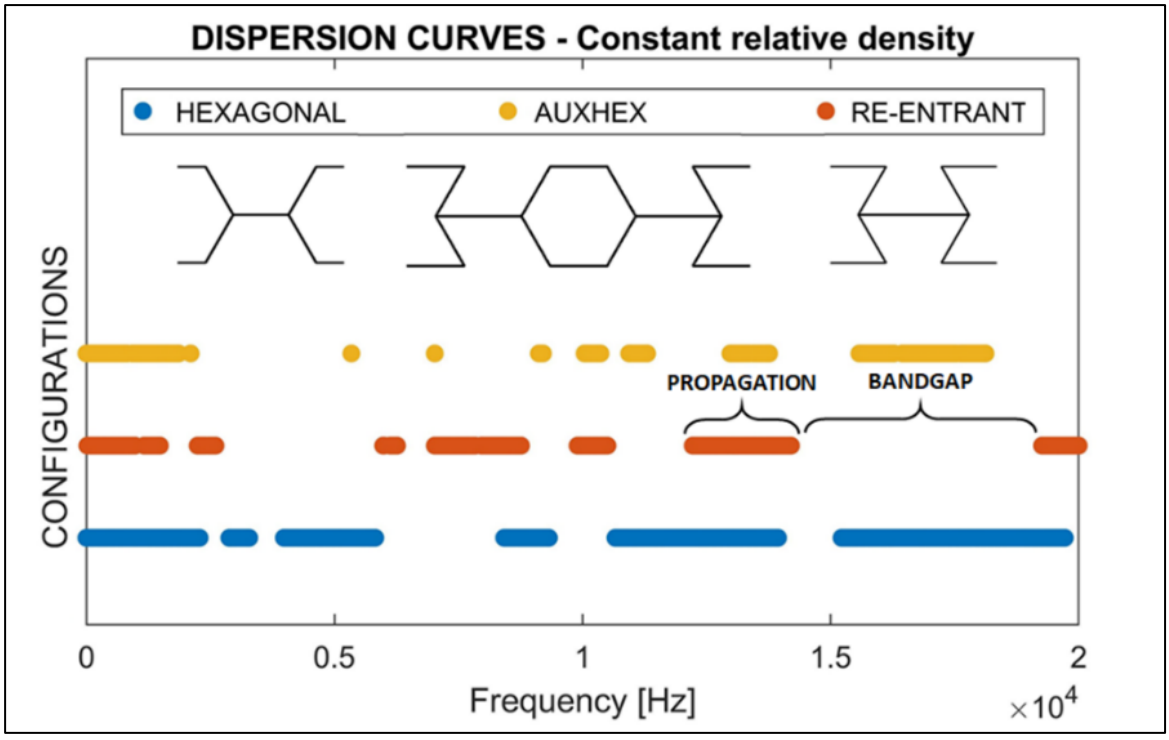

Figure 52 - Dispersion curves summary for constant relative density core comparison.

2.4 INHERITANCE

This section is focused on the results obtained for the AuxHex configuration. The recurrence of the re-entrant peaks in the AuxHex topology required further analysis. This was attempted by normalising the parametric graphs obtained for all three configurations analysed in 2.3. In *Figure 53* the assembly of the hybrid core is shown. By repeating in space (alternating) the unit cells of the homogeneous cores, the AuxHex configuration is obtained. In *Figure 54*, a representation of the dispersion curves and relative bandgaps produced by each homogeneous topology (left) and the hybrid AuxHex *(right)*, are proposed, while varying the aspect ratio and therefore the unit cell scaling factor.

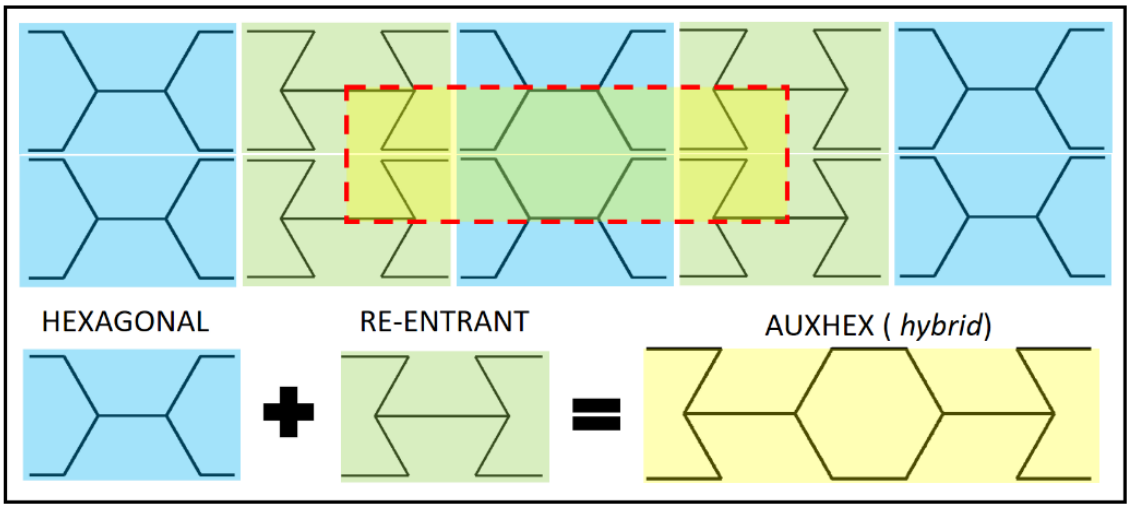

Figure 53 - AuxHex unit cell assembly from the hexagonal and the re-entrant WFEM 1D unit cells

Each horizontal red line refers to the frequency values at which $Re(\mu) \neq 0$. The normalisation adopted, which is done by dividing the computed frequencies by the 1st natural frequency of the smallest beam used to model the unit cell, underlines how the bandgap frequency range is dependent from the unit cell scaling factor. In *Figure 54 (left)* the bandgap frequency ranges are highlighted with vertical rectangles in blue, for the hexagonal grid, and in green, for the re-entrant grid. *Figure 54* (right) instead, refers to the hybrid core AuxHex; the blue and green bandgap vertical rectangles of the "parent" cells are sub-plotted to the propagative component possessed by the AuxHex topology. Comparing the results displayed on the left with the ones obtained for the AuxHex, the bandgap capability of the "parent" cells (hexagonal and re-entrant), to filter waves of certain frequency ranges, seems to be inherited by the hybrid topology. This bandgap inheritance could potentially lead to bandgap-designed hybrid panels, provided that the spectral signature of the "parent" unit cells is known.

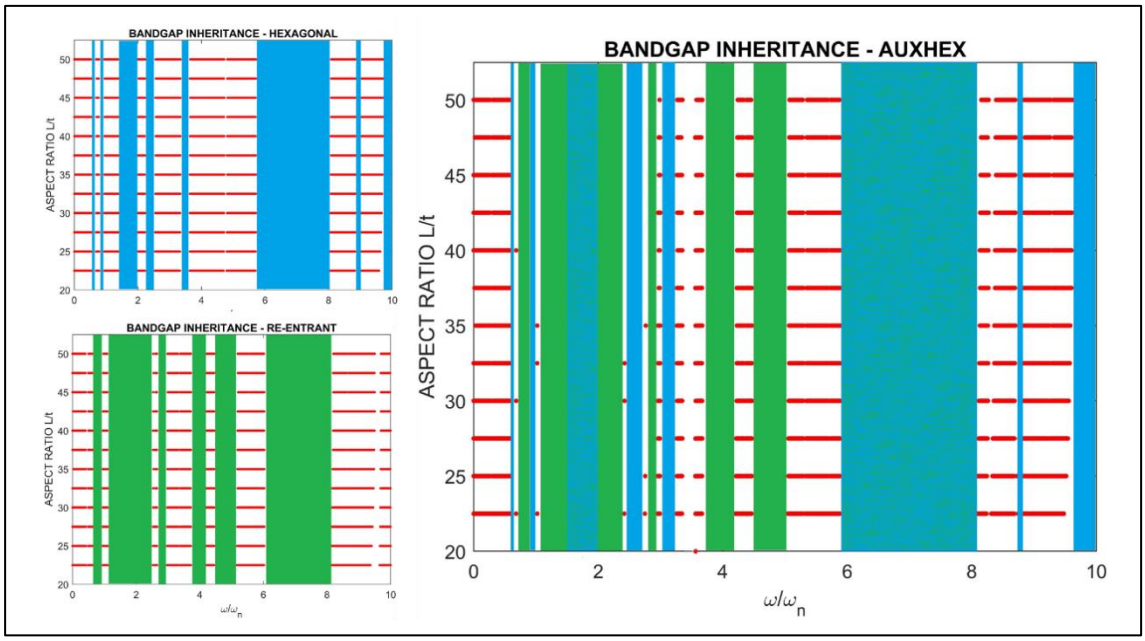

Figure 54 - Inheritance normalised parametric dispersion curves for the hexagonal (top left), the re-entrant (bottom left) and the AuxHex (right).

Furthermore, other simulations using ANSYS software to perform traditional FEM (Harmonic analysis) was carried out to produce FRF's on different truss structures. The latter are shown in *Figure 55* where *(a)* is a chain containing 10 hexagonal unit cells, *(b)* is a composite structure made of 10 hexagonal cells followed by 10 re-entrant cells and finally *(c)* shows a structure made with 10 AuxHex cells. All structures were modelled with BEAM4 elements and keep the same relative density. No effect on the bandgap position and width was noticeable, as shown in *Figure 56.* Consequently to this verification, the output at the end of the whole truss (output 3, green arrow) was considered reliable and compared with the reading at the end of the AuxHex truss (output 4, black arrow in *Figure 55*).

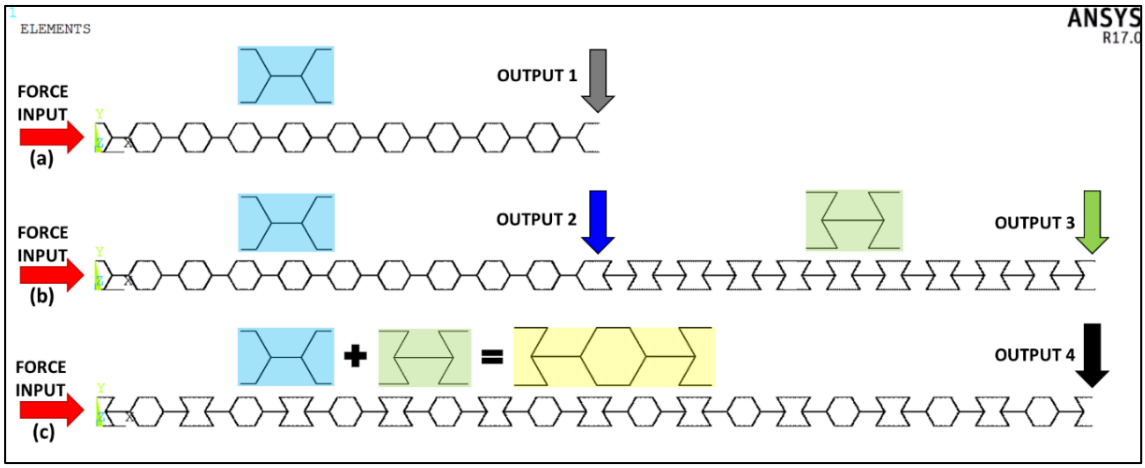

Figure 55 – (a) Truss structure composed of 10 hexagonal cells; (b) Truss structure made of 10 hexagonal cells followed by 10 re-entrant cells; (c) Truss structure made with 10 AuxHex cells. The red arrow is the input force and the grey, blue, green and black are the output readings, colour-matched with the graphs in Figure 56 and Figure 57.

The results are plotted in *Figure 57* where the FRF's for the AuxHex and the composite truss seem to be quite close to each other and the bandgap similar in terms of width, other than some internal local resonances which unfortunately destroy the desirable wide bandgap. Furthermore, on the same graph, circled in blue, perfect matching between some resonant modes is visible.

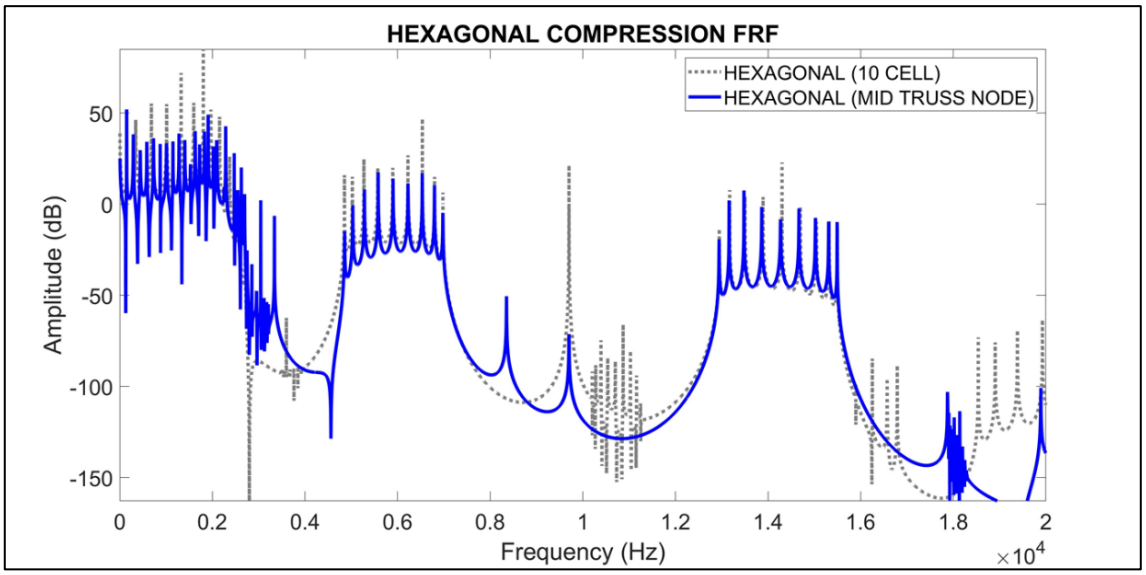

Figure 56 - FRF comparison between a truss structure made of 10 hexagonal unit cells and the output 1 from figure 53

Applying a compressive solicitation at 13360 Hz, frequency at which waves propagate across the hexagonal core but not trough the AuxHex one, waves are unable to propagate until the end of the truss, as shown in *Figure 58*.

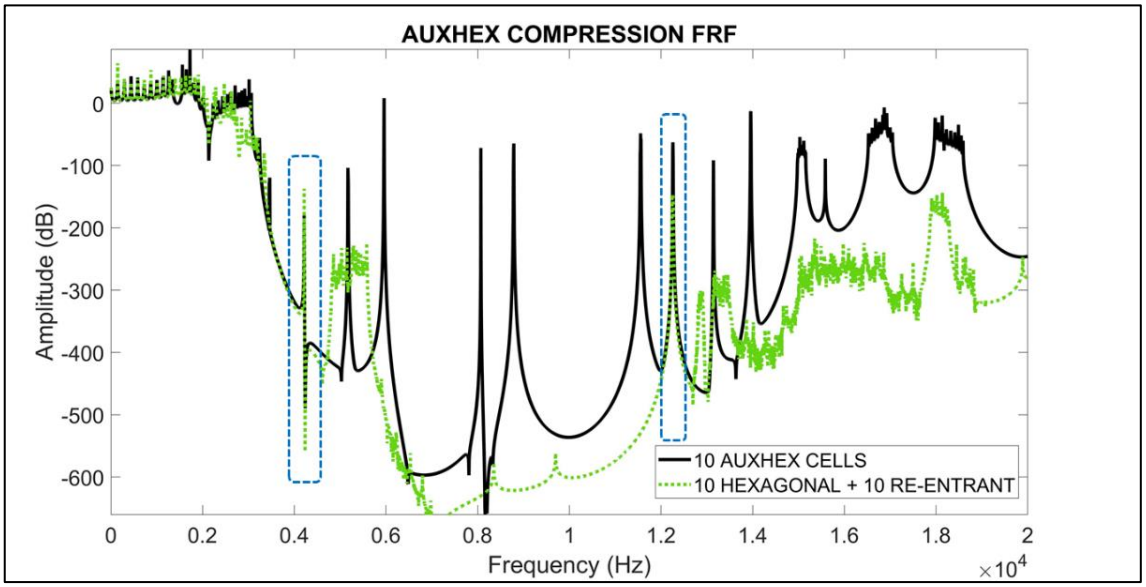

Figure 57 - FRF comparison between the composite truss structure (green) and the AuxHex output 2 (black). Localised modes are highlighted with dashed blue line

2.4.1 Inheritance conclusions

From the numerical simulations carried out using both, fast design WFEM tools (dispersion diagrams) and classic FEM (FRF's) the inheritance topic for this specific structure and solicitation has been confirmed.

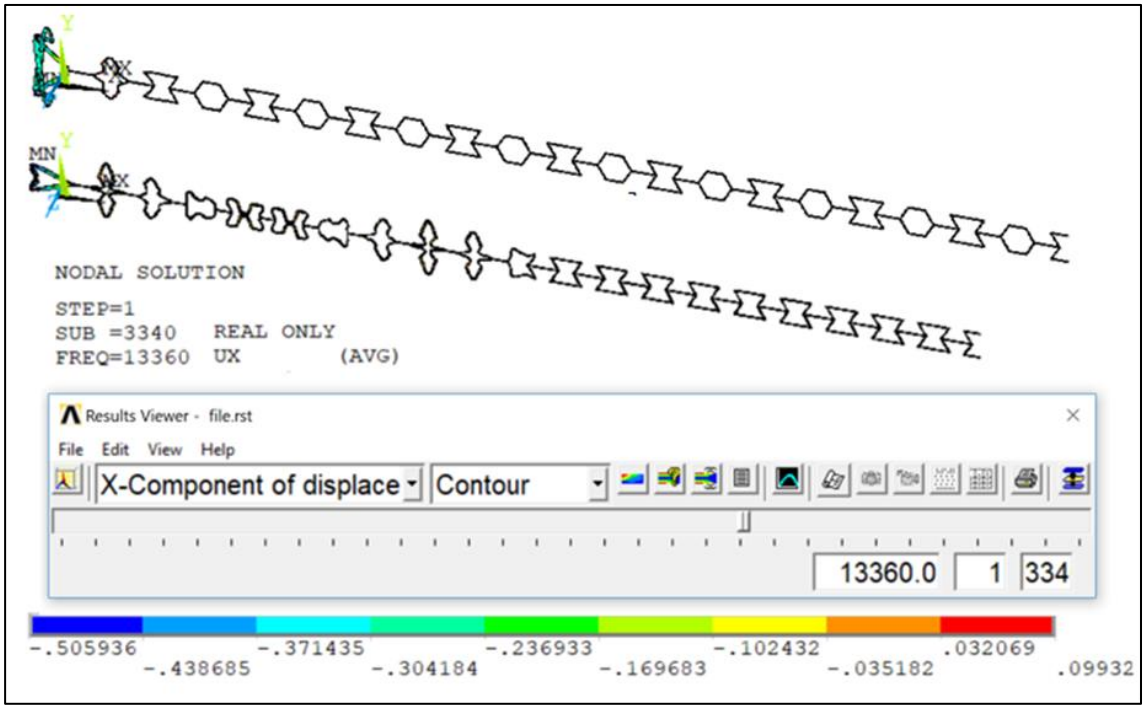

Figure 58 - AuxHex and composite truss deformed shapes subjected to harmonic force at 13360 Hz. Both structures clearly show filtering effects.

This means that each unit cell from a homogeneous periodic core is frequency-selective in terms of wave propagation and hybrid cores such as the AuxHex, inherit the filtering property of the parent-unit cells to a certain extent, since no matter in which way the truss is assembled, the resultant FRF maintains the bandgaps width and central frequency. Local internal resonant peaks although do appear which is not ideal, but if the aim is to increase the bandgap density in certain frequency ranges, this could maybe become a new vibration design strategy which also allows to maintain the static out of plane properties.

2.5 KIRIGAMI-COMPATIBLE ISOVOLUMETRIC POLYGONAL CORES

2.5.1 Motivation

After examining core topologies which can be classified as "classical tessellations" or at least considered more common, the need of exploring new geometries seemed to be the next

natural step. This had to be conceived respecting the stringent rules of Kirigami, technique which is anyway not usual when manufacturing honeycombs. The attention shifted to regular polygons, which were after a preliminary analysis, good kirigami candidates. Especially after the investigation of hybrid cores, the self-tessellation condition was not essential and neglecting it led to original findings.

2.5.2 Polygons and Kirigami

For this kind of investigation, a parametric script to create the unit cell based on regular polygons kirigami compatible was written. Parameters like thickness t, core height h, material properties, type of analysis and overall unit-cell occupancy (L_x, L_y and L_z) could be edited from Matlab. The type of unit cell chosen to create such tool is not optimal in terms of minimization of boundary nodes. This choice was made to avoid creating a separate script for each polygon considered, which would have taken considerable amount of time. All polygons have therefore a unit cell that can be described as two half-moons with their backs connected by a rib. In this way, the unit cells maintain a symmetry, which is an important parameter when searching for bandgaps, as mentioned in chapter 2. The kirigami compatible core structures must keep two parallel sides, parallel to the folding line that closes the semi cell onto itself. For this reason, not all polygons could be analysed, and the number of sides considered ranged from 4 to 20 with a sub step of 2. For completeness, a configuration with circular cells was analysed as well. Those cellular patterns can all be geometrically classified according to what was introduced in section *1.1.2* and covered in depth by D. Schattschneider [25] and R. Veysseyre [26].

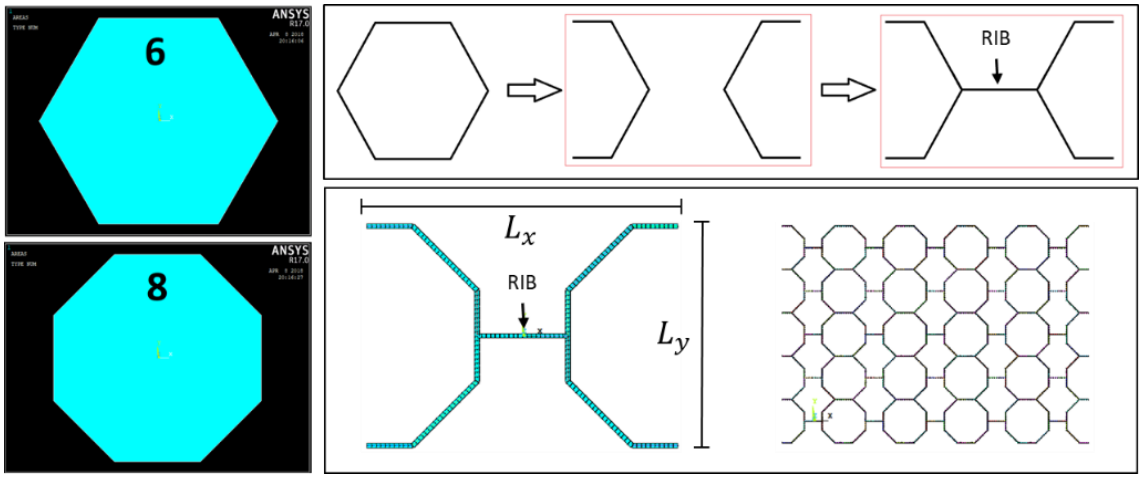

Figure 59 - Polygonal unit cell automated assembly

To produce unit cells with same relative density and exact volume occupancy, dimensions L_x, L_y and L_z were kept constant and the thickness of the cellular core unit cell varied to

maintain the same mass and therefore same relative core density[70]. Without varying the thickness, the relative density of our unit cell would increase and behave asymptotically (*Figure 60)* toward the configuration where two semicircles would be connected by the rib.

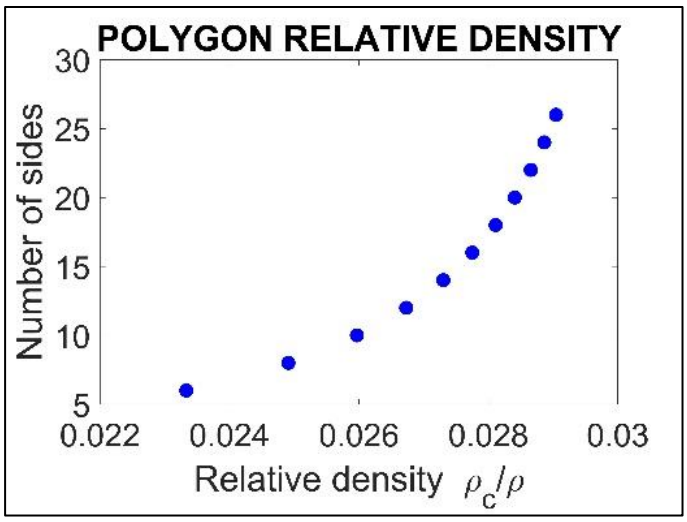

Figure 60 - Polygonal cell relative density if the beam section was kept constant

The relative density is defined as ρ_c/ρ where ρ_c is the density of the actual cell calculated with the unit cell mass and its volume, while ρ is the density calculated with the unit cell mass and the volume encumbrance of the unit cell. This was chosen in order to provide the same static out of plane properties[69] as the investigation for bandgaps was performed.

2.5.3 Polygon numerical model

To create the variable polygon unit cells, the ANSYS command for regular polygons which only needs number of sides and the radius in which inscribe the shape was used. From there, the polygon volume was carved to retrieve symmetrical semi-shapes and depending on the final structure or type of analysis to be conducted, the unit cell was modelled using BEAM4 (sufficient if the aim is to analyse the core behaviour) or SHELL 181 elements (if the interest is to analyse a sandwich panel structure). Finally, a rib was added to connect the two half-moons, as shown in *Figure 59*. This analysis was carried out for 1D periodicity (considering only left and right boundaries) and only considering the core, with the purpose of searching the skinless configuration which would have produced the widest bandgaps within the frequency range up to 30kHz, which was chosen arbitrarily. Since the models were created using Timoshenko beam elements (BEAM4), the in-plane and out-of-plane behaviour of the core were analysed.

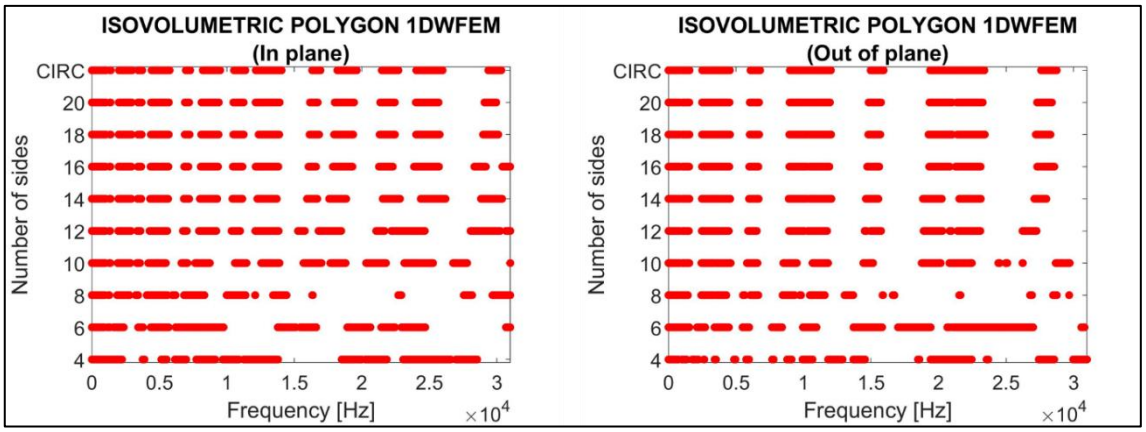

Figure 61 - Isovolumetric in plane and out of plane parametric dispersion curves for WFEM 1D

2.5.4 Results

The configuration which showed the widest in-plane and out-of-plane bandgap was the octagon, with 6324 Hz and 5146 Hz respectively. Also, the bandgaps seemed to follow a pattern as the number of sides was increased. Just like the relative density, the dispersion curves revealed a sort of bandgap mid-frequency convergence towards the circle configuration, as shown in *Table 6*. This became clearer starting from the configuration with 10 sides onwards where the middle frequency shifted towards the circular cell, while the bandgap width increased and finally stabilised.

2.6 CONCLUSIONS

This chapter focussed on the in-plane and out of plane dynamic behaviour of kirigami compatible classic cellular structure geometries which recur in sandwich panel cores. The numerical simulations were carried out using 1DWFEM as a fast prediction tool for wave propagation and further analysis was conducted to verify those findings using ANSYS APDL software to produce FRF's plots, neglecting structural and material damping. A parametric analysis, using the hexagonal grid was performed to understand the effect of certain parameters and evaluate their effect on existing bandgaps. Such variables were the wall in-plane thickness (t), the scaling factor which was based on the side length of the regular hexagon (l), and finally the internal angle (ϑ). All those parameters are well visible in *Figure 40*. The effect of (t) is to shift the bandgaps to higher frequency as the increase in thickness acts as a stiffening parameter while the increase in size of the unit cell, maintaining the constituent beam cross section causes the opposite effect and so the bandgaps shift to lower frequencies. The variation of the internal angle instead creates new geometries which cause a widening effect on the main visible bandgap, as shown in *Figure 45*. Other than the

hexagonal and re-entrant topologies, a non-typical core, defined as hybrid and called AuxHex was analysed and compared with the performances of the "parent" self -tessellating unit cells. Comparing the results displayed in *Figure 54* on the left with the ones obtained for the AuxHex, the bandgap capability of the "parent" cells (hexagonal and re-entrant), to filter waves of certain frequency ranges, is inherited by the hybrid topology. This concept for these unit cells is further investigated and confirmed using FEM tools. Furthermore, this gave insight to investigate a new class of kirigami-compatible cores which is based on regular polygons and which, to the authors knowledge, is a novelty in the field. The configuration which showed the widest in-plane and out-of-plane bandgap within the 30 kHz range is the octagon. As we increase the number of sides, the dispersion curves revealed a sort of bandgap mid-frequency convergence towards the circle configuration, as shown in *Table 6*, which became more evident starting from the configuration with 10 sides onwards.

SIDES	**IN PLANE**			**OUT OF PLANE**		
	$\Delta f\ [Hz]$	$\Delta f/f_{mid}$	$f_{mid}\ [Hz]$	$\Delta f\ [Hz]$	$\Delta f/f_{mid}$	$f_{mid}\ [Hz]$
4	4705.0	0.291	16150.5	3914.0	0.153	25645.0
6	5970.0	0.216	27684.0	3553.0	0.123	28791.5
8	6324.0	0.324	19532.0	5146.0	0.213	24199.0
10	3189.0	0.108	29393.5	3592.0	0.212	16953.0
12	3385.0	0.128	26351.5	3119.0	0.126	24658.5
14	2619.0	0.095	27509.5	3957.0	0.158	25115.5
16	2611.0	0.097	27019.5	4174.0	0.166	25213.0
18	3206.0	0.117	27370.0	3772.0	0.149	25318.0
20	3394.0	0.124	27379.0	4016.0	0.159	25287.0
circle	3383.0	0.122	27675.5	4195.0	0.165	25496.5

Table 6- Bandgap width and middle frequency for the polygonal investigation

CHAPTER 3

INTERLOCKED SANDWICH PANEL CORES

3.1 INTERLOCK TECHNOLOGY

The main geometrical limitation for the kirigami technique when producing cores which must also possess improved vibration filtering properties is that the sheet of material needs to be folded over trapezoidal bars. Only in this way, the back and forwards folding process of the thermoformed sheet onto itself can be obtained and centrosymmetric or non, cellular structures produced. Triangular cells or even a square grating for example (*Figure 62)*, cannot be created. As shown in *Figure 9* and *Figure 10*, bars necessarily need to have cross-sections containing two parallel sides to produce centrosymmetric geometries.

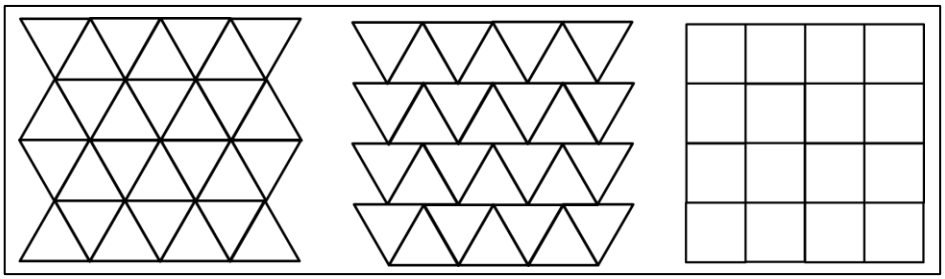

Figure 62 - Self-tessellating patterns not allowed with kirigami

The lack of geometrical tessellations producible with Kirigami and the will to investigate new hybrid cores while introducing also a second degree of periodicity in the structures conveyed into what has been called the Kirigami Interlock technique. The interlocking pattern technique allows to obtain a completely new family of topologies, by press-locking onto each other different cellular structures. This result was obtained thanks to a new slit pattern created during the Kirigami manufacturing process (pre-process), in addition to the one which would convey the cellular cross section shape. Traditional Hexagonal cell honeycomb produced with Kirigami would have the cutting pattern shown in *Figure 63* where are also immediately evident, the additional vertical cuts in the direction of the mold bar length. The main difference between the assembled 3D structures lies in the vertical cuts which are performed onto what becomes a wall with single thickness. Such cuts face all the same side, and this allows the separately manufactured honeycombs to compenetrate

each other through all their original out of plane height, since each one of them, has cuts that are half their height. This operation creates in the end, a new honeycomb with higher relative density and different topology compared to the "parent" pair.

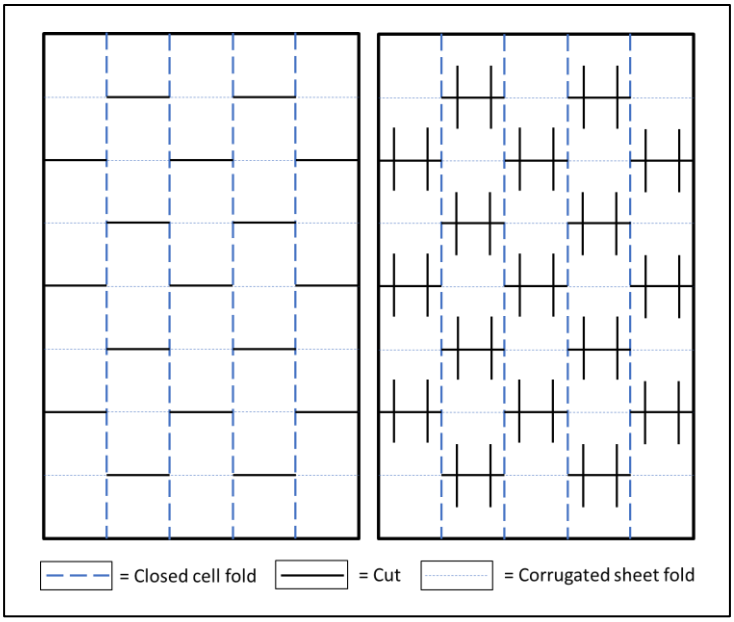

Figure 63 - Kirigami cutting pattern (left), Interlock cutting pattern (right)

Figure 64 shows a geometry which has regular hexagons and regular rhombus obtained when two over extended hexagonal honeycomb cores are interlocked. This pattern was previously non-obtainable since the structure should have folded over a corner which would end with a point connection between adjacent cells.

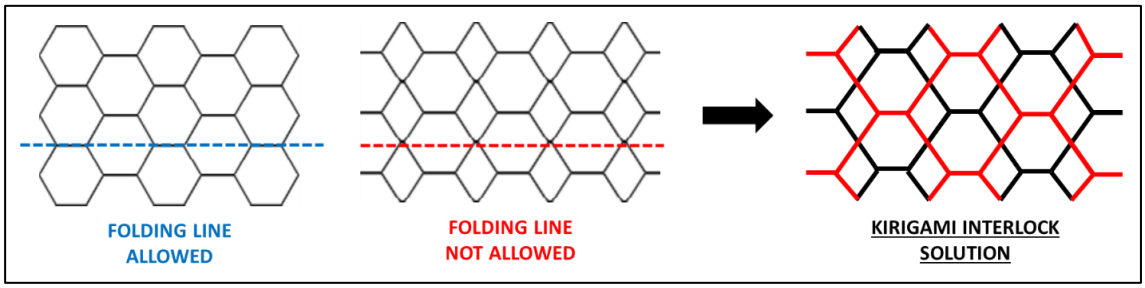

Figure 64 - Folding line detail for two hexagonal cores interlocked

If the distance between the vertical cutting pattern is changed, an in-plane translation is obtained, and this allows to create complex hybrid cores as shown in *Figure 66*. Furthermore, the square pattern that was not producible with simple kirigami, which was allowing only shifted square or shifted rectangular topologies, is now manufacturable. The geometries shown in *Figure 66* won't all be investigated, as combinations are numerous, but the configurations obtained by interlocking hexagonal and re-entrant cells with a vertical shift will be analysed in search for bandgaps along 1D and 2D periodicity.

Figure 65 - HexHex 3D printed demonstrators

An innovative aspect brought with this technology is the possibility to assemble panels with different wall thickness which translates into periodically variable stiffness. This can be also achieved maintaining the same geometrical dimensions, but through the change in one of the cores constituent material. Interlocking therefore allows different geometrical and material periodicity, alone or simultaneously. The term hybrid therefore here can be extended to constituent material as well.

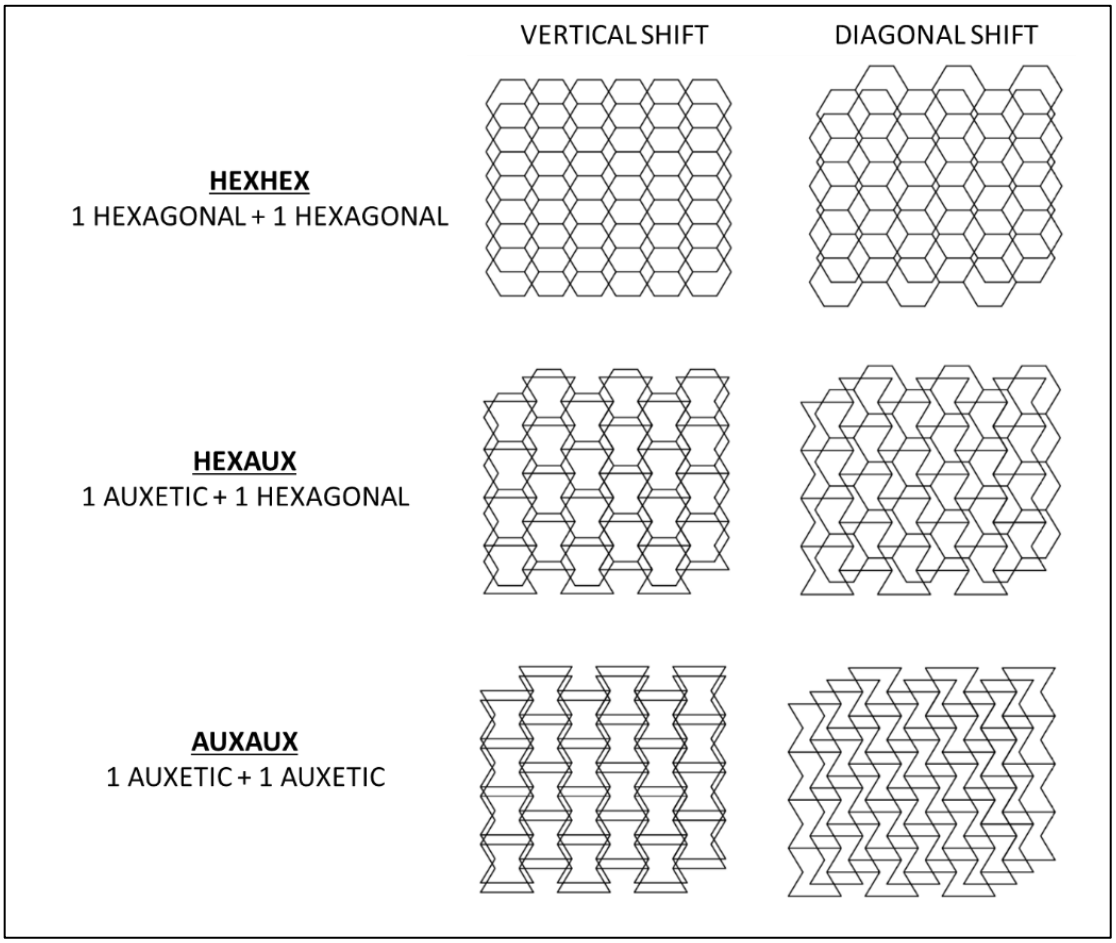

Figure 66 - Vertical and Diagonal interlock shifts between hexagonal and re-entrant configurations

The two cores can be glued together or can simply maintain their configuration exploiting the static friction contact between them. The two cores left unglued could also keep their respective spectral signature and once press-locked one onto another, create completely

new bandgaps. Amongst the improvements and possibilities that this technological change has brought, there is also the creation of gaps which can act as vent holes without having to drill them in the 2D sheet of paper. The resultant vent holes are shown in *Figure 65*, where two 3D printed hexagonal honeycombs are interlocked. To obtain this effect, it is enough to increase the length of the interlock cuts, beyond the half of the core's height, during the early stages of manufacturing. The demonstrator has been assembled with cores of different colour to visually simulate different constituent material or geometrical properties.

3.2 INTERLOCKED CELLULAR STRUCTURES AND THEIR VIBRATION FILTERING EFFECTS

In this section, hybrid cellular cores obtained with the Kirigami derived technique "Interlock" and intended to be used for sandwich panels were analysed using both 1DWFEM and 2DWFEM. The numerical investigation was performed parametrically as certain geometrical features were varied between each analysis. From the topologies presented in *Figure 66*, only the ones with vertical shift were considered and this choice was made at early stages because the eventual manufacturing later on would have been less complicated. The vibration filtering characteristic of these innovative cellular cores were also compared to more classic configurations. The aim of the investigation was to see whether the new cores possessed vibration filtering properties superior to the ones of their parent cores, the Hexagonal and Re-entrant tessellations. More precisely, the eventual detection of the Bragg bandgaps was followed by the attempt to enlarge existing or "open" new ones, through the variation of the geometrical parameters. The models were conceived here as if the structure was perfectly bonded using ANSYS APDL BEAM 4 elements and made of homogeneous material. This was a first step which allowed us to uncouple in-plane and out of plane behaviours. Material properties and involved variables for the parametric analysis are listed below, in *Table 7*.

MATERIAL PROPERTIES	
$Young's\ Modulus, E\ [GPa]$	8.1
$Density, \rho\ [kg\ m^{-3}]$	1040
$Poisson's\ Ratio, \upsilon$	0.2
$Shift\ Ratio, \gamma$	[0 - 1]
$Internal\ angle, \vartheta$	[10° - 85°]

Table 7 -Interlock simulation parameters for WFEM 1D and 2D

3.2.1 HexHex WFEM 1D (in-plane)

The first core considered is the HexHex. This represents one of the many alternatives that the interlock concept can produce. The result of such interlocking is shown in *Figure 67* where the side length of the hexagon is $l = 5\,mm$ and $t = 0.2\,mm$ the thickness of the squared cross-section beam.

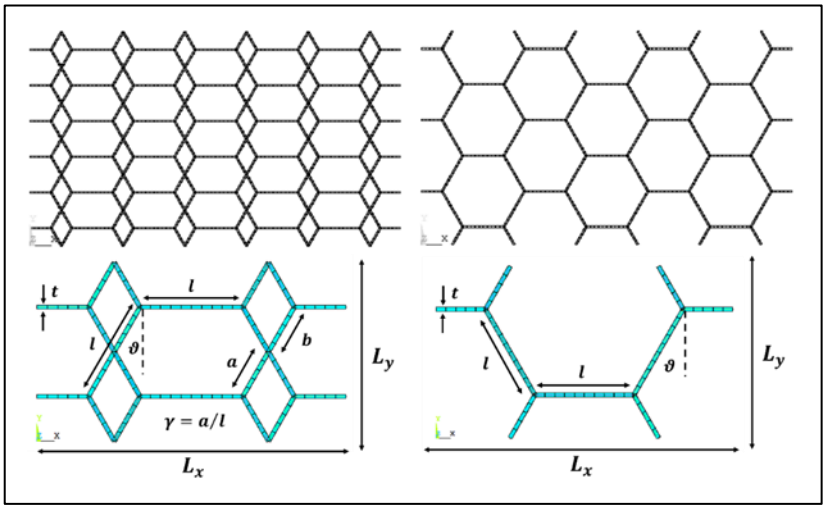

Figure 67 – HexHex topology and unit cell parameters (left), hexagonal topology and unit cell (right)

The investigation, both for 1D and 2D periodicity, was performed varying parameters like the shift ratio (which happens in the Y direction) between the two hexagonal cores $\gamma = a/l$, where $l = a + b$, and then the hexagonal internal angle ϑ. As shown in *Figure 68*, when the shift ratio is varied, the unit cell overall dimensions L_x and L_y are kept constant. This also means, since the core thickness in the Z direction is constant, that the overall relative density of the core will be constant and therefore the compression static properties in the Z direction will be equal.

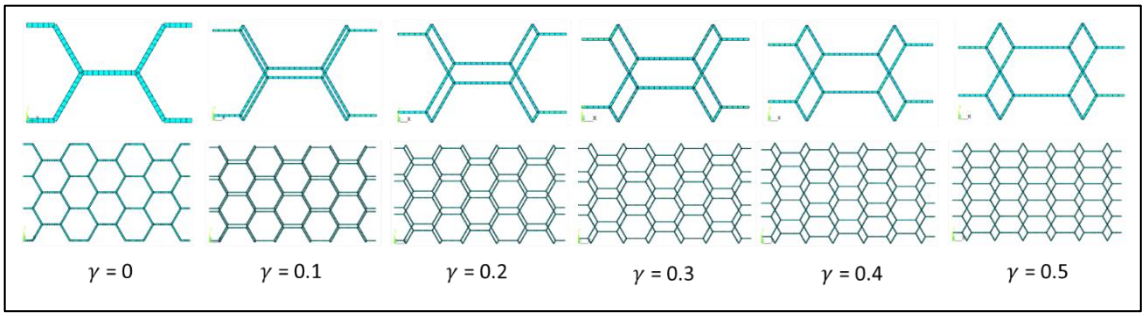

Figure 68 – HexHex variable shift ratio unit cells and topologies

In *Figure 68*, two extreme configurations (for $\gamma = 0$ and $\gamma = 1$) representing regular hexagonal lattices are shown. To keep static out of plane properties constant, walls for those configurations were doubled where appropriate.

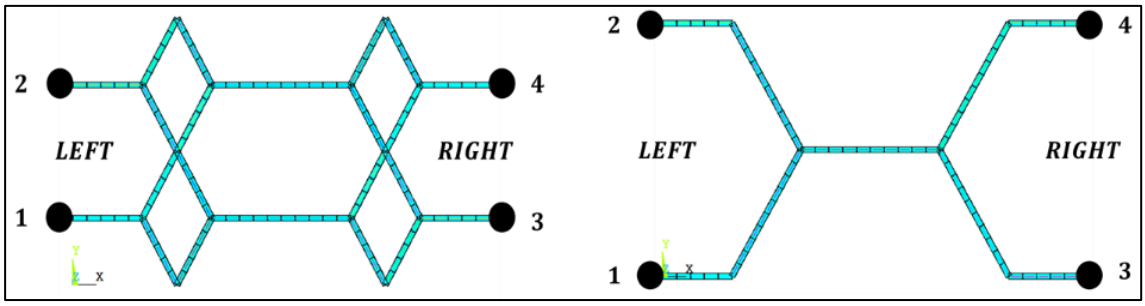

Figure 69 - 1DWFEM unit cells for HexHex (left) and Hexagonal (right) configurations

3.2.1.1 Variable shift ratio

The analysis will be carried out keeping $\vartheta = 30°$ and $l = 5mm$ constant. As consequence, a constant relative density is obtained since L_x and L_y do not vary, as shown in *Figure 70*. The shift only happens in the Y direction. In *Figure 71* the dispersion plot for all the configurations is shown. Apparently, a minimum shift between the two initial hexagonal cores produces a bandgap that begins at 7410 Hz and has a bandwidth of 8910 Hz (see shift ratio $\gamma = 0.1$). For the latter shift ratio, we also obtain three very narrow bandgaps respectively starting at 4120 Hz, 17980 Hz and finally 18370 Hz.

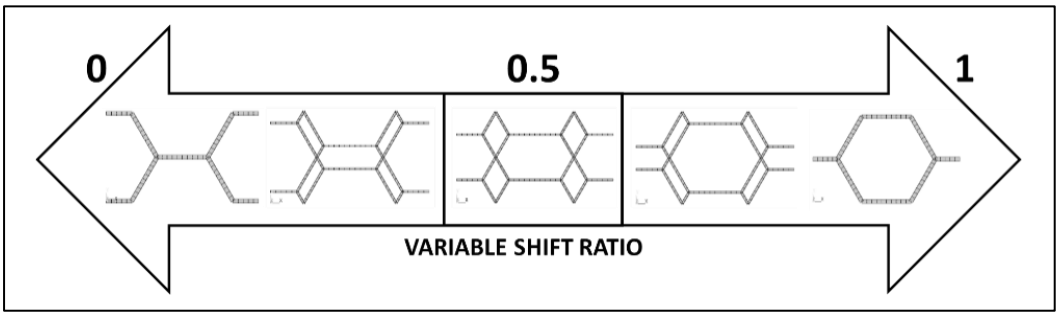

Figure 70 – HexHex unit cells according to the shift ratio variation

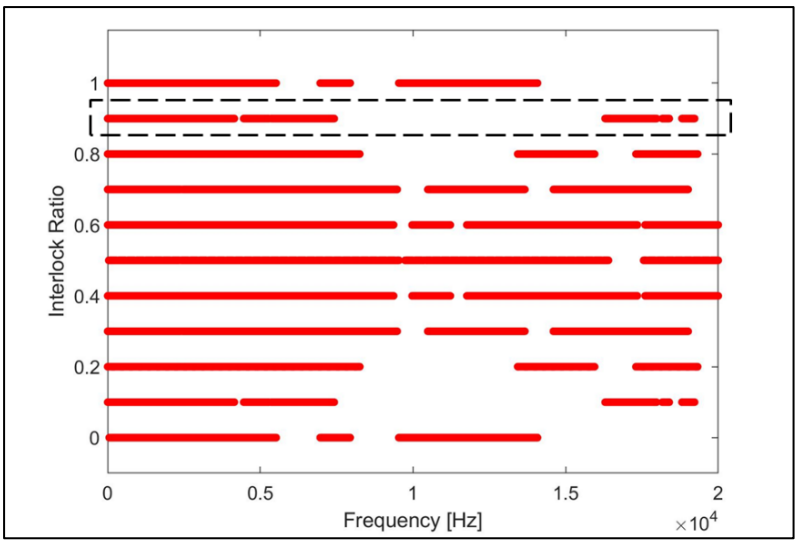

Figure 71 - Parametric dispersion curves for HexHex with variable shift ratio (WFEM 1D analysis)

It is interesting also to point out how the dispersion curves obtained for the considered shift ratios are symmetrical with respect to the $\gamma = 0.5$. Configurations for $\gamma = 0$ and $\gamma = 1$ produce therefore the same dispersion curves as their respective unit cells can recreate the same structure as one is simply the shifted version of the other. Both unit cells maintain X and Y-axis symmetry and are therefore defined as being centrosymmetric.

3.2.1.2 Variable internal angle

The variable angle analysis will be carried out keeping γ and l constant and the direct consequence is the change of relative density since L_x and L_y vary, as shown in *Figure 72*.

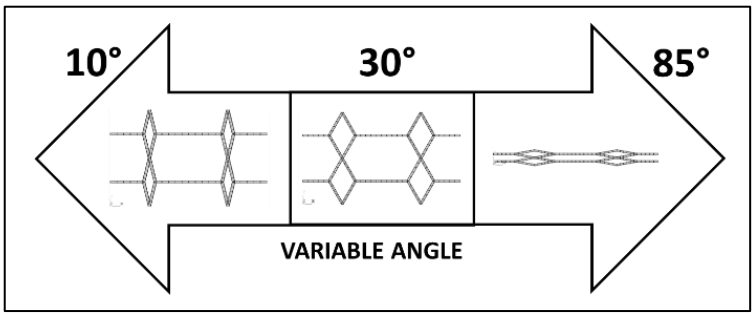

Figure 72 - HEXHEX unit cells according to internal angle variation

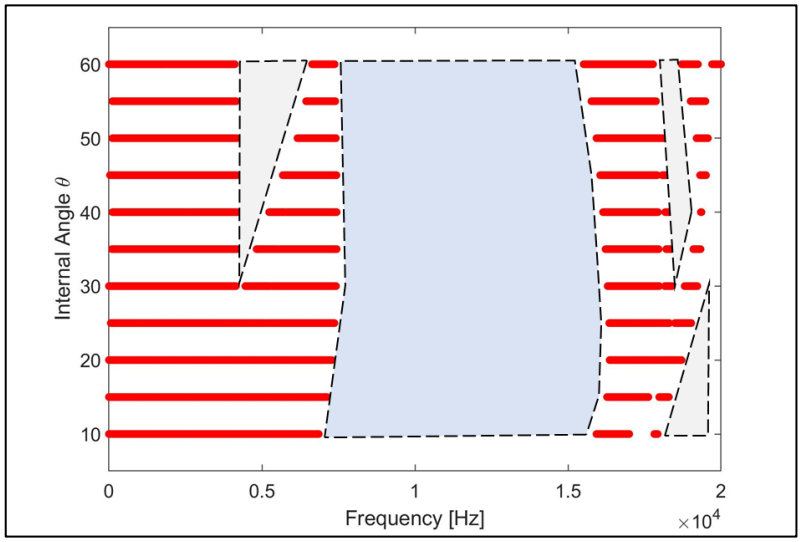

Figure 73 - Parametric dispersion curves for HexHex with variable internal angle (WFEM 1D analysis)

The selected configuration to perform a variable angle analysis was the $\gamma = 0.1$ as it possessed the wider bandgap (8910 Hz) at lower frequencies (both aspects are within the investigation aim). In *Figure 73* the dispersion plots for $\gamma = 0.1$ and variable angle configurations is shown. The variation of the internal angle ϑ has a minimum effect upon the large bandgap which we observed during the shift ratio analysis (its width drops to 8170 Hz), but it opens two of the minor bandgaps. The one starting at 4120 Hz, enlarges, keeping

its left boundary roughly fixed and changing from an initial width of only 345 Hz to a width of 2580 Hz. The bandgap appearing at 17980 Hz tends to close as we increase ϑ, but the bandgap starting at 18370 Hz and finishing at 18830 Hz (width of 460 Hz) maintains the right boundary fixed and enlarges the left one reaching a width of 950 Hz.

3.2.2 Interlock WFEM 2D

The unit cells used for the bidimensional periodicity analysis of the HexHex core as well as the ones for the hexagonal and re-entrant cores are shown in *Figure 74*. The one for the hexagonal configuration is different to the one previously considered. The reason behind this is that the number of nodes to be computed for the top and bottom boundaries would be elevated and would lead to increased simulation time, which is never ideal. As mentioned in section 3.2, the interlock unit cells are considered as if the structure was perfectly bonded and so, the interlock contact points are not modelled. Both in-plane as well as out-of-plane analyses were performed this time, contrary to the 1D periodicity case, and a total of 20 eigenvalues computed for all configurations.

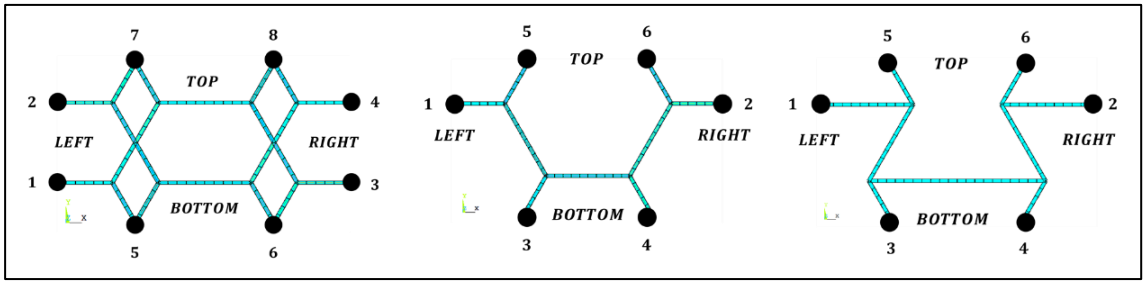

Figure 74 - 2DWFEM unit cells for HEXHEX (left) and HEXAGONAL (middle) and RE-ENTRANT (right) configurations

3.2.2.1 HexHex WFEM 2D

In *Figure 75* (top-left and top-right) the 2D dispersion relation (Brillouin's contour) of a regular hexagonal lattice with $\vartheta = 30°$ and $l = 5mm$. Both in-plane and out-of-plane hexagonal configurations do not show presence of full bandgaps for the frequency range considered in this analysis. When we vary the internal angle though shifting from a hexagonal to a re-entrant lattice, bandgaps in the out-of-plane analysis appear, as shown in *Figure 75* (bottom-right). The respective bandgap widths starting from lower frequencies are: 5464 Hz ($\Delta f/f_{mid} = 0.653$) and 7899 Hz ($\Delta f/f_{mid} = 0.222$). Another visible aspect is that the frequency range of the 20 plotted eigenvalues changed between the configurations. This is probably linked with the increase in mass of the structure, since to maintain the unit cell overall occupancy fixed while keeping the beam element cross section constant, the re-entrant configuration possesses a higher effective volume.

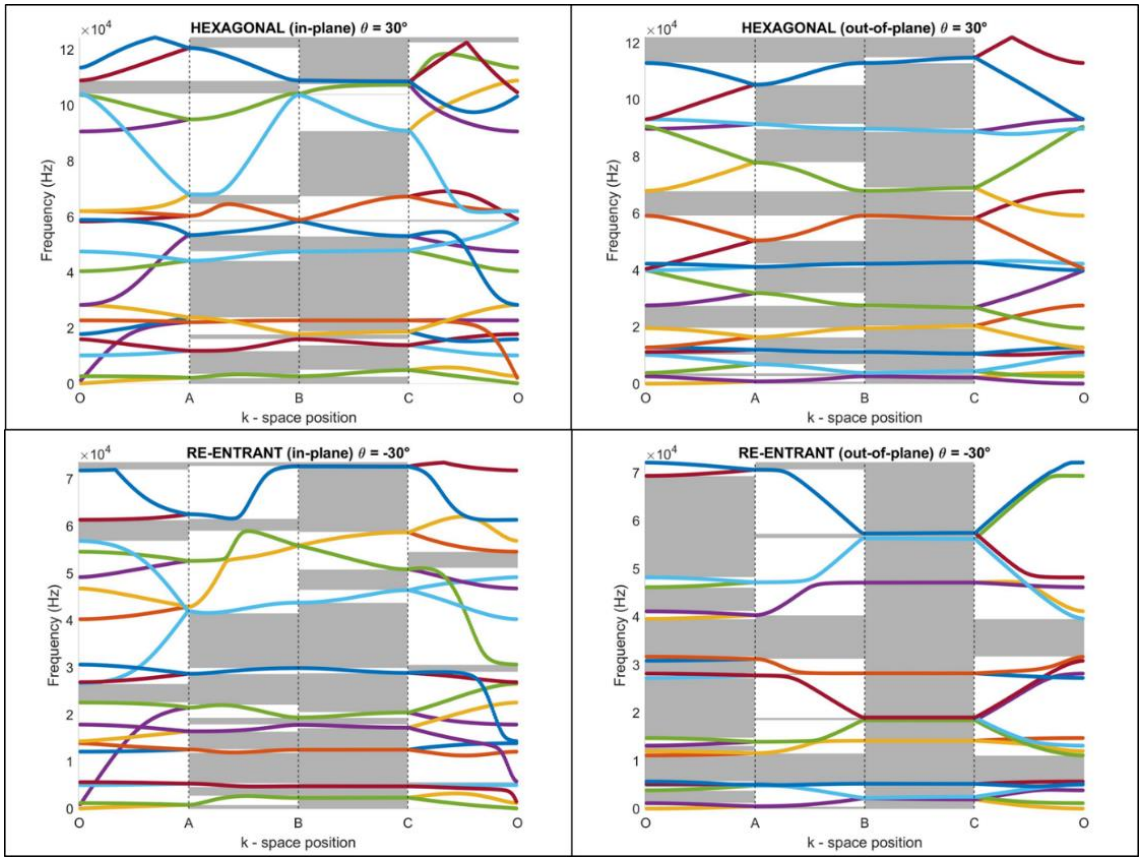

Figure 75 - 2DWFEM dispersion curves for Hexagonal and Re-entrant configuration (In-plane and out-of-plane)

Figure 76 shows respectively the 2D dispersion relation in-plane and out-of-plane for the initial HexHex lattice with $\vartheta = 30°$, $\gamma = 0.5$ and $l = 5mm$. The in-plane configuration does not show presence of full bandgaps for that frequency range, just like the hexagonal case. The out-of-plane configuration instead does, and its bandwidth is 1072 Hz ($\Delta f/f_{mid} = 0.026$). Clearly this is very narrow and cannot be considered relevant, but it is a sign that the resultant cells such as the irregular hexagon, rhombus, and parallelogram, introduce a level of impedance mismatch which opens the bandgap.

Keeping in mind the initial objective, parameters ϑ and γ were varied within the range listed in *Table 7* and the following results were obtained, listed in *Figure 77*. The variation of those parameters affected the dynamic behaviour by producing filtering properties, and in some cases enlarged pre-existing bandgaps.

Figure 77 shows the configurations which exhibited the larger bandgaps. The widest in-plane full bandgap was obtained for $\vartheta = 35°$ and $\gamma = 0.2$ (left) with a value of 2179 Hz ($\Delta f/f_{mid} = 0.063$), whilst out of plane, for $\vartheta = 65°$ and $\gamma = 0.5$ (*Figure 77*, right) with a value of 2611 Hz ($\Delta f/f_{mid} = 0.064$).

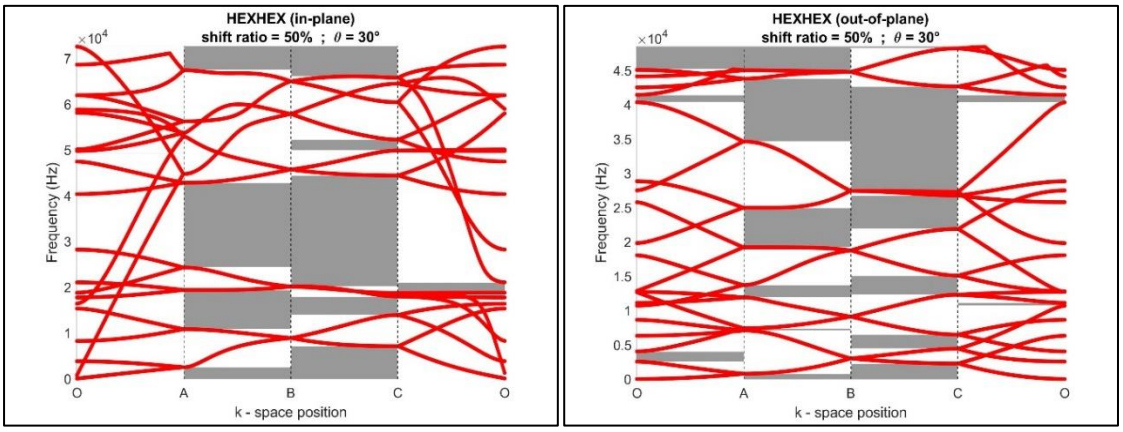

Figure 76 - 2DWFEM HEXHEX initial configuration dispersion curves (γ= 0.5; ϑ = 30°) in-plane and out-of-plane

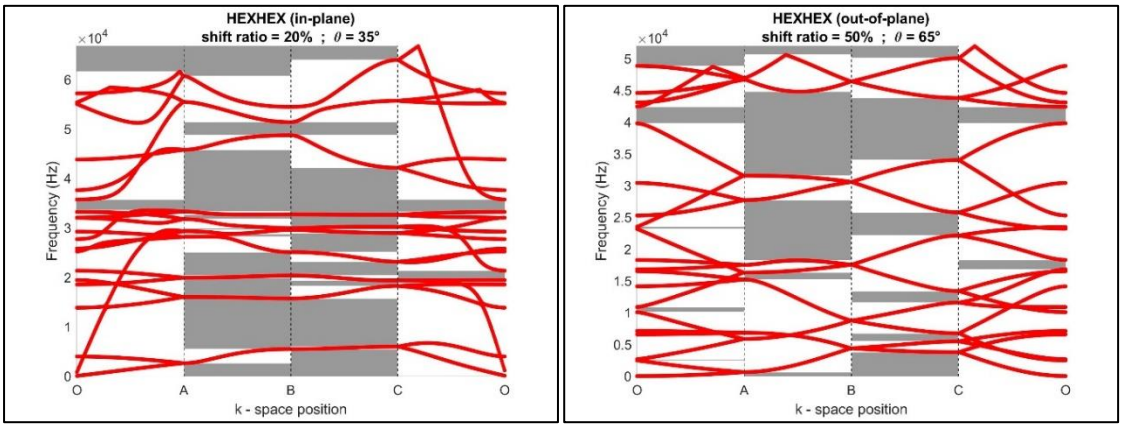

Figure 77 - 2DWFEM HEXHEX dispersion curves. In-plane and out-of-plane best performance obtained

3.2.2.2 MixHex WFEM 2D

The second interlocked geometry studied was the one where a hexagonal core and a re-entrant core were pressed locked together. This configuration has been named MIXHEX. As done for the previous configuration, the in-plane and out of plane behaviours were explored and the results presented and compared with the parent topologies.

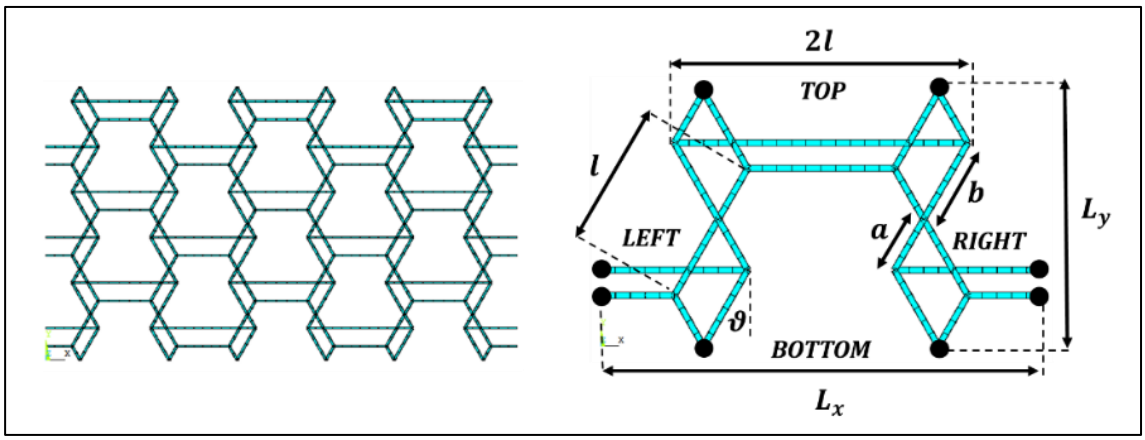

Figure 78 - MIXHEX topology (left) and unit cell's parameters (right)

The analysis was only performed for 2D periodicity. Contrary to the HEXHEX topology, here the cores cannot be shifted up to $\gamma = 0.5$ because due to the nature of the unit cell, walls would overlap, which is not possible.

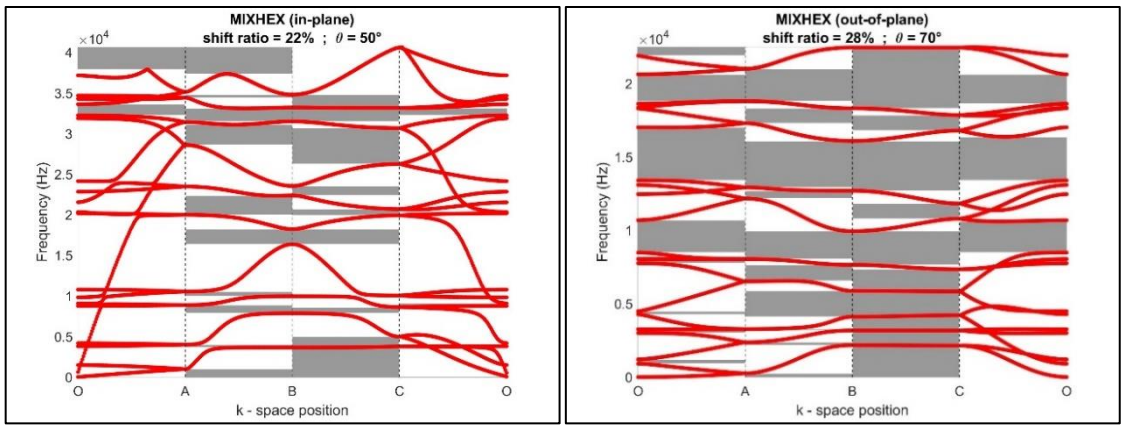

Figure 79 - MIXHEX in plane and out of plane best configurations varying the shift ratio (left) and internal angle (right)

Shifting the core vertically and varying the internal angle had an impact in both in plane and out of plane wave propagation.

In *Figure 79* (left) for a combination of $\vartheta = 50°$ and $\gamma = 0.22$ a full in plane bandgap was obtained, although very narrow and equal to 981 Hz ($\Delta f/f = 0.03$). The out of plane analysis for $\vartheta = 70°$ and $\gamma = 0.28$ reviled instead three full out of plane bandgaps within the 30 kHz frequency range. The width starting from the lower frequency bandgap were 1458 Hz ($\Delta f/f = 0.153$), 2690 Hz ($\Delta f/f = 0.179$) and 1834 Hz ($\Delta f/f = 0.094$).

3.2.2.3 AuxAux WFEM 2D

Finally, the configuration where two re-entrant cores are interlocked was studied. The configuration was named AuxAux and the 2DWFEM dispersion curves computed. Just like the previous MixHex core, the shift ratio cannot reach the value of 0.5 as the walls would compenetrate.

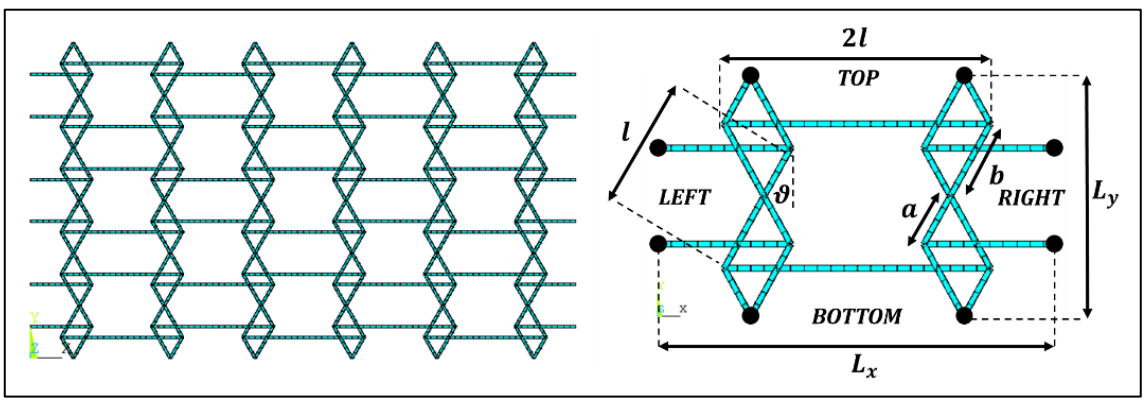

Figure 80 – AuxAux topology (left) and unit cell's parameters (right)

In *Figure 80* an array of 4x4 cells as well as the unit cell is shown. The in-plane analysis produced the widest full bandgap of all interlocked configurations, 2149 Hz ($\Delta f/f = 0.068$) for $\vartheta = 80°$ and $\gamma = 0.32$. The out of plane performance of this interlocked configuration possesses instead three wide full bandgaps within the 15 kHz range, as shown in *Figure 81*. The width starting from the lower frequency bandgap were 1136 Hz ($\Delta f/f = 0.252$), 4124 Hz ($\Delta f/f = 0.55$) and 4391 Hz ($\Delta f/f = 0.351$).

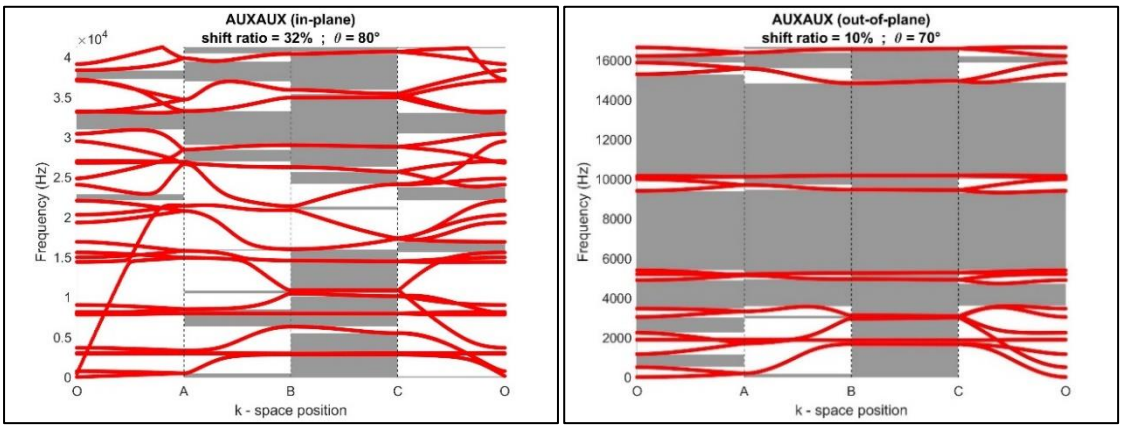

Figure 81 - AuxAux out of plane out of plane best configurations varying the shift ratio (left) and internal angle (right)

3.2.3 Conclusion on interlock shift impact

The variation of the shift ratio γ and the internal angle ϑ had a marked impact on the dynamical behaviour of the proposed interlocked gratings. The Timoshenko beam used to model the structures allowed to decouple the in plane and out of plane behaviours. The hexagonal classic core has poor vibration filtering effect compared to the re-entrant configuration. This also reflects on the performance of the interlocked cores which embed it. The bandgaps produced by the HexHex configuration in fact, both in plane and out of plane are narrow and at relatively higher frequencies than the ones produced by the other interlock combinations. The MixHex topology has an improved filtering effect compared to the HexHex. Finally, the AuxAux configuration seems to be the one which produces at lower frequencies, the higher number of bandgaps which are also found in frequency ranges which are relatively close to each other. Compared to the re-entrant out of plane performance, that the bandgap density of the AuxAux is higher although the re-entrant still has the widest bandgap of all.

3.3 DIRECTIONALITY AND ISO-FREQUENCIES

In some applications, the designer might require panels or structures with partially vibration isolated or with increased energy flow zones. This might arise for various reasons and amongst them, some of the most interesting ones might be the need of isolating delicate electrical components or designing energy harvesting devices. The information which can be retrieved from the dispersion curves as mentioned before, is not limited to the presence of bandgaps. The dispersion surfaces, if we recall that the phase velocity is $v_p = \omega/k$, where k is the wavenumber (or propagation constant) and that $\mu = kL$ is the reduced wavenumber, are basically a plot of phase constants vs frequency. For this reason, they are also called phase constant surfaces and can be used to predict the direction of free propagation of elastic waves (energy flow vector) within the core[71],[72],[73],[74],[75],[76], since the energy flow vector will lie along the line of steepest ascent, but it becomes less graphically intuitive to interpret.

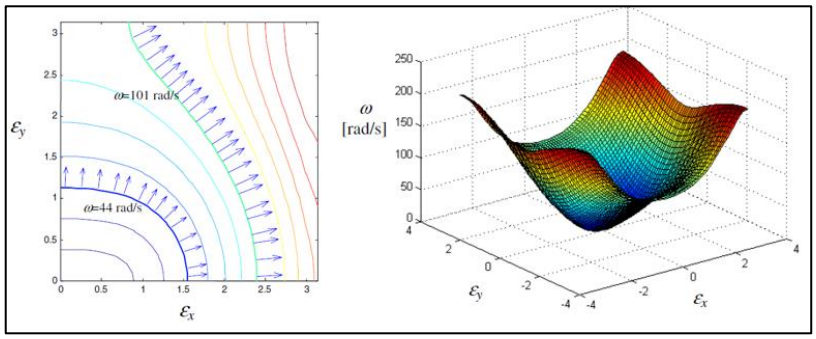

Figure 82 - Iso-frequency and 1st Phase constant surface where ε_x and ε_y are the notation for the propagation constants used by Ruzzene et al. [73]

The computation of the dispersion surfaces can be very time demanding because in order to obtain detailed images, the discretization of the propagation constants μ_x and μ_y must be very fine and therefore, the combinations to be considered are numerous. The matter becomes less relevant if the computation is confined to the irreducible Brillion zone which depends on the unit cell geometrical symmetries. A centre-symmetric unit cell allows in fact to limit the computation for values of $\mu \in [0; \pi]$, as shown in *Figure 82*. Instead of computing all the values for the dispersion surface, another method to retrieve directional information is with the iso frequency plots, which again make use of the2DWFEM technique. They are the contours created by slicing the dispersion surfaces at a given frequencies. The direction of propagation can be graphically derived because the group velocity v_g is equal to the normal to the tangent of the contour at any point. This is computationally much more efficient than computing the dispersion surfaces. The iso-frequency plots for the first phase

constant surface of various configurations were produced and can be seen from *Figure 83* to *Figure 88*. The mode which has the highest amount of energy is the out of plane bending mode and for this reason, the investigation was performed focusing the attention on the 1st phase constant surface and respective iso-frequency plot. The comparison between the different configurations was carried out at an arbitrary frequency of 4000 Hz because from the results, some topologies showed clear directional propagation preference for this type of wave at the selected frequency (and higher).

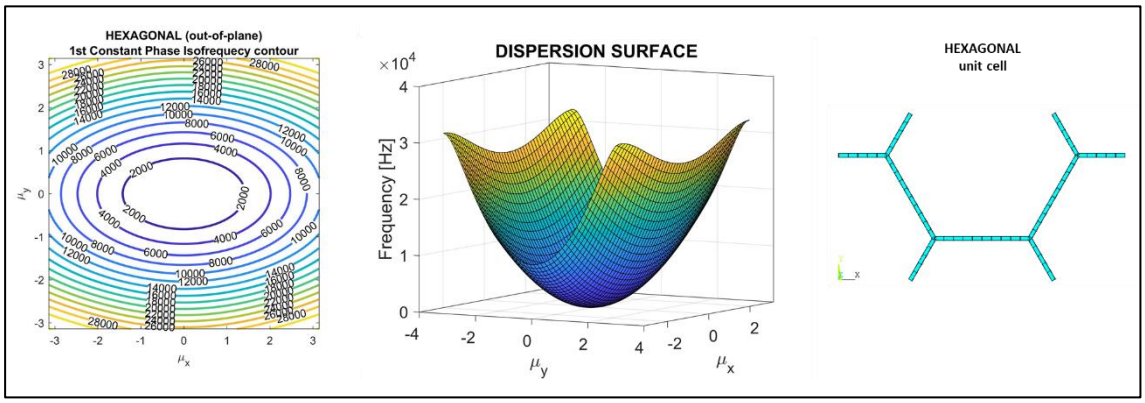

Figure 83 - Hexagonal 1st constant phase surface (bending) and iso-frequency contour.

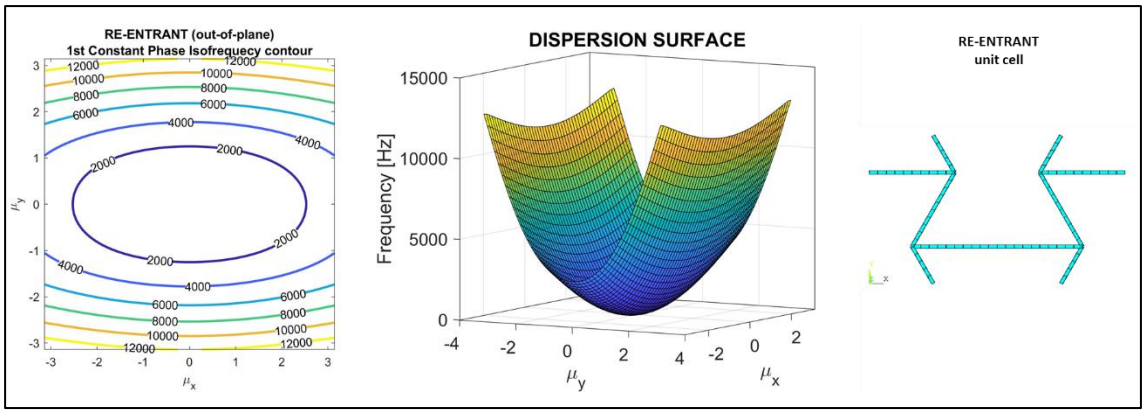

Figure 84 - Re-entrant 1st constant phase surface (bending) and iso-frequency contour.

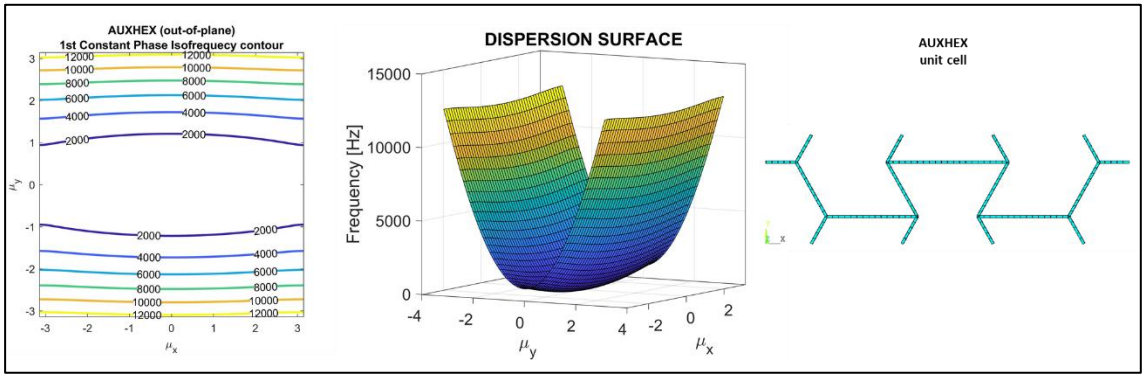

Figure 85 - AuxHex 1st constant phase surface (bending) and iso-frequency contour.

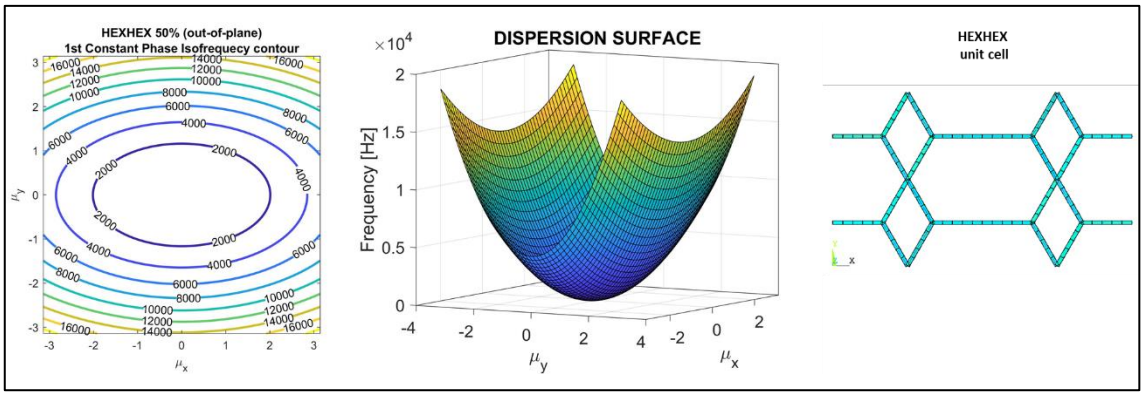

Figure 86 - HexHex 1st constant phase surface (bending) and iso-frequency contour.

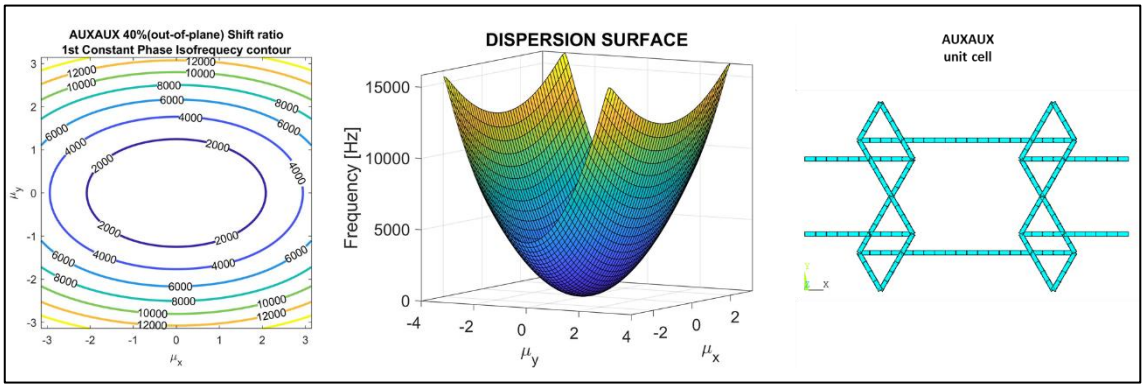

Figure 87 - AuxAux 1st constant phase surface (bending) and iso-frequency contour.

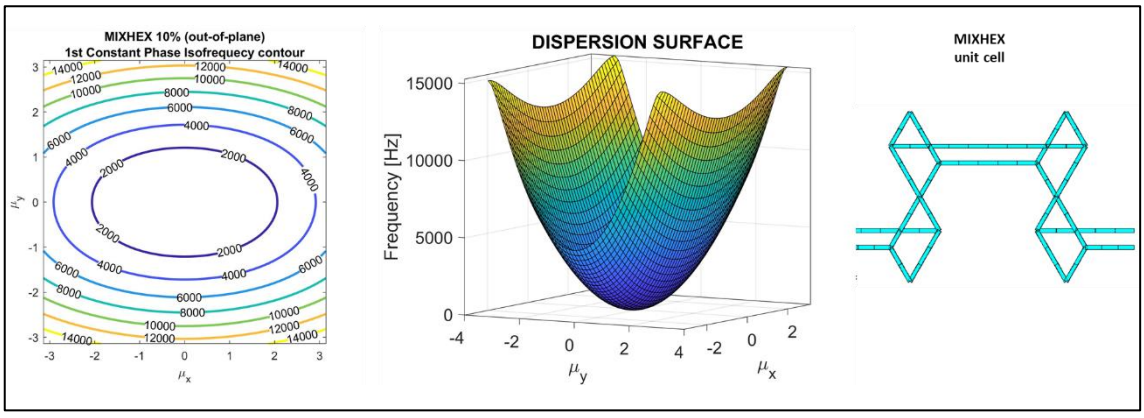

Figure 88 - MixHex 1st constant phase surface (bending) and iso-frequency contour

The ones which show "open" contours at this frequency are the re-entrant and the AuxHex. Furthermore, the AuxHex seems to be the one with the most accentuated directionality amongst them all as no closed contour is shown already at 2000 Hz, contrary to the competitors.

3.4 FULL SCALE CELLULAR CORE

The results obtained through the 2DWFEM, are now compared with a full-scale core grids, undergoing an out-of-plane sinusoidal external solicitation. The transient analysis was performed on a finite structure made of 12 unit cells in the X direction and 16 in the Y direction. This beam grid was modelled with ANSYS BEAM 4 elements neglecting damping effects and allowing only out of plane displacements and rotations (3 DOF's). The excitation was set at 4000 Hz in search of correspondence with the iso-frequency predictions. In fact, only few configurations did not produce a closed contour at this frequency. For the interlock configurations, different shift ratios γ were also considered to see the effect of such parameter on the directional behaviour. As a reminder, the shift ratio does not vary the relative density of the panel and therefore it can be considered a geometrical impact parameter. *Figure 89* to *Figure* 92 are the visual representation of the propagating waves within the core grid. The sinusoidal force was applied at the centre of the structure and the grid boundaries were fixed. The plotted results were all taken before the wave fronts reached the borders so to avoid reflection and consequent interaction with the propagating wave, since the main objective here was to validate the directionality characteristics of each configuration shown by the faster propagation prediction tool constituted by the isofrequency contours.

It appears that the AuxHex and the AuxAux (the latter with smallest analysed shift ratio $\gamma = 0.1$) inherit the directionality from the re-entrant cell. This is coherent with a visual analysis done on the structure since the hybrid pattern AuxHex contains re-entrant cells and the AuxAux with $\gamma = 0.1$ resembles a double-walled re-entrant configuration. Furthermore, as we increase the shift ratio for this configuration, we tend to lose the directional effect while the HexHex instead, seems to gain some wave propagation preference path due to the full structure internal reflection, which occurs at this frequency. There is good agreement between the FEM finite structure transient analysis and the infinite structure approach iso-frequency plots in terms of degree of directionality and an analytical prediction can be made according to the work by F. Scarpa and M. Ruzzene [73]. Since the reasoning here is pursued in terms of direction of energy flow, the isofrequency contours could be used as a prediction tool, in case of periodic grid or panel design with embedded vibration damping solutions like resonators or viscoelastic patches. This would allow the designer to optimise the spatial distribution of such add-ons and therefore reduce the number of features to be included, saving weight, and reducing costs, as their amount would be minimised.

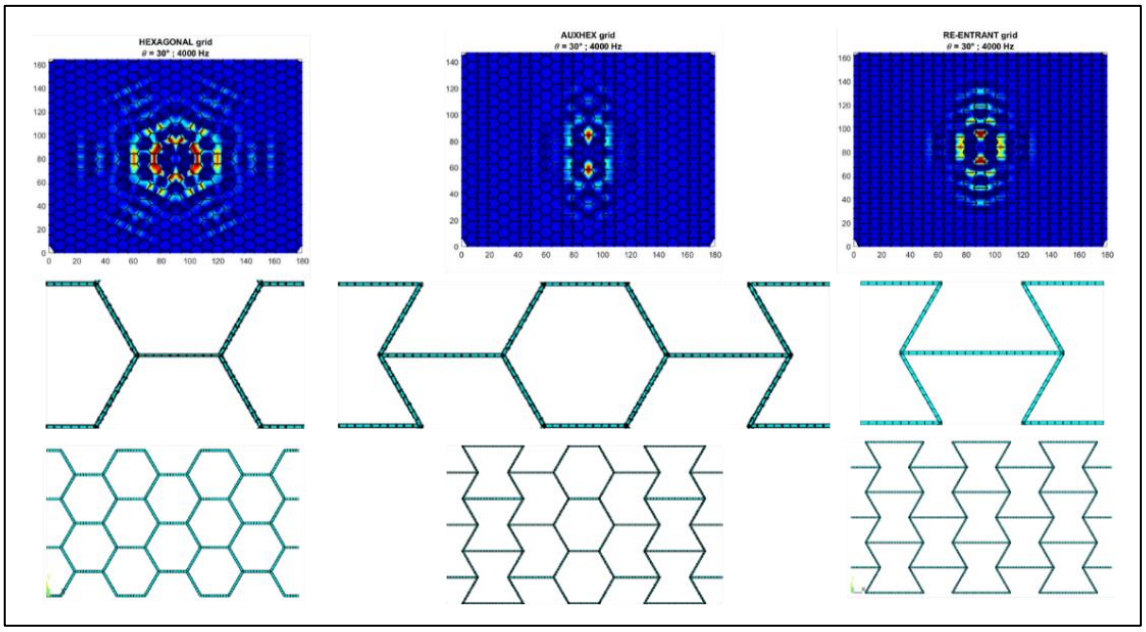

Figure 89 - Directionality out of plane wave propagation for the Hexagonal, AuxHex and Re-entrant configurations

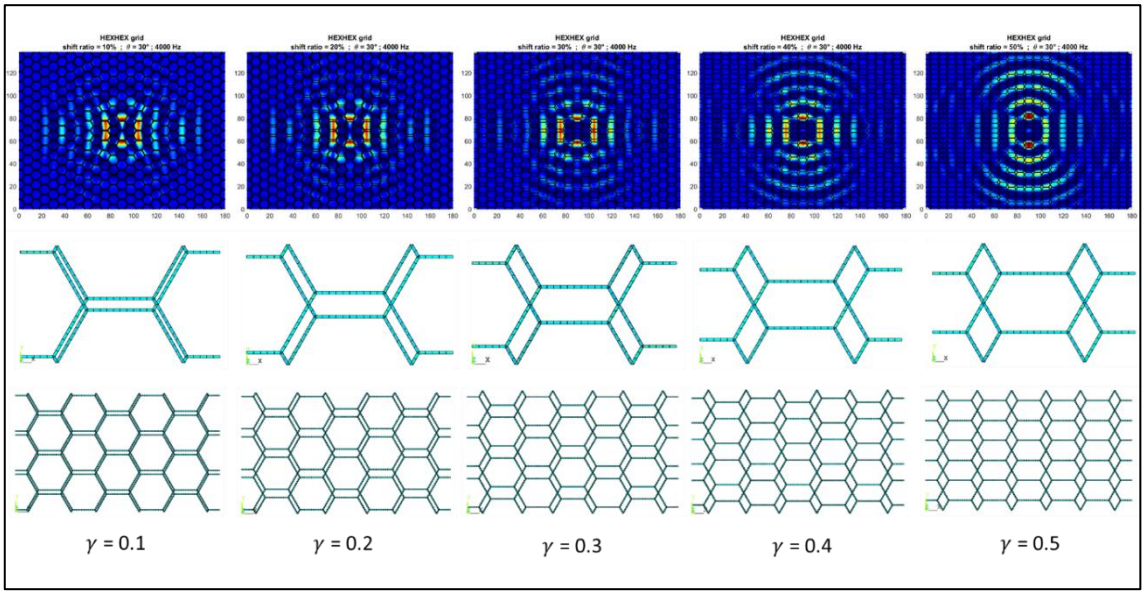

Figure 90 - Propagation of a monochromatic wave set at 4000 Hz for the HexHex cellular grid as the shift ratio is varied from $\gamma = 0.1$ *to* $\gamma = 0.5$.

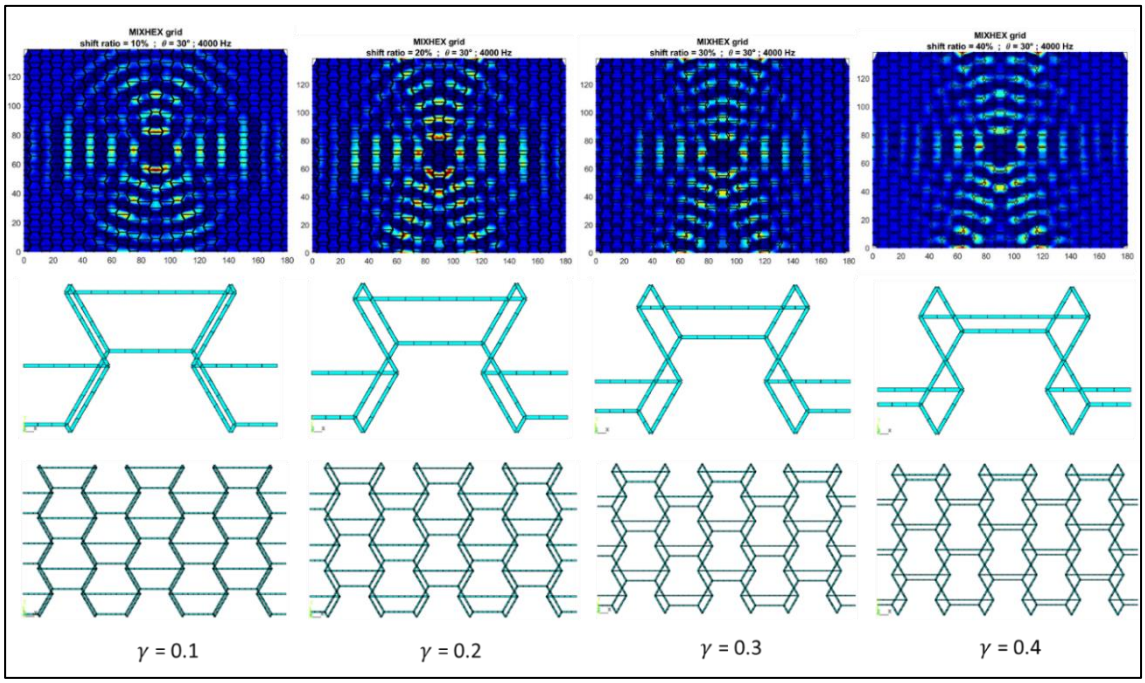

Figure 91 - Propagation of a monochromatic wave set at 4000 Hz for the MixHex cellular grid as the shift ratio is varied from $\gamma = 0.1$ *to* $\gamma = 0.4$*. The shift ratio is limited to 0.4 to avoid structures compenetrating.*

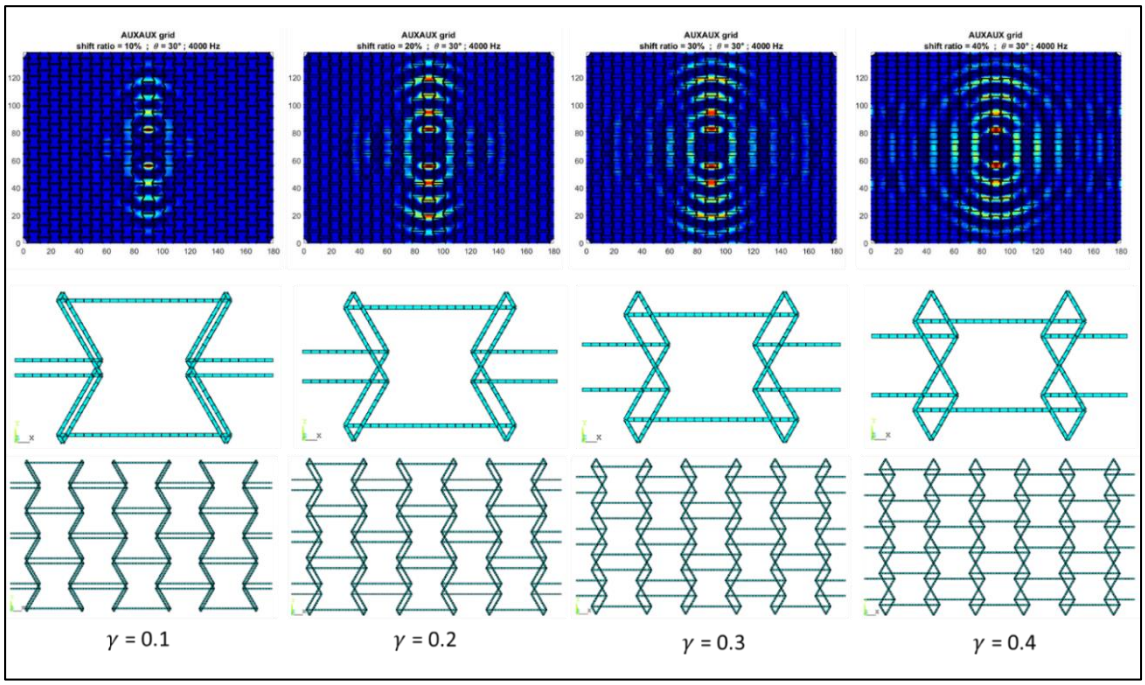

Figure 92 - Propagation of a monochromatic wave set at 4000 Hz for the AuxAux cellular grid as the shift ratio is varied from $\gamma = 0.1$ *to* $\gamma = 0.4$*. The shift ratio is limited to 0.4 to avoid structures compenetrating.*

3.5 FINITE PERIODIC STRUCTURE EXAMPLE

A finite structure example using hexagonal and re-entrant unit cells was performed to see whether iso-frequencies could be used as a fast prediction tool to produce tailored hybrid cell core assemblies with vibration isolated portions. This was modelled using ANSYS BEAM4 elements and allowing only out of plane nodal displacements and rotations (3 DOF's). The dimension of the unit cell (refer to Figure 40 and Figure 46 for the hexagonal and re-entrant unit cell respectively) were set to $l = 5mm$ and the squared cross section of the beam had a side of 0.4 mm while $\vartheta = 30°$. The border of the panel was fixed while the element size was dimensioned according to equation (1.2.4).

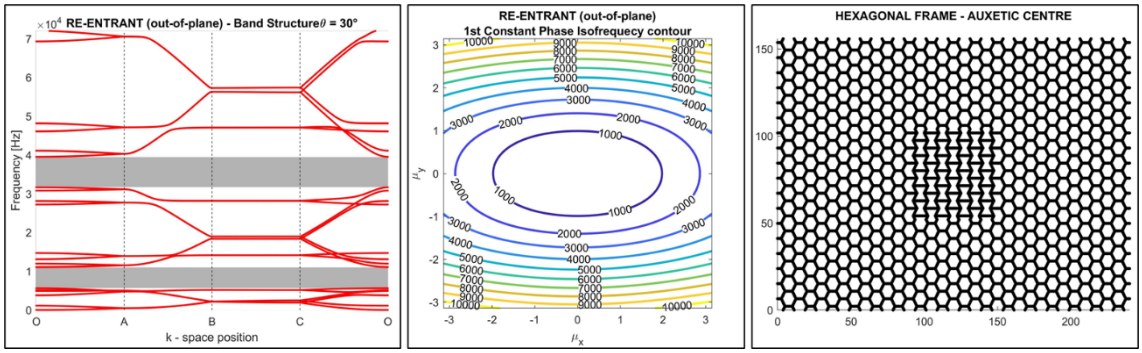

Figure 93 - Re-entrant WFEM 2D dispersion curves out of plane (left), iso-frequency (middle), analysed structure (right)

The analysis captured frames of the propagating waves (out of plane solicitation) and the results were displayed trough 2D nodal plot of the grid, where nodes were removed if displaced by the propagating wave. From the dispersion curves iso-frequency plot of the hexagonal configuration it seemed that the wave could propagate in both directions, X and Y while the re-entrant tends to block one of them, depending upon the orientation of the cell. In *Figure 94* the structure excited at different frequencies is proposed. The material properties were the same used when performed the extended iso-frequency investigation on the various topologies. The new iso-frequency plot and the dispersion curves for the re-entrant cell are shown in *Figure 93* and are to be taken as reference to interpret the resulting displaced structure (shown in *Figure 94*) firstly excited at 2000 Hz (frames (a) to (d)) and then at 8000 Hz (frames (e) to (h)). At 2000 Hz, both the hexagonal and re-entrant cells do not have full out of plane bandgaps. The absence of full out of plane bandgaps for a hexagonal core within this frequency range was discussed in section *3.2.2.1*. For this reason, although the re-entrant cell possesses a partial bending bandgap in the x- direction (quadrant OA in *Figure 93*) waves can still propagate in the y-direction (quadrant CO in *Figure 93*). This is visible in *Figure 94* (left) where the wave propagates within the finite

structure (FEM) in all directions with almost the same energy. On the right instead, the structure excited at a frequency which falls within the re-entrant cell full bandgap, shows a directional vibration filtering effect. It is worth to depict the radial propagation behaviour that the structure re-obtains as soon as the wave reaches the hexagonal grid (no bandgap).

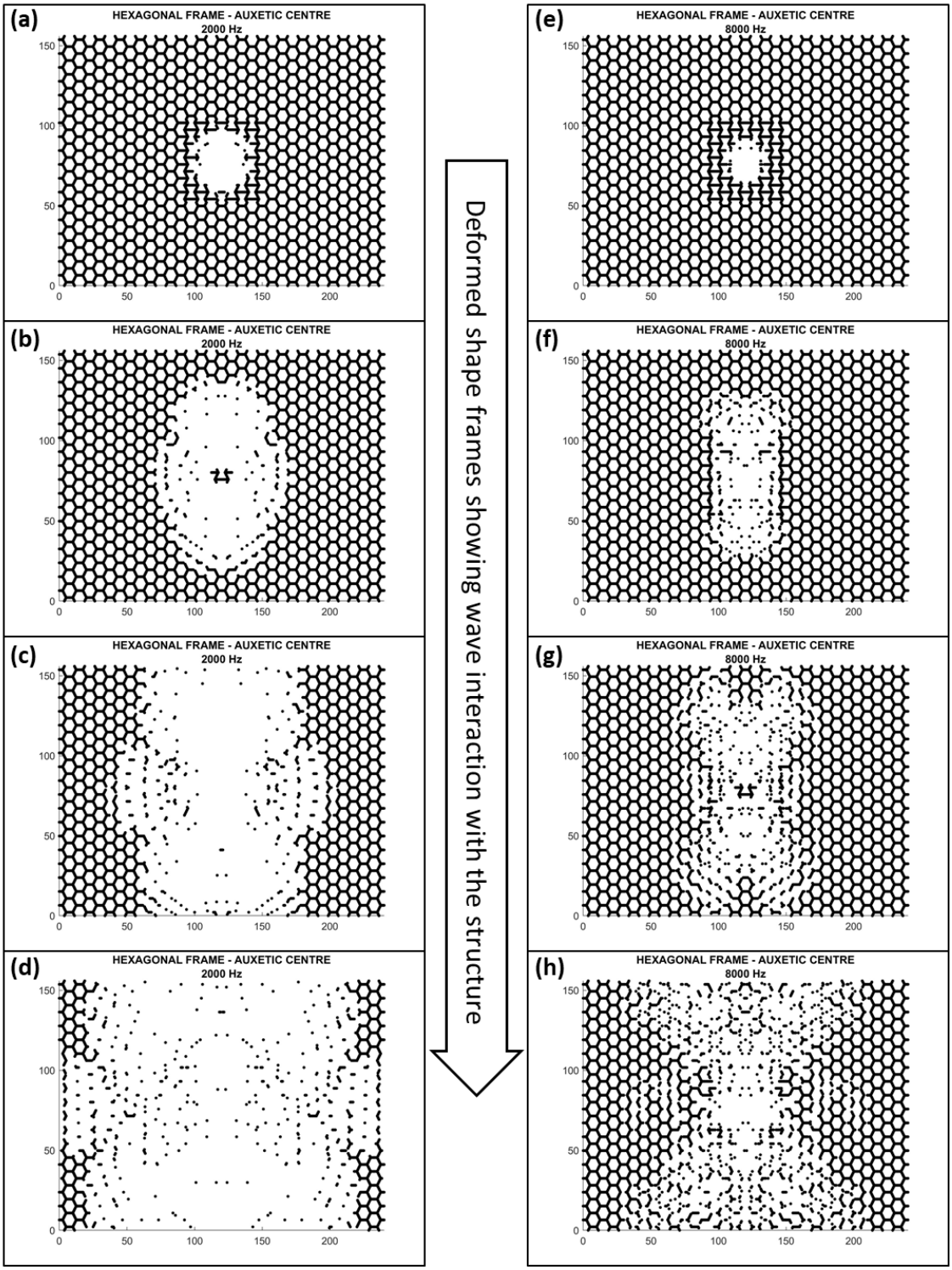

Figure 94 - Out of plane transverse wave propagation in a hexagonal and re-entrant assembled grid nodal displacement at 2000 Hz (left) and 8000 Hz (right). Displaced nodes are removed from the undeformed structure, which is shown in Figure 93.

3.6 NOVEL RE-ENTRANT CELL

This cellular core was derived from the classic re-entrant configuration, which exhibited directional wave propagation characteristics [54],[71],[72],[73],[75] when exposed to out of plane solicitation and was therefore inspired by the work carried out in this chapter. Although this is an interesting feature, it is limited to the out of plane bending waves. The aim was to use the information gathered so far to produce a cellular core possessing full Bragg bandgaps. The Directionality and hierarchy concepts [77] in this case were used as a tool to create a full in-plane bandgap by placing "child" re-entrant cells of smaller size and different orientation onto the main frame constituted from "parent" re-entrant cells. The starting configuration is therefore the classical re-entrant cell and as we increased the size of the "child" cell (e), the cell's wall thickness was reduced to maintain the core's encumbrance and mass constant, as shown in *Figure 95*. The overall cell encumbrance was 20mm*12.125mm*15mm.

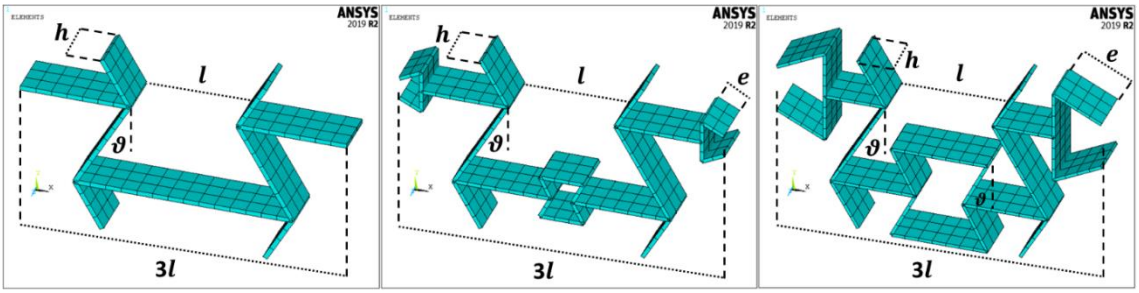

Figure 95 - Re-entrant unit cell (left), Optimised cell evolution (middle), Optimised unit cell (right)

The 2D in-plane periodicity dynamic analysis was carried out adopting the inverse WFEM formulation and the full set of numerical tools developed and presented in the appendix. The model parameters used for the simulation are listed in *Table 8*. Initially, the dispersion curve for the classic re-entrant configuration was produced and then the geometrical optimization was carried out.

MODEL DETAILS		**MATERIAL PROPERTIES (MDF)**	
Element Type	SHELL 181	Young's Modulus	4.20 GPa
Element Size	1.00 mm	Density	818 kg/m^3
Element thickness	0.30 - 0.19 mm	Poisson's Ratio	0.33

Table 8 - Model and material details

The unit cell for the re-entrant core was modelled using ANSYS SHELL 181 elements, and it is shown in *Figure 96* as well as the dispersion curves for the frequency range 0-10 kHz. SHELL 181 elements are suitable for analysing thin to moderately-thick shell structures. It

is a four-node element with six degrees of freedom at each node. This geometry clearly shows some partial bandgaps across the XY plane direction for all types of waves traveling the media (AB & BC in the k-space). The steepest branch starting from zero in both, quadrants O-A and C-O are compression modes in the x- and y-in-plane directions which translates into no compression full bandgap within this frequency range. Directional (x-axis) in-plane and out of plane bending bandgaps are present because if we remove the compression branch, we notice two bandgaps: [4743 Hz – 7854 Hz] and [9083 Hz – 9154 Hz] both highlighted in quadrant O-A.

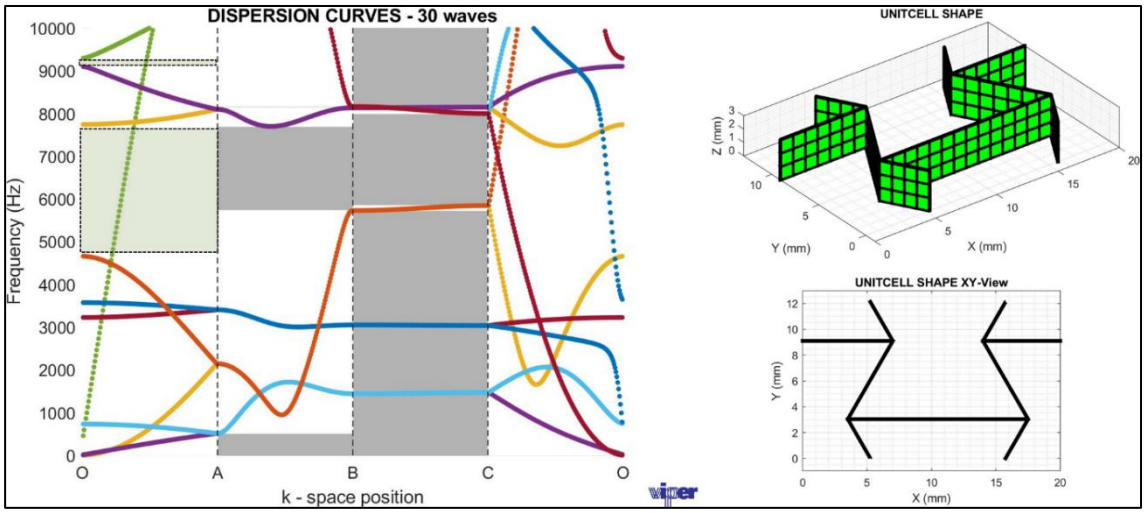

Figure 96 - Re-entrant unit cell and dispersion curves

The parametric investigation conducted produced configurations possessing a full Bragg bandgap which reached its maximum width when the aspect ratio reached $e/l = 0.465$. This is a valid improvement of the dynamic behaviour of the "parent" cellular core.

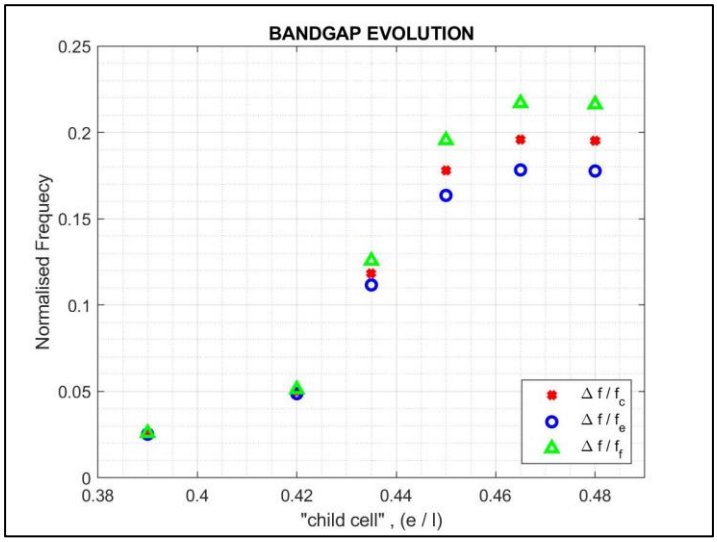

Figure 97 - Bandgap evolution during geometrical parametric investigation.
(f_c = central frequency; f_i = initial frequency; f_f = final frequency)

The normalisation is carried out by dividing the bandgaps width by its central (*c*), initial (*i*) and final frequency (*f*). The overall full bandgap evolution can be observed in *Figure 97* as parameter e is increased to its maximum admissible value (*l*=constant), dictated by isovolumetric and mass restrictions. The novel auxetic unit cell is shown in *Figure 98* as well as the dispersion curves for the frequency range 0-10 kHz. A full bandgap of noticeable width (1.1 kHz) between 4.9 kHz and 6.0 kHz can be seen.

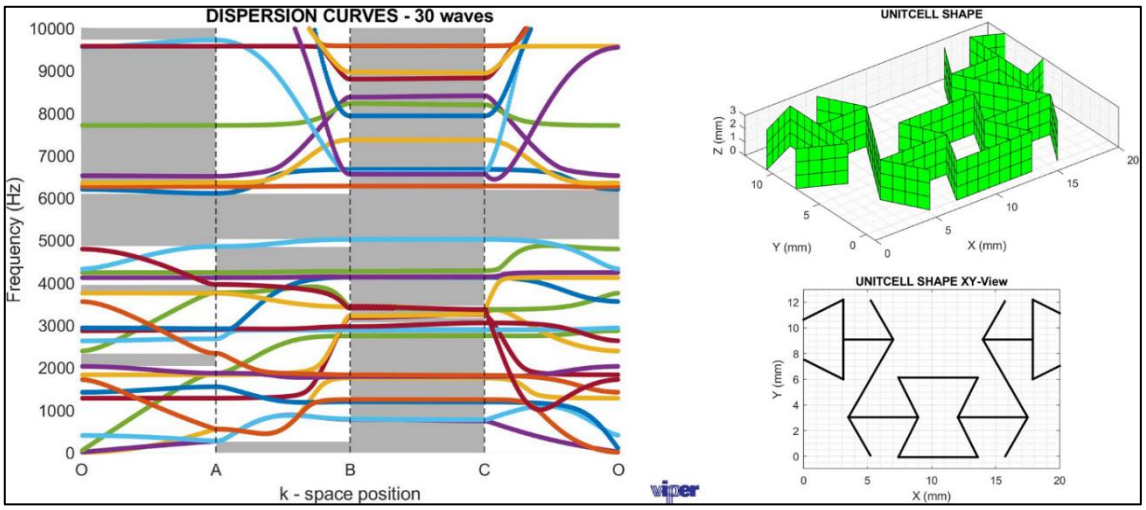

Figure 98 – Re-entrant modified unit cell and dispersion curves

The geometrical complexity and the thinner walls are probably the cause of the increased modal density visible from the dispersion curves in *Figure 98.* Although the out of plane compression buckling load is maintained, the overall bending in-plane and out of plane stiffness must be lower. The buckling assumption is made following a similar procedure to the one proposed by Gibson and Ashby [69], where all walls constituting the unit cell buckle simultaneously. This study is a good example of how the information acquirable using the fast wave propagation tools WFEM-derived, can be used to conceive novel structures with desirable mechanical vibration isolation properties maintaining the static out of plane constraints which might be set up front.

CHAPTER 4

TRANSMISSIBILITY OF INTERLOCKED NATURAL FIBRE CORES

4.1 INTRODUCTION

For a single degree of freedom system, Transmissibility, $\mathbb{T}$, is calculated as the ratio between the measured output quantity over the input, as introduced in section *1.3.2*. The quantities that can be used for the calculation, and therefore measured, are force, displacement, velocity, or acceleration. A typical transmissibility graph is shown in Figure 17, where two sections can be depicted and those refer to amplification and isolation frequency ranges. On the graph the frequencies have been normalised with the 1st natural frequency of the system ω_n and multiple curves for various damping ratios are proposed. Here, the out of plane transmissibility of sandwich panels was investigated to show the vibration damping potential conferred to these notarial stiff structures by the novel kirigami interlock manufacturing technique. The interlocked core configuration chosen was the HexHex as the hexagonal kirigami honeycomb was the easiest to assemble. The calculation of the mechanical loss factor, η and the damping, ξ will be carried out using the well-known half power bandwidth method[78],[79].

4.2 MANUFACTURING

The materials chosen for the manufacturing of the samples were both flax fibres-based prepregs and they were the Evopreg PFC polyfurfuryl alcohol (PFA) thermoset resin and the Biotex Flax polypropylene (PP) thermoplastic 400 g/m^2 2x2 Twill. Both prepregs were in twill weave but due to the different nature of the matrix, the manufacturing process differed under certain aspects. Mostly, the PFA prepreg was new to the community and therefore no datasheet with thermal cycles were given by the manufacturer, reason a whole characterisation campaign had to be carried out. The ASTM report of the latter is given in the Appendix. The characterisation was all carried out at the Advanced Composites Centre (ACCIS, University of Bristol) as well as the sample manufacturing. The prepreg was subjected to tensile tests following standard ASTM D3039/D3039M which allowed us also

to calculate the shear modulus using D3518/D3518M. This was possible because the tensile test samples were manufactured with weaves oriented ±45° and 0/90°. The tested material properties, which were used for the numerical simulations are shown in *Table 9*.

Property	**Mean value, $\bar{x}$ [GPa]**	**Standard Deviation, s**
Elastic modulus ±45°	4.771	0.004 [GPa]
Poisson's Ratio	0.323	0.020
Shear Modulus	0.957	0.0656 [GPa]

Table 9 - Material properties for Flax/PFA natural fibre

The characterisation followed two consolidation techniques and those were carried out using a hot press and the autoclave. Laminates manufactured with the PFA resin were particularly challenging since once the resin reached the fluid state, spilling occurred.

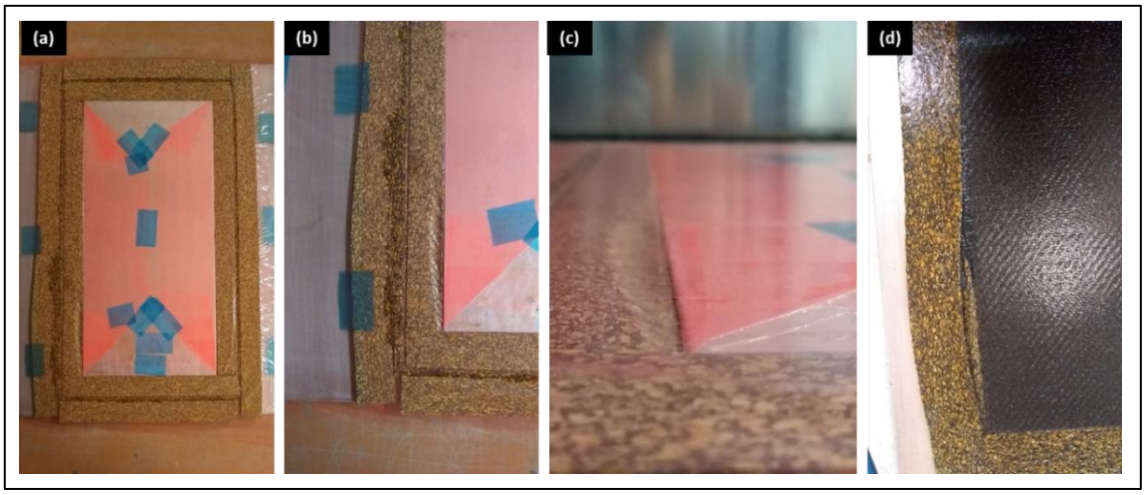

Figure 99 – (a) Hot press double cork multilayer frame, (b) resin pushing away lower cork layer, (c) cork deformation at the end of the curing process.

This was happening at the early stages of manufacturing, when a cork frame was applied around the preform and onto the tool plate (*Figure 99* and *Figure* 100 *(a)*). The pressure was the main parameter to control to avoid leakages and guarantee laminate density.

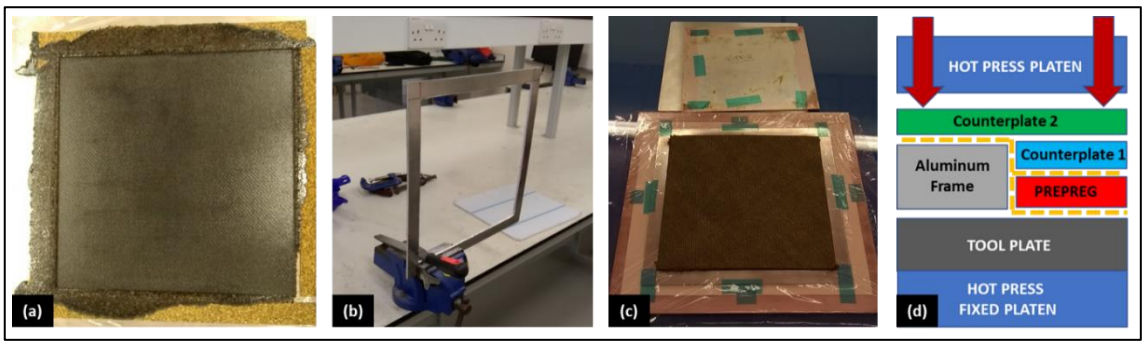

Figure 100 – (a) Hot press resin leak with cork frame, (b) custom made aluminium frame, (c) Layup with aluminium frame, (d) Hot press outline.

For this reason, the cork frame was abandoned, and a custom made aluminium frame (*Figure 100(b),(c)*) with silicon patches, manufactured.

The use of the autoclave instead presented less problems since during this process, pressure is not only applied from the top, as it happened with the hot press, and therefore the cork received distributed pressure around the edges as well. This avoided the resin, in liquid form, from pushing the cork sideways. Indeed, other problems were arising as anyways a datasheet was not provided and processes like these are anyways dependant from the hardware quality and layup knowledge as well as experience. In *Figure 101* the layup procedure carried out in the clean room is shown:

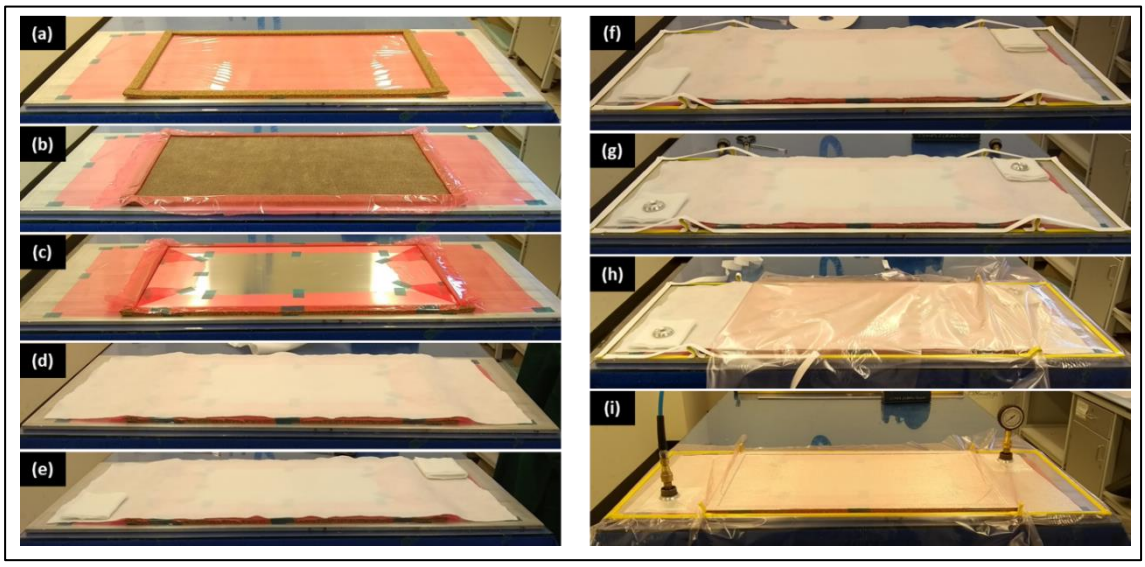

Figure 101 - Autoclave lay-up process for flax/PFA prepreg laminates: (a) Release film and cork frame, (b) prepreg layup, (c) caul plate, (d) breather, (e) valve breather, (f) tacky tape frame, (g) valves, (h) vacuum bag, (i) completed layup and vacuum pump in action.

Overall, the two techniques had some advantages and disadvantages, listed in *Table 10* but the samples produced with the autoclave were generally of better quality in terms of performance repeatability and density. The interlock samples were produced using the hot press since the process was much faster and the elastic moduli for the ±45° laminates were comparable and the laminate skins were produced with the autoclave.

AUTOCLAVE	HOT PRESS
Advantages	
+ Better quality laminates (higher density)	+ Shorter production cycles
+ Larger laminates manufacturable	+ Cheaper than autoclave
Disadvantages	
- Long production cycles	- Low consolidation
- Expensive	- Temperature fluctuations

Table 10-Advantages and disadvantages of bio-based long fibre composite laminate manufacturing techniques

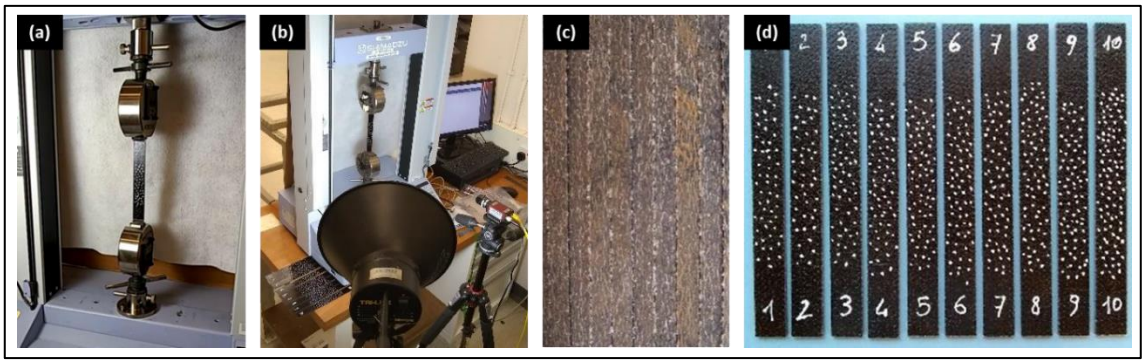

Figure 102 - tensile tests with and without video gauge, sample cross section and samples with dot pattern

For the core manufacturing, another problem rose which was the slight twist that the single layer of prepreg was undergoing once cured or thermoformed. This was probably caused by the twill weave and the non-homogeneous distribution of the fibers in the prepreg. Natural fibers are known to be complicated to weave and to control in thickness. A remedy to this was to cut the prepregs along the ±45° optics to obtain a slight bending rather than the twist. This was preferred since the bending happens parallel to the kirigami slits and therefore the effect compensated once folded. The interlock cutting pattern was performed for both after the consolidation process and the samples assembled with epoxy bio-derived resin. In *Figure 104* different interlock sample configurations assembled with cores of same flax fibre composite prepreg as well as "hybrid material" ones are shown, together with some manufacturing/assembly steps.

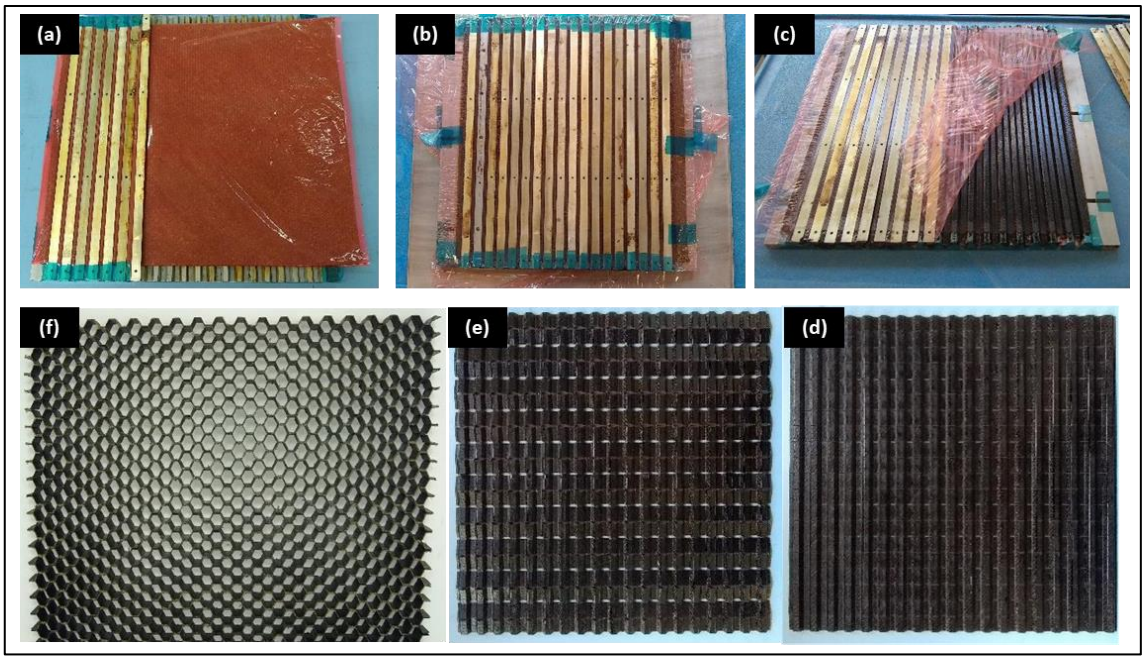

Figure 103 - Kirigami Flax/PFA manufacturing: (a) prepreg mold fitting, (b) prepreg ready for the hot press cycle, (c) cured corrugated sheet, (d) laser cut corrugated sheet, (e) corrugated sheet folding prior to adhesive application, (f) final honeycomb.

The assembly can happen in two different ways: the cores can be initially interlocked together as a first step and then the skins glued to it, or and the skins can be glued separately, one on each sample and then the semi-panels interlocked. In the second case, the sandwich panel is only kept together with the aid of friction, while in the second case, friction would still happen inside the core interlocked surfaces, but the structure would be connected from one side to the other.

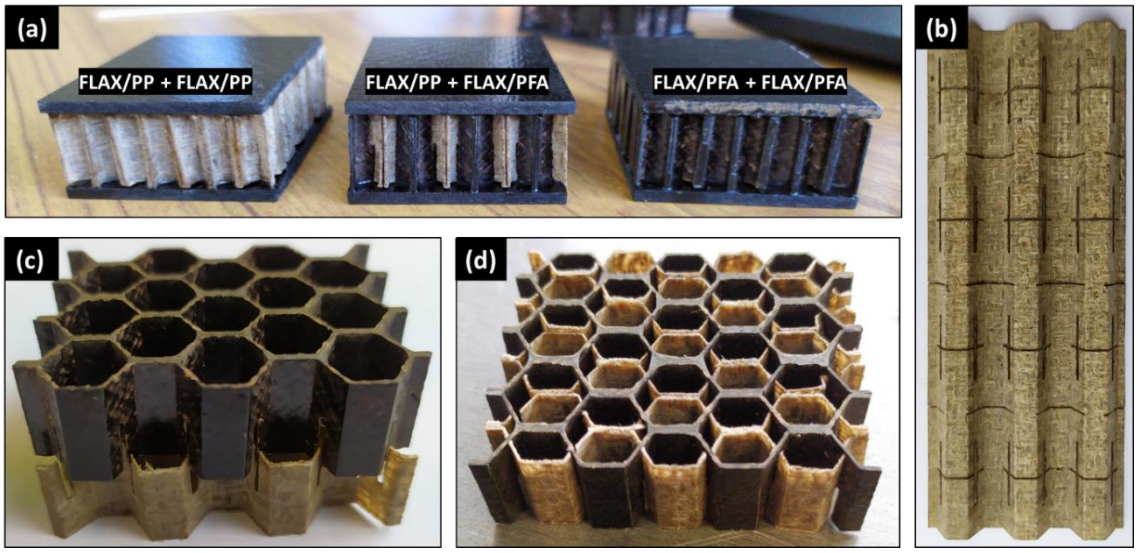

Figure 104 - (a) Interlock manufactured samples, (b) Laser cut corrugated sheet, (c) and (d) interlocked cores

4.3 NUMERICAL SIMULATIONS

The aim of this numerical simulation is to understand the frequency range which would include the first out of pane transmissibility peak of the interlocked sandwich panels and to achieve this, the model was created using ANSYS SHELL 181 elements for a total of 29345 elements. The script, also based on a combination of Matlab and ANSYS commands, just like the one written for the directionality simulations in section *3.3*, was written so that parameters like the wall thickness, height, size and material of each core could be controlled as well as the skins. The materials were modelled as isotropic. Furthermore, the unit cell was designed to simulate the interlock sample dimensions cutting pattern; at this stage, the intersections between the cores was not modelled for friction and the way ANSYS deals with this, is assuming perfect gluing, merging nodes and assigning average material properties. This was done to recreate the multi-material periodicity. The test procedure is described in section *4.4.* Thee numerical simulations were performed to understand which one was the frequency range where the first peak of transmissibility occurred for each of the configurations shown in *Figure 106*. The constituent material damping was set at a value of 4% with the assumption that the two cores were perfectly glued. Two added masses of 100g

and 222g were available and therefore simulations were performed to see which one was more adequate to use for the experimental procedure which was carried out following the one suggested by Jones [78].

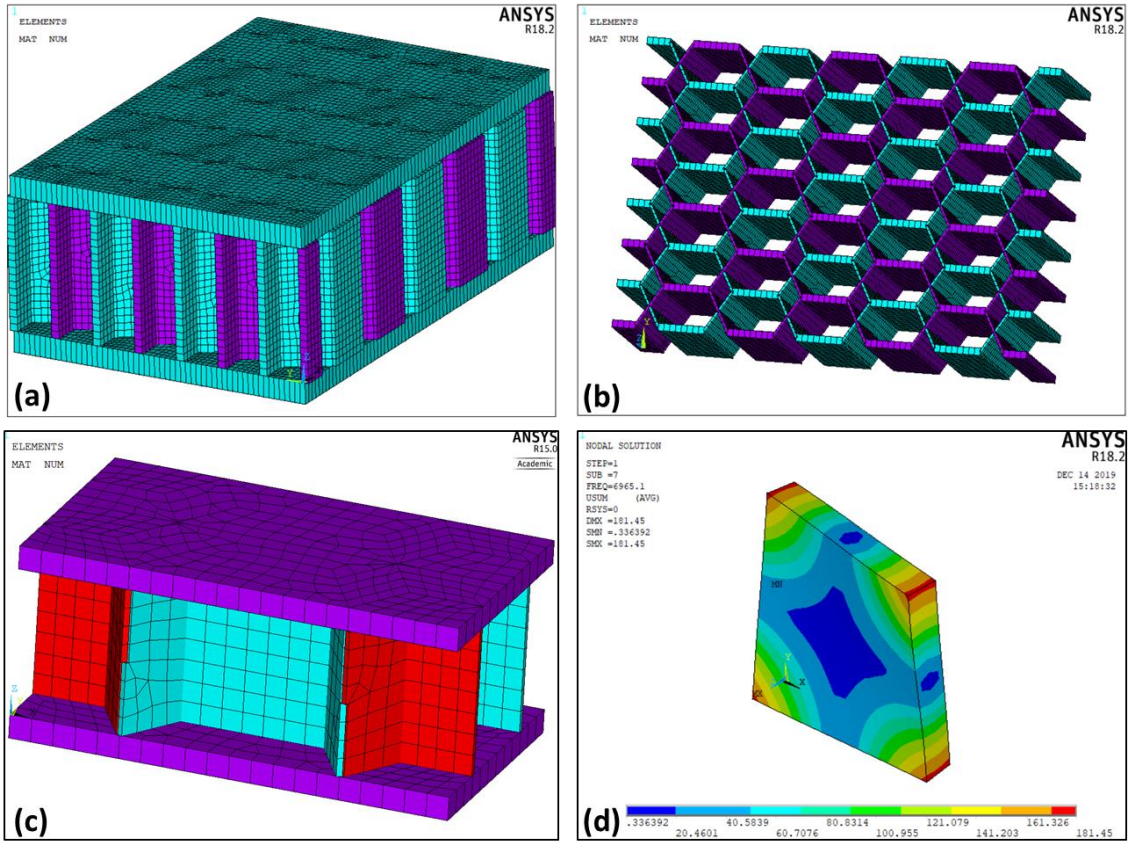

Figure 105 – (a) HexHex (3x4) sandwich panel in hybrid material configuration, (b) HexHex bare core in hybrid configuration, (c) detail of a sandwich panel unit cell, (d) aluminium plate modal analysis.

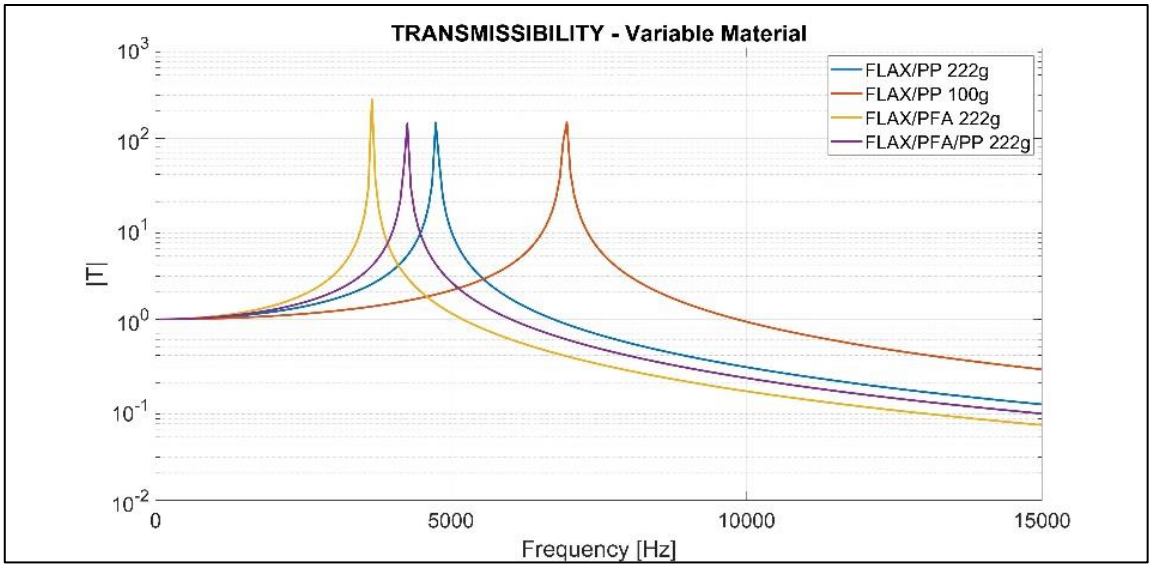

Figure 106 - Transmissibility numerical simulation for variable interlock core material and variable added mass

Furthermore, a modal analysis of the selected aluminium plate was performed to be sure that the base support would not deform during the test and therefore appear within the test results frequency range. The first mode of the base plate, shown in *Figure 105 (d)*, was found to be 6975 Hz. From the results shown in *Figure 106* the heavier mass was chosen to proceed with the experimental campaign since the effect was to shift the transmissibility peak to lower frequencies and therefore further away from the first mode frequency of the base.

4.4 TESTING

The test was performed following [78] and the setup shown in *Figure 107*. The mass applied on the top weighted 222g and the input white noise signal generated with the aid of a MATLAB script and fed to the shaker. The unbonded interlocked cores are kept together only through the contact friction between them and so the test was performed with 3 different amplitudes to evaluate if such parameter would have any effect on the results. The initiation of a dynamic friction contact would be a supplementary source of energy leakage and would increase the damping of the system. The results for the three tested configurations which were the PFA/PFA, PFA/PP and PP/PP interlocked cores were postprocessed for a frequency range up to 5000 Hz and are shown in *Figure 108*, *Figure 109* and *Figure 110*.

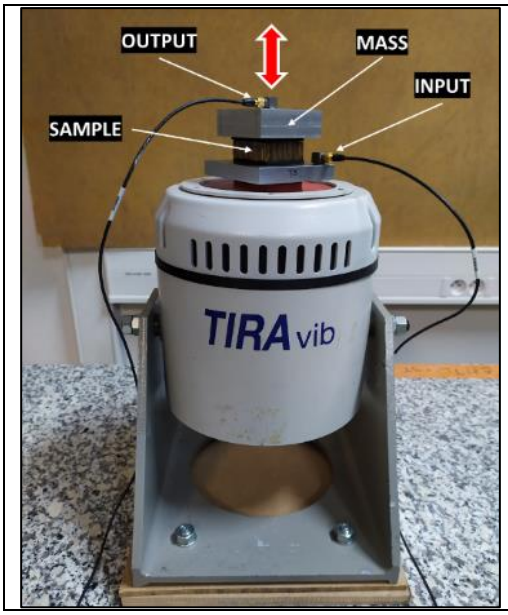

- NI cDAQ 9234
- NI cDAQ
- Amplifier
- Accelerometers
- Shaker
- Aluminium plate (78 mm x 83.5 mm x 12.5 mm)
- Mass (222 g)
- Notebook
- Adhesive wax
- Cyanoacrylate glue

Figure 107 - Transmissibility test rig

The first panel to be tested was the one with both cores in flax/polypropylene (PP/PP) which had flax/polyfurfuryl laminate skins *Figure 104(a)*. From the graph in *Figure 108* we

denote that the highest peak was actually obtained with the lowest amplitude of excitation. This suggests that there was some interaction between the two interlocked cores which we remind to be not glued to each other nor to the opposite panel skin. The peak also shifts towards the lower frequencies. The same behaviour appears also in the rest of the samples tested which were the hybrid configuration (PFA/PP) and the full PFA/PFA panel, both also shown in *Figure 104 (a)*.

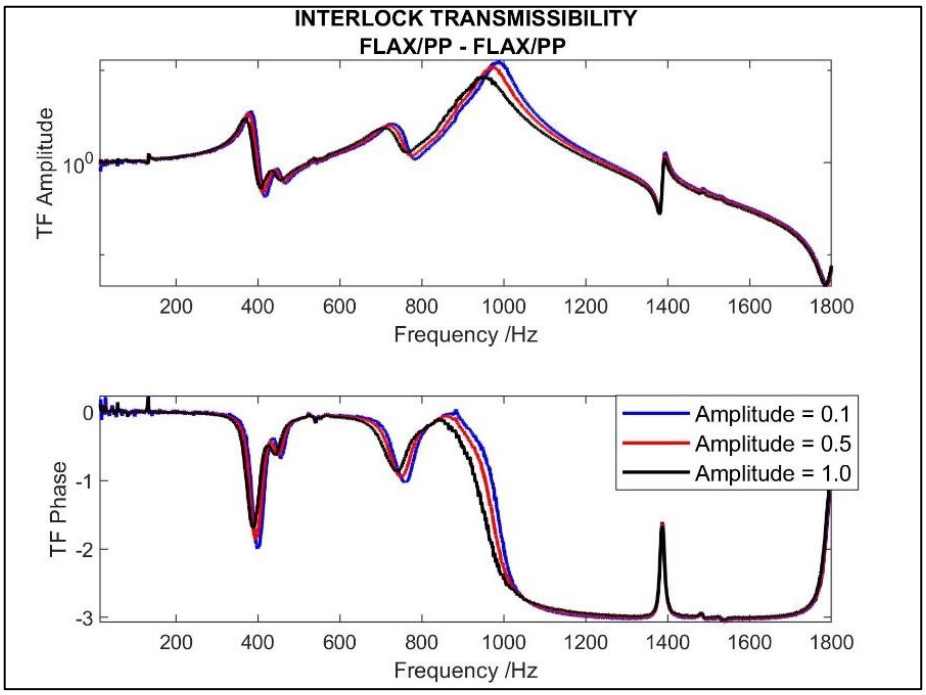

Figure 108 - Transmissibility for HexHex homogeneous Polypropylene cores

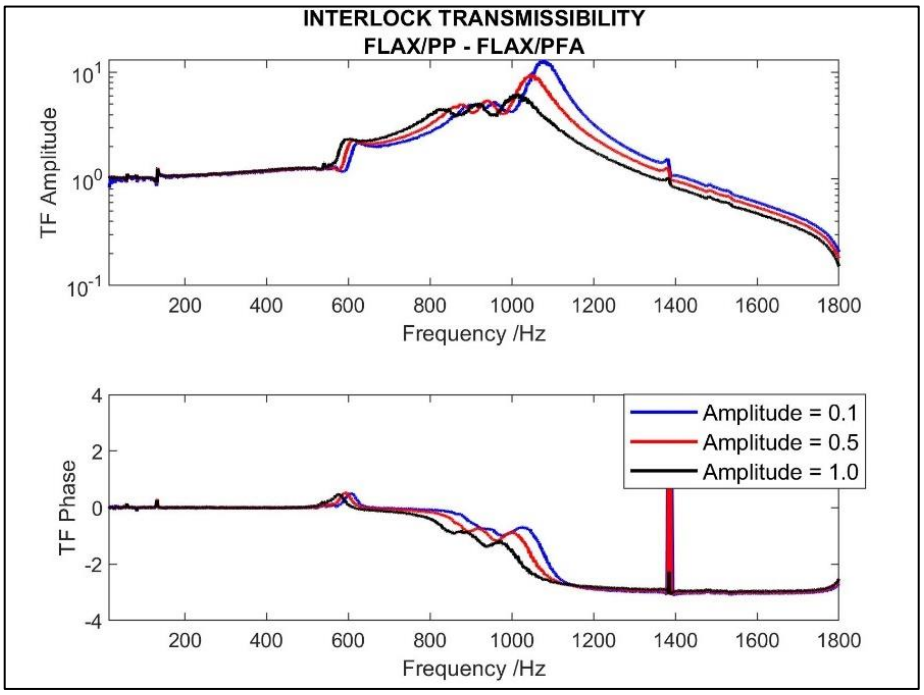

Figure 109 - Transmissibility for HexHex hybrid core (Polypropylene and Polyfulfurfuryl)

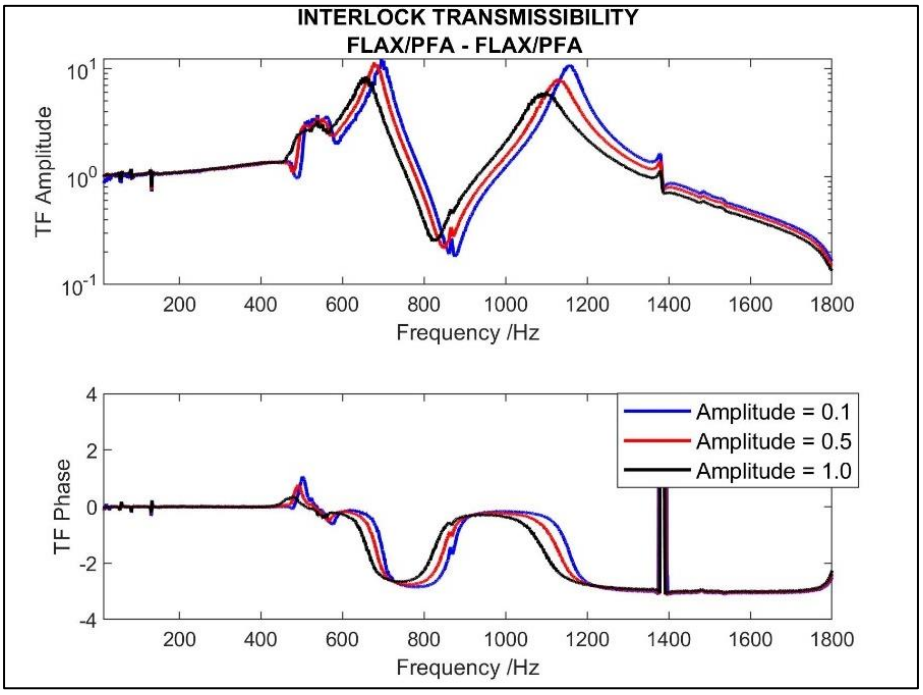

Figure 110 - Transmissibility for HexHex homogeneous Polyfurfuryl cores

The hybrid configuration has for every tested amplitude, a repetition of three lower peaks. Another feature that distinguishes the behaviour of this configuration with the others is that the peak value difference is higher than the rest. In the full flax/PFA sandwich core test, a second mode appeared. Since this behaviour was noticed only with this sample, the first thing was to unmount and remount the test rig to see whether the mode was belonging to the rig or to the specimen. The results remained unchanged and this was attributed to the specimen not being perfectly flat, with consequent excitation of bending or torsional modes. The interlocked cores are not glued between them and so there is a high chance of misalignment during the test. This could be investigated by positioning multiple accelerometers on the top skin at opposite angles, or by using a 3D scan vibrometer, and see if those unwanted modes are being solicitated.

The calculation of the mechanical loss factor and the damping of all specimens and amplitudes is shown in *Table 11*. The configuration which produced the highest value of damping was the hybrid material core, highlighted in grey. The damping ratio ξ calculated on the collected data (three different input amplitudes) denotes an increase as the amplitude is increased. Furthermore, the hybrid material interlocked core showed a higher ξ at every tested input amplitude. The polypropylene homogeneous interlocked core, while it has higher ξ at lower amplitudes, it converges towards the performance of the full PFA homogeneous interlocked core, as shown in

Sample	Ampl.	w_n	w_1	w_2	Damping, ξ	Loss factor, η
PP	0.1	988.125	960.000	1011.875	0.026	0.052
PP	0.5	973.750	938.000	1000.000	0.032	0.064
PP	1	954.375	919.000	990.000	0.037	0.074
PP/PFA	0.1	1077.500	1047.500	1111.250	0.030	0.059
PP/PFA	0.5	1051.250	1013.000	1084.000	0.034	0.068
PP/PFA	1	1013.750	973.125	1062.500	0.044	0.088
PFA	0.1	698.000	680.000	713.750	0.024	0.048
PFA	0.5	685.000	655.000	698.125	0.031	0.063
PFA	1	633.125	635.652	683.125	0.037	0.075

Table 11 - Damping ratio and loss factor

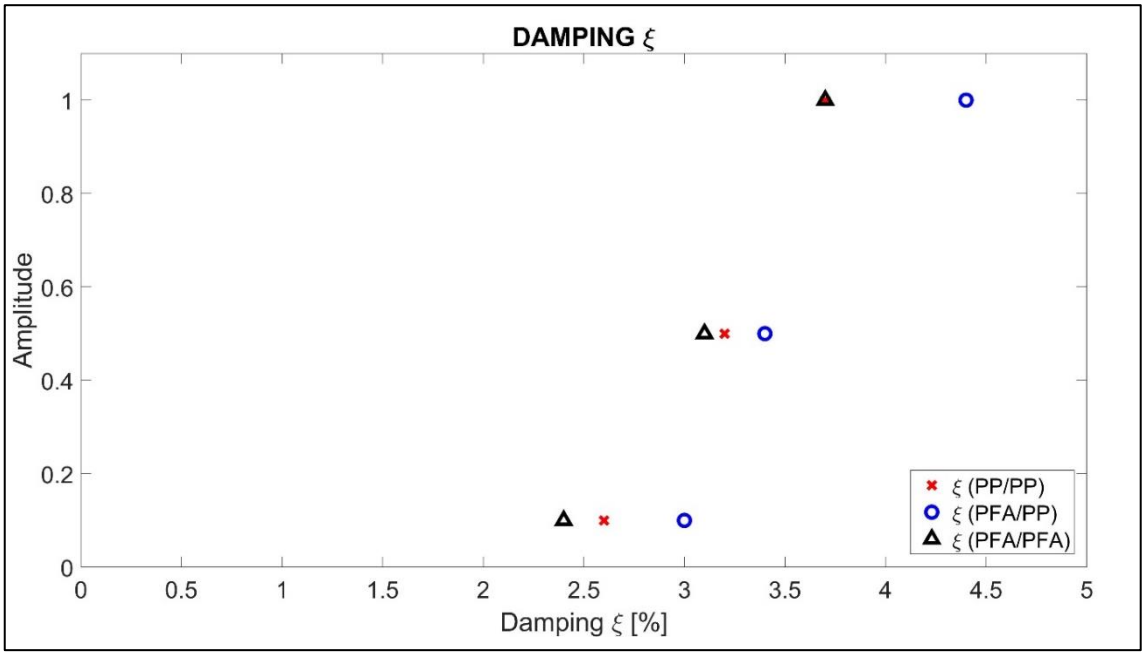

Figure 111 - Damping value obtained for interlocked PP/PP, PFA/PP and PFA/PFA cores at increasing solicitation amplitudes.

GENERAL CONCLUSIONS

The objective of this thesis was to investigate the topology effects of kirigami cellular cores and their vibroacoustic performance by exploiting the Floquet-Bloch Theory and the Wave finite element methodology. The topic is very broad, and the research had to be pursued keeping in mind the manufacturing feasibility of the investigated solutions, which led to create a new cellular core manufacturing approach, which still respected the kirigami rules. Due to the various geometries explored, a full set of tools needed to be developed to produce parametric CAD models and perform investigations following the classical "finite" approach and the WFEM "infinite" approach. Finally, the out of plane transmissibility of the interlocked selected geometry was investigated.

The kirigami concept and manufacturing technique represents a very appealing tool to produce non-conventional cellular structures. Cores with homogeneous and hybrid cells made of thermoplastics or long fibre composite materials can be produced and used for morphing applications and sandwich panels. The latter is a well-known building component and can be found in many industrial engineering fields where light and stiff structures are required. The VIPER project and the author produced an intense effort to improve its dynamic behaviour since many of its applications are in fields where multiple external excitations are transferred from the surroundings to the structure, causing acoustic discomfort and shortening its lifespan. For this reason, novel cellular cores (hybrid cell configurations produced with the polygonal tool and AuxHex), were analysed and new natural fibre composite materials with thermoplastic and bio-derived thermoset resins were explored and characterised. The intended outcome was to build structures which would also help the community to face the emerging problem which afflicts the composite material world, which is the very low recyclability of failed components and machining scraps and bypass products.

The combination of topology investigation and kirigami technique conveyed into the Interlock concept, which is a novelty in the field. Thanks to Interlock, the geometrical limiting boundaries imposed by the traditional Kirigami were overcome and this led to configurations which increased bandgap density and, in some cases, opened previously absent full bandgaps. The interlock concept has great potential in terms of energy dissipation caused by internal friction. This could be a great improvement, if the goal is to obtain vibration isolation. Furthermore, Interlock gives the possibility to detach the

assembled core and combine geometries and materials according to the required level of absorption and frequency range target. This is something which the author believes being attractive for potential industrial applications. In addition to the broadened spectrum of core geometries unleashed with Interlock which converges to Bragg bandgap tailoring, this technique also allows to create unconventional sandwich panels which constitute a prototyping platform for mechanical resonators or foam inserts embedding as well as hybrid material cellular cores.

The perspective that this ITN Joint Doctorate has conferred me, thanks to the many networking opportunities it offered, is a view of collaboration and shared effort aimed to push research boundaries a little further.

FUTURE PERSPECTIVES

The natural following step of this work would be to pursue the path of investigating the new sandwich panel assemblies.

- Numerical simulations:

Most of the numerical analyses carried out at early stages of this PhD work were conducted using beam elements to model the structures. This had a clear advantage in terms of computational time and in understanding the wave types which were propagating through the structures, but the model can be updated to elements which best represent the real cores. Especially for the transmissibility parameter, the update to solid elements would allow to model the contact forces which happen between the interlocked cores. In this way, static and dynamic coefficients could be implemented, producing more accurate results. In any case, scripts fully coded in sparse form would allow faster predictions. Ideally, a GUI interface including all the tools developed for the WFEM and FEM simulations, for classic cellular, and interlock geometries, could be produced. This could also be merged with the CNC machine cutting pattern Python script based on the kirigami-compatible polygonal cell family.
The Matlab scripts include the possibility to adding skins to the cores and therefore analyse a full sandwich panel. A possible task would be to perform a dedicated WFEM campaign to analyse the effects of adding the panel skins to the cores in terms of Bragg bandgaps.

- Manufacturing technique improvement:

The manufacturing technique has some crucial points where improvement is required. Firstly, the process needs to be tailored based on the materials to be used. Thermoplastic solutions are easier than thermoset options, mainly because the latter requires a consolidation technique with more sensitive variables. The curing process parameters of the resin as well as the optimal tooling to avoid leakage does not make thermoset prepregs the best candidates for such technique. Thermosets also tend to break during the folding process due to the fragile nature of the resin which cracks under bending forces. This has been improved by Ruzzene, as shown in a work where he replaced the resin contained in the prepreg in the folding areas, chemically, with silicone, to avoid matrix cracking. This could of course be used to produce kirigami cores and would improve the geometrical accuracy of the final structures. Thermoplastics build internal stresses as they are bent, but those can be relaxed with a thermal post process cycle. For this reason, as well as that they

do not require the matrix to reach a fluid state (no leakage problem), are why thermoplastics are better candidates for kirigami applications. Thermoplastics have also the huge advantage in terms of thermoforming time. As they only require undergoing a thermal cycle that reaches the glass transition temperature T_g and in most cases can quickly be cooled down (this may depend upon the type of crystallization desired) , they are good candidates to be used in combination with a hot press, which has definitely shorter heating and cooling ramps compared to an autoclave. Especially since the cooling may happen outside the hot press (kept at temperature), the process can be easily automated making it industrially appealing. If thermosets must be used, an improvement, since the cellular core manufactured samples were produced with the hot press and not the autoclave, is to use the latter for the thermal process since it produced better quality laminates.
As mentioned in the conclusions, Interlock allows to produce hybrid material cellular cores, which are not yet spread on the market, and the idea of having a sandwich panel where one of the interlocked cores withstands structural loads while the other increases the overall dynamic performance, is an attractive concept.
Furthermore, natural fibre skins could also be perforated with a tailored pattern or undergo a surface treatment increasing the engineered features and therefore the meta-sandwich panel intrinsic characteristic.

- Experimental work:

During the secondment at the University of Bristol, various natural fibre cores of different sizes were manufactured, and those can be used to produce different specimens like larger sandwich panels and sandwich beams for further vibroacoustic investigation tests, focussed on parameters like the loss factor and structural damping caused by frictional forces.
A deeper investigation about the transmissibility rig could also be carried out by using laser scan vibrometers to map the sample as it undergoes the out of plane solicitation test, to see if other modes are being excited other than the one of interest.

APPENDIX

NUMERICAL TOOLS OUTLINE

Here, an overview of the role of each script used for all the work performed is presented. Some of the challenges found are briefly discussed and solutions outlined, with the hope that this will be of help to the reader. In *Figure 112*, a diagram outlining the sequence with which the scripts are run, as an extension to the diagram shown in *Figure 22* and *Figure 23*.

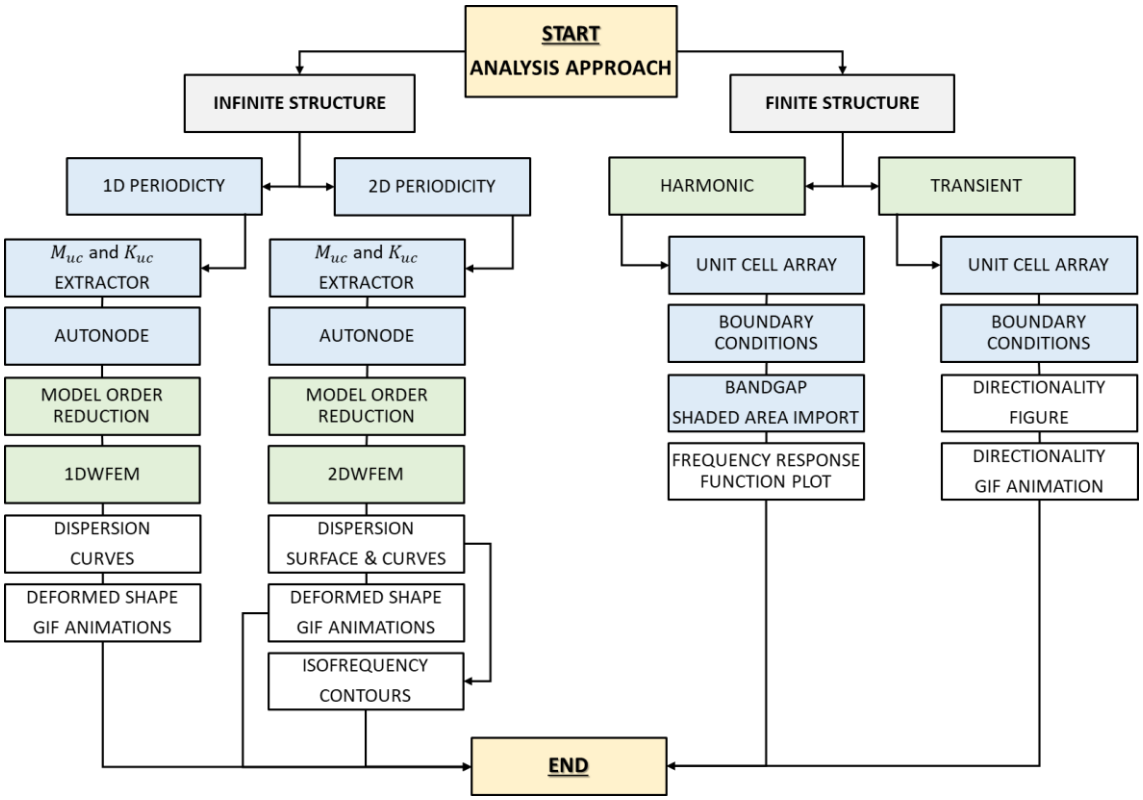

Figure 112 – Flow chart sequence for all the scripts produced. This includes numerical simulations carried out using WFEM and the classical FEM approach

Main

This script is unique to each geometry considered and it includes variables which allows to change certain geometrical features parametrically. In some cases, such variables had an impact on the topology itself. This is the case of the classic hexagonal/re-entrant configurations where the internal angle can be gradually varied to obtain one or the other configuration, or the polygonal investigation, where one of the CAD functions provided by

ANSYS was exploited allowing to create a full set of different topologies. A set of possible inputs contained in the main script which range from the material properties and unit cell variables to the mesh and type of analysis are listed in *Table 12*:

UNIT CELL GEOMETRY	MATERIAL PROPERTIES	MESH	ANALYSIS TYPE
Occupancy (L_x, L_y, L_z)	Young's Modulus	Element type	Modal
Core wall thickness	Poisson's Ratio	Element size	Harmonic
Internal angle	Density	Boundary conditions	Transient
Core height	Hysteretic damping		

Table 12 - Variables considered while writing the scripts and types of possible automated simulations

M *&* ***K*** *Extractor*

The modal analysis in ANSYS is one of the most time-efficient computations offered. To perform such analysis, ANSYS needs to calculate Mass and Stiffness matrices of the unit cell. This script has the purpose to retrieve from an output txt file these matrices in sparse form with the nodes being numbered by the software, which for future reference, will be named as "Ansys order".

Autonode

This script has the purpose to relief the user from having to know a priori which node refers to which boundary. Before, this was a requirement to be able to apply the Floquet-Bloch conditions. It retrieves information like the unit cell occupancy (L_x, L_y and L_z) from the MAIN SCRIPT and depending on the type of WFEM analysis to be performed (1D or 2D), it commands ANSYS to group the nodes according to which unit cell boundary they belong to and it prints separate txt files containing associated node number and cartesian coordinates. It then creates a new node list (which will be named "User order") according to the boundaries. The User order is then used to rearrange the extracted mass and stiffness matrices, which are in "Ansys order". The boundary combinations that the script is able to identify are, for 1D and 2D (refer to *Figure 20*):

WFEM 1D	WFEM 2D
L – R	L – R – B – T – LB – LT – RB – RT
B – T	L – R– LB – LT – RB – RT
	B – T – LB – LT – RB – RT
	L – R – B – T
	LB – LT – RB – RT

Table 13 - Possible boundary node combinations considered

The outputs of the script are the reordered M and K which can be now given in input to the Floquet Bloch formulation.

Model order reduction

This script is used when performing WFEM and is based on the model order reduction method proposed by Craig and Bampton in 1968 [64] which fits perfectly with the Floquet-Bloch formulation since it maintains the physical information contained in the boundary nodes of the unit cell [65], and condenses the nodal information belonging to the internal nodes. The eigenvalue problem therefore must deal with matrices of much smaller dimensions since the number of internal nodes is much higher than the boundary ones, reducing computational time whilst maintaining accuracy. The number of reduced internal nodes has an impact on the high frequency branch accuracy just like the model's mesh would have. The inputs here are the Mass and Stiffness matrices in "User order" and the number of internal nodes that we wish to keep.

WFEM 1D

This script is written for both Direct and Indirect formulations and it computes the eigenvalue problem according to the direction of propagation the user chooses to analyse the unit cell. The eigenvalues are either the reduced wave numbers or the angular frequency, according to the formulation chosen.

WFEM 2D

This script is written for both Direct and Indirect formulations and it computes the eigenvalue problem for wave propagation prediction for structures possessing periodicity in 2D. The eigenvalues are either the reduced wave numbers or the angular frequency, according to the formulation chosen. There are cases, especially using shell or beam elements, where nodes do not. Depending upon the number of nodes considered for the model, the number of degrees of freedom might be very high (large matrices) and this might cause, especially if using the 2DWFEM Direct form, ill-conditioning of the eigenvalue problem solutions and lead to inaccurate results.

Dispersion curves plotter

This script is written to plot dispersion curves for 1DWFEM and 2DWFEM. The user can choose to plot only propagative components or include in the plot also the evanescent

waves (Direct methods). The program is coded to identify partial or full bandgaps and shade accordingly those areas in grey. Sometimes, depending on the results and especially in 2DWFEM contour plots, bandgaps are not always evident and snap tool is required to analyse the maximum frequency of one branch and the minimum frequency of the following branch. Most of the works and journal papers seen so far had this done as a manual post-process leading sometimes to poor visual representations. With this script, the bandgaps are immediately visible and are accurate as well as elegantly displayed. The bandgap areas are stored in a matrix and can be used for validation in combination to the FRF result plots.

Dispersion surfaces plotter

This script computes the dispersion surfaces associated to the 2DWFEM analyses performed on the unit cell. In fact, by now, we know that in 2D periodic structures, the lambda vector which contains contributions from both μ_x and μ_y, scans the unit cell in its entirety and so the wave propagation in all the in-plane direction is considered. Values for μ_x and μ_y are varied between $[-\pi\,;\,\pi]$ and the eigenvalue problem solved. The visual representation of the result is a dispersion surface for each eigenvalue computed. Depending upon the symmetry of the unit cell, the values of the reduced wavenumbers van be restricted to $[0\,;\,\pi]$ since the dispersion surfaces would also be symmetric.

Iso-frequency

This MATLAB script has in input a frequency value or an array, and it creates slices of the dispersion surfaces parallel to the xy plane. The dispersion surfaces have μ_x and μ_y on the x- and y-axes respectively and the frequency on the z-axis. The visual outcome are iso-frequency contours and those can belong to a single dispersion surface of interest to the user sliced at different frequencies or several dispersion surfaces at a single frequency. The iso-frequency script is therefore based on WFEM Direct methods as frequency is given in input.

Directionality

This MATLAB script is used to visually represent the information that can be retrieved from the iso-frequency prediction. This was coded to see out-of-plane bending wave propagation in finite core panels. It writes in ANSYS language a code which creates a finite core panel of $(n \times m)$ unit cells and it commands a transient analysis. The transient analysis allows the creation of sinusoidal unit displacement (arbitrarily discretized) which is then applied to

the nodes in the centre of the panel for an arbitrarily number of cycles. As this type of simulation is time dependent, the temporal interval between one position of the displaced node and the next must be programmed according to the frequency we want to apply. The output is a visual representation of the propagating wave.

Branch tracker

Dispersion curves and contours can be difficult to visually distinguish. When we compute the eigenvalues, MATLAB does it according to the values of the reduced wave number which the user gives in input. But for each value of μ, a finite number of frequency solutions are calculated (according on the number of eigenvalues requested). The calculated array though will be ordered always from the lowest frequency to the highest, without any means to re-establish to which eigenvalue each frequency belongs.

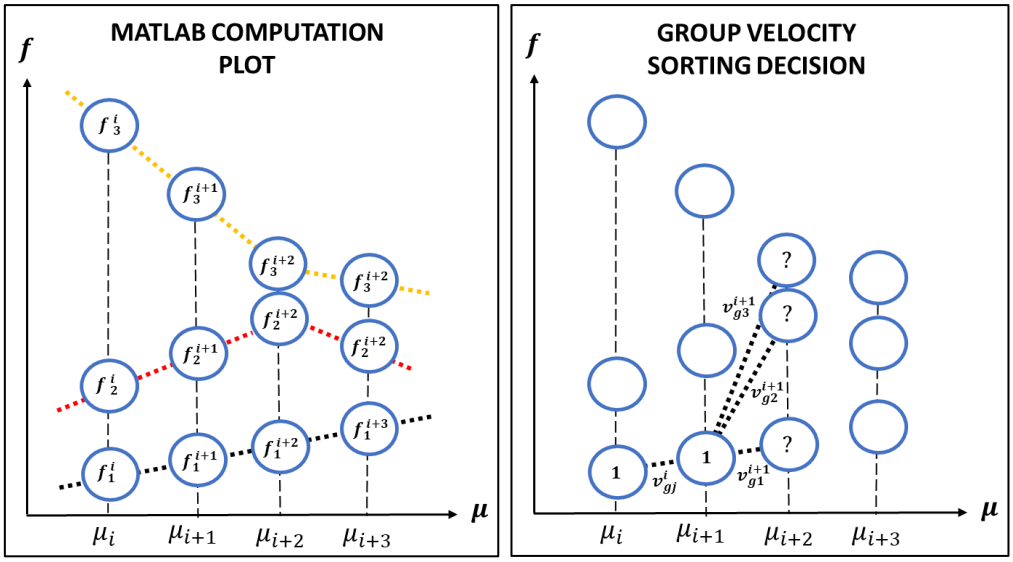

Figure 113 - Dispersion curves colour plot according to MATLAB matrix (left), and Group velocity sorting decision criteria

Another way of presenting the problem is the following: Let us supposedly compute the frequencies for the initial value of μ. The value of the first frequency calculated will be the lowest and the one computed for the second eigenvalue might have a higher value. This is not true along all the plot because some branches may cross each other. When this happens, the value of the frequency calculated for the first eigenvalue is higher in frequency than the value computed for the second eigenvalue, but this information gets lost.

In order to follow a branch in all the contour and therefore give each branch a different colour or symbol, the group velocity v_g can be used as a sorting parameter, as suggested by Billon[77]. As mentioned in section 1.4.1.1, the group velocity is represented by the steepness of the dispersion curve which is computed for discretized reduced wave numbers.

For each value of μ, several solutions (frequency values) will be available according to the number of eigenvalues which were computed. Suppose j eigenvalues were requested and i was one of the discretized values of μ: to accomplish the branch tracking, the script compares the steepness of one solution $(\mu_{\mathrm{i}}\,;\mathrm{f}_1)$ with every next value plotted $\left(\mu_{\mathrm{i+1}}\,;\mathrm{f}_{1-\mathrm{j}}\right)$ where $\mathrm{f}_{1-\mathrm{j}}$ is each frequency solution from 1 to j.

$$v_g = \frac{\delta\omega}{\delta k} \qquad\qquad \Delta v_{g\mathrm{j}}^{\mathrm{i}} = v_{g\mathrm{j}}^{i+1} - v_{g\mathrm{j}}^{\mathrm{i}} \qquad (1)$$

The value for which $\Delta v_{g\mathrm{j}}^{\mathrm{i}}$ is minimum is selected as the correct value to follow and which becomes the reference for the comparison.

Figure 113 and *Figure 114* show the decision process and the sorted curves while *Figure 115* shows the method applied to a set of dispersion curves.

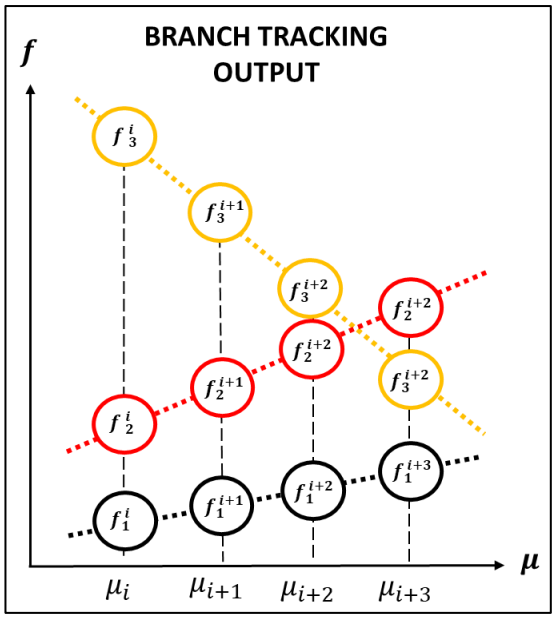

Figure 114- Branch tracking output

Although this is already of huge help this type of branch tracking has no physical meaning because it is just a mathematical exercise which sorts according to steepness. But the ideal branch tracking would be sorting the right curve according to the type of propagating wave (compression, bending, torsional). A more physical branch tracking is the one based on a MAC-derived indicator proposed by Collet[50], which later was applied to the deformed shapes of the unit cell by Laude[81], who suggested to exploit the real orthogonality properties of the shape. This script, together with each set of eigenvalues, computes the associated eigenvectors, which summed to the original position of each node, produces the deformed shape. Through a procedure very similar to the one just presented, eigenvectors

of $(\mu_i\ ; f_1)$ are compared to the ones calculated for $(\mu_{i+1}\ ; f_{1-j})$, and through a MAC criterion, the best fitting match is chosen. Clearly, the comparison done with the group velocity deals with arrays much smaller than the one used with the MAC criterion since for the latter the array dimensions are related to the number of degrees of freedom, while the group velocity method deals with arrays with dimensions according to the discretization of μ and requested eigenvalues in output.

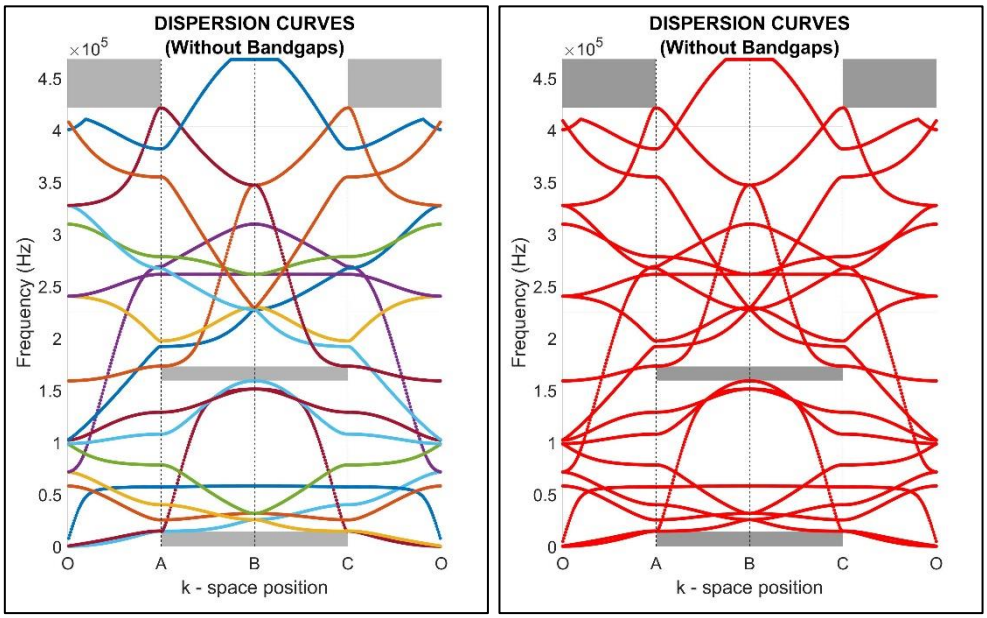

Figure 115 - Dispersion curves with Branch tracking (left) and without (right)

Deformed shape

This script calculates the eigenvectors associated to the requested eigenvalues for each value of μ. These are then summed to the original shape nodes cartesian coordinates to produce a plot of the deformed shape of the unit cell, as if it were part of an infinite panel undergoing that solicitation. The script produces different plots:

- *Multi plot*

This script produces a single figure containing the dispersion curves, the 3D original unit cell shape (skeleton in dashed lines) and deformed shape (plotted with a degree of transparency to allow the vision of the original shape) and the orthogonal projections. This can be performed for each value of μ. Also, the user can select whether to plot the deformed shape at all frequencies for a single value of μ or to plot all the intermediate nodal positions of the unit cell between deformed and original shape. The deformed shape is coloured according to the modulus of the displacement, for which a custom colour-chart was produced in RGB values.

- *Gif creator*

The figures produced with the Multi Plot script can be used to produce a GIF image to visualize a single mode vibration between its undisturbed and maximum displaced structure, or to have a quick identification of the wave type associated to each branch, as the GIF will be composed of a collection of images at a selected value of μ for all branches. Those visual tools help the user to identify whether the changes in certain physical or geometrical parameters affect a certain type of propagating wave. An example of the output figure produced for a simple plate unit-cell is shown from *Figure 116* to *Figure 119*.

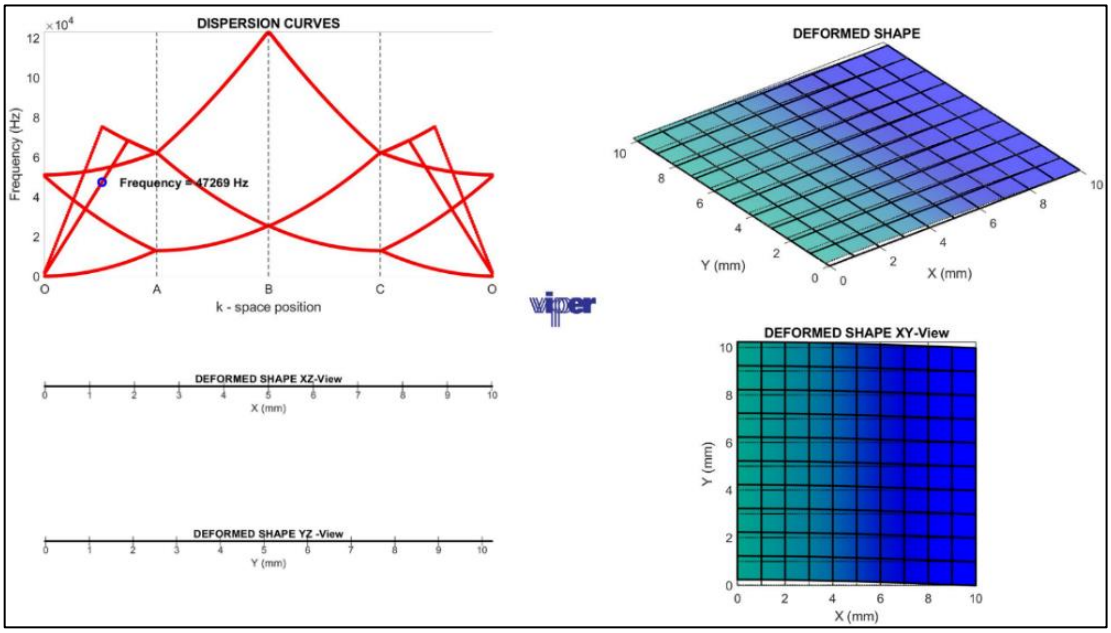

Figure 116 - Deformed shape script output (in-plane bending) for a simple plate

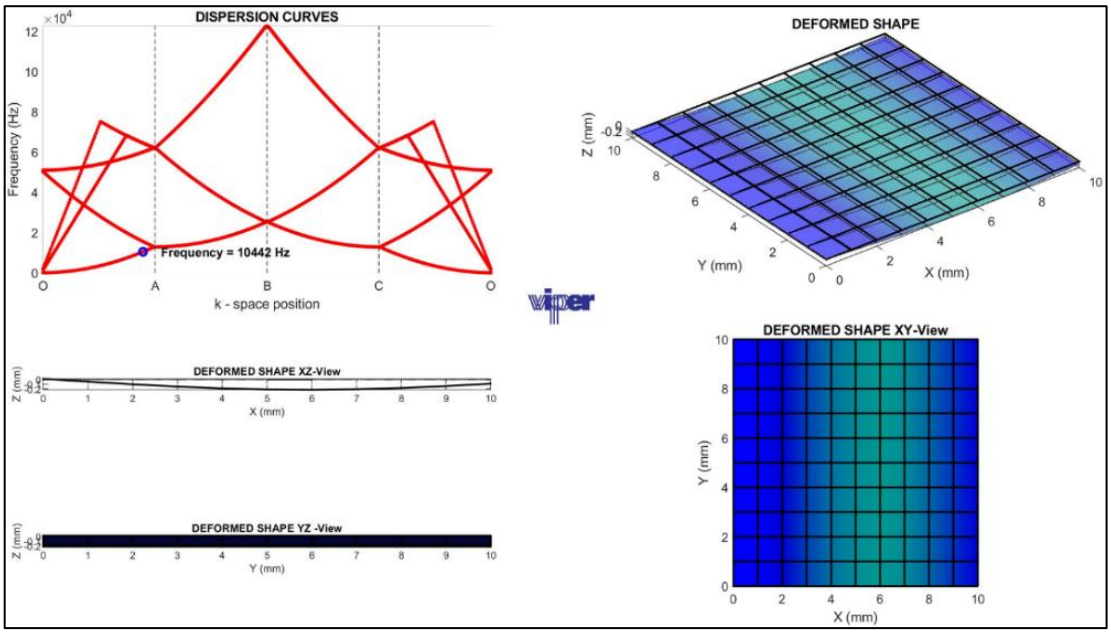

Figure 117 - Deformed shape script output (out of plane bending) for a simple plate

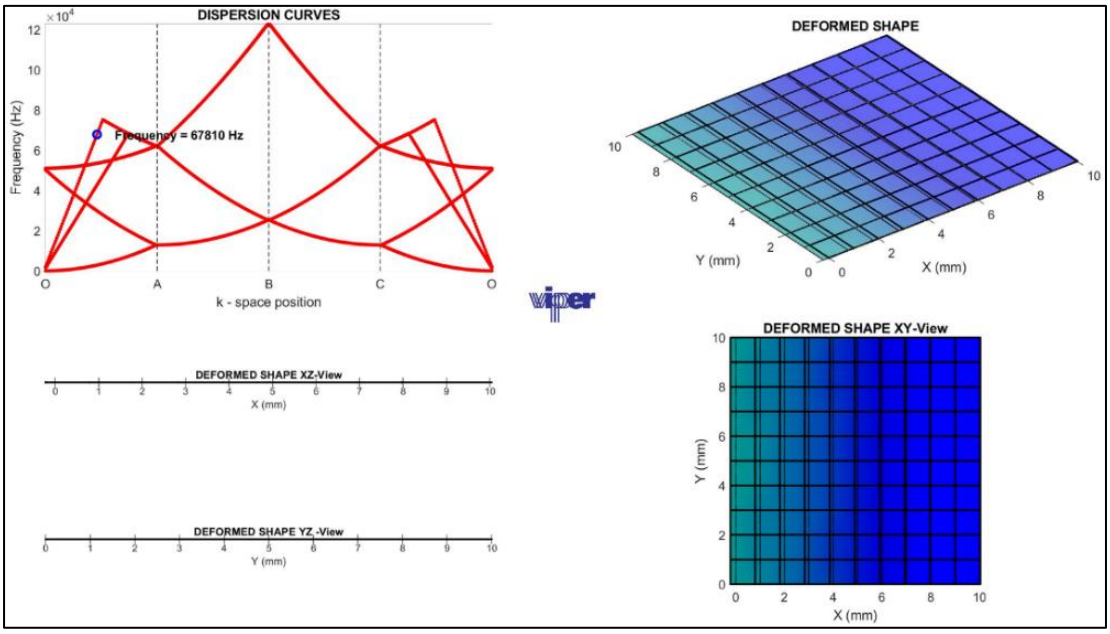

Figure 118 - Deformed shape script output (in-plane compression) for a simple plate

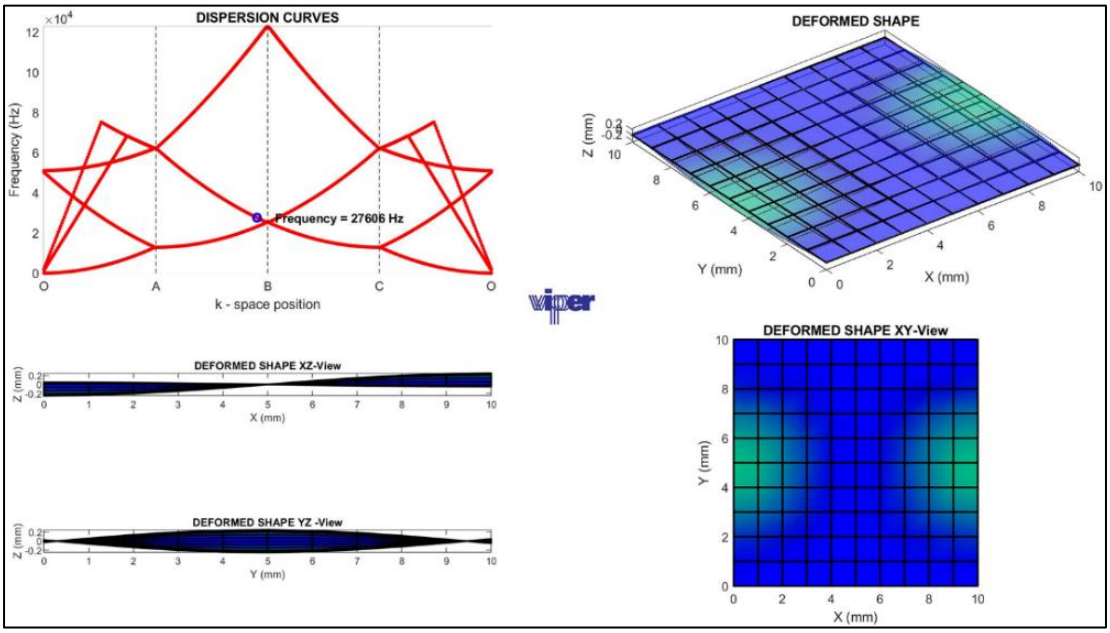

Figure 119 - Deformed shape script output (torsion) for a simple plate

FLAX/PFA EVOPREG CHARACTERISATION

STANDARD: ASTM D3039/D3039M – 17

DATES: 08/02/2019 – 12/02/2019

LOCATION: ACCIS - University of Bristol

OPERATORS: Simone Del Broccolo

No equipment problems nor anomalies occurred during the test.

MANUFACTURER: Composites Evolution

MATERIAL: Evopreg PFC502 (Fire-retardant prepreg with low environmental impact).

This is a 100% bio composite made of flax fibers and PFA (Polyfurfuryl Alcohol) thermoset bio resin matrix. The manufacturer, Composites Evolution, claims that their product, Evopreg PFC, is most well suited to markets and applications that have stringent fire requirements including mass transport (aeronautical), maritime, offshore and infrastructure. They also claim it possesses the following characteristics other than mechanical properties which makes it suitable for secondary structure components:

- Outstanding fire performance
- Non-toxic and low emissions for improved operator health and safety
- Low environmental impact
- Outstanding FST performance - passes FAR 25.853 & ABD0031 (aero), EN 45545 HL3 (rail)
- Low toxicity and low VOC emissions
- Low environmental impact
- Flexible cure temperature 120-160°C
- Suitable for vacuum bag/oven, autoclave, and press molding
- Suitable for bonding to core materials including Nomex honeycomb
- 21 days out-life at room temperature
- 6 months storage life at -18°C
- Available on a wide range of reinforcement fabrics

Standard techniques including vacuum bagging, autoclaving, and press molding can be used to produce components. The prepreg consists of a TWILL 2x2 weave with tow and yarn filaments of equal diameters. The prepreg came in two rolls of 1.25m x 20m. The batch codes are written below, and the roll reports are found as attachments.

- CE50015 FF 22T – 705 -1
- CE50015 FF 22T – 705 -2

FABRICTION OF THE LAMINATES:

The initial investigation carried out, having no experimental data nor datasheet from the manufacturer regarding the Flax/PFA prepreg combination, is the tensile test following the ASTM D3039 standard. To perform such procedure, test samples of accurate dimensions (250mm x 25mm x 2.5mm) are required. The thickness of the sample is a recommended value and it is possible to manufacture thicker samples. The post cure thickness of this laminate was also unknown, so the first step consisted in laying up different laminates and measure their thickness after the curing cycle. This allowed us to have a better idea of the type of layup necessary to produce our samples. The curing cycle on the datasheet provided by the prepreg manufacturer (temperature ramps, cooldown, and pressure), might not be suitable to our prepreg, as they refer to a glass-fibre/PFA prepreg.

A total of 6 laminate plates with 300mm x 300mm dimensions and variable thicknesses were produced by laying up on two different tool plates, 3 laminates, each one with 1 to 6 plies of prepreg. This allows us to see first, the final thickness obtained with the autoclave in function of the number of plates, and additionally the number of plies to which this curing cycle best adapts. The same curing cycle is often not optimal for different thicknesses and different heating rates and dwell times are usually required to avoid conspicuous exothermic reaction.

In parallel to the autoclave process, laminates using a HARE hot-press (up to 50t) were also manufactured.

The **AUTOCLAVE** lay-up sequence is described in the following steps:

A. Select amount of composite to manufacture depending on the test samples to be obtained.
B. Select the tool plate which would allow them to be manufacture.
C. Clean the tool plate with acetone.
D. Apply releasing agent to the tool plate.
E. Fix release film N1 to the tool plate.
F. Lay-up the composites prepreg (balanced and symmetric).
G. Apply cork strips on the laminates contour to prevent resin overflow.
H. Fix release film N1 covering all the composite and cork.
I. Apply cowl plate if required.
J. Cover with one layer of breather.

K. Position the suction valve lower parts in opportune positions.
L. Apply tacky tape on the tool plate contour.
M. Cover everything with the vacuum bag.
N. Screw in the suction valves.
O. Create void and check with the pressure gauge that no leaks are present.
P. Place in Autoclave

After those actions, the lay-up is concluded and the tool plate ready to be put into the autoclave for composite curing. The laminates were dimensioned to obtain 10 samples for tensile testing.

The **HOT-PRESS** lay-up sequence is instead the following:

A. Select amount of composite to manufacture depending on the test samples to be obtained.
B. Select the tool plate which would allow them to be manufacture.
C. Clean the tool plate with acetone.
D. Apply releasing agent to the tool plate.
E. Fix release film N1 to the tool plate.
F. Apply a cork or metallic frame on the laminate contour to prevent resin overflow.
G. Fix release film N2 over the frame.
H. Lay-up the composites prepreg (balanced and symmetric).
I. Fix release film N3 covering all the composite and cork/frame.
J. Place in the Hot-press

Phase I showed that flat laminates were only obtainable with 4plys or multiples. For tensile tests, both 4 plies and 8 plies laminates were manufactured using both autoclave and hot-press techniques.

FABRICATION DETAILS:

Start date: 16/01/2019

End date: 05/02/2019

Cure temperature	Minimum cure time
130°C	1.5 hours
140°C	45 minutes
150°C	25 minutes

Table 14 - Curing temperatures suggested from Composites Evolutions for glass fibre/PFA prepregs

- Recommended ramp rate 1-3°C/min

- Recommended pressure 3.5bar

There are two types of cure cycles. One is a single ramp up to 140°C with a 45' dwell time and the second one is a ramp up to 80°C (dwell 30') and a ramp to 140°C with a 45' dwell time.

PLY ORIENTATION:

The prepreg has been cut at 0°/90° and ±45°. Stacking of 4 or 8 plies was performed by following the basic lay-up theory; this means that plies were stacked in a balanced and symmetrical order.

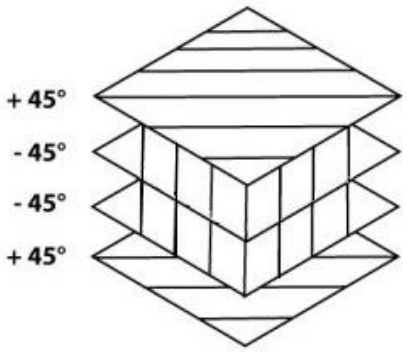

The average thickness of a single ply was 0.6mm and for the cured laminate we obtained:

- 4 PLIES: 2.2 ± 0.2 mm
- 8 PLIES: 4.5 ± 0.4 mm

SPECIMEN DESCRIPTION:

The specimens had the following dimensions, as required by the standards:

- 4 PLIES: 250mm x 25mm x 2.2 ± 0.2 mm
- 8 PLIES: 250mm x 25mm x 4.5 ± 0.4 mm

SPECIMEN PREPARATION:

The laminates produced were 300x300mm of 4 and 8 plies, respectively. This allowed us to cut out 10 samples per each laminate. The samples were cut using a diamond blade saw. The saw blade had a 2mm thickness. Samples were thoroughly cleansed using acetone before testing to avoid poor gripping. Emery paper distributed by the company 3M was used instead of end tabs as a dummy sample showed no signs of poor gripping (scratches).

The cured PFA resin has a dark colour so samples were marked and numbered using a white paint pen.

NUMBER OF SPECIMENS: Batches of 10

SPEED OF TESTING: 2mm/min

MACHINE TYPE & CALIBRATION DATE:

A Shimadzu electronic tensile test machine with a 10kN load cell was used.

TESTING LABORATORY ENVIRONMENTAL DETAILS:

Temperature: 22°C

VIDEO GAUGE:

Additionally, to the displacement recorded with the Shimadzu for each sample, a video gauge was used to measure vertical and horizontal relative displacement of several targets drawn on the sample. This allowed to measure effective strains for both, Young's modulus calculation through stress/strain plots as well as Poisson's ratio. The targets consisted in dost drawn with a white paint marker.

STRESS / STRAIN DATA:

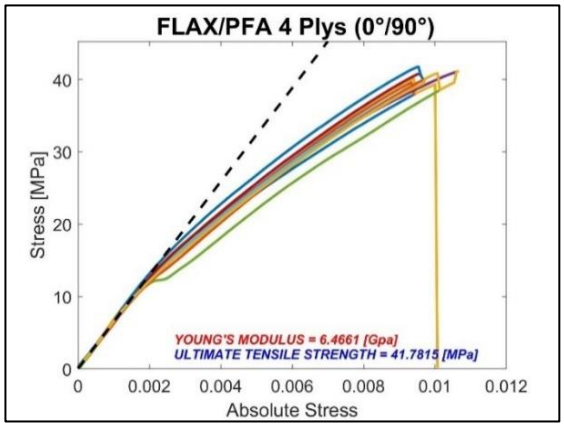

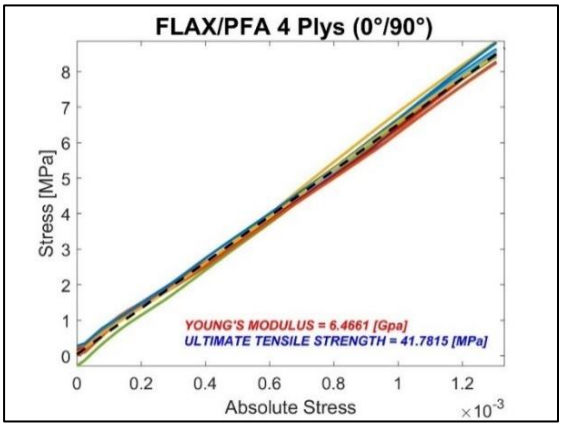

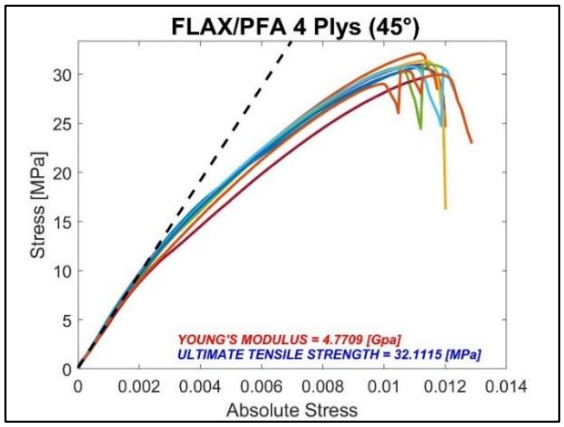

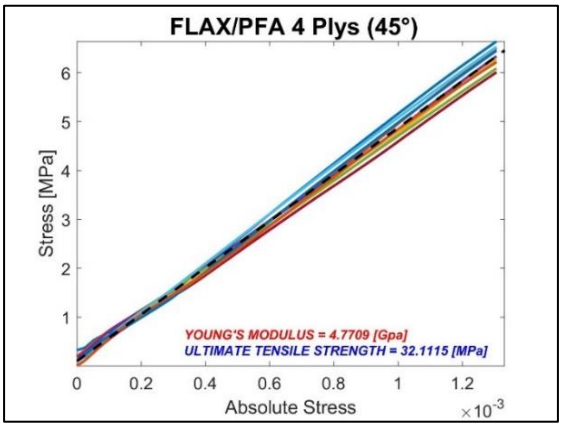

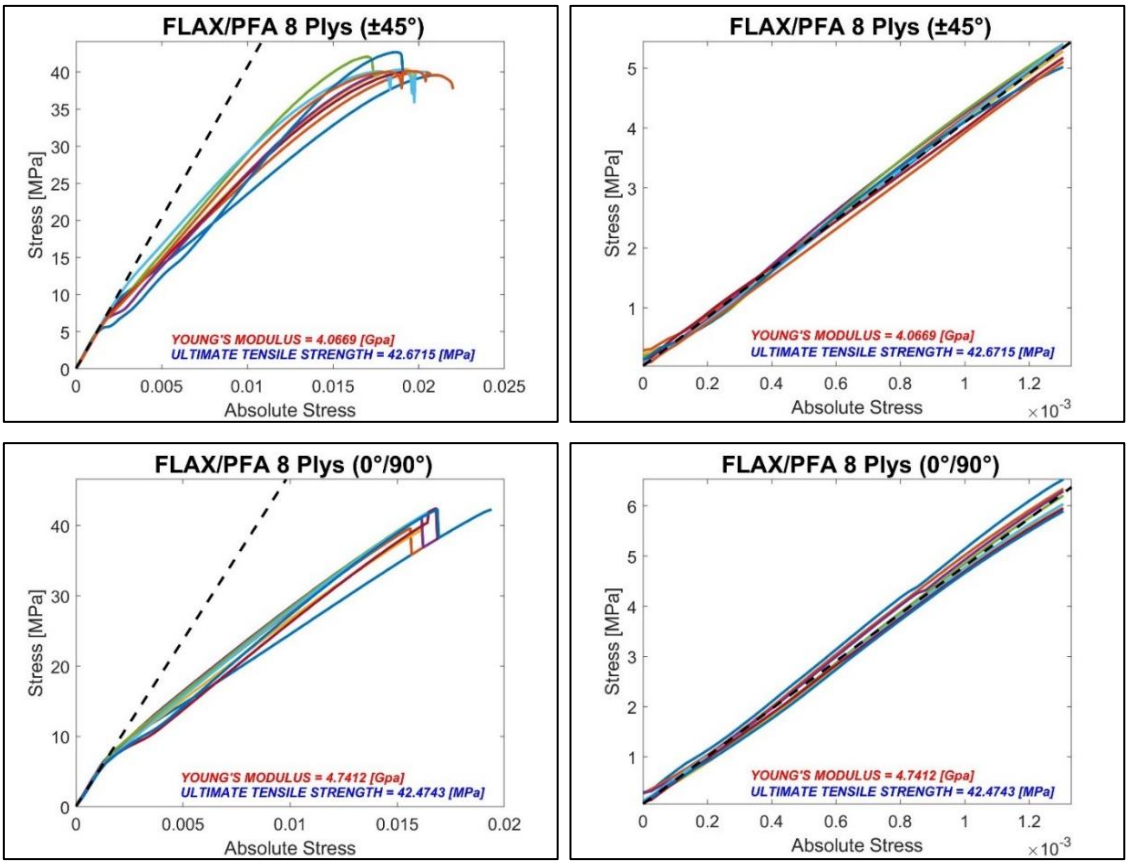

STRENGHT, [MPa]							
N°OF PLYS	**ORIENTATION**	**N°OF SAMPLES**	**Max**	**Min**	$\bar{x}$	s	CV
4	**(0/90°)**	10	41.781	39.432	40.266	0.264	0.655
8	**(0°/90°)**	9	42.474	39.392	40.913	0.531	1.298
4	**(± 45°)**	8	32.111	29.022	30.656	0.578	1.885
8	**(± 45°)**	9	42.671	39.569	40.569	0.206	0.507

Table 15 – Ultimate strength calculations for all specimen types

MODULUS, [GPa]							
N°OF PLYS	**ORIENTATION**	**N°OF SAMPLES**	**Max**	**Min**	$\bar{x}$	s	CV
4	**(0°/90°)**	10	6.740	6.196	6.466	0.009	0.133
8	**(0°/90°)**	9	4.938	4.593	4.741	0.056	1.177
4	**(± 45°)**	8	5.019	4.540	4.771	0.004	0.085
8	**(± 45°)**	9	4.258	3.871	4.067	0.043	1.069

Table 16 – Elastic modulus calculation for all specimen types

POISSON'S RATIO:

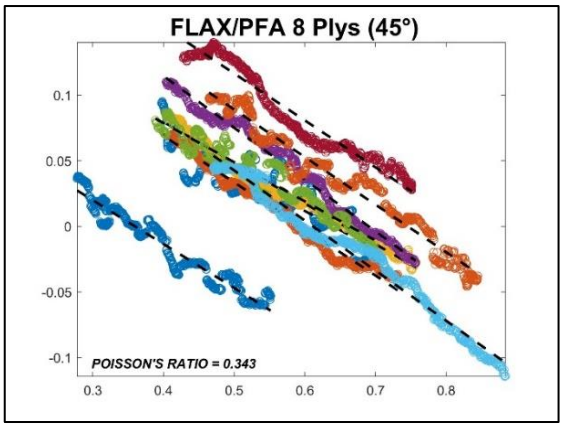

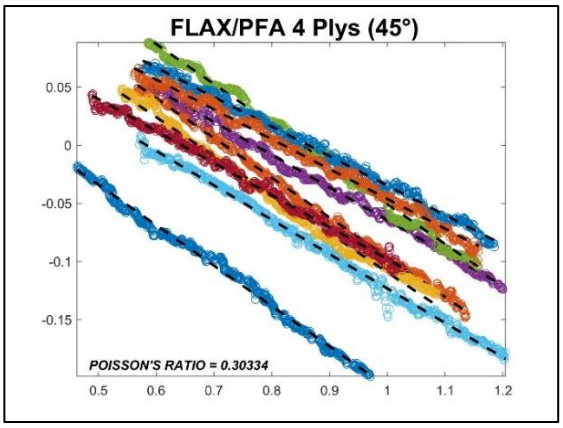

REFERENCES

[1] Brillouin, L. Wave propagation in periodic structures; electric filters and crystal lattices. 1946.

[2] Langley, M. The History of Metal Aircraft Construction. *The Aeronautical Journal* 1971, 75, 19–30.

[3] PEI curved honeycomb. https://www.euroshop-tradefair.com

[4] Carbon fiber sandwich panels. https://www.china-composites.net

[5] Scott Carpenter inside Hangar S at the White Room Facility at Cape Canaveral, Florida, examines the heat shield honeycomb on his Mercury capsule. https://www.space.com

[6] CuriOdyssey Bee honeycomb.

[7] Wikipedia Sandwich panel with honeycomb core and face sheets.

[8] Wadley, H. N. G. Multifunctional periodic cellular metals. *Philosophical Transactions of the Royal Society A: Mathematical, Physical and Engineering Sciences* 2006

[9] Origami crane. http://www.1000crane.com

[10] Papercraft, T. St. Pauls cathedral kirigami artwork.

[11] Nojima, T. Origami Modeling of Functional Structures based on Organic Patterns. *Presentation Manuscript at VIPSI Tokyo* 1996

[12] Nojima, T. and Saito, K. Development of newly designed ultra-light core structures. *JSME International Journal, Series A: Solid Mechanics and Material Engineering* 2006

[13] Neville, R. M. , Monti, A. , Hazra, K. , Scarpa, F. , Remillat, C. , and Farrow, I. R. Transverse stiffness and strength of Kirigami zero-ν PEEK honeycombs. *Composite Structures* 2014

[14] Lira, C. , Scarpa, F. , Tai, Y. H. , and Yates, J. R. Transverse shear modulus of SILICOMB cellular structures. *Composites Science and Technology* 2011

[15] Del Broccolo, S. , Laurenzi, S. , and Scarpa, F. AUXHEX – A Kirigami inspired zero Poisson's ratio cellular structure. *Composite Structures* 2017

[16] Saito, K. , Agnese, F. , and Scarpa, F. A cellular kirigami morphing wingbox concept. *Journal of Intelligent Material Systems and Structures* 2011

[17] Neville, R. M., Pirrera, A., and Scarpa, F. *In Open shape morphing honeycombs through kirigami*, 2014.

[18] Saito, K. , Pellegrino, S. , and Nojima, T. Manufacture of arbitrary cross-section composite honeycomb cores based on origami techniques. *Journal of Mechanical Design, Transactions of the ASME* 2014

[19] Zhang, X.-C. , Scarpa, F. , McHale, R. , Limmack, A. P. , and Peng, H.-X. Carbon nano-ink coated open cell polyurethane foam with micro-architectured multilayer skeleton for damping applications. *RSC Advances* 2016, 6, 80334–80341.

[20] Neville, R. M. . and Scarpa, F. *In Design of Shape Morphing Cellular Structures and their Actuation Methods*, Kobe, Japan, 2015.

[21] Systems, P. CNC Cutting and trimming.

[22] Scarpa, F. , Ouisse, M. , Collet, M. , and Saito, K. Kirigami auxetic pyramidal core: Mechanical properties and wave propagation analysis in damped lattice. *Journal of Vibration and Acoustics, Transactions of the ASME* 2013

[23] Del Broccolo, S., Palumbo, R., Campana, M.-A., Dobah, Y., Scarpa, F., Ouisse, M., and Ichchou, M. Kirigami inspired natural fibre cellular structures for future vibroacoustics applications. (2017).

[24] Ju, J. , Summers, J. D. , Ziegert, J. , and Fadel, G. Design of honeycombs for modulus and yield strain in shear. *Journal of Engineering Materials and Technology, Transactions of the ASME* 2012

[25] Schattschneider, D. The Plane Symmetry Groups: Their Recognition and Notation. *The American Mathematical Monthly* 1978, 85, 439–450.

[26] Veysseyre, R. , Weigel, D. , Phan, T. , and Veysseyre, H. Crystallography in Spaces Isomorphism. *Advances in Pure Mathematics* 2015, 05, 137–149.

[27] Shyu, T. C. , Damasceno, P. F. , Dodd, P. M. , Lamoureux, A. , Xu, L. , Shlian, M. , Shtein, M. , Glotzer, S. C. , and Kotov, N. A. A kirigami approach to engineering elasticity in nanocomposites through patterned defects. *Nature Materials* 2015

[28] Blees, M. K. , Barnard, A. W. , Rose, P. A. , Roberts, S. P. , McGill, K. L. , Huang, P. Y. , Ruyack, A. R. , Kevek, J. W. , Kobrin, B. , Muller, D. A. , and McEuen, P. L. Graphene kirigami. *Nature* 2015

[29] Scarpa, F. *In Auxetic and kirigami systems in multiphysics and EMC applications*, IEEE: 2014.

[30] Zigoneanu, L. , Popa, B. I. , and Cummer, S. A. Three-dimensional broadband omnidirectional acoustic ground cloak. *Nature Materials* 2014

[31] Cai, W. , Chettiar, U. K. , Kildishev, A. V. , and Shalaev, V. M. Optical cloaking with metamaterials. *Nature Photonics* 2007, 1, 224–227.

[32] Ergin, T. , Stenger, N. , Brenner, P. , Pendry, J. B. , and Wegener, M. Three-Dimensional Invisibility Cloak at Optical Wavelengths. *Science* 2010, 328, 337–339.

[33] Valentine, J. , Li, J. , Zentgraf, T. , Bartal, G. , and Zhang, X. An optical cloak made of dielectrics. *Nature Materials* 2009, 8, 568–571.

[34] Schurig, D. , Mock, J. J. , Justice, B. J. , Cummer, S. A. , Pendry, J. B. , Starr, A. F. , and Smith, D. R. Metamaterial electromagnetic cloak at microwave frequencies. *Science* 2006

[35] Chen, J. S. , Sharma, B. , and Sun, C. T. Dynamic behaviour of sandwich structure containing spring-mass resonators. *Composite Structures* 2011

[36] Ouisse, M., Billon, K., Sadoulet-Reboul, E., and Collet, M. *In Design of smart metamaterials for vibration control: extension of Bloch approach to handle finite system boundary conditions*, Kundu, T. Eds.; SPIE: 2018.

[37] He, Z. C. , Xiao, X. , and Li, E. Design for structural vibration suppression in laminate acoustic metamaterials. *Composites Part B: Engineering* 2017

[38] SAS, A.O. Noise reduction sandwich panel, notably for aircraft turbojet engine. (2001).

[39] Bolt, B. A. Earthquakes and Geological Discovery. Scinetific American Library: 1993.

[40] Lachat, J. C. and Watson, J. O. Effective numerical treatment of boundary integral equations: A formulation for three-dimensional elastostatics. *International Journal for Numerical Methods in Engineering* 1976

[41] Bettess, P. Infinite elements. *International Journal for Numerical Methods in Engineering* 1977

[42] Zienkiewicz, O. C. , Bando, K. , Bettess, P. , Emson, C. , and Chiam, T. C. Mapped infinite elements for exterior wave problems. *International Journal for Numerical Methods in Engineering* 1985

[43] Rizzi, S. A. and Doyle, J. F. A Spectral Element Approach to Wave Motion in Layered Solids. *Journal of Vibration and Acoustics* 1992, 114, 569–577.

[44] Lyon, R. H. Statistical Energy Analysis of Dynamical Systems. MIT Press: 1975.

[45] Langley, R. S. , Smith, J. R. D. , and Fahy, F. J. Statistical energy analysis of periodically stiffened damped plate structures. *Journal of Sound and Vibration* 1997

[46] Langley, R. S. A general derivation of the statistical energy analysis equations for coupled dynamic systems. *Journal of Sound and Vibration* 1989

[47] Mencik, J. M. and Ichchou, M. N. Multi-mode propagation and diffusion in structures through finite elements. *European Journal of Mechanics, A/Solids* 2005

[48] Mencik, J. M. New advances in the forced response computation of periodic structures using the wave finite element (WFE) method. *Computational Mechanics* 2014

[49] Mace, B. R. , Duhamel, D. , Brennan, M. J. , and Hinke, L. Finite element prediction of wave motion in structural waveguides. *The Journal of the Acoustical Society of America* 2005

[50] Mead, D. J. Wave propagation in continuous periodic structures: Research contributions from Southampton, 1964-1995. *Journal of Sound and Vibration* 1996

[51] Floquet, G. Sur les équations différentielles linéaires à coefficients périodiques. *Annales scientifiques de l'École normale supérieure* 1883

[52] Bloch, F. Über die Quantenmechanik der Elektronen in Kristallgittern. *Zeitschrift für Physik* 1929, 52, 555–600.

[53] Cremer, L.; Heckl, M.; and Petersson, B. A. T. Structure-borne sound: Structural vibrations and sound radiation at audio frequencies. 2005.

[54] Hussein, M. I. , Leamy, M. J. , and Ruzzene, M. Dynamics of phononic materials and structures: Historical origins, recent progress, and future outlook. *Applied Mechanics Reviews* 2014

[55] Mace, B. R. and Manconi, E. Modelling wave propagation in two-dimensional structures using finite element analysis. *Journal of Sound and Vibration* 2008

[56] Duhamel, D. , Mace, B. R. , and Brennan, M. J. Finite element analysis of the vibrations of waveguides and periodic structures. *Journal of Sound and Vibration* 2006

[57] Hoang, T., Duhamel, D., and Foret, G. Wave finite element method for vibration of periodic structures subjected to external loads. (2018).

[58] Thierry, V. , Brown, L. , and Chronopoulos, D. Multi-scale wave propagation modelling for two-dimensional periodic textile composites. *Composites Part B: Engineering* 2018

[59] Ruzzene, M. and Scarpa, F. *In Control of wave propagation in sandwich beams with auxetic core*, 2003.

[60] Zhong, W. X. and Williams, F. W. On the direct solution of wave propagation for repetitive structures. *Journal of Sound and Vibration* 1995

[61] Nobrega, E. D. , Gautier, F. , Pelat, A. , and Santos, J. M. C. Dos Vibration band gaps for elastic metamaterial rods using wave finite element method. *Mechanical Systems and Signal Processing* 2016

[62] Maurin, F., Claeys, C., Deckers, E., and Desmet, W. Corrigendum to "Probability that a band-gap extremum is located on the irreducible Brillouin-zone contour for the 17 different plane crystallographic lattices" [International Journal of Solids and Structures, 135 (2018) 26–36] (International Journal of So. *International Journal of Solids and Structures*. . (2020).

[63] Maurin, F. , Claeys, C. , Deckers, E. , and Desmet, W. Probability that a band-gap extremum is located on the irreducible Brillouin-zone contour for the 17 different plane crystallographic lattices. *International Journal of Solids and Structures* 2018

[64] Craig, R. R. and Bampton, M. C. C. Coupling of substructures for dynamic analyses. *AIAA Journal* 1968

[65] Fan, Y. , Zhou, C. W. , Laine, J. P. , Ichchou, M. , and Li, L. Model reduction schemes for the wave and finite element method using the free modes of a unit cell. *Computers and Structures* 2018

[66] Tian, B. Y. , Tie, B. , Aubry, D. , and Su, X. Y. Elastic wave propagation in periodic cellular structures. *CMES - Computer Modeling in Engineering and Sciences* 2011

[67] Project, V.M. VIPER School slides.

[68] Hvatov, A. and Sorokin, S. Free vibrations of finite periodic structures in pass- and stop-bands of the counterpart infinite waveguides. *Journal of Sound and Vibration* 2015

[69] Gibson, L. J. and Ashby, M. F. Cellular solids: Structure and properties, second edition. 2014.

[70] Boldrin, L. , Scarpa, F. , and Rajasekaran, R. Thermal conductivities of iso-volume centre-symmetric honeycombs. *Composite Structures* 2014

[71] Langley, R. S. The response of two-dimensional periodic structures to point harmonic forcing. *Journal of Sound and Vibration* 1996

[72] Langley, R. S. On the modal density and energy flow characteristics of periodic structures. *Journal of Sound and Vibration* 1994

[73] Ruzzene, M., Scarpa, F., and Soranna, F. Wave beaming effects in two-dimensional cellular structures. *Smart Materials and Structures*. . (2003).

[74] Ruzzene, M. , Mazzarella, L. , Tsopelas, P. , and Scarpa, F. Wave propagation in sandwich plates with periodic auxetic core. *Journal of Intelligent Material Systems and Structures* 2002

[75] Ruzzene, M. and Scarpa, F. Directional and band-gap behavior of periodic auxetic lattices. *Physica Status Solidi (B) Basic Research* 2005

[76] Jeong, S. M. and Ruzzene, M. *In Directional and band-gap behavior of periodic grid-like structures*, 2004.

[77] Billon, K. , Zampetakis, I. , Scarpa, F. , Ouisse, M. , Sadoulet-Reboul, E. , Collet, M. , Perriman, A. , and Hetherington, A. Mechanics and band gaps in hierarchical auxetic rectangular perforated composite metamaterials. *Composite Structures* 2017

[78] Jones, D. I. G. Handbook of Viscoelastic Vibration Damping. Wiley: 2001.

[79] Irvine, T. The half power bandwidth method for damping calculation. (2005).

[80] Collet, M. , Ouisse, M. , Ruzzene, M. , and Ichchou, M. N. Floquet-Bloch decomposition for the computation of dispersion of two-dimensional periodic, damped mechanical systems. *International Journal of Solids and Structures* 2011

[81] Laude, V. , Escalante, J. M. , and Martínez, A. Effect of loss on the dispersion relation of photonic and phononic crystals. *Physical Review B - Condensed Matter and Materials Physics* 2013

[82] Neville, R. M. , Scarpa, F. , and Pirrera, A. Shape morphing Kirigami mechanical metamaterials. *Scientific Reports* 2016, 6, 31067.

[83] Evolution, C. Evopref PFC502 Provisional data sheet.

[84] ASTM International ASTM 3039/D3039M Standard test method for tensile properties of polymer matrix composite materials.

[85] Phillips, S. , Baets, J. , Lessard, L. , Hubert, P. , and Verpoest, I. Characterization of flax/epoxy prepregs before and after cure. *Journal of Reinforced Plastics and Composites* 2013

[86] ASTM International ASTM Standard C365/C365M, 2003, 'Standard Test Method for Flatwise Compressive Properties of Sandwich Cores'. *Current.* , i, 2–4. (2003).

[87] Mahmoudi, S. , Kervoelen, A. , Robin, G. , Duigou, L. , Daya, E. M. , and Cadou, J. M. Experimental and numerical investigation of the damping of flax–epoxy composite plates. *Composite Structures* 2019

[88] Prabhakaran, S., Krishnaraj, V., Senthil Kumar, M., and Zitoune, R. *In Sound and vibration damping properties of flax fiber reinforced composites*, 2014.

[89] Huang, G. and Liu, L. Research on properties of thermoplastic composites reinforced by flax fabrics. *Materials & Design* 2008, 29, 1075–1079.

[90] Del Broccolo, S., Ouisse, M., Foltete, E., and Scarpa, F. Bandgap investigation of hierarchical isovolumetric periodic cores with negative Poisson's ratio. (2019).

[91] Del Broccolo, S., Ouisse, M., Foltete, E., and Scarpa, F. Interlocked hybrid-cell Kirigami inspired cellular structures and their vibroacoustic performance. (2018).

[92] Del Broccolo, S., Ouisse, M. , Foltete, E. , and Scarpa, F. Bandgap capability of hybrid Kirigami inspired cellular structures. *Advances in Aircraft and Spacecraft Science* 2019, 6, 481–497.

[93] Biotex EC-TDS-Biotex Flax/PP Data sheet.

[94] Lamoureux, A. , Lee, K. , Shlian, M. , Forrest, S. R. , and Shtein, M. Dynamic kirigami structures for integrated solar tracking. *Nature Communications* 2015

[95] Chronopoulos, D. Wave steering effects in anisotropic composite structures: Direct calculation of the energy skew angle through a finite element scheme. *Ultrasonics* 2017, 73, 43–48.

[96] Gonella, S. and Ruzzene, M. Analysis of in-plane wave propagation in hexagonal and re-entrant lattices. *Journal of Sound and Vibration* 2008

[97] Droz, C. , Zergoune, Z. , Boukadia, R. , Bareille, O. , and Ichchou, M. N. Vibro-acoustic optimisation of sandwich panels using the wave/finite element method. *Composite Structures* 2016

[98] Lorato, A. , Innocenti, P. , Scarpa, F. , Alderson, A. , Alderson, K. L. , Zied, K. M. , Ravirala, N. , Miller, W. , Smith, C. W. , and Evans, K. E. The transverse elastic properties of chiral honeycombs. *Composites Science and Technology* 2010

[99] Zhu, D. , Huang, X. , Hua, H. , and Zheng, H. Vibration isolation characteristics of finite periodic tetra-chiral lattice coating filled with internal resonators. *Proceedings of the Institution of Mechanical Engineers, Part C: Journal of Mechanical Engineering Science* 2016

[100] Boucher, M. A. , Smith, C. W. , Scarpa, F. , Rajasekaran, R. , and Evans, K. E. Effective topologies for vibration damping inserts in honeycomb structures. *Composite Structures* 2013

[101] Greaves, G.N., Greer, A.L., Lakes, R.S., and Rouxel, T. Poisson's ratio and modern materials. *Nature Materials*. . (2011).

[102] Huang, J. , Zhang, Q. , Scarpa, F. , Liu, Y. , and Leng, J. In-plane elasticity of a novel auxetic honeycomb design. *Composites Part B: Engineering* 2017

[103] Collet, M., Ouisse, M., Scarpa, F., and Ichchou, M. *In Kirigami pyramidal auxetic active core for wave propagation control*, 2014.

[104] Rafsanjani, A. , Derome, D. , Guyer, R. A. , and Carmeliet, J. Swelling of cellular solids: From conventional to re-entrant honeycombs. *Applied Physics Letters* 2013

[105] Lira, C. and Scarpa, F. Transverse shear stiffness of thickness gradient honeycombs. *Composites Science and Technology* 2010

[106] Yan, L. , Chouw, N. , and Jayaraman, K. Flax fibre and its composites – A review. *Composites Part B: Engineering* 2014, 56, 296–317.

[107] Boldrin, L. , Hummel, S. , Scarpa, F. , Maio, D. Di , Lira, C. , Ruzzene, M. , Remillat, C. D. L. , Lim, T. C. , Rajasekaran, R. , and Patsias, S. Dynamic behaviour of auxetic gradient composite hexagonal honeycombs. *Composite Structures* 2016

[108] Zuhri, M. Y. M. , Guan, Z. W. , and Cantwell, W. J. The mechanical properties of natural fibre based honeycomb core materials. *Composites Part B: Engineering* 2014, 58, 1–9.

[109] Ampatzidis, T. and Chronopoulos, D. Mid-frequency band gap performance of sandwich composites with unconventional core geometries. *Composite Structures* 2019

[110] Petrone, G. , Rao, S. , Rosa, S. De , Mace, B. R. , Franco, F. , and Bhattacharyya, D. Initial experimental investigations on natural fibre reinforced honeycomb core panels. *Composites Part B: Engineering* 2013

[111] Yan, L. , Chouw, N. , and Jayaraman, K. Flax fibre and its composites - A review. *Composites Part B: Engineering* 2014

[112] Scarpa, F. *In Auxetic and kirigami systems in multiphysics and EMC applications*, 2014.

FIGURE LIST

TABLE LIST

CREDITS

MARIE SKŁODOWSKA-CURIE ACTIONS (ITN)

Project name

Academic Partners

Industrial Partners

This project has received funding from the European Union's Horizon 2020 research and innovation programme under Marie Curie grant agreement No 675441